

# **SURFACE MODIFICATION OF MATERIALS BY CUMULATIVE LASER IRRADIATION**

STEPHEN R. FOLTYN

Los Alamos National Laboratory  
Los Alamos, New Mexico

## **4.1 INTRODUCTION**

Pulsed laser deposition (PLD) is often described as a three-step process consisting of vaporization of a target material, transport of the vapor plume, and film growth on a substrate. These steps are repeated thousands of times in a typical deposition run. If each laser pulse were incident on a virgin target surface or if the target were left unchanged after each pulse, these three steps would indeed provide a complete description of PLD, and there would be no need for this chapter.

Laser pulses rarely, however, remove material in a clean, orderly, layer-by-layer fashion. Instead, laser-irradiated surfaces become altered both physically and chemically. Morphological changes take the form of periodic structures such as ripples, ridges, and—the most intriguing features of all—cones. In addition, laser exposure of compound materials typically results in a modified surface layer having a composition much different from that of the original target material. The net effect of these changes is that, at some point during film deposition, the irradiated target surface bears very little resemblance to that which was load locked into the vacuum chamber before film deposition began. In this chapter we examine the various manifestations of target modification and discuss the mechanisms at work. In addition, and perhaps of greatest importance to those practicing the art of PLD, we detail the effects of target modification on both the process and the product.

## **4.2 THERMAL RESPONSE OF THE TARGET TO A LASER PULSE**

Studies on the coupling of high optical flux densities into absorbing media began in the early 1960s when invention of the laser brought about an

unprecedented ability to concentrate light on a target. In Ready's now classic 1971 text, the mechanisms and effects of laser-material interactions were considered in detail. Issues of relevance here included calculations and data on surface temperatures, melt depths, hole depths, and vaporization velocities, all as functions of incident flux density. Details of the process of material removal at fluence levels relevant to PLD were elaborated in a four-part series by Rothenberg and Kelly (1984), Kelly et al. (1985), Kelly and Rothenberg (1985), and Dreyfus et al. (1986); a comprehensive theory of PLD is presented by Kelly in the preceding chapter.

For the purpose of elucidating the mechanisms of surface modification, however, we turn to the work of Singh and Narayan (1989). Using a finite-difference analysis of the one-dimensional heat flow equation, the authors provide a quantitative model of the rapid thermal cycle induced in a solid by a laser pulse. This analysis was later extended (Singh et al., 1991) to include evaporative cooling effects at the surface. Details of the thermal cycle depend on laser fluence and pulse length; the optical absorption coefficient; and thermal properties of the solid, such as heat capacity and conductivity. A brief qualitative summary of points relevant to surface modification follows:

1. The maximum temperature reached in the solid, and the melt depth, increase with laser fluence.
2. The thermal pulse penetrates deeper into solids with low absorption coefficients and high thermal conductivities.
3. Shorter pulse lengths produce higher melting and solidification velocities.

As a consequence of the interrelationships between laser-pulse conditions and the thermal and optical properties of the solid being irradiated, the terms "low" or "high" fluence as used in this chapter are not absolute, but instead are relative measures that depend on the optical and thermal properties of the material being irradiated.

The basic thermal cycle is illustrated in Figure 4.1.

### 4.3 LOW-FLUENCE IRRADIATION: LASER-INDUCED PERIODIC SURFACE STRUCTURES

The earliest studies of surface modification by lasers (we neglect in this chapter the high-power or high fluence laser material interactions employed in cutting, welding, drilling, and so forth, in order to better focus on the lower fluence levels appropriate to PLD) were concerned not with thin-film deposition, but instead with a fundamental obstacle to the operation of high-power lasers: the unfortunate tendency of laser energy to destroy the optical components that create, shape, and direct the beam. The formal history of this field is embodied in the proceedings of the Conference on Laser-Induced Damage in Optical

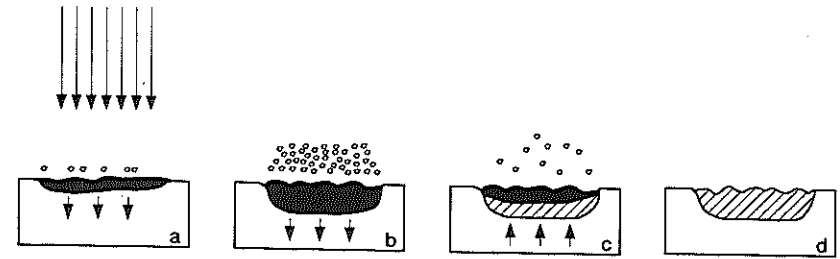


**Figure 4.1.** Schematic of the basic thermal cycle induced by a laser pulse. (a) Laser pulse is absorbed, melting and vaporization begin (shaded area indicates melted material, arrows indicate motion of the solid-liquid interface). (b) Melt front propagates into the solid, accompanied by vaporization. (c) Melt front recedes (cross-hatched area indicates resolidified material). (d) Solidification complete, frozen capillary waves alter surface topography. The next laser pulse will interact with some or all of the resolidified material.

Materials (1969–present), but even before this conference began, Birnbaum (1965) had described a new and interesting optical damage phenomenon, which is worthy of examination here because it is observed at the lower limit of PLD fluence levels.

What Birnbaum described was a stable pattern, formed on a polished Ge surface by ruby laser irradiation, that consisted of a series of parallel grooves or ripples with a period of 2–3  $\mu\text{m}$ . The proposed formation mechanism was nonuniform etching caused by diffraction effects at the focus of a lens. An example of a more complex ripple pattern, produced in an aluminum mirror with a single unpolarized pulse at 248 nm, is shown in Figure 4.2.

Ripples were again the topic when Emmony et al. (1973) investigated Ge mirror damage by  $\text{CO}_2$  laser radiation. This time, however, the ripple pattern was ascribed to interference between the incident beam and radiation scattered parallel to the mirror surface by dust or scratches. One interesting prediction of this theory was the possibility of two different ripple periods, depending upon whether the scattered wave had components traveling with or against the incident wave vector. Specifically, the period ( $d$ ) was expressed as:

$$d = \frac{\lambda}{1 \pm \sin \theta}$$

where  $\lambda$  is the laser wavelength and  $\theta$  the incident angle. This prediction was successfully tested, prompting a rich exchange in the technical literature that continues to this day.

By the early 1980s ripple patterns, now known as *laser-induced periodic surface structures* (LIPSS), had been produced in metals, semiconductors, and

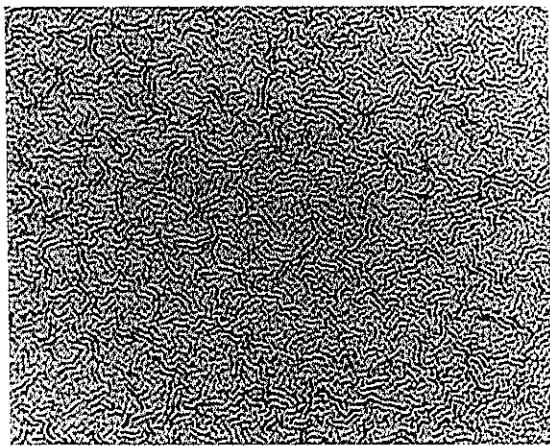


Figure 4.2. Laser-induced periodic surface structure produced on an aluminum mirror with a single 248-nm pulse at  $0.3 \text{ J/cm}^2$ . The ripple spacing is approximately  $1 \mu\text{m}$ .

dielectrics, by laser light ranging from visible wavelengths to the midinfrared. Patterns were created with linearly, circularly, and unpolarized radiation. The formation of periodic surface structure was referred to as a "universal phenomenon" by van Driel et al. (1982), although numerous modifications and revisions of the simple scattered surface wave model were required to accommodate the growing body of experimental results.

Temple and Soileau (1981) invoked a model for dielectric materials in which the interfering field is a result of induced polarization charge on defect boundaries. This led to a predicted ripple spacing of  $\lambda/n$  (where  $n$  is the index of refraction), which was experimentally confirmed in a number of dielectrics by Soileau and Van Stryland in 1982. Other aspects of this work were growth of ripple patterns due to the constructive nature of the fields produced by the ripples themselves, and the measurement of increased optical absorption for rippled surfaces.

In the next theoretical refinement, Keilmann and Bai (1982) described ripple patterns in quartz as holographic recordings of surface polaritons that are launched by defects such as scratches and dust. This model led to a revision of ripple spacing to incorporate the polariton phase velocity ( $v_{ph}$ ):

$$d = \frac{\lambda}{(c/v_{ph})^2 - \sin^2 \theta^{1/2}}$$

Young et al. (1982) pointed out that the propagating surface waves need not originate at such extrinsic defects as dust and scratches, but can be generated

as a result of roughness and inhomogeneity characteristic of any surface. In a further generalization of ripple formation models, van Driel et al. (1982) demonstrated that approximately 20 laser pulses could produce a steady-state pattern that was independent of the original surface condition, and that such patterns could be expected on any material.

Detailed theoretical works followed (Ehrlich, 1982; Guosheng et al., 1982; Sipe et al., 1983) that provided comprehensive—and in some areas divergent—explanations for ripple formation. A comparison of the Sipe theory with experimental results was published by Young et al. (1983), and in Young et al. (1984) the role of laser fluence in producing different types of surface morphology on Ge was investigated. This latter work also introduced the concept of ripple formation at higher fluence levels by the freezing of capillary waves that are induced by the laser in a uniformly melted surface.

Confirming the connection between surface interference and the thermal nature of ripple formation, Kerr et al. (1988) demonstrated the existence of a transient periodic heating pattern in the 248-nm irradiation of GaAs and Ge, and a direct correlation between this pattern and ripple formation. Clark and Emmony (1989b), and Clark et al. (1989a), proposed a mechanism for ripples of anomalously large period that were observed at higher 248-nm fluence levels. This mechanism involved the constructive interference at a beat frequency of two surface waves of slightly different period. Finally, Niino and Yabe (1992), studying the excimer laser etching of polymers, reported a monotonic increase in ripple period with incident laser fluence, suggesting a relationship between spacing and laser penetration depth.

The study of LIPSS is aimed mainly at understanding low-fluence laser-material interactions that lead to reduced performance or failure of optical components. In the following sections we examine surface phenomena that are produced at the higher fluence levels employed to vaporize material in sufficient quantities for practical film growth. These higher levels of irradiation also produce periodic surface structures, but ones that have a significantly different character than that already described. Whether ripples are strictly a low-fluence phenomenon, or a precursor to these larger scale structures is not clear at this time; either way, LIPSS is an important consequence of the laser irradiation of solids. Figure 4.3 is an illustration of the melting behavior and surface modification of solids in three relevant fluence regimes.

#### 4.4 IRRADIATION AT PLD FLUENCE LEVELS: CONE FORMATION

As part of a 1984 study of the mechanisms of laser sputtering, Rothenburg and Kelly, irradiating single-crystal  $\text{Al}_2\text{O}_3$  at 266 nm, reported that after a few hundred pulses a pattern of unusual conical structures had formed in the bottom of the etch pit. This pattern, as with Birnbaum, was attributed to

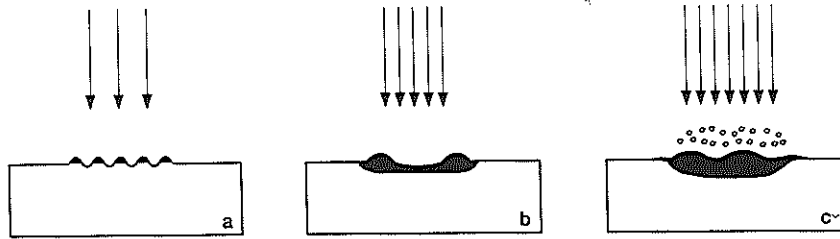


Figure 4.3. Schematic response of a solid to three fluence levels. (a) At low fluence, near the threshold for surface modification, periodic melting leads to ripple formation. (b) At higher fluence, the surface is uniformly melted and larger scale capillary waves develop. (c) At PLD fluence levels the melt depth is greater and significant vaporization occurs, and capillary waves still form.

diffraction effects in the beam. In support of this hypothesis, it was noted that scanning the target produced linear features in the scan direction instead of cones, and that irradiation—also at  $0.5 \text{ J/cm}^2$ —with a spatially incoherent KrF laser produced no cones.

This was the first of numerous reports—summarized in Table 4.1—detailing cone formation in laser irradiated materials. As seen in the table, this phenomenon occurs more generally in cases without the aforementioned diffraction effects (e.g., with scanned excimer beams), and, as with LIPSS, cone formation appears to be a universal response of solids to repetitive laser exposure in a specific fluence range. PLD is typically carried out in this range (while there is no precise value suitable for the deposition of thin films, fluence levels between 1 and  $10 \text{ J/cm}^2$  are common, in contrast to the  $0.1$ – $1 \text{ J/cm}^2$  range in which LIPSS is usually observed). As an illustration of cone formation at various fluence levels, a rotating target of the superconducting material  $\text{YBa}_2\text{Cu}_3\text{O}_{7-\delta}$  (YBCO) was continuously irradiated at  $308 \text{ nm}$ ,  $10 \text{ Hz}$ , producing a circular track. The total exposure was  $\sim 1000$  shots/site, this being calculated by multiplying the total number of shots by the ratio of beam area to total exposed area. Figure 4.4a is a scanning electron microscope (SEM) image of a portion of the track. Cones have formed in the center of the beam, where the fluence was  $5.6 \text{ J/cm}^2$ ; at the track's edge, in the low fluence wings of the beam's Gaussian intensity distribution, LIPSS is evident. Figure 4.4b shows higher magnification views of the cones, and c shows the transition region between ripples and cones.

#### 4.4.1 Attributes of Laser Cones

While there is considerable variation in reported cone morphology, the following description provides a general set of cone attributes. What are here

TABLE 4.1 Laser-Induced Cone Formation

Target Material	Laser/Fluence	No. of Pulses	Suggested Mechanism	Comments	Reference
Single-crystal $\text{Al}_2\text{O}_3$	266 nm, 6 ns $0.5 \text{ J/cm}^2$	100s	Diffraction effects	LIPSS but no cones at 248 nm, same fluence	Rothenberg and Kelly (1984)
Single crystal Si	248 nm, 12 ns $6 \text{ J/cm}^2$		Cumulative thermal expansion	Cones above surface, LIPSS at edge	Rothenberg and Kelly (1984)
$\text{Al}_2\text{O}_3$ , MgO, $\text{MgO} \cdot \text{Al}_2\text{O}_3$ , $\text{SiO}_2$ , glass	193 nm, 12 ns $2.5 \text{ J/cm}^2$	$\sim 3000$	Plasma-surface interaction	No cones unless target masked, reduced etch rate	Kelly (1985a)
Al	248 nm, 12 ns $2.8 \text{ J/cm}^2$	2000	Hydrodynamic sputtering	Droplets on cone tips	Kelly (1985b)
CdTe/InSb	$1.06 \mu\text{m}$ , 90 ns $2/4 \text{ J/cm}^2$	1000	Related to plasma/indium spheres	Reduced deposition rate observed	Dubowski (1986)
Polyimide, PET	308 nm, 8 ns $70 \text{ mJ/cm}^2$	300	Seeded impurities, redeposition	Cone shape related to fluence	Dyer et al. (1986)
YBCO	308 nm, 45 ns $3 \text{ J/cm}^2$	100s	Melting and resolidification	Comparison with sputter cones, Cu deficient	Auciello and Krauss (1988a), Auciello et al. (1988b)
Polyimide, PET	308 nm, 7–300 ns $0.1 \text{ J/cm}^2$	$\sim 600$	Redeposition	Cones removed at high fluence	Taylor et al. (1988)
YBCO	193 nm $0.41 \text{ J/cm}^2$	5000	Melting and resolidification	Cu-rich, Y-deficient	Sudarsan et al. (1988)
YBCO	248 nm, 25 ns $0.2 \text{ J/cm}^2$	2000	Redeposition		Geohegan et al. (1988)
YBCO	193 nm, 30 ns $7 \text{ J/cm}^2$	$\sim 1000$	Related to phase segregation	Deposition rate correlated with cone formation	Hoffman (1990)
BN	308 nm, 20 ns $6 \text{ J/cm}^2$	$\leq 2000$		Cones on edge of irradiated area (low fluence)	Folyn et al. (1990)
YBCO	248 nm, 22 ns $4 \text{ J/cm}^2$	$\sim 2000$		Fluence affects falloff of deposition rate	Doll et al. (1991)
YBCO	308 nm, 20 ns $2$ – $8 \text{ J/cm}^2$	$\leq 2000$		Cones track angle of incidence, high fluence restores rate	Folyn et al. (1991)
Polyimide	248 nm, 16 ns $40$ – $480 \text{ mJ/cm}^2$	100–2000	Y-rich "cap rocks"		Krajnovich and Vasquez (1992a)
Graphite (HOPG)	248 nm, 16 ns $0.7 \text{ J/cm}^2$	4000	C-rich "radiation hardening"		Krajnovich et al. (1992b)



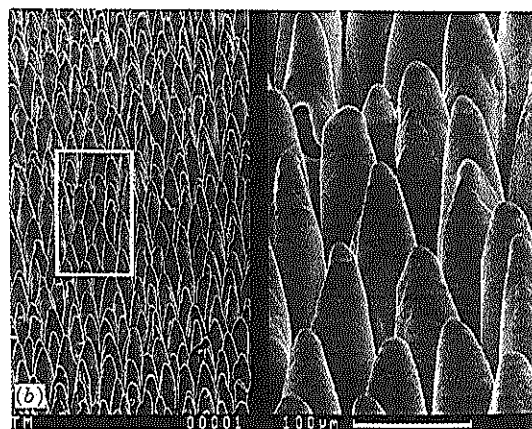
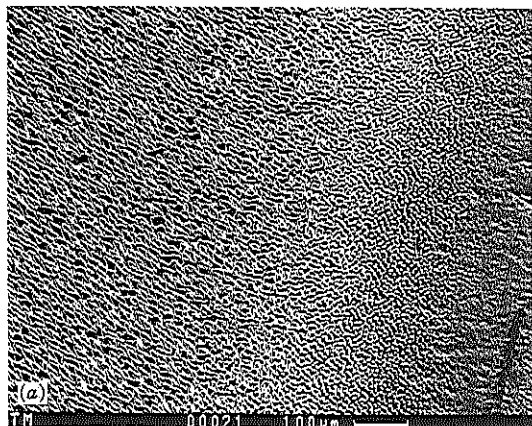


**Figure 4.4.** Low-magnification scanning electron micrograph of a track produced in a rotating YBCO target. Exposed at 308 nm to approximately 1000 shots/site, the track has been irradiated at a range of fluence values because of the beam's Gaussian intensity distribution. (a) Peak laser fluence of  $5.6 \text{ J/cm}^2$  produced the cone-populated surface at left, lower fluence levels produced the LIPSS patterns at right center, and unexposed target is visible at far right. (b) Higher magnification views of cone structures produced at  $5.6 \text{ J/cm}^2$ . Scale marker is for the left half of the micrograph. (c) Transition region between cones and ripples; fluence in this region was approximately  $1 \text{ J/cm}^2$ .

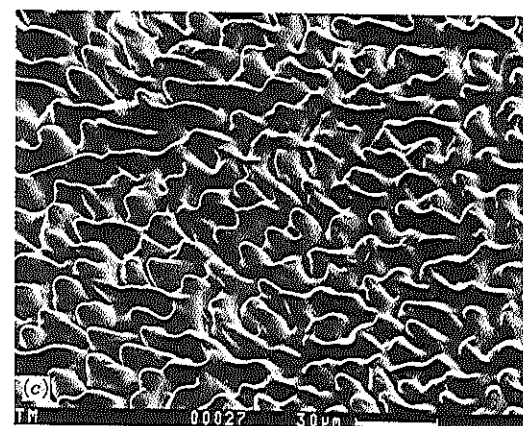


**Figure 4.4. (Continued)**

termed cones vary in shape from the namesake right circular form (Figure 4.5) to more irregular shapes, including columns, clusters of cones, cones with spherical globules on the ends, cones with flat tips, and ones with sharp points. Throughout these permutations, the scale size is roughly constant at 10–20 microns diameter. With few exceptions, cones are formed as surrounding material is removed by successive laser pulses, and as a result of this erosional formation process, they grow in length as laser exposure increases, and they point in the direction of incoming laser radiation.

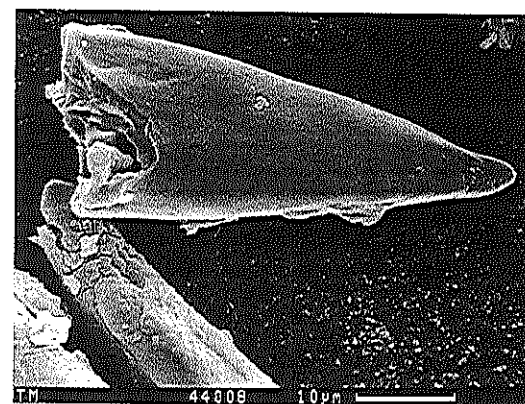


**Figure 4.5.** An individual cone scraped from the surface of an exposed YBCO target.

#### 4.4.2 Cone-Formation Mechanisms

##### 4.4.2.1 Sputter Cones

Cone formation in solids is not a unique feature of laser irradiation, but is also a commonly discussed occurrence in ion bombardment of surfaces. As will be seen, the quantity of experimental evidence and the level of theoretical development relevant to laser-cone formation is roughly equivalent to the state of affairs vis-à-vis sputter-cone formation in the early 1970s. Some of the research on sputter cones that has taken place in the past 20 years is directly applicable to the study of laser cones; throughout the remainder of this chapter we draw upon this work, pointing out the similarities as well as a number of notable differences.

In 1971, Wehner and Hajicek described the formation of cones on a Cu surface subjected to ion bombardment in a Hg plasma. In this case, Mo atoms (from a separate target) were arriving on the Cu surface as the sputtering progressed. Discrete, localized aggregates of these atoms, the authors concluded, shielded the underlying Cu, leaving cones behind as the surrounding material was sputtered away. This concept, similar to the role of erosion-resistant boulders in the geologic formation of "tent rocks," appears to be the predominant mechanism at work in laser-cone formation. Wehner also described other features of sputter cones that are analogous to laser cones: He found that cones point in the direction of bombardment, and that they impart a velvetlike appearance to the target surface. Unlike laser cones, however, Wehner found that sputter cones altered the angular distribution of sputtering flux.

As use of the SEM became more routine in the study of ion-induced surface topography, a growing body of experimental evidence prompted more complex theoretical treatments to explain the observations. A comprehensive text on the subject, edited by Auciello and Kelly, was published in 1984. A common theme throughout this work (notably in the Introduction by Auciello and in chapters by Carter and Nobes; and Wilson, Belson, and Auciello) is that the primary mechanism for cone formation is preferential erosion due to a variation in sputter yield with ion angle of incidence, a concept introduced by Wehner in 1959. An example of this functional behavior appears in Figure 4.6. The important feature is that the sputter yield is at a maximum for large incident angles (usually between  $60^\circ$  and  $80^\circ$ )—sputter cones develop with surfaces at this maximum yield angle.

This preferential erosion mechanism addressed a much broader range of experimental results, since it allowed for cone development not only from sputter-resistant impurities, but also from easily sputtered impurities, ion-induced defects, grain boundaries, or any general convex-up protuberance. Thus cone development was predicted for nearly any ion-bombarded surface.

An optical analog of this erosional model, if one exists, awaits the availability of suitable yield-vs.-angle data for laser vaporization. Complicating this development are marked differences in energy deposition and material ejection

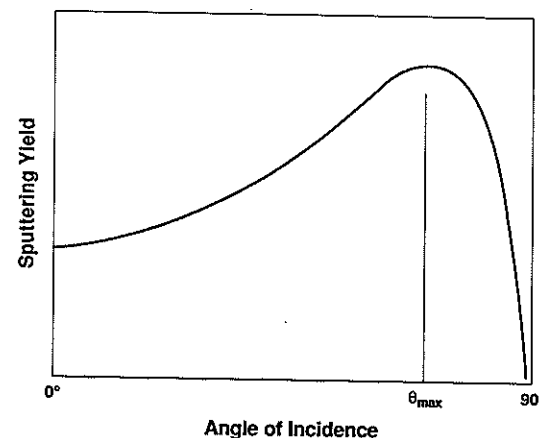


Figure 4.6. Typical sputtering yield for ion-bombardment at different angles of incidence. The yield increases approximately as  $\cos^{-1}\theta$  for small angles, and decreases for large angles as the ion reflection coefficient becomes significant. Erosional processes in sputtering lead to development of cones with surfaces at  $\theta_{\max}$ .

mechanisms. Other significant differences arise in considering ion versus optical reflection coefficients, momentum transfer from ions, and the existence of a fluence threshold for optical vaporization. Intuitively, one might expect the maximum laser-induced "yield" to occur at normal incidence, but since the sputtering model predicts development of cones with surfaces oriented for maximum sputtering yield, the optical analog would predict no cone formation at all. Another consequence of the sputtering model is that cones are transient features that shrink and disappear with continuing ion bombardment (unless additional cone nuclei are supplied). This is in contrast to the current evidence for laser cones, which suggests that they are indeed stable features of photon bombardment.

##### 4.4.2.2 Laser Cones

We are left, then, in a situation where the only concrete evidence available suggests that vaporization-resistant impurities are responsible for laser-cone formation. The first conclusive experiments were carried out during studies involving excimer laser etching of polyimide films. Hypothesizing that cones that formed on "clean" films were due to an impurity shielding effect, Dyer et al. (1986) deliberately seeded films with alumina and rare-earth particles, and demonstrated a direct relationship between these impurities and laser-cone development.

Dyer also suggested that redeposited ablation debris could provide cone nuclei in the absence of intrinsic impurities. This was reiterated by Taylor et al. (1988), who suggested that carbon-rich debris from the excimer laser etching

of polymers was responsible for cone formation in high-purity polyimide film. Continuing this dialogue, Krajnovich and Vasquez (1992) have concluded that, indeed, carbon-rich material is responsible for cone formation on excimer-irradiated polymers, but that the carbon enrichment mechanism is not redeposition. The authors observed that similar conical morphologies evolved regardless of whether ablation occurred in air or vacuum, while the air exposures produced much greater quantities of debris. Further analyses with X-ray photoelectron spectroscopy and mass spectrometry suggested that certain low molecular weight species were preferentially emitted, leaving the surface rich in carbon.

Related cone-formation mechanisms have been observed in the excimer laser deposition of YBCO thin films, beginning with a report by Auciello et al. (1988) of cone formation associated with a Cu-deficient composition. Foltyn et al. (1990) noted that, from energy dispersive spectroscopy, cone surfaces had a Y-rich, Cu-deficient composition, but that composition approached the normal 1-2-3 ratios as the probe depth was increased. Electron microprobe analysis was employed to quantify this phase segregation in YBCO (Foltyn et al. 1991), revealing a threefold increase in the Y:Cu ratio in an exposed laser track.

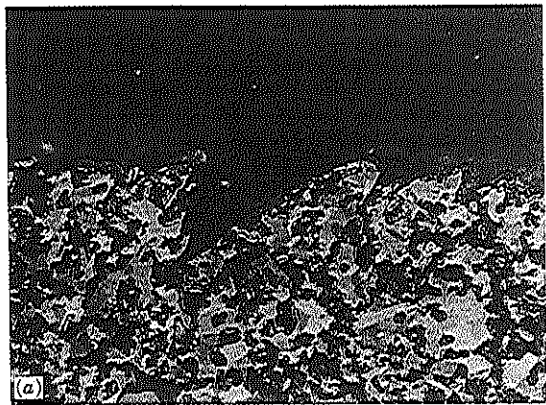


**Figure 4.7.** (a) Optical micrograph of a sectioned and polished YBCO target with cones that have formed after 1000 shots/site at a 308-nm fluence of  $2\text{ J/cm}^2$ . The laser was incident at  $45^\circ$  from the upper right. A modified shell, visible on the surface, surrounds undisturbed polycrystalline target material inside the cones. The field of view is  $200\text{ }\mu\text{m}$ . (b) SEM of a different cone on the same target. (c) Electron microprobe scan along the dashed path in Figure 4.7b. The cone interior has the 1-2-3 composition characteristic of the original target; as the scan enters the tip region, an enrichment of yttrium is measured, along with a corresponding decrease in copper and barium concentrations.

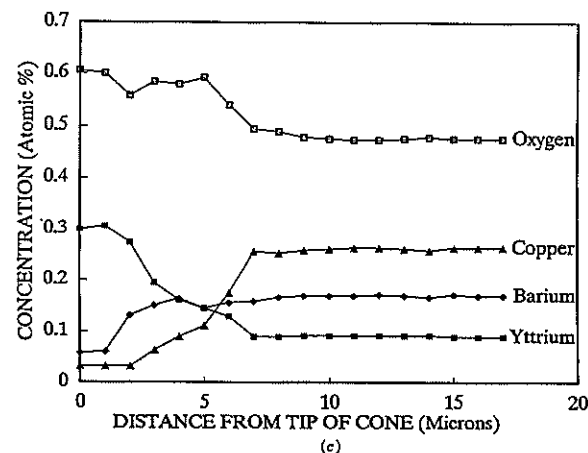
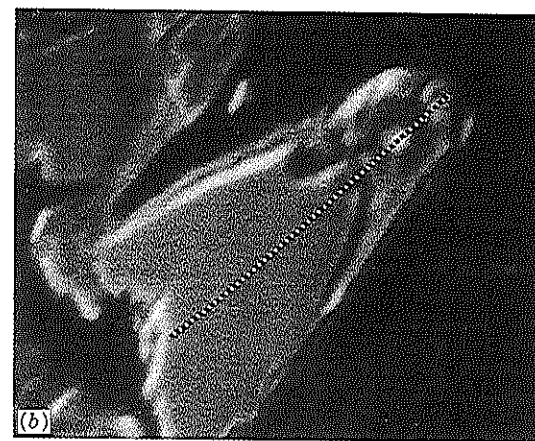


**Figure 4.7.** (Continued)

To investigate the phenomenon of cone formation by shielding, a sample was prepared by irradiating a track in a rotating YBCO target to an exposure of approximately 1000 shots/site. The target was then sectioned, potted, and polished as for a conventional metallographic cross section. The optical micrograph of Figure 4.7a reveals that the cone interior consists of undisturbed polycrystalline material, but that the cone surface appears to be modified; the SEM image (Figure 4.7b) of a different cone on the same sample shows more clearly the core and shell configuration. To determine the nature of the modified surface layer, an electron microprobe analysis was conducted along the path of the dashed line in Figure 4.7b. The results (Figure 4.7c) confirm

that the cone interior has the 1-2-3 cation stoichiometry of the original target. As the probe enters the modified area, the yttrium concentration begins to increase, while Cu and Ba concentrations decline until, at the cone tip, the Y:Cu ratio is 10:1. As is discussed in a later section, this Y-rich shell is resistant to laser vaporization. Unlike preexisting or seeded impurities, it has formed from the starting material as a result of laser irradiation, but the result is the same: Target material in the shadow of the impurity is protected as surrounding material is eroded away.

The impurity shielding mechanism, however compelling, may not be the only explanation for laser-cone formation. It may prove, like LIPSS and sputter cones, that laser cones are universal and need not be connected to defects or impurities. For example, Kelly and Rothenberg (1985) attribute cone formation in aluminum to "hydrodynamical sputtering," an outward, thermal expansion-powered growth of asperities. Perhaps capillary waves can assure that such asperities are always present on laser-melted surfaces. Finally, there appear to be exceptions to the "universal" nature of laser-cone formation: Flat-bottomed etch features have been reported in the excimer laser micro-machining of  $\text{LiNbO}_3$  (Eyett and Bäuerle, 1987), and Ni-Zn or Mn-Zn ferrites (Tam et al., 1991).

#### 4.4.2.3 Surface Segregation

The preceding discussion of compositional changes is an example of surface segregation—the preferential enrichment, at a surface or grain boundary, of one or more components of a multicomponent host. This phenomenon is important in the context of this chapter, not only because of its role in cone formation, but because it is a process that likely occurs even when cones are absent.

PLD excels at producing stoichiometrically correct films of multicomponent materials that are difficult to produce by conventional evaporation techniques. For example, YBCO melts and evaporates incongruently, yet the rapid nonequilibrium heating provided by laser pulses overcomes this problem and, to first order, yields a vapor plume with the same composition as the target. Surface segregation is a higher order PLD phenomenon that—along with incongruent redeposition, and the angular variation of plume stoichiometry discussed in Chapter 7—complicates any simple picture of laser vaporization.

The study of surface segregation (see, for example, Dowben and Miller, 1990) is a highly developed and complex field. Additional complexity is introduced in laser-material interactions due to evaporation at the surface, and thermal time scales that are short relative to solid-state diffusion processes. With this in mind, we construct a hypothetical model for the Y-rich surfaces described in the previous section.

The process of interest here is the propagation into and withdrawal from the bulk target of a melt front, as illustrated in Figure 4.1. As resolidification begins, higher melting point components of the liquid, such as  $\text{Y}_2\text{O}_3$  and

$\text{Y}_2\text{BaCuO}_5$  (Aselage and Keefer, 1988), freeze first, driving copper-and-barium-rich liquid toward the surface. This type of process has been observed in the segregation of Au from a  $\text{TeO}_2$  matrix (Marinero et al., 1985) and is analogous to laser "zone refining" of Pt impurities from Si (Cullis et al., 1980), although impurity solubility is the driving mechanism in the latter case.

Little segregation is likely to occur in a single thermal pulse of a few hundred nanoseconds, but in a film deposition the cycle is repeated thousands of times. As Cu-rich material segregates to the top of the melt it is removed by evaporation during successive pulses, leaving behind an Yttrium-enriched surface. As Y enrichment proceeds, the laser begins interacting with an increasingly transparent material— $\text{Y}_2\text{O}_3$  is transparent enough to be used in optical interference coatings for ultraviolet wavelengths—that allows a greater melt depth. This is why the depth of modification (see Figure 4.7b, c) is much greater than the  $\sim 0.1 \mu\text{m}$  penetration depth for 308-nm radiation in YBCO. The process is self-limiting, however, as the distance over which Cu must diffuse toward the surface becomes large.

We have seen that Y-rich material shields underlying YBCO, leading to cone formation. We have examined a means whereby a surface layer of Y-rich material can form. What is missing is a mechanism that connects surface segregation with formation of the Y-rich cells or islands in the surface plane that become cone tips. Robinson and Rossmagel (1984) present a model in which clustering of impurities by surface diffusion leads to the conical topography found in sputtering, and note that such clustering has been observed on ion-bombarded surfaces with scanning Auger microscopy. Another possibility that is related to segregation is constitutional supercooling (von Allmen, 1987), which results from spatially periodic fluctuations in solidification velocity, and which leads to a cellular structure with impurity-rich boundaries (typical cell sizes, however, are much smaller than cones).

Clearly, no comprehensive model yet exists to describe the complex interactions leading to laser-cone formation. As previously noted, cones may develop in the absence of impurities, and phase segregation probably occurs without cone formation, yet in the case of YBCO the two phenomena seem inextricably linked. In the next section, we move from causes of surface modification to effects, specifically: What effects do cones have on the process of film deposition?

## 4.5 EFFECTS OF SURFACE MODIFICATION ON PULSED LASER DEPOSITION

### 4.5.1 Film Composition

After the preceding discussion, it is logical to be concerned about the effect of surface modification on film composition. Again, YBCO is a useful system to study because it is severely modified by cumulative laser irradiation, and

because proper stoichiometry is essential in achieving optimum superconducting performance.

The topic of film composition, as affected by target exposure, has received little attention, probably because target modification does not appear to be an obstacle to the deposition of nominally stoichiometric films. This situation is not without precedent. For example, in thin-film sputtering of multicomponent materials, a compositionally modified target surface must develop before proper film stoichiometry can be achieved. Auciello and Krauss (1988) have noted this effect in sputtering of YBCO.

To investigate the effect in PLD, Foltyn et al. (1990) deposited four films in succession from the same target track irradiated at 308 nm, 3.3 J/cm<sup>2</sup>. The first film was from a surface with no cones (0–200 shots/site), the last was from a surface with a highly developed cone structure (1900–3100 shots/site). Within the accuracy of the measurement technique (Rutherford backscattering spectrometry), all four coatings had the same 1-2-3 composition. More recently, Foote et al. (1992) reported that for 1-J/cm<sup>2</sup>, 248-nm exposures, films were initially copper and barium rich until—at 40 shots/site—a steady-state composition was reached. These results suggest that laser preconditioning of the target is necessary, as with sputtering (at least at low fluence), and also that surface segregation occurs at very low exposures.

#### 4.5.2 Film-Deposition Rate

If surface modification is benign with respect to film composition, one aspect of PLD that is affected is film-deposition rate. Figure 4.8 is a plot of deposition rate (308 nm, 3.5 J/cm<sup>2</sup>) versus exposure, as measured with a quartz crystal microbalance (QCM). The initial rate in vacuum is about 0.9 Å/shot, but, at an exposure of 1000 shots/site, it has dropped by a factor of 4, accompanied by a marked decrease in plume size. The rate in oxygen is lower due to collisional scattering and broadening of the vapor plume by background gas; however, the drop in deposition rate is proportional. This downward trend in rate has been linked directly to a reduction in the amount of target material being vaporized (Foltyn et al., 1990), and it has been shown quantitatively by Krajnovich and Vasquez (1992) that the trend stops when cones have been completely formed.

At higher fluence, rate falls off more gradually, and saturates at a higher level (Foltyn et al., 1991). Target properties, however, appear to have little influence on this behavior. Figure 4.9 shows the results of a target evaluation series in which six targets were exposed at 308 nm, 4.4 J/cm<sup>2</sup>. Materials were supplied by four commercial vendors and two in-house sources; densities ranged from 62% to 93% of theoretical maximum, and preparation techniques varied from conventional pressing to proprietary forging or isostatic consolidation methods. Although minor differences are apparent, the behavior of each

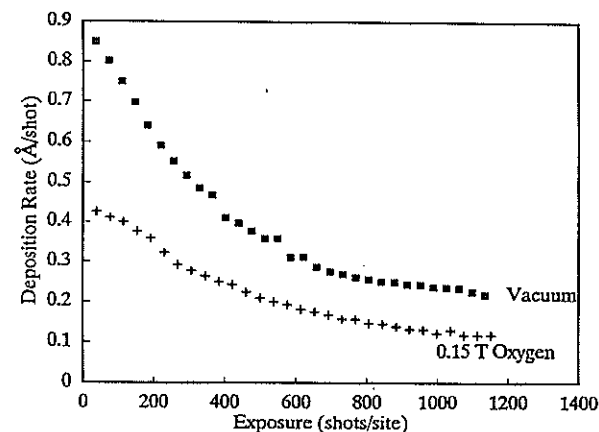


Figure 4.8. Deposition rate for YBCO exposed at 308 nm and 3.3 J/cm<sup>2</sup>, as measured with a QCM placed in the center of the plume at ~6 cm from the target. The decay in rate with cumulative exposure occurs in nearly every material, and is most often observed as a decrease in size of the luminous plume. The two curves are for the same target irradiated under different ambient pressures (see text).

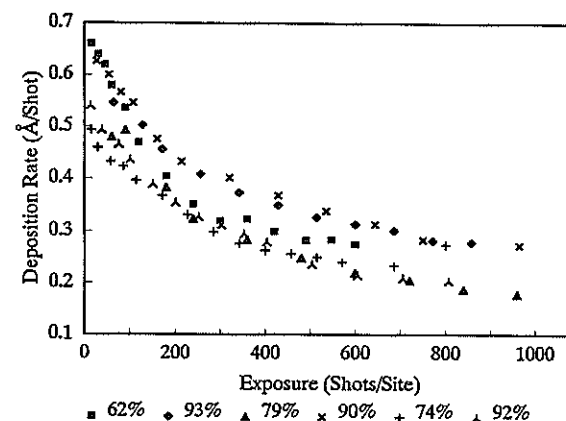


Figure 4.9. A set of exposure curves for six different YBCO targets illustrating that rate decay is independent of target microstructure. The legend refers to target density, expressed as a percentage of theoretical maximum.

target was essentially the same. There was no correlation between the functional differences and preparation technique or any readily observable target property such as density.

An exposure-dependent deposition rate is not a feature that is unique to YBCO. Kelly et al. (1985) noted that the 193-nm etch rate of sapphire was halved after ~4000 shots, attributing the change to material trapping by cones. Dubowski (1986) reported a fivefold decrease to a constant rate in CdTe after 500–600 pulses of 1.06- $\mu\text{m}$  radiation. And Krajnovich and Vasquez (1992) have observed a decreasing mass spectrometer signal coincident with cone formation in polyimide exposed to 248-nm pulses; further, the falloff was more rapid for higher mass fragments, and the mass spectrometer signal dropped to nearly zero at 1200 pulses.

In sputtering as well, changes in yield are related to cone formation (Auciello, 1982); however, reports differ as to whether yield decreases or increases after cones are formed. For ion beams of 1–1.5 keV, the general tendency is to increasing yield, which is associated with erosion of cone walls toward the angle of maximum sputtering yield. At lower ion energies, decreasing yields are observed and attributed to trapping of sputtered particles.

Mechanisms for the observed exposure-dependent laser vaporization rate fall into several categories. Trapping of vaporized material is probable, but difficult to prove since anything trapped on cone surfaces would be subject to successive laser pulses, and would either be reevaporated or incorporated into the cone surface (another mechanism for chemical surface modification?). Two phenomena that are more readily apparent are discussed in the following sections.

#### 4.5.2.1 Fluence Dilution

As cones form, or as an irradiated surface develops any kind of structure, the exposed surface area increases and the average laser fluence on the surface decreases as a result. This leads to an interesting effect reported by Dyer et al. (1986) in which, during low-fluence excimer etching of polyimide, the cone apex angle was found to be fluence dependent. Essentially, the cones became more acute until the fluence on the cone walls dropped below the etch threshold, at which point cone development ceased. This effect was modeled by considering that the surface area of a right-circular cone increases as  $1/\sin \gamma$ , where  $\gamma$  is the apex half-angle. For an incident fluence of  $\Phi_0$  and a threshold fluence of  $\Phi_t$ , cones will develop until

$$\gamma = \sin^{-1} \frac{\Phi_t}{\Phi_0}$$

Dyer obtained fair experimental agreement with this prediction for  $\gamma > 15^\circ$ , and was able to improve it somewhat by incorporating increased reflection losses into the model.

Another manifestation of fluence dilution is seen in Figure 4.7b. On the tip of the cone, the modified shell is about 7  $\mu\text{m}$  deep, but on the sides, where the fluence is 15–20% of the normally incident value, the shell is only about 1  $\mu\text{m}$  thick. This is indicative of a reduced melt depth associated with the lower fluence on the cone walls.

#### 4.5.2.2 Vaporization-Resistant Surfaces

The modified surface itself has an effect on vaporization rate. For example, Krajnovich and Vasquez (1992) used the term “radiation hardening” to describe the response of polymers being etched at low excimer fluence levels. In this case, the term refers to formation of a carbon-rich skin due to preferential evaporation late in the thermal cycle. This skin inhibits vaporization, leads to cone formation, and can bring the etching process nearly to a halt.

This is similar to the Y-rich shell discussed previously in the case of YBCO vaporization. To analyze the influence of this shell on vaporization rate, an X-ray powder diffraction pattern was first obtained on scrapings from a modified target surface: The Y-rich, Cu-deficient phases  $\text{Y}_2\text{BaCuO}_5$ ,  $\text{Y}_4\text{Ba}_3\text{O}_9$ ,  $\text{Y}_2\text{BaO}_4$ , and  $\text{Y}_2\text{O}_3$  were identified. Target pellets of the last three were fabricated and exposed—along with a 1-2-3 target—at 308 nm, 3.7 J/cm<sup>2</sup>, in 0.15-T O<sub>2</sub>, with a QCM again used to monitor deposition rate. The results are shown in Table 4.2. Higher yttrium concentrations lead to significantly lower vaporization rates. Not reflected in the table is that the Y-rich targets exhibited a decreasing rate with exposure, as with 1-2-3.

#### 4.5.3 Vaporization from Voids

Before moving on to other effects of surface modification, it is necessary to bring together some of the previous discussion into a model for vaporization from a cone-populated YBCO surface. We have seen that cone surfaces are highly yttrium enriched, yet film composition is essentially unaffected. It is also evident that radiation incident on the walls of a 20° cone must be near the threshold fluence for 1-2-3, and may be below threshold for the Y-rich phases.

TABLE 4.2 Initial Deposition Rate of Yttrium-Rich Phases

Target Material	Rate (Å/shot)
$\text{YBa}_2\text{Cu}_3\text{O}_{7-\delta}$	0.50
$\text{Y}_4\text{Ba}_3\text{O}_9$	0.16
$\text{Y}_2\text{BaO}_4$	0.14
$\text{Y}_2\text{O}_3$	0.04



These observations suggest that little or no vaporization is occurring on cone surfaces.

The only remaining possibility is that vaporization is occurring predominantly in the voids between cones, a hypothesis supported by examination of Figure 4.7a, which reveals a discontinuity in the modified shell at the bottom of the deepest void. This channel provides access to fresh 1-2-3 material in the target, and also provides a means of keeping itself clear (i.e., free of an Y-rich coating).

Krajnovich and Vasquez (1992) reported that the vaporization-resistant skin produced on polymers could be removed by a single laser pulse of sufficiently high fluence. Such high fluence levels can also be achieved in the voids between cones due to light channeling, a consequence of multiple grazing-incidence reflections off the cone walls. A numerical simulation by Bailey and Modak (1989) modeled this effect, and found that intensity (or fluence for pulsed lasers) is enhanced by channeling in voids with apex angles as broad as  $120^\circ$ . The effect becomes stronger for more acute angles, reaching a fivefold increase at  $45^\circ$ , and continuing to increase for narrower voids. This effect not only enables continued congruent evaporation from cone-populated surfaces, but it may be an additional cone-formation mechanism as well.

## 4.6 SECONDARY EFFECTS OF SURFACE MODIFICATION

There is evidence—some well-founded and some anecdotal—of other, secondary consequences of target modification on the laser deposition process. A few of these effects are discussed briefly in this section.

### 4.6.1 Translational Energy Distributions

Using time-of-flight mass spectrometry, Krajnovich and Vasquez (1992) have observed a threefold reduction in mean translational energy of ablation products following cone formation in polyimide. The effect on film properties in PLD is not clear; however, as the authors point out, one consequence is that target exposure must be taken into account in the measurement and reporting of translational energy distributions.

### 4.6.2 Particulates

As discussed in Chapter 6, particulates are an undesirable product in the laser vaporization of surfaces. In PLD folklore, one source of particulates is cone tips that eventually break off and end up in the film. But, at least in YBCO, particulates tend to be 10–100 times smaller than cone tips, and are close to the 1-2-3 composition (not yttrium-rich). If it is shown that modified surfaces produce more particulates, a more likely culprit is fluence enhancement in the

voids, following the accepted notion that higher fluence exacerbates the particulate problem. One well-founded connection between particulates and cones can be found in metals (Kelly and Rothenberg, 1985) where, as part of a hydrodynamic sputtering process, conical forms result when ejected liquid droplets cannot escape the surface and are frozen in place. In this case, cones result from the particulate-formation process instead of the other way around.

### 4.6.3 Plume Direction/Distribution

It has been suggested that the measured decay in deposition rate might result from a change in plume direction caused by cones that are tilted away from the target surface normal. Any such plume steering would reduce the incident flux on the detector (QCM crystal, mass spectrometer, etc.), as would a broadening of the plume distribution. This question was addressed by using an optical monitor, which was insensitive to plume direction or distribution, in conjunction with a QCM (Foltyn et al., 1990). The two monitors gave essentially identical results throughout lengthy exposures, indicating that the presence of cones had not spatially altered the plume.

Still, with vapor originating in the voids and traveling parallel to the cone axes in order to escape, it seems intuitive that the plume direction would be affected. Even in the Knudsen-layer formulation of Kelly (1990), in which plume expansion is reordered in a collision-dominated surface layer, the original center-of-mass velocity is preserved. Perhaps a solution can be found by considering the bottom of the voids as a “phased array” of emitters that lie in a plane parallel to the original target surface. In this analogy, plume expansion is still perpendicular to the emitting surface, even if the exact motion of vapor through the thicket of cones is not obvious.

### 4.6.4 Target Coupling

The vapor yield from a target is dependent on the fraction of laser energy that is absorbed, which, for opaque materials equals  $(1 - R)$ , where  $R$  is the total percentage of incident radiation that is reflected. To measure the change in  $R$  due to cones formed in YBCO, an integrating sphere was set up in a weak, collimated 308-nm beam. For a freshly sanded target surface oriented at  $45^\circ$ , the reflectivity (specular plus diffuse) was 4.4%. The target was then irradiated in a scanning beam to populate the entire surface with cones tilted at  $45^\circ$  to the surface normal. When the target was returned to the integrating sphere, the reflectivity for light parallel to the cone axes had dropped to 0.8%. This change, which is an indication of the light channeling effects discussed previously, is insignificant in terms of absorbed energy (99.2% versus 95.6%), and its effect on the PLD process. The change in absorption due to light trapping may be more pronounced, however, for relatively transparent materials.



#### 4.7 AVOIDING SURFACE MODIFICATION

We have seen that the major effect of surface modification on PLD is a reduction of the deposition rate. This complicates film thickness control and slows the deposition process, and, while neither issue greatly inhibits progress in a research laboratory, both are significant obstacles to an efficient production process. In a laboratory the target can be periodically resurfaced by sanding or scraping, restoring the deposition rate to its original level; this would be impractical in production. One solution is to preirradiate to a modified state before deposition, and simply use the target at high exposure levels where the deposition rate is nearly constant, perhaps increasing fluence somewhat to compensate for the reduced rate (at the expense of increased particulate levels). Another is a periodic high-fluence pulse (with the substrate shuttered to avoid particulates) to restore the deposition rate (Krajnovich and Vasquez, 1992). Finally, very-high-fluence levels could be employed to vaporize all impurities and circumvent the problem altogether, but again, particulate generation must be considered.

##### 4.7.1 Irradiation Geometry

Cones can also be eliminated without resorting to excessive fluence levels. In ion milling, for example, cone-free surfaces have been achieved by sputtering at grazing incidence (Bulle-Lieuwma and Zalm, 1987), and, while not yet demonstrated, a laser analogy may be possible. Also, because cones develop only under unidirectional laser irradiation, they can be avoided by altering irradiation geometry. Some possibilities include the use of two beams incident on the same spot from opposing angles, or scanning the beam across the full diameter of a rotating target.

In preliminary investigations of cone elimination, a third technique was used, which involved simply irradiating the center of a rotating target at a 45° incident angle. While not a practical PLD geometry, the elliptical beam footprint (approximately 1 mm × 5 mm) produced two different regions for examination: In the central region, the surface was continuously exposed at 45° from a full azimuthal range of angles; the surrounding annulus was exposed twice per target revolution, once each from opposing 45° incident angles. The central region developed a topography consisting of long slender columns oriented perpendicular to the original target surface (Muenchausen et al., 1991). The surrounding area consisted of a less-organized undulating surface with oblique features, but no cones or columns. Both regions exhibited surface segregation and were yttrium rich.

The elimination of cones, however, did not significantly impact the decrease in deposition rate with exposure. Using a cone-producing circular track configuration on the same target at the same fluence (308 nm, 3.0 J/cm<sup>2</sup>), the deposition rate dropped to 30% of its initial value at an exposure of 400 shots/

site. During central irradiation, the asymptotic rate was reached more quickly (200 shots/site), but saturated at a higher level (40%). Detailed analysis awaits further experiments to more cleanly separate the various effects of morphology and segregation. For example, cone-elimination techniques may prove effective in single-phase materials that do not exhibit surface segregation.

Regardless of future developments, it is now evident that surface modification is an expected consequence of PLD, and that, under cumulative irradiation conditions, the stable surface configuration is generally one that is resistant to further vaporization. In addition, surface segregation appears unavoidable in multicomponent materials, and it may prove to be necessary for congruent vaporization from surfaces without cones and light channels. Finally, while it is useful to understand the nature of these dramatic laser-induced transformations of the target surface, it is also evident that, surface modification notwithstanding, PLD remains a viable and important technology for the deposition of thin films.

#### ACKNOWLEDGEMENTS

The author would like to acknowledge numerous helpful discussions, notably with coauthors listed in Foltyn et al. (1990). In addition, the author is particularly grateful to W. B. Hutchinson for the microprobe data and SEM of Figures 4-7b and 4-7c, and to T. Martinez for the SEMs of Figures 4-4 and 4-5.

#### REFERENCES

- Aselage, T., and K. Keefer (1988), *J. Mater. Res.* 3(6), 1279–1291.
- Auciello, O. (1982), *Radiat. Eff.* 60, 1–26.
- Auciello, O., and R. Kelly, eds. (1984), *Ion Bombardment Modification of Surfaces*, Elsevier, Amsterdam.
- Auciello, O., A. R. Krauss, J. Santiago-Ausles, P. F. Schreiner, and D. M. Gruen (1988b), *Appl. Phys. Lett.* 52(3), 239–241.
- Auciello, O., and A. R. Krauss (1988), *Am. Inst. Phys. Conf. Proc.* 165, 114–121.
- Bailey, A. W., and A. Modak (1989), *J. Thermophys.* 3(1), 42–45.
- Birnbaum, M. (1965), *J. Appl. Phys.* 36, 3688–3689.
- Bulle-Lieuwma, C. W. T., and P. C. Zalm (1987), *Surf. Interface Anal.* 10, 210–215.
- Clark, S. E., and D. C. Emmony (1989), *Phys. Rev.* B40(4), 2031–2041.
- Clark, S. E., N. C. Kerr and D. C. Emmony (1989), *J. Phys. D: Appl. Phys.* 22, 527–534.
- Cullis, A. G., H. C. Webber, J. M. Poate, and A. L. Simons (1980), *Appl. Phys. Lett.* 36(4), 320–322.
- Doll, G. L., T. A. Perry, and J. A. Sell (1991), *Mater. Res. Soc. Symp. Proc.* 201, 207–212.

- Dowben, P. A., and A. Miller, eds. (1990), *Surface Segregation Phenomena*, CRC Press, Boca Raton, Fla.
- Dreyfus, R. W., R. E. Walkup, and R. Kelly (1986), *Radiat. Eff.* **99**, 199–211.
- Dubowski, J. J. (1986), *SPIE Conf. Proc.* **668**, 97–101.
- Dyer, P. E., S. D. Jenkins, and J. Sidhu (1986), *Appl. Phys. Lett.* **49**(8), 453–455.
- Ehrlich, D. J., S. J. Brueck, and J. Y. Tsao (1982), *Appl. Phys. Lett.* **41**(7), 630–632.
- Emmony, D. C., R. P. Howson, and L. J. Willis (1973), *Appl. Phys. Lett.* **23**(11), 598–600.
- Eyett, M., and D. Bäuerle (1987), *Appl. Phys. Lett.* **51**(24), 2054–2055.
- Foltyn, S. R., R. E. Muenchausen, R. C. Estler, E. Peterson, W. B. Hutchinson, K. C. Ott, N. S. Nogar, K. M. Hubbard, R. C. Dyer, and K. D. Wu (1990), *Mater. Res. Soc. Symp. Proc.* **191**, 205–209.
- Foltyn, S. R., R. C. Dye, K. C. Ott, E. Peterson, K. M. Hubbard, W. Hutchinson, R. E. Muenchausen, R. C. Estler and X. D. Wu (1991), *Appl. Phys. Lett.* **59**(5), 594–596.
- Foote, M. C., B. B. Jones, B. D. Hunt, J. B. Barner, R. P. Vasquez, and L. J. Bajuk (1992), *Physica C* **201**, 176–182.
- Geohegan, D. B., D. N. Mashburn, R. J. Culbertson, S. J. Pennycook, J. D. Budai, R. E. Valiga, B. C. Sales, D. H. Lowndes, L. A. Boatner, E. Sander, D. Eres, D. K. Christen, and W. H. Christie (1988), *J. Mater. Res.* **3**(6), 1169–1179.
- Guosheng, Z., P. M. Fauchet, and A. E. Siegman (1982), *Phys. Rev.* **B26** (10), 5366–5381.
- Hoffman, A. (1990), *Supercond. Sci. Technol.* **3**, 118–120.
- Keilmann, F., and Y. H. Bai (1982), *Appl. Phys.* **A29**, 9–18.
- Kelly, R. (1990), *J. Chem. Phys.* **92**(8), 5047–5055.
- Kelly, R., J. J. Cuomo, P. A. Leary, J. E. Rothenberg, B. E. Braren, and C. F. Aliotta (1985a), *Nucl. Instrum. Meth. Phys. Res.* **B9**, 329–340.
- Kelly, R., and J. E. Rothenberg (1985b), *Nucl. Instrum. Meth. Phys. Res.* **B7/8**, 755–763.
- Kerr, N. C., S. E. Clark, and D. C. Emmony (1988), *NBS Spec. Publ.* **775**, 273–285.
- Krajnovich, D. J., and J. E. Vasquez (1992a), *J. Appl. Phys.* **73**, 3001–3008.
- Krajnovich, D. J., J. E. Vasquez, and R. J. Savoy (1992b), *Science* **259**, 1590–1592.
- Marinero, E. E., W. Palmer, M. Chen, V. Jipson, and W. Y. Lee (1985), *J. Vac. Sci. Technol.* **B3**(5), 1560–1562.
- Muenchausen, R. E., S. R. Foltyn, N. S. Nogar, R. C. Estler, E. J. Peterson and X. D. Wu (1991), *Nucl. Instrum. Meth. Phys. Res.* **A303**, 204–207.
- Niino, H., and A. Yabe (1992), *J. Photochem. Photobiol. A: Chem.* **65**, 303–312.
- Ready, J. F. (1971), in *Effects of High-Power Laser Radiation*, Academic Press, Orlando, Fla., pp. 67–125.
- Robinson, R. S., and S. M. Rossnagel (1984), in *Ion Bombardment Modification of Surfaces* (O. Auciello and R. Kelly, eds.), Elsevier, Amsterdam, pp. 299–305.
- Rothenberg, J. E., and R. Kelly (1984), *Nucl. Instrum. Meth. Phys. Res.* **B1**, 291–300.
- Singh, R. K., and J. Narayan (1989), *Mater. Sci. Eng.* **B3**, 217–230.
- Singh, R. K., D. Bhattacharya, and J. Narayan (1991), *Mater. Res. Soc. Symp. Proc.* **201**, 427–432.

- Sipe, J. E., J. F. Young, J. S. Preston, and H. M. van Driel (1983), *Phys. Rev.* **B27**(2), 1141–1154.
- Soileau, M. J., and E. W. Van Stryland (1982), *NBS Spec. Publ.* **669**, 406–414.
- Sudarsan, U., N. W. Cody, M. J. Bozack, and R. Solanki (1988), *J. Mater. Res.* **3**(5), 825–829.
- Tam, A. C., W. P. Leung, and D. Krajnovich (1991), *J. Appl. Phys.* **69**(4), 2072–2075.
- Taylor, R. S., K. E. Leopold, D. L. Singleton, G. Paraskevopoulos, and R. S. Irwin (1988), *J. Appl. Phys.* **64**(5), 2815–2818.
- Temple, P. A., and M. J. Soileau (1981), *IEEE J. Quant. Electr.* **QE-17**(10), 2067–2071.
- van Driel, H. M., J. E. Sipe, and J. F. Young (1982), *Phys. Rev. Lett.* **49**(26), 1955–1958.
- von Allmen, M. (1987), in *Laser-Beam Interactions with Materials*, Springer-Verlag, Berlin, pp. 122–130.
- Wehner, G. (1959), *J. Appl. Phys.* **30**(11), 1762–1765.
- Wehner, G. K., and D. J. Hajicek (1971), *J. Appl. Phys.* **42**(3), 1145–1149.
- Young, J. F., J. E. Sipe, J. S. Preston, and H. M. van Driel (1982), *Appl. Phys. Lett.* **41**(3), 261–264.
- Young, J. F., J. S. Preston, H. M. van Driel, and J. E. Sipe (1983), *Phys. Rev.* **B27**(2), 1155–1172.
- Young, J. F., J. E. Sipe, and H. M. van Driel (1984), *Phys. Rev.* **B30**(4), 2001–2015.

## DIAGNOSTICS AND CHARACTERISTICS OF PULSED LASER DEPOSITION LASER PLASMAS

DAVID B. GEOHEGAN

Solid State Division  
Oak Ridge National Laboratory  
Oak Ridge, Tennessee

### 5.1 INTRODUCTION

The successes of pulsed laser deposition (PLD) have far outpaced the understanding of the laser ablation process in the regime of laser energies used for film growth. This is principally a result of the fact that PLD is a pulsed process, involving a wide range of physical phenomena, which requires diagnostics with nanosecond speed. These diagnostics are typically costly and are not normally a part of a materials-science-based laboratory.

The extension of PLD to many new materials, however, has fueled a thrust to characterize the film growth environment with fast, in situ diagnostics in order to efficiently correlate gas-phase conditions with film properties such as stoichiometry, morphology, uniformity, and crystallinity. Experience gained with one material can hopefully be exploited with similar materials and, ultimately, the results and techniques will be applied during deposition for in situ process control.

This chapter attempts to characterize the formation, propagation, and properties of plasma plumes typically used for PLD, as revealed by gas-phase diagnostics. Moreover, this chapter attempts to survey a variety of diagnostic techniques and discuss the applicability of each for PLD plume analysis and in situ monitors.

The physics of laser ablation plasmas limits the applicability of the different diagnostic techniques. For example, some of the most sensitive diagnostics are overwhelmed by the robust environment of dense laser plasmas, while rugged diagnostics are insensitive in low-density plumes. Results obtained within the

physical range of one technique may not apply at higher or lower laser energies. Generally, more complicated experimental arrangements have simpler diagnostic interpretations, while more applicable and simple experimental arrangements require more complicated interpretations. Finally, each diagnostic usually allows a view of just one or two components of the plasma plume (monatomic atoms and ions, molecules, clusters, particles, etc.). Total characterization of the PLD plume therefore requires an understanding of the advantages and limitations of several techniques, as well as their results.

Despite the variety of diagnostic experiments designed to study PLD laser plumes, a number of major questions remain to be resolved, including:

- The roles of nonthermal (electronic) and thermal (evaporation) ejection mechanisms in the ablation of material amounts necessary for film growth.
- The extent and explanation of laser absorption by the initial ejectants.
- The etching effects of the laser plasma on the target.
- The expansion mechanism(s) responsible for the high kinetic energy of the ejectants: the competition between adiabatic expansion and space charge acceleration models.
- The fractional ionization of the plasma plume and the range of distances over which it can be electromagnetically steered.
- The role of clusters and particulates in the mass transfer to the substrate.
- The collision kinetics within the plume in the "collisionless" regime.
- The roles of scattering, diffusion, and hydrodynamics in the slowing and thermalization of the plume by background gases.
- The major factors (i.e., kinetic energy, deposition rate, etc.) determining the optimal film growth distance for various materials.
- The role of chemistry with the background gas.
- The role of target surface morphology and phase on the ejecta.

Much of the current understanding of PLD plasmas and diagnostics is derived from past experimental and theoretical research on laser fusion and damage. Many of the previously listed issues were therefore studied at much higher laser power densities ( $>1 \text{ GW cm}^{-2}$ ) than typically used for PLD ( $\sim 50 \text{ MW cm}^{-2}$ ). Lower power densities were investigated as part of this research, however and several excellent books (Ready, 1971; Hughes, 1975; Bekefi, 1976; Radziemski and Cremers, 1989) and papers (Kelly, 1990; Kelly, 1979; Chuang, 1985; Cheung and Sankur, 1988; Dubowski, 1988; and Richter, 1990) have reviewed the theory, experiments, and diagnostics of laser-solid and laser-gas interactions. This chapter examines the techniques as they become applicable in order of increasing energy density.

## 5.2 GENERAL FEATURES OF LASER PLASMAS AND THEIR CHARACTERIZATION

At low laser energy densities, small quantities of neutral and ionized species become detectable with the most sensitive diagnostics. In general, the quantity of these emitted species is highly nonlinear with laser energy density. Repeated irradiation of the surface at these energy densities does not, however, produce a measurable etch pit. This range of energy density is sometimes referred to as the *below-threshold* or *near-threshold* regime. A great variety of desorption processes have been proposed to account for photodesorption measurements in this regime (Chuang, 1985).

For film growth, reasonable deposition rates ( $\geq 1 \text{ Å/laser shot}$ ) are generally required. For many materials, significant removal rates begin at high temperatures, which, in turn, necessitate high laser energy densities. This fact can be used to define a *threshold* for laser ablation (i.e., the energy density, in  $\text{J/cm}^2$ , at which measurable material-removal begins). This threshold is usually determined by measurement of etch pits with a profilometer.

Increasing the laser energy usually results in two threshold effects: significant material removal and the appearance of the luminous plasma plume. These threshold effects are most often described by evaporation and subsequent absorption of part of the laser pulse by the vapor (see Chapter 3 by Kelly and Miotello, this book). The evaporation threshold can be understood by the exponential increase in the vapor pressure with temperature predicted by the Clausius-Clapeyron equation. At a certain laser energy density, the rapid laser heating rates ( $\sim 10^{11} \text{ K s}^{-1}$ ) overcome the thermal diffusion and radiation losses and evaporation proceeds nonlinearly (see Chapter 3).

For a gas in local thermodynamic equilibrium (LTE), the Saha equation predicts the ratio of singly charged ions to neutrals in the plasma to be

$$\frac{n_i}{n_n} = 2.4 \times 10^{15} \frac{T^{3/2}}{n_i} e^{-U_i/kT} \quad (5.1)$$

where  $n_i$  and  $n_n$  are the ion and neutral densities in  $\text{cm}^{-3}$ ,  $T$  is the temperature in K, and  $U_i$  is the first ionization potential in electronvolts (Chen, 1974). The exponential factor keeps the fractional ionization,  $n_i/(n_n + n_i)$ , of the plume very small until the temperature is raised to where  $U_i$  is only a few times  $kT$ . The fractional ionization then rises suddenly and the vapor becomes a plasma. For example, the fractional ionization of  $10^{14}$  atoms of a material with  $U_i = 7 \text{ eV}$  confined to a typical ablation volume of  $A\Delta t = (0.04 \text{ cm}^2)(10^6 \text{ cm s}^{-1})(50 \text{ ns}) = 0.002 \text{ cm}^3$  ( $n_n = 5 \times 10^{16} \text{ cm}^{-3}$ ) is only 0.0001 for  $T = 3000 \text{ K}$ , but rises to 0.80 at  $10,000 \text{ K}$ .

Typical plasma temperatures measured by emission spectroscopy during the initial expansion are  $\sim 10,000 \text{ K}$  ( $\sim 1 \text{ eV}$ ), well above the boiling points of most materials ( $\lesssim 3000 \text{ K}$ ). Heating of the plasma to these temperatures is thought

to occur by inverse-Bremsstrahlung absorption of the laser light in a free-free transition of an electron-ion pair. The absorption coefficient for this process (Hughes, 1975)

$$\alpha = (3.69 \times 10^8) \frac{Z^3 n_i^2}{T^{1/2} v^3} (1 - e^{-h\nu/kT}) \quad \text{in cm}^{-1} \quad (5.2)$$

predicts better absorption at longer laser wavelengths; however, it requires high densities  $n_i \sim 10^{19} \text{ cm}^{-3}$  for significant absorption. At very high laser powers, these densities are achieved quickly; however, for PLD conditions the situation is not so clear.

For a KrF laser with  $h\nu = 5 \text{ eV}$ , a plasma with temperature  $T = 5000 \text{ K}$  and average charge  $Z = 1$ , and a path length of  $0.050 \text{ cm}$  (assuming  $v\Delta t \sim (10^6 \text{ cm s}^{-1}) (50 \text{ ns})$ ), a 1% absorption would require  $\alpha = 0.2 \text{ cm}^{-1}$ , requiring an average ion density of  $n_i \sim 8 \times 10^{18} \text{ cm}^{-3}$ . For  $10^{15}$  atoms liberated in the pulse, and a beam area of  $0.04 \text{ cm}^2$ , however, this number density could only exist for distances  $< 0.003 \text{ cm}$ ! This apparent contradiction shows the need for dynamic modeling of the combined thermal, radiative, plasma, and hydrodynamic phenomena with step sizes  $\ll 1 \text{ ns}$ . Since  $\alpha \propto n_e^2$  in Eq. 5.2, local "hot spots" may arise from spatially nonuniform laser beams (Dreyfus, 1990). Other absorption processes, such as photoionization and dissociation of clusters, may also be important.

During a  $\sim 30\text{-ns}$  PLD laser pulse in vacuum, therefore, a high pressure ( $\sim 10\text{--}500 \text{ atm.}$ ) bubble of hot plasma is formed  $\lesssim 50 \mu\text{m}$  from the target. The expansion of this bubble has been modeled successfully by fluid dynamics involving linear pressure gradients (Ready, 1971; Singh et al., 1990); however, interbeam collisions result in interesting hydrodynamic effects such as Knudsen-layer formation, redeposition of material on the target, and shock fronts (see Chapter 3 by Kelly and Miotello, this book) (Kelly and Dreyfus, 1988). The expansion produces a supersonic beam similar to that from a pulsed nozzle jet, except for the plasma effects (Anderson, 1974; Zheng et al., 1989; and Saenger, 1989). The angular distributions of the different species' "beams" are different, which can lead to stoichiometry variations in the deposited film (see Chapter 7 on angular distributions, K. Saenger, this book) as revealed by film deposits that can be analyzed by *wet chemistry* (Lynds et al., 1989).

Electrons are much more mobile than the ions and neutrals, but are restricted from escaping the dense plasma by the strong space-charge field incurred by collectively moving away from the ions. In fact, this is the basis for the *space-charge acceleration model* for the ions in the plume; the Coulomb attraction of the ions by electrons that nearly escape at the plume boundary, producing a space-charge field that tends to accelerate ions according to their charge,  $Ze$  (Opower and Press, 1966; Bykovskii et al., 1974; Demtröder and Jant, 1970).

As examples will show, time-of-flight (TOF) data often substantiates this

model, with multiply charged ions traveling faster than singly ionized atoms or neutrals. The existence of fast neutrals can be explained by stepwise recombination of the ions with electrons and/or resonant charge exchange between fast ions and slow neutrals.

The electrons in the plasma respond quickly to internal or external potentials, forming a sheath that shields the majority of the plasma from the applied field. The Debye length,  $\lambda_D$ , is a measure of this shielding distance and is given by (Chen, 1965).

$$\begin{aligned} \lambda_D &= \left( \frac{kT_e}{4\pi n_e e^2} \right)^{1/2} = 6.9 \left( \frac{T_e}{n_e} \right)^{1/2} \text{ cm} \quad [\text{for } T_e \text{ in K}] \\ &= 740 \left( \frac{kT_e}{n_e} \right)^{1/2} \text{ cm} \quad [\text{for } kT \text{ in eV}] \end{aligned} \quad (5.3)$$

where  $n_e$  is in  $\text{cm}^{-3}$ . Even after expansion of the plasma plume, this shielding distance is quite significant from diagnostic and applied perspectives. For example, after expanding to a density of only  $n_e \sim 10^8 \text{ cm}^{-3}$  and cooling to  $kT_e \sim 0.01 \text{ eV}$ , a plasma will still exhibit shielding on the order of  $\lambda_D = 25 \mu\text{m}$ , a distance comparable to the finest screen meshes. Attempts to strip or steer the plume with external fields in denser, hotter regions of the plume will only penetrate a layer of the plume  $\approx$  a Debye length.

### 5.3 DIAGNOSTIC TECHNIQUES

#### 5.3.1 Mass Spectroscopy

*Time-of-flight mass spectroscopy* (TOFMS) is very sensitive to the first ions ejected from the laser-irradiated surface. Ions, charge  $Ze$ , are collected using electric fields and then accelerated by a potential,  $V$ , down a field-free drift tube, each acquiring energy  $ZeV$ . The ions travel at different velocities  $v = (2ZeV/m)^{1/2}$  and arrive at a high gain detector, such as a microchannel plate (MCP) or channeltron, at different times, from which the mass-to-charge ratio  $m/Z$  is derived. Unfortunately, the actual velocity with which the ions travels to the collection region is convoluted with the drift velocity. Careful timing and a mathematical simulation are required to extract the actual kinetic energy (KE) distribution of the photoejected species (Vertes et al., 1988).

Alternatively, the plume can be directed through an aperture and the ions' velocity can carry them directly into a quadrupole mass filter that can be tuned to select ions of different mass for *quadrupole mass spectroscopy* (QMS) (Friichtenicht, 1974). Assuming the velocity of the particles does not change when passing through the quadrupole, the kinetic energy can be directly inferred from their arrival time. The QMS has a mass throughput function that must be known for quantitative ratios of the different ions. Pulse-counting

electronics can be used to statistically record the TOF for ions at a selected mass (Namiki et al., 1986; van Veen et al., 1986).

Figure 5.1 shows a combined TOFMS and time-of-flight quadrupole mass spectroscopy (TOFQMS) setup (Wiedeman and Helvajian, 1991). An ionizer stage (hot filament) in front of the quadrupole input is used to ionize neutrals by electron impact. In addition, retarding grids (screens) are placed in front of the mass spectroscopy (MS) inputs to verify the kinetic energies and screening of the ions in the plume.

Alternatively, neutrals can be photoionized by a time-delayed pulsed laser and the resulting ions extracted into a TOFMS for *laser ionization mass spectroscopy* (LIMS) (Venkatesan et al., 1988). Mass spectroscopy involving nonresonant single-photon ionization (LIMS, also SALI) or resonantly enhanced multiphoton ionization (REMPI) can be used in this step (sometimes called RIMS) (Estler and Nogar, 1991).

In general, because these mass-spectrometric techniques rely on steering the ions in the plume with electromagnetic fields, they are most useful in vacuum at low plasma densities. Ideally, the velocities of particles that originate from thermal equilibrium with a hot surface (temperature  $T_s$ ) should exhibit a

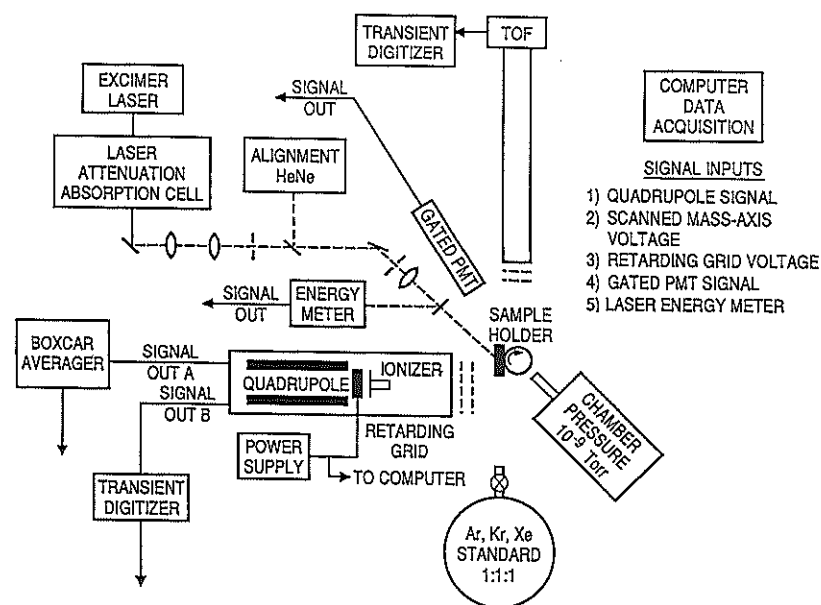


Figure 5.1. Experimental arrangement for near-threshold laser ablation measurements of ejected species population distributions and initial kinetic energies using both TOFMS and TOFQMS. (Reprinted from L. Wiedeman and H. Helvajian, *J. Appl. Phys.* 70, 4513 (1991), with permission.)

Maxwellian distribution, that is,  $f(v) \sim v^3 \exp(-mv^2/2kT_s)$ . Knudsen-layer collisions are expected to modify this distribution (see Chapter 3 by Kelly and Miotello, this book) to  $f(v) \sim v^3 \exp(-m(v - v_{cm})^2/2kT_{eff})$ .

Results of these near-threshold MS studies usually show (a) a nonlinear dependence of ablation yield on the laser fluence, (b) a threshold fluence, (c) variations between yields of different species with laser wavelength, (d) non-Maxwellian velocity distributions of the ejected species, and (e) ions traveling faster than neutrals.

Figure 5.2i shows TOFQMS spectra for neutral P atoms and P<sup>+</sup> ions ejected from a GaP sample after irradiation at 540 nm for a variety of laser energy densities (Nakayama, 1983). As the energy density is raised, the signal intensity rises nonlinearly, and several components to the neutral P-atom velocity distribution become, in this example, clearly visible. The fastest neutral component mimics the ion signal. Figure 5.2ii shows that fitting Maxwellian distributions to the neutrals and ions gives disparate temperatures of 600 K and 10,000 K, respectively. From this data it is clear that the threshold sputtering from GaP is not a thermal effect, but electronic. An ejection model based on the formation of a dense electron-hole surface plasma or localized surface defect sites was proposed to explain the data (Nakayama, 1983).

Figure 5.3a shows TOFMS arrival data for Sr<sup>+</sup> ions following near-threshold XeF-laser ablation of Bi<sub>2</sub>Sr<sub>2</sub>Ca<sub>2</sub>Cu<sub>2</sub>O<sub>8</sub> (BiSCCO) in vacuum (Wiedeman et al., 1991). These first few ions exhibit a very nonthermal (lacking a low-energy velocity component) and sharp KE distribution, which does not vary with the laser energy over a small range. As the energy density is raised, suddenly the energy distribution broadens, as shown in Figure 5.3b. This effect is attributed to space-charge spreading effects due to the higher ion densities (Wiedeman et al., 1991). As the energy density is raised higher, more neutrals are observed at thermal KEs, and the ion KE begins to depend on the laser energy. At still higher energy densities both ions and neutrals accelerate in accordance with plasma acceleration observations from other techniques (Wiedeman et al., 1991).

These two examples only begin to introduce the wide variety of interesting near-threshold phenomena that cannot be explained on the basis of thermal evaporation models. In general, ions are generated from undetermined electronic mechanisms in quantities far greater than predicted on the basis of the Saha equations and the assumption of LTE. The temperatures estimated from fits of the data to the thermal distribution can be higher or lower than what seems reasonable for the surface temperature. Surface defects can play a major role in the ejected species' kinetic energy distributions (Itoh et al., 1991; Dickinson et al., 1991).

As the energy density is raised further, a plasma forms and the velocity distributions show evidence of gas phase collisions. The short Debye lengths in the dense part of the plasma plume eventually render mass spectroscopy useless at distances close to the target.

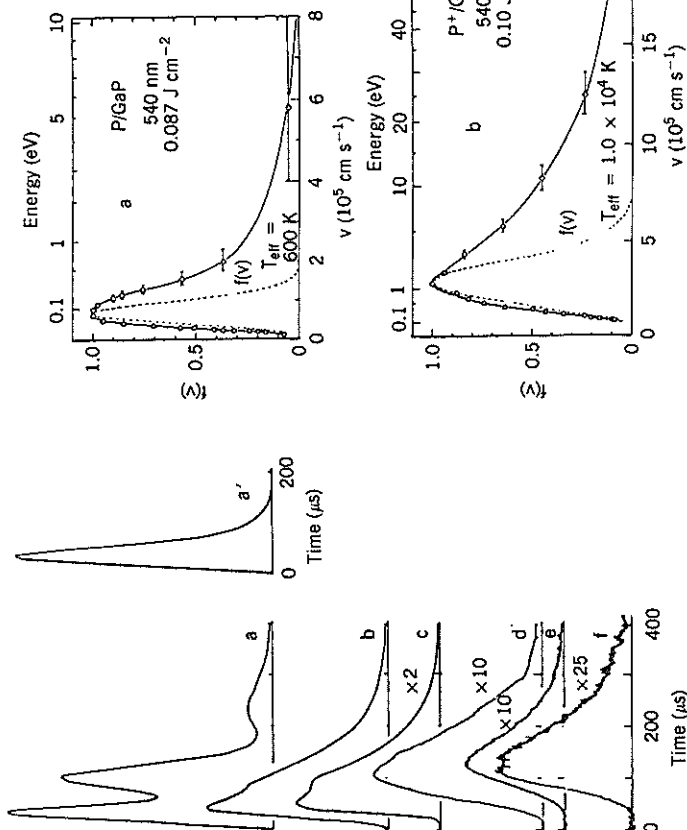


Figure 52. (i) TOFMS spectra of P atoms sputtered from GaP by irradiation of 540-nm laser pulses at fluences (in  $\text{J cm}^{-2}$ ) of curves (a) 0.10, (b) 0.080, (c) 0.063, (d) 0.049, (e) 0.038, and (f) 0.029. Several components to the neutral TOF are observed, the fastest similar to that of the P ions. Curve (a') shows the signal due to P ions only, which was obtained by irradiation at  $0.10 \text{ J cm}^{-2}$ . (ii) Velocity distributions,  $f(v)$ , for (a) neutral P atoms and (b)  $\text{P}^+$  ions laser sputtered from GaP. The dashed curves are Maxwellian functions,  $f_M(v)$ , which have effective temperatures of 600 K for neutral P atoms and 10,000 K for  $\text{P}^+$  ions at the indicated fluences. (Reprinted from T. Nakayama, *Surface Science* 133, 101 (1983) with permission.)

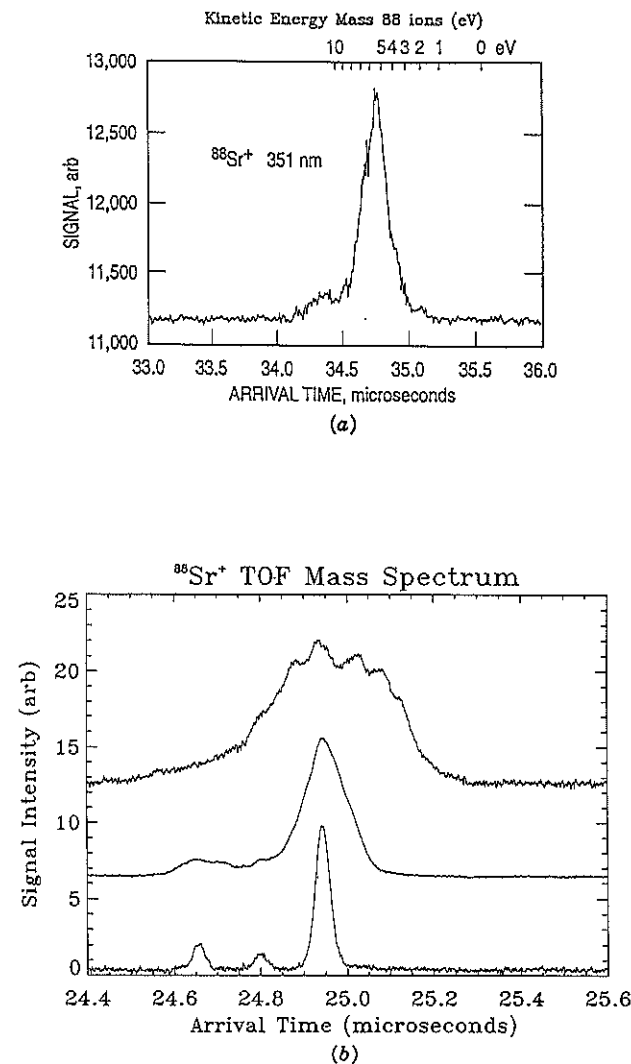


Figure 53. Time-of-flight arrival data for  $\text{Sr}^+$  ions ejected from near-threshold XeF laser (351-nm) irradiation of  $\text{Bi}_2\text{Sr}_2\text{Ca}_1\text{Cu}_2\text{O}_8$ , averaged over 300 laser shots. (a) The sharp kinetic energy distribution ( $\langle \text{KE} \rangle = 5 \pm 1 \text{ eV}$ ) lacks a low-velocity (thermal) component, indicating a nonthermal ejection mechanism. (b) As the laser energy density is raised, the TOF distribution broadens due to ion-ion repulsion in the plume at the higher ion densities. (Reprinted from L. Wiedeman, H. S. Kim, and H. Helvajian, in *Surface Chemistry and Beam Solid Interactions*, H. A. Atwater, F. A. Houle, and D. H. Lowndes, Eds., *Mat. Res. Soc. Symp. Proc.*, 201, 575 (1991) with permission.)



### 5.3.2 Ion Probes

Ion probes are extremely useful diagnostics of flowing laser plasmas such as those used for PLD (Demtröder and Jantz, 1970; Lubben et al., 1985; Hughes, 1975; Talbot, 1973; Gekelman, et al., 1978; Dyer et al., 1992; Balazs et al., 1991; Bhat et al., 1986; and Chrisey, 1990). Electrostatic ion probes (or Langmuir probes) are among the oldest plasma diagnostics, and were developed to provide electron temperature and density information in nonflowing plasmas (Chen, 1965; Swift and Schwar, 1970). They are inexpensive and rugged, and have the advantage of providing *local* information on plasma conditions, unlike most spectroscopic or imaging techniques that average along the line of sight. They can be immersed into denser plasmas and higher background pressures than other diagnostics, such as mass spectrometers, can tolerate.

The probe can be as simple as a wire tip or small electrode that is immersed directly into the plasma. A power supply or battery provides positive or negative voltages to the probe and the collected current is displayed on an oscilloscope. A thin plasma sheath is formed around a biased probe in a stationary plasma. The steady-state sheath thickness depends on the combined potential formed by probe and plasma. The current collected versus probe voltage can be explained by a complicated theory that involves calculations of particle trajectories through this sheath (Laframboise, 1966).

For fast-flowing PLD laser plasmas, the high plasma densities shield the charge within the plume from the probe potential until distances  $\sim \lambda_D$  (Debye length) from the electrode are reached. The probe potential therefore does not accelerate or decelerate the ions until they are within  $\sim 10 \mu\text{m}$  of the probe so accurate TOF for the ions and electrons are recorded. At negative biases, a positive current pulse is collected that records the flux  $(N(t)v(t))$  of ions arriving at the probe. The probes can be operated with a negative bias of typically  $-100 \text{ V}$ , which is sufficient to effectively repel all of the electrons in the arriving plasma (Segall and Koopman, 1973). Fast ( $\sim 5\text{-ns}$ ) electrical circuit response can be achieved, but attention must be paid to the design of the bias/detection circuit and unwanted points of grounding on chamber feedthroughs and in power supplies.

Several designs of ion probes include wires (Swift and Schwar, 1970; Segall and Koopman, 1973), plane discs (Goel et al., 1982; Mashburn and Geohegan, 1989), double probes (Chen, 1965), parallel plate probes (Mashburn and Geohegan, 1989; Ehler, 1972) and multigrid retarding-potential probes (Demtröder and Jantz, 1970). Examples of ion-probe signals and their usefulness in background gases are made later in the section on background gas interactions. The large amounts of charge collected by small ion probes typically imply fractional ionizations in luminous PLD plumes of  $\sim 0.1\text{--}10\%$ , depending on factors such as laser energy and distance. Their time dependence and magnitude can be checked by other techniques, such as optical absorption spectroscopy.

Figure 5.4 shows a schematic of a multigrid retarding potential probe that

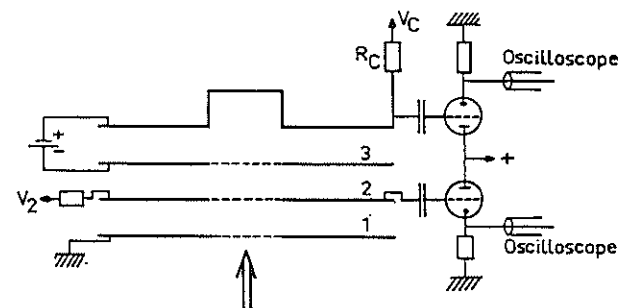


**Figure 5.4.** Schematic diagram of a multigrid retarding potential probe utilized for fast ( $t < 50 \text{ ns}$ ) time response analysis of laser-ablated aluminum and copper plumes produced by 30-ns full width at half maximum (FWHM) pulsed ruby-laser pulses. The probe utilizes several grids in front of a Faraday cup detector, maintained at suitable retarding potentials to select electrons and differently charged ions. (Reprinted from W. Demtröder and W. Jantz, *Plasma Physics*, 12, 691 (1970) with permission.)

utilizes a Faraday cup to collect the charge passing through three fine screen meshes (Demtröder and Jantz, 1970). The cup collector is maintained a few volts positive with respect to grid 3 in order to recapture secondary electrons that may be produced by high-energy neutral particles impacting with the collector. Mesh 2 is biased negatively in order to reject the low-energy electrons in the plasma. One discovery with this type of probe is that the finest mesh apertures are still too coarse to charge-separate the laser plasma at distances of a few centimeters from the target, but they must be used  $\sim 100\text{--}200 \text{ cm}$  away after the plasma has expanded to densities  $\sim 10^9 \text{ cm}^{-3}$ . Time-of-flight mass spectrometers and *electrostatic energy analyzers* (Shea et al., 1990) similarly must operate on low-density plasmas (far from the target) in order to avoid the Debye shielding effects.

When the electrons are eliminated, the ions can be energy-discriminated by applying increasing positive voltages to the collector. Figure 5.5 shows the

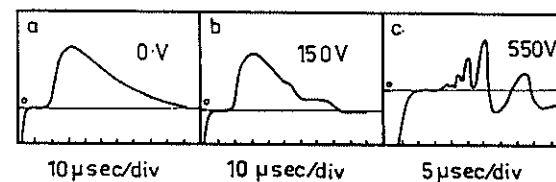


**Figure 5.5.** Ion-probe collector signals obtained with the ion probe of Figure 5.4 with potentials of (a)  $V_c = 0 \text{ V}$  (b)  $V_c = +150 \text{ V}$ , (c)  $V_c = +550 \text{ V}$  applied to the collector to repel positive copper ions with  $KE < ZeV_c$  at a distance of 170 cm from the target. The TOF ion current displays breaks from ions of charge  $Ze$  at energy  $ZeV_c$ . (Reprinted from W. Demtröder and W. Jantz, *Plasma Physics*, 12, 691 (1970) with permission.)

ion-probe signal for 693.4-nm laser ablation of copper (30-ns pulse,  $5 \times 10^{11} \text{ W cm}^{-2}$ ) at three different retarding potentials (Demtröder and Jantz, 1970). Ions of charge  $Ze$  are detected only if their kinetic energy exceeds  $ZeV_c$ . In this case, the velocity distributions of multiply charged copper atoms were overlapped in the TOF data. Analysis of the ion-probe signals enables KE distributions for the various ions to be determined, as shown in Figure 5.6 (Demtröder and Jantz, 1970).

Fast time-response Langmuir probes do not provide species resolution, but do provide the most versatile in situ monitor of the overall plasma conditions, including the magnitude and arrival time of the ion current in harsh conditions (see section on background gas effects for representative waveforms). Figures 5.7 and 5.8 show the dependence of the integrated ion current and the plume velocity on the KrF-laser energy density incident on a target of  $\text{Y}_1\text{Ba}_2\text{Cu}_3\text{O}_{7-x}$  (YBCO) in vacuum (Geohegan, 1992a). The probe reveals two regimes in Figure 5.7: a highly nonlinear ( $\Phi^{7.4}$ ) near-threshold regime where a visible plume is barely perceptible, and a ( $\Phi^{1.5}$ ) dependence where the plume emission becomes much brighter. The transition between the two regimes ( $\sim 0.37 \text{ J cm}^{-2}$ ) may signal the onset of plasma absorption of the laser pulse. Figure 5.8 shows that the velocity of the plasma smoothly increases throughout the same range of energy densities as in Figure 5.7.

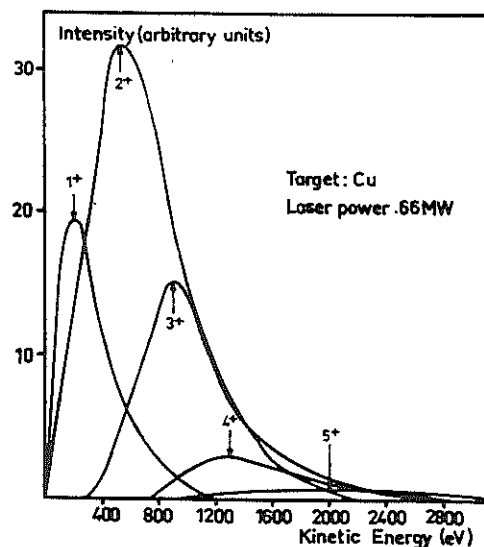


Figure 5.6. Energy distributions of the different charged Cu ions obtained with the ion probe of Figure 5.4 using data such as that of Figure 5.5, corrected for recombination. (Reprinted from W. Demtröder and W. Jantz, *Plasma Physics*, 12, 691 (1970) with permission.)

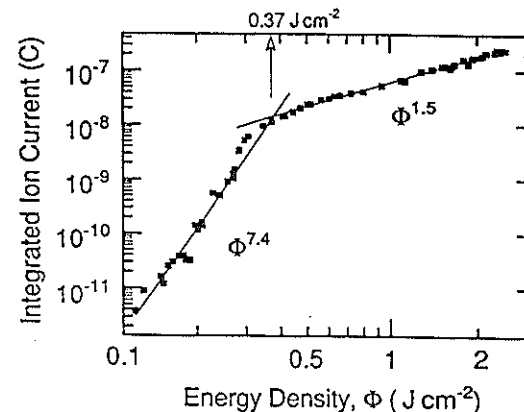


Figure 5.7. Dependence of total integrated positive charge collected 2.9 cm along the normal from a YBCO pellet (through a  $0.125\text{-cm}^2$  aperture at  $10^{-5}$  torr with a Cu planar ion probe biased at  $-100 \text{ V}$ ) on KrF-laser energy density,  $\Phi$ . The highly nonlinear yield of ions ( $\sim \Phi^{7.4}$ ) becomes more gradual ( $\sim \Phi^{1.5}$ ) circa  $0.37 \text{ J cm}^{-2}$ , where the optical emission from the plume becomes much brighter, indicating plasma absorption of the incoming laser pulse. (Reprinted from D. B. Geohegan, p. 73 in *Laser Ablation of Electronic Materials: Basic Mechanisms and Application*, ed. by E. Fogarassy and S. Lazare, North-Holland (1992) with permission.)

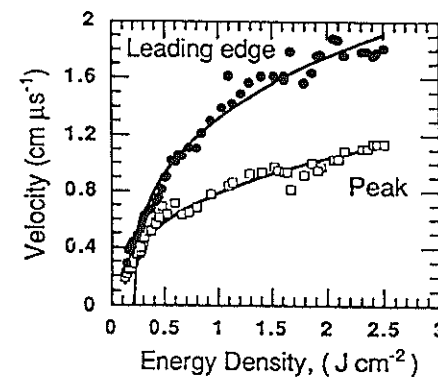


Figure 5.8. Corresponding increase in time-of-flight velocity of the expanding plasma front for the charge collection data of Figure 5.7, as measured by a fast-response (5-ns) ion probe following KrF-laser ablation of YBCO at  $10^{-5}$  torr. Velocities corresponding to the arrival of the peak and the leading edge ( $\equiv 10\%$  of peak) of the ion current pulse are shown. Curve fits to the data are of the form  $v = a(\Phi - \Phi_{th})^n$ , where  $n = 0.35$  (leading edge) and  $n = 0.37$  (peak) are shown. (Reprinted from D. B. Geohegan, p. 73 in *Laser Ablation of Electronic Materials: Basic Mechanisms and Application*, ed. by E. Fogarassy and S. Lazare, North-Holland (1992) with permission.)

The magnitude and velocity of the ion-probe signal combine to serve as a very sensitive in situ monitor of ablation reproducibility during PLD. Loss of ablation effectiveness, due to attenuation of the laser beam by window deposits or by cratering of the target surface, becomes evident as a loss of signal and velocity at the probe.

### 5.3.3 Optical Spectroscopy

Optical emission spectroscopy can be employed quite simply or in a very elegant fashion to yield information about PLD plumes. An inexpensive, yet sensitive monitor of ablation reproducibility is a simple *photodiode* that is used to record the entire visible plume emission for each laser shot. A study with a photodiode and a *quartz crystal monitor* has shown that the mass removal rate for YBCO is linearly correlated with the integrated plume emission (Foltyn et al., 1990).

Figure 5.9 diagrams an experimental apparatus used for optical emission and absorption spectroscopy, as well as ion probe measurements and fast photography (Geohegan, 1992b). Optical emission spectroscopy is well suited as a diagnostic for PLD ablation plumes since the laser energy densities required for reasonable film-deposition rates usually result in plasma ignition and a bright plume extending several centimeters from the target (as viewed by the naked eye). The plume is usually viewed from the side and optically imaged on the entrance port of a spectrometer such that the spectrometer slits sample a slice of the plume at a given distance along the target normal.

Emission spectroscopy is principally utilized for identifying the species in the laser plume from tabulated atomic lines and molecular bands. Time-integrated spectra from the entire plume volume is adequate for this task; however, spatially and temporally resolved measurements are necessary to infer the species' TOF and local populations. The spectral emission intensity is initially very bright during the initial stages of plume expansion due to Bremsstrahlung emission (free-free transitions) from the hot plasma. The Bremsstrahlung radiation results in a broad continuum of radiation that extends through the visible spectrum and produces the "white hot" region of the plume in the first  $\sim$ mm of expansion. Time-resolved spectral scans during this phase of the expansion reveal broadened emission lines (see below) from atoms and ions in addition to the Bremsstrahlung continuum. Emission lines from multiply charged ions quickly disappear as the plasma cools, in accordance with the Saha equations.

After expansion to distances of a few millimeters, PLD plumes generally exhibit a rich assortment of atomic and ionic lines, as shown in Fig. 10 (top trace) (Girault et al., 1989; Champeaux et al., 1992). The spectrally broader molecular bands can be resolved from the atomic transitions if a spectrometer with sufficient dispersion (as in Figure 5.10, bottom trace) is employed. The spectral intensities change dramatically with distance and time. By tuning the

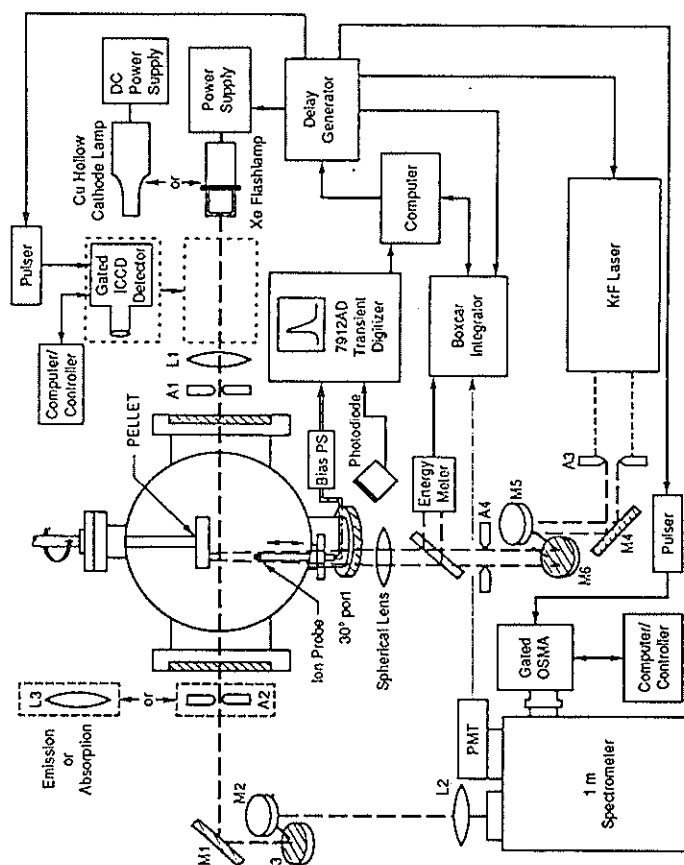
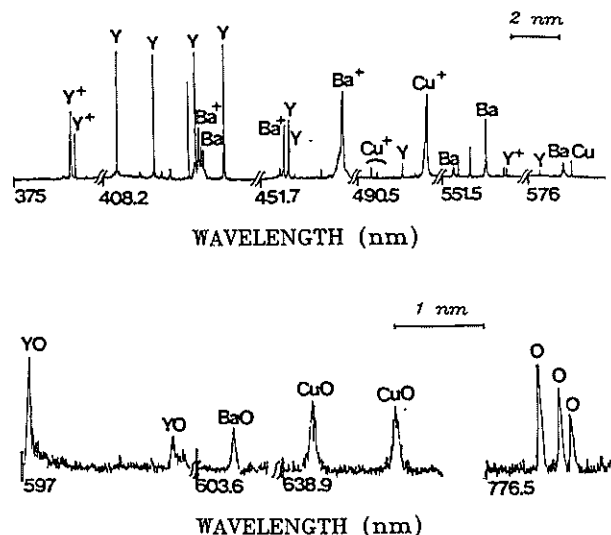


Figure 5.9. Block diagram of experimental apparatus useful for temporally (5 ns) and spatially resolved optical emission and absorption spectroscopy, ion-probe measurements, and fast photography of laser plumes used for PLD. (Reprinted from D. B. Geohegan, p. 73 in *Laser Ablation of Electronic Materials: Basic Mechanisms and Applications*, ed. by E. Fogarassy and S. Lazare, North-Holland (1992) with permission.)



**Figure 5.10.** High-resolution emission spectrum (0.3 Å) of the KrF-laser-induced plasma plume on an YBaCuO superconducting target. Observations are performed at  $d = 2$  mm using a boxcar gate width of 40 ns located 180 ns after the beginning of the interaction. (Reprinted from C. Girault, D. Damiani, J. Aubreton, and A. Catherinot, *Appl. Phys. Lett.* 55, 182 (1989) and C. Champeaux, D. Damiani, C. Girault, P. Marchet, J. Aubreton, J. P. Mercurio, and A. Catherinot, p. 141 in *Laser Ablation of Electronic Materials: Basic Mechanisms and Applications*, ed. by E. Fogarassy and S. Lazare, North-Holland (1992) with permission.)

spectrometer to a certain transition, such as the 613.2-nm YO bandhead in Figure 5.11, clues to the expansion dynamics of the various species are obtained from their TOF to the observation region (Girault et al., 1989; Champeaux et al., 1992). For example, the growth of the second, delayed YO emission component in Figure 5.11 is indicative of YO production by gas phase collision processes such as electron-collisional excitation or recombination.

It must be emphasized that most observed atomic transitions have typical lifetimes  $\sim 10$  ns, yet are observed many microseconds after the initial laser pulse. Emission spectroscopy therefore reveals the results of a collision event that occurred within  $\sim 10$  ns of the observation of emission.

Within the dense region of the initial plasma expansion, collisions are presumed to result in local thermodynamic equilibrium (LTE) of the plasma. Where LTE applies, the populations of the bound states follow a Boltzmann distribution. The plasma temperature can be estimated if relative intensities are measured for different transition frequencies,  $\nu_{mn}$ , in the same atom or ion via

$$\ln\left(\frac{\varepsilon_{mn}}{g_m A_{mn} \nu_{mn}}\right) = \ln\left(\frac{N}{Z}\right) - \frac{E_m}{kT} \quad (5.4)$$

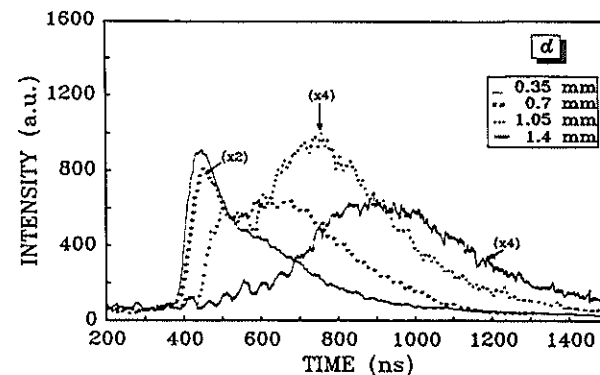


**Figure 5.11.** Temporal evolution of the 613.2 nm YO band head intensity for different values of the distance  $d$  from the YBaCuO target. LP indicates the laser pulse temporal location. Two YO populations are inferred from the double-peaked TOF data. (Reprinted from C. Girault, D. Damiani, J. Aubreton, and A. Catherinot, *Appl. Phys. Lett.* 55, 182 (1989) and C. Champeaux, D. Damiani, C. Girault, P. Marchet, J. Aubreton, J. P. Mercurio, and A. Catherinot, p. 141 in *Laser Ablation of Electronic Materials: Basic Mechanisms and Applications*, ed. by E. Fogarassy and S. Lazare, North-Holland (1992) with permission.)

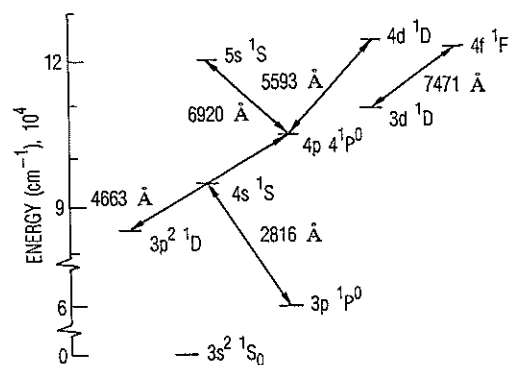
provided the transition probabilities,  $A_{mn}$ , are known (where  $\varepsilon_{mn}$  are the emissivities,  $E_m$  and  $g_m$  are the energy and degeneracy of the upper state) (Demtröder, 1982). The number density,  $N$ , and partition function,  $Z$ , are not needed since a plot of the left-hand side versus  $E_m$  has slope  $-1/kT$ . Figure 5.12 shows a Boltzmann plot for an aluminum plasma that is used to obtain a temperature of  $\sim 8130$  K at  $d = 1.27$  mm at  $\Delta t = 1 \mu s$  following  $5.3 \times 10^7 \text{ W cm}^{-2}$  irradiation of aluminum at 583 nm (Knudtson et al., 1987). Temperatures deduced from Boltzmann plots for many PLD materials typically yield plasma temperatures ranging from 5000 K to 15,000 K.

The transfer of thermal energy to kinetic energy during an adiabatic expansion into vacuum is predicted to result in velocities (Zel'dovich and Raizer, 1966)

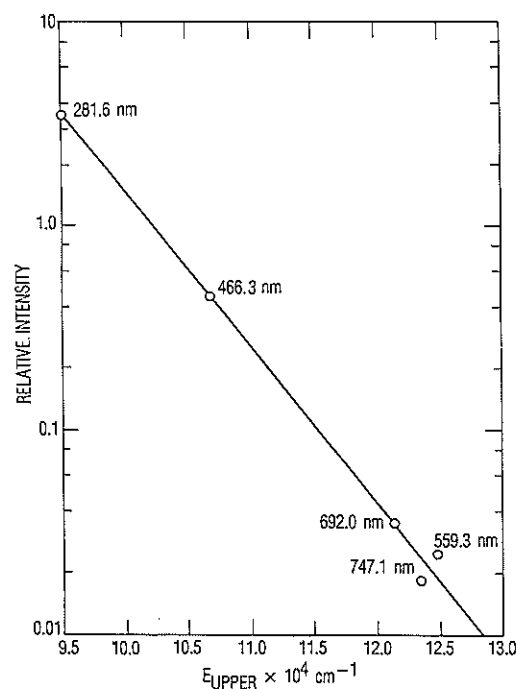
$$v = \left(\frac{2}{\gamma - 1}\right) \left(\frac{\gamma kT}{m}\right)^{1/2} \quad (5.5)$$

where  $\gamma$  is the ratio of specific heats ( $C_p/C_v$ ) for the plume. Using  $\gamma \approx 1.2$ ,  $T = 10,000$  K, and  $m \approx 100$  amu, velocities  $\sim 1 \times 10^6 \text{ cm s}^{-1}$  are predicted for plume atoms, very close to those observed.

Figure 5.13 shows TOF emission profiles for  $Y^*$ ,  $Ba^*$ , and  $Cu^*$  atoms observed 7.2 cm from a YBCO target following KrF ablation in vacuum (Zheng et al., 1989). The TOF arrival data indicate that the velocity distributions are different for each species, but are well represented by shifted



(a)



(b)

**Figure 5.12.** (a) Partial Grotrian diagram for Al(II) showing transitions used for temperature calculations. (b) Boltzmann plot for the Al(II) transitions diagrammed in (a) with the relative emissivities corrected for degeneracy and radiative rate as in Eq. 5.4 (see text). The slope gives a temperature  $= (8.13 \pm 0.27) \times 10^3$  K, at 1.27 mm from the target surface and 1- $\mu$ s delay time for a laser intensity of  $5.3 \times 10^7$  W cm $^{-2}$  ( $\lambda = 583$  nm). (Reprinted from J. T. Knudtson, W. B. Green, and D. G. Sutton, *J. Appl. Phys.* 61, 4771 (1987) with permission.)

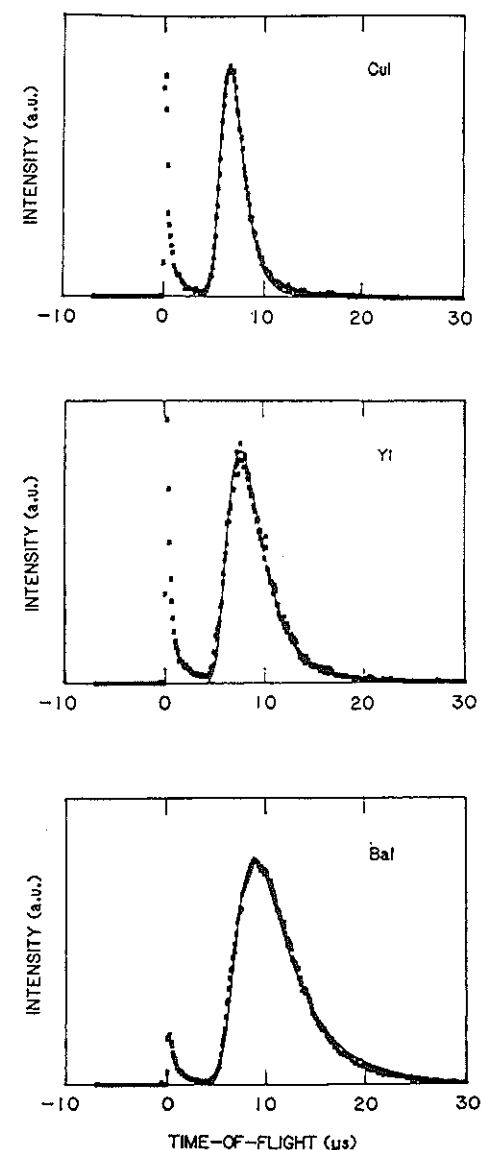


**Figure 5.13.** TOF emission profiles for Cu\*, Y\*, and Ba\* atoms observed 7.2 cm from a YBCO target following KrF ablation in vacuum. The TOF arrival data indicate that the velocity distributions are different for each species, but are well represented by shifted CMMB distributions of the form  $f(v) \sim v^3 \exp(-m(v - v_{cm})^2/2kT_{eff})$ . (Reprinted from J. P. Zheng, Z. Q. Huang, D. T. Shaw and H. S. Kwok, *Appl. Phys. Lett.* 54, 280 (1989) with permission.)

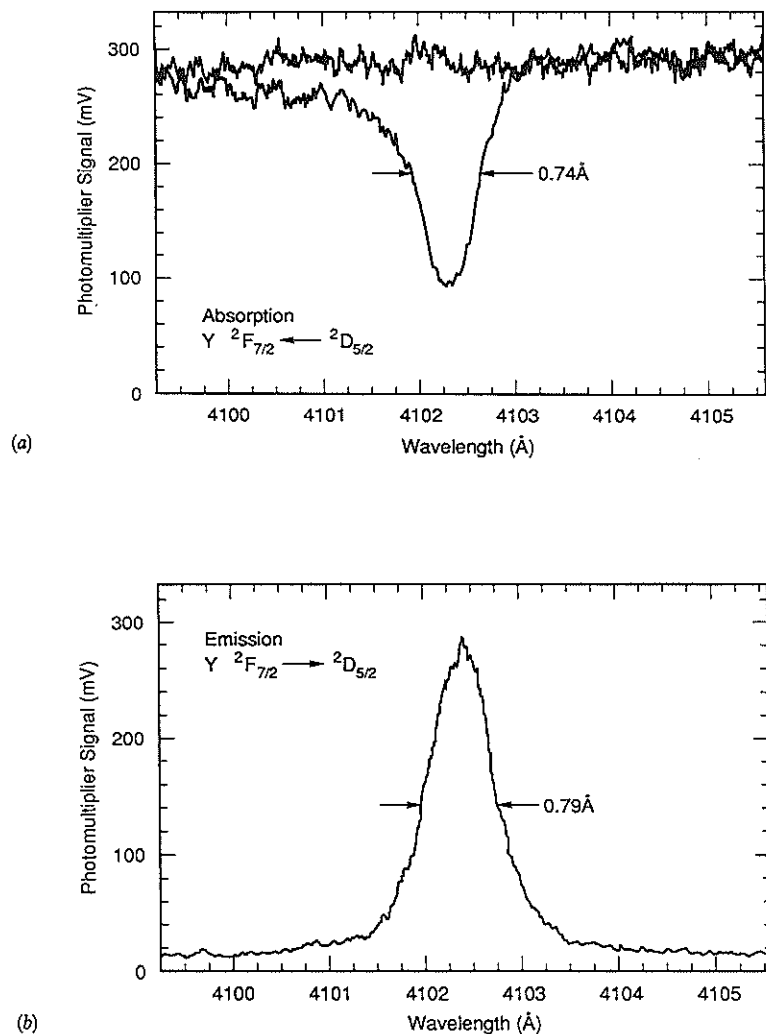


**Figure 5.14.** Spectrally broadened profiles of the  $Y2F_{7/2} - 2D_{5/2}$  transition at 4102.38 Å in (a) absorption and (b) emission at a distance of 2 mm from the surface of the YBCO pellet, 400 ns following irradiation by  $1\text{ J cm}^{-2}$  ArF-laser pulses. The lamp spectrum is included for comparison with the absorption profiles. (c) Temporal history for atomic Ba, 5 mm from the irradiated pellet as monitored by  $Ba^*$  emission and ground-state Ba absorption (of the xenon lamp beam) on the same  $6p^1P_1 - 6s^2^1S_0$  transition at 5535.48 Å. (d) The resulting TOF velocity distributions show a pronounced low-velocity component not revealed by the plume fluorescence. (Reprinted from D. B. Geohegan and D. N. Mashburn, *Appl. Phys. Lett.* 55, 2345 (1989) with permission.)

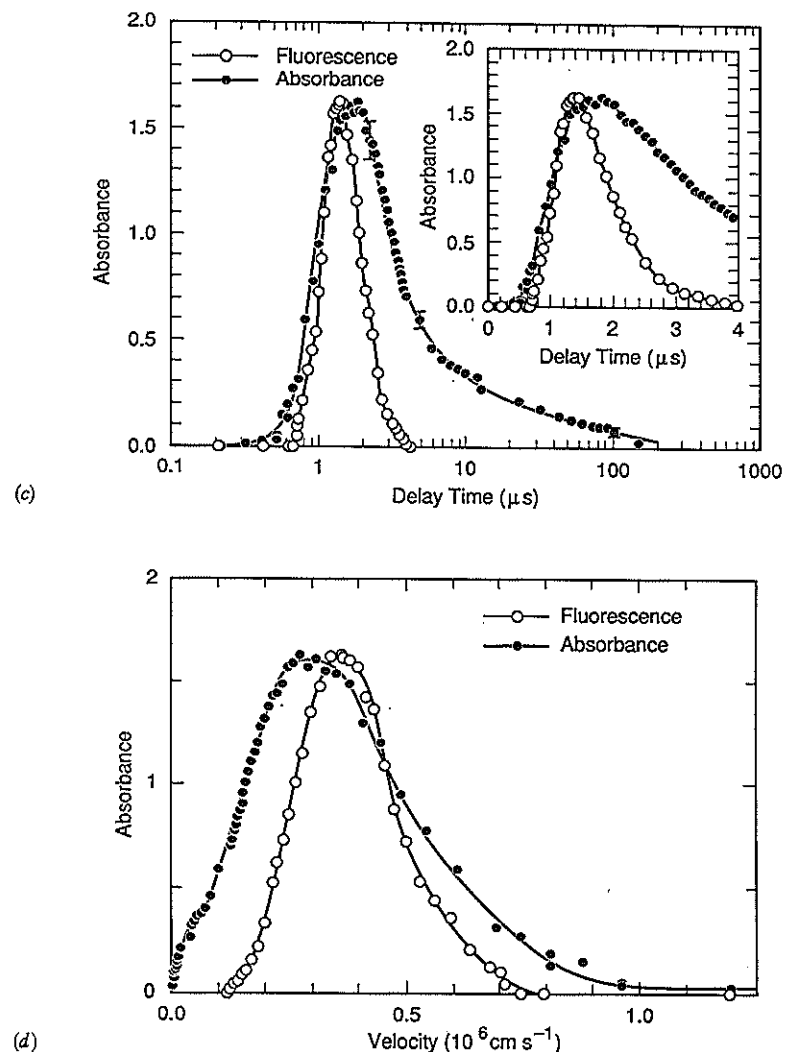


**Figure 5.14. (Continued)**

center-of-mass, Maxwell Boltzmann (CMMB) distributions of the form  $f(v) \sim v^3 \exp(-m(v - v_{cm})^2/2kT_{off})$ . These distributions are not observed to vary appreciably after the plume has expanded to distances  $d \sim 5\text{ mm}$  from the target, indicating that the species' translational energies (40–70 eV in this example) are “frozen” in a collisionless expansion at greater distances. Similar emission studies have been performed on many materials. The most probable velocities are generally closer to one another than predicted by the  $m^{-1/2}$

dependence of Eq. 5.5, however. Clearly, early interplume collisions between the species appear to moderate the expected disparity of velocities (as well as the expected spread in angular distribution (see Chapter 7 by K. Saenger, this book). It should be remembered that plasma collisions, such as electron impact excitation and three-body recombination, are necessary to produce the fluorescence observed at such late times in the "collisionless" regime. These collisions may arise from microturbulence induced by local Coulomb forces in the plasma.

Aside from a fraction undergoing excitation collisions, most of the plume species remain in their ground states after the initial expansion, and are therefore not observable in emission. The ground-state atoms and ions are observable in *absorption*, however, by a variety of techniques. One simple and versatile technique involves the use of a pulsed xenon flashlamp and a high dispersion spectrometer, as diagrammed in Figure 5.9. The xenon flashlamp emits a  $\sim 1\text{-}\mu\text{s}$  FWHM pulse of continuum emission that covers the visible and UV. The lamp pulse can be time delayed with respect to the ablation laser and the absorption at any wavelength is observed as a drop of lamp intensity by a photomultiplier and boxcar averager.

Figure 5.14a shows the absorption of the xenon flashlamp beam by ground-state yttrium atoms, a distance of only 2 mm from a YBCO pellet at a time delay of 400 ns following  $1\text{ J cm}^{-2}$ , 248-nm ablation in vacuum (Geohegan and Mashburn, 1989). The atomic line is considerably broadened compared to its natural linewidth (see below) in both absorption and emission (Figure 5.14b)). If the spectrometer is tuned to the maximum absorption wavelength and the lamp is delayed, the temporal profile of the ground-state species is obtained as in Figure 5.14c. The TOF profile inferred from optical absorption reveals an additional low-velocity component to the plume transport that is not implied by the optical emission (Figure 5.14d).

Alternatively, hollow cathode lamps are available for different elements that emit DC emission on resonance lines, as shown in Figure 5.9 (Akhsakhalyan et al., 1982a). Densities on the order of  $10^9\text{ cm}^{-3}$  can be detected on strong transitions. The temporal profile of the ground-state atoms can then be observed on a single laser shot, instead of incrementing the lamp delay over multiple shots. However, the wavelength is fixed and cannot reveal the line broadening as a function of position and time.

Comparison between optical emission, optical absorption, and ion-probe TOF data show that the optical emission time dependence is very similar to that of the ions (plasma) which might be expected since the emission is believed to arise from plasma excitation or recombination collisions. Figure 5.15a overlaps TOF dependences of optical absorption from ground state  $\text{Ba}^+$  and Ba, with optical emission from excited  $\text{Ba}^*$  atoms following  $2.7\text{ J cm}^{-2}$  KrF-laser ablation of YBCO in vacuum (Geohegan, 1991). The excited-state fluorescence clearly mimics the ground-state ion population, while the ground-state neutrals exhibit a bimodal velocity distribution, which is more clearly

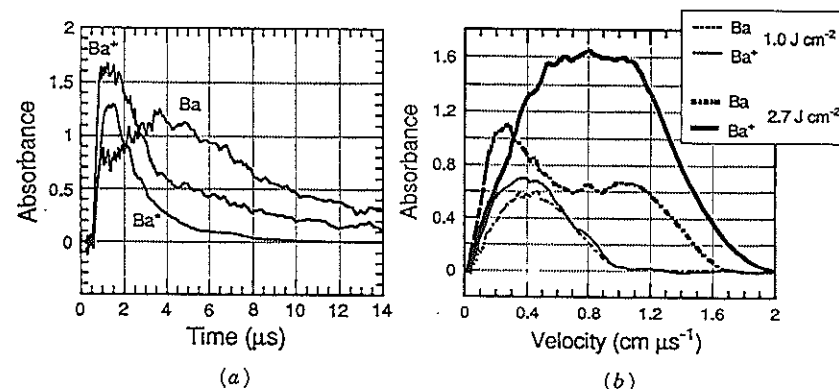


**Figure 5.15.** (a) Comparison between the temporal profiles of  $\text{Ba}^+$  and Ba ground-state absorption (at 455.4 nm and 553.5 nm, respectively), and  $\text{Ba}^*$  fluorescence (553.5 nm, not to scale) monitored at  $d = 1.0\text{ cm}$  following  $2.7\text{ J cm}^{-2}$  irradiation of YBCO at  $10^{-5}$  torr. The neutral fluorescence follows the ground-state ion population and the fast component of the ground-state neutral population. (b) The ground state  $\text{Ba}^+$  and Ba absorption TOF profiles show that the neutrals exhibit a bimodal velocity distribution and lag the ions at  $2.7\text{ J cm}^{-2}$ . (Reprinted from D. B. Geohegan p. 28 in *Laser Ablation: Mechanisms and Applications*, ed. by J. C. Miller and R. F. Haglund, Springer-Verlag, Heidelberg, 1991.)

seen in Figure 5.15b. The fast component of the ground-state neutral population appears to be partially fed from recombining ions through the excited-state fluorescence. From the measured peak absorbances, the  $\text{Ba}^+$  ions were found to outnumber the Ba neutrals by at least 5 to 1 (Geohegan, 1991).

### 5.3.3.1 Line Broadening

As shown in Figure 5.14a and b, emission or absorption spectroscopy of PLD plasmas can reveal that the linewidths of the measured spectral lines are noticeably broadened above the natural ( $\sim 10^{-4}\text{-}\text{\AA}$ ) linewidth. For example, a high-dispersion spectrometer can readily provide  $0.1\text{-}\text{\AA}$  resolution and spectral lines are often observed close to the target with a FWHM of several angstroms. The lines are also shifted in position, which may not be as apparent as the broadening unless the wavelength is known absolutely. Line broadening is a principal plasma diagnostic technique for stationary plasmas, (Griem, 1974), but has not been utilized as widely for PLD plasmas. Valuable information relevant to the physics (and diagnostics) of the ablation process is contained in the shape of these spectral lines.

The extreme broadening is observed early in the expansion of the laser plasma, when the plume density and temperature are the highest. When the plume arrival is observed at farther distances from the target, the maximum



linewidth drops precipitously within  $\sim 5$  mm and then levels off to a near constant value, larger than what might be expected on the basis of pressure or Doppler broadening mechanisms. These are discussed below.

There are three likely broadening mechanisms in PLD plumes: Doppler broadening resulting from motion of the atoms; Stark broadening from collisions with charged species; and resonance broadening from collisions between like neutral species on strong resonance lines (Griem, 1974; Griem, 1964; Hughes, 1975; Bekefi, 1976).

The high expansion velocities and angular spread of PLD plasma plumes results in a variation of observed wavelengths for a given emission line due to the Doppler shifts  $\Delta\lambda = \lambda(v_x/c)$  created by the different velocity components of the emitting particles along the viewing axis,  $v_x$ . For an atom moving with  $v_x \sim 1 \times 10^4$  m/s and emitting a 5000-Å photon, this amounts to a 0.17-Å shift, which is just detectable using a  $\sim 1$  m spectrometer and high-dispersion grating. Spectral lines, such as in Figure 5.14a and b, are often broadened considerably more than can be explained by *Doppler broadening* alone.

In the densest, hottest region of laser plasmas used for PLD, the Stark effect results in a broadening of atomic and ionic emission lines as well as a shift in the line-center wavelength. *Stark broadening* results from collisions of electrons (and ions) that Stark-shift the energy levels of the emitting atom. The linewidth of a Stark-broadened atomic line is approximately given by the sum of two (electron-impact and ion-impact) terms

$$\Delta\lambda = 2W\left(\frac{n_e}{10^{16}}\right) + 3.5A\left(\frac{n_e}{10^{16}}\right)^{1/4}\left(1 - 1.2N_D^{-1/3}\right)W\left(\frac{n_e}{10^{16}}\right) \quad (5.6)$$

and can yield the electron density  $n_e$  if the two constants  $W$  (the electron-impact width parameter) and  $A$  (the ion-broadening parameter) are among those tabulated from plasma spectroscopy measurements. The number of particles in the Debye sphere,  $N_D$ , at plasma temperature  $T_e$  is given by

$$N_D = 1.72 \times 10^9 \frac{[T_e(\text{eV})]^{3/2}}{[n_e(\text{cm}^{-3})]^{1/2}} \quad (5.7)$$

Using a 1-eV plasma temperature and  $n_e = 1 \times 10^{17} \text{ cm}^{-3}$ , one finds that  $N_D = 5.4$  and from Eq. 5.6, with  $W \approx A \approx 0.1 \text{ Å}$ , Stark-broadened linewidths of  $\Delta\lambda = 2 \text{ Å}$  are predicted. The contribution is almost entirely due to electron impact, and the halfwidth of the Stark-broadened transition can be estimated by the first term in Eq. 5.6 to a good approximation. For heavy neutrals, Stark broadening should be observable for electron densities  $n_e > 10^{14} \text{ cm}^{-3}$ .

However, *self-absorption* of the emission from the hot core of the plasma by the surrounding cooler shell of expanding vapor affects the shape of measured emission profiles, so that peak-heights and linewidths are not easily interpreted. Figure 5.16 shows a line-broadened  $\text{Ba}^+$  emission line with the center of the

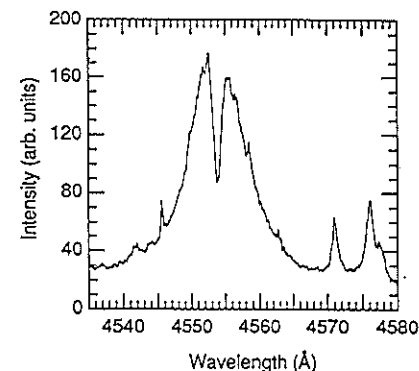


Figure 5.16. Spectral broadening and self-absorption of the 4554-Å  $\text{Ba}^+$  ( $6p^2P_{3/2} \rightarrow 6s^2S_{1/2}$ ) resonance line fluorescence measured at  $d = 1$  mm from a YBCO pellet irradiated with  $3.0 \text{ J cm}^{-2}$  at 248 nm in  $10^{-6}$  torr at  $\Delta t = 140\text{--}200$  ns following the laser-pulse arrival. The central portion of the spectral line is absorbed by the cooler plume surrounding the hotter central region of the plume. (Reprinted from D. B. Geohegan, p. 73 in *Laser Ablation of Electronic Materials: Basic Mechanisms and Applications*, ed. by E. Fogarassy and S. Lazare, North-Holland (1992) with permission.)

line inverted due to radiation trapping (Geohegan, 1992d). The wings of the emission are not absorbed enroute to the detector, while the peak is strongly absorbed by a shell of ground-state ion vapor.

Collisions between atoms in the high-pressure region during the initial stage of plume expansion can lead to pressure broadening of observed atomic transitions. The energy levels of an emitting atom can be perturbed by another atom via nonresonant (van der Waals  $\sim -C_6/r^6$ ) or resonant (dipole  $\sim -C_3/r^3$ ) interactions. The resonant interaction only occurs when an excited atom interacts with an identical atom in the ground state and when a strong allowed electric dipole transition, usually the resonance line of the atom, connects the two levels. This perturbation leads to *resonance broadening* of the resonance line transition and the transition FWHM,  $\Delta\lambda$ , is linearly proportional to the density,  $N$ , of identical perturbers and the oscillator strength,  $f$ , of the transition. For example, the 5535-Å resonance line of barium would be broadened to 0.3 Å by a ground-state density of  $1.5 \times 10^{17} \text{ cm}^{-3}$ . The situation would thus be expected to be observable within the first millimeter of plume expansion.

Figure 5.17 shows an example of careful emission spectroscopy of a carbon laser plasma in which annular regions of ion density were interpreted from spatial measurements of the Stark shifts of the different ion transitions at different times (Irons, 1972). The measurements show that the more highly ionized carbon ions are in the central core of the plume and that recombination

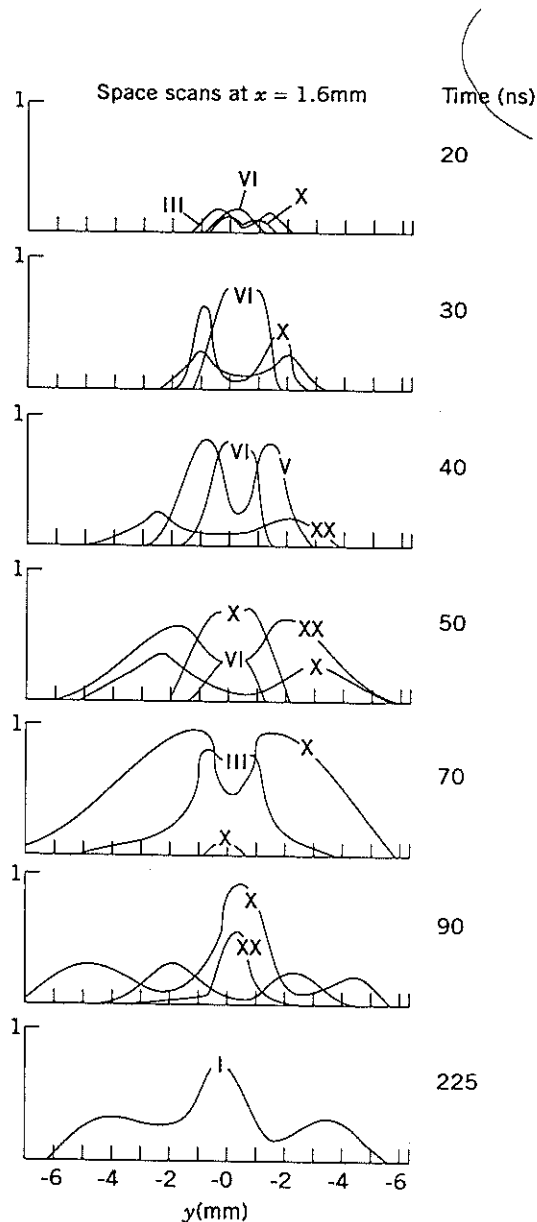


Figure 5.17. A sequence in time showing the development of the spatial distribution of C(I-VI) species at  $d = 1.6$  mm from a polyethylene foil irradiated with a ruby laser (5-J, 17-ns FWHM pulse). The measured Stark and Doppler spectral broadening was interpreted to obtain the cross sections of the plume at  $d = 1.6$  mm in the figure. The higher charged ions occupy the central annular regions at early times, recombining to feed the lower charged state populations at later times. (Reprinted from F. E. Irons, R. W. P. McWhirter and N. J. Peacock, *J. Phys. B: Atom. Molec. Phys.* 5, 1975 (1972) with permission.)

of these ions leads to emission from daughter ions at later times along the same directions.

In summary, optical emission and absorption spectroscopy of PLD plumes reveals that both the intensity and the lineshape of spectral lines vary as a function of the distance from the target and the time delay following the laser pulse. A true measure of the absorbance versus time at a given distance, for example, would require measurements of the spectral linewidth at each time. One or more of the variables is usually sacrificed, depending on the detailed information that is required.

For more sophisticated measurements of plasma properties, such as the local vibrational or rotational temperature of a particular molecule in the laser plume, a pulsed, tunable dye laser beam can be used in place of the broad-band lamp in Figure 5.9.

### 5.3.4 Laser-Induced Fluorescence

Ground-state atoms and molecules can also be observed by *laser-induced fluorescence* (LIF). A tunable dye laser pulse is used to optically pump the ground-state species to a selected excited state (Demtröder, 1982; Dreyfus, 1990; Otis and Dreyfus, 1991; Dreyfus, 1991). This absorption is followed by spontaneous emission of the excited state to lower energy levels. An interference filter or spectrometer tuned to one of these wavelengths is used to record the LIF signal intensity. Tunable laser pulses (FWHM  $\sim 10$  ns) and excited-state lifetimes ( $\tau \sim 10$  ns) are sufficiently short to provide good TOF velocity information in PLD plumes.

Laser-induced fluorescence is most useful in determining local vibrational and rotational temperatures of molecules in laser plumes. Often it is found that three different temperatures will be measured for a molecule in laser plumes: translational,  $T_k$ ; vibrational,  $T_v$ ; and rotational,  $T_r$ . The rotational temperature is estimated by comparison between the measured occupation of a rotational manifold using LIF, and that calculated from a Boltzmann distribution. Figure 5.18a shows an LIF spectrum of AlO molecules detected via the  $B^2\Sigma^+ - X^2\Sigma^+$  transition following KrF-laser ablation of  $\text{Al}_2\text{O}_3$  (Dreyfus et al., 1986). The molecules were rotationally fairly cool,  $T_r \approx 500$  K, while the TOF data of Figure 5.18b implies translational temperatures  $kT_k \approx 1.2$  eV ( $T_k \approx 14,000$  K). Vibrational temperatures are estimated from the populations of the vibrational levels and yielded  $T_v \approx 600$  K in this study. In this case, the low vibrational and rotational temperatures could not be reconciled with a thermal sputtering mechanism, and pointed to an electronic material removal mechanism for  $\text{Al}_2\text{O}_3$  ablation at 248 nm consistent with the translational energy distribution (Dreyfus et al., 1986).

Time-of-flight data for ground-state atoms and ions can also be measured, as shown in Figure 5.18b and Figure 5.19. The TOF velocities of ground state Y and  $\text{Y}^+$  after YBCO ablation at two energy densities is shown in Figure 5.19 (Otis et al., 1993). The ions are observed to precede the neutrals in the plume

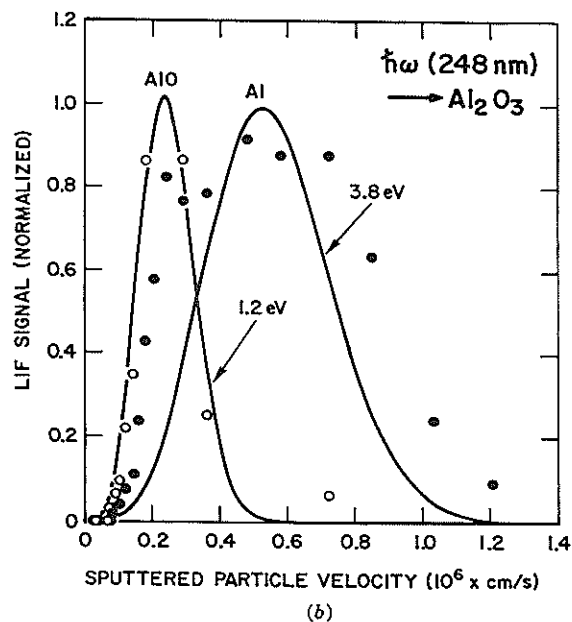
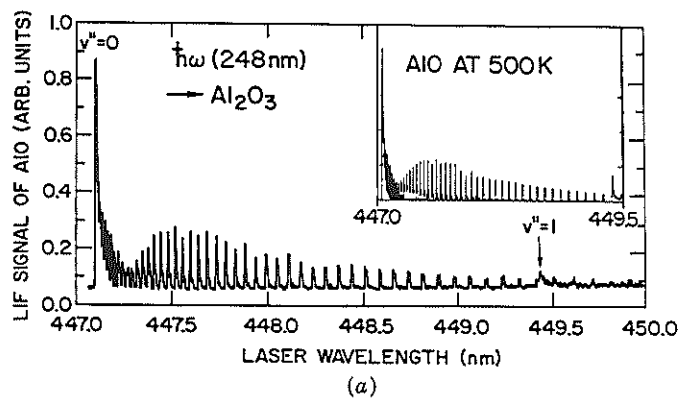


Figure 5.18. (a) Laser-induced fluorescence spectrum of AlO molecules detected via the  $B^2\Sigma^+ - X^2\Sigma^+$  transition following KrF-laser ablation of  $\text{Al}_2\text{O}_3$ . The rotational distribution is approximately Boltzmann with  $T_r \approx 500$  K. (b) TOF velocity distribution for Al atoms and AlO molecules after  $0.7 \text{ J cm}^{-2}$  KrF-laser ablation of  $\text{Al}_2\text{O}_3$  in vacuum. In contrast to the rotational temperature for AlO, the AlO translational temperature implied by a Maxwell-Boltzmann distribution (solid lines) is  $kT_k \approx 1.2 \text{ eV}$  ( $T_k \approx 14,000$  K). (Reprinted from R. W. Dreyfus, Roger Kelly, and R. E. Walkup, *Appl. Phys. Lett.* 49, 1478 (1986) with permission.)

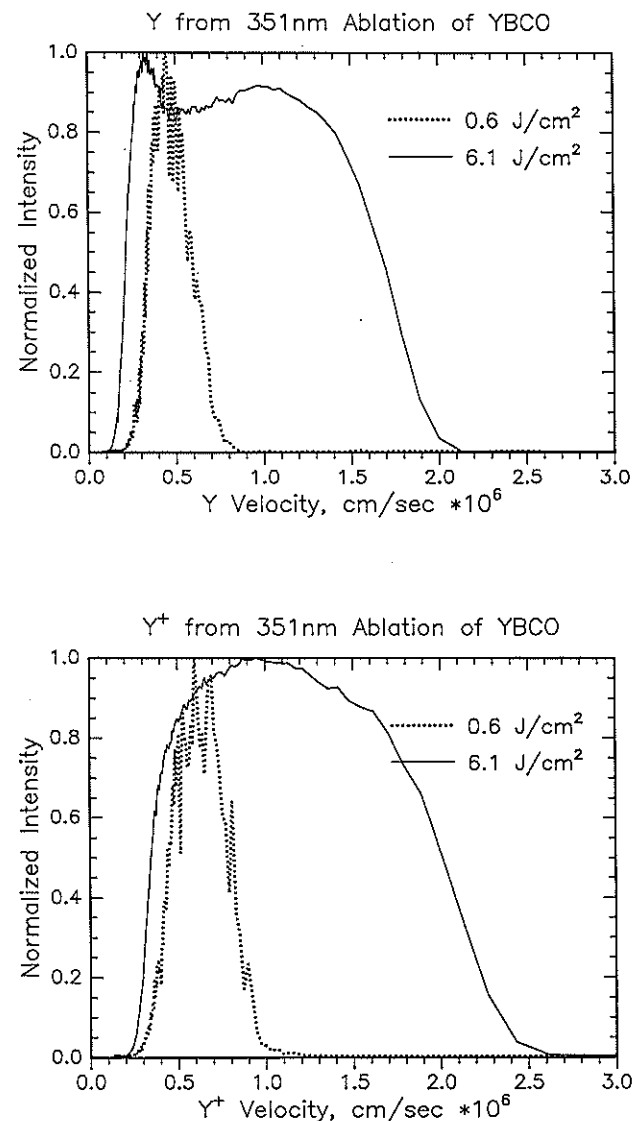


Figure 5.19. Laser-induced fluorescence TOF velocity distributions of the ground-state Y and  $\text{Y}^+$  populations after YBCO ablation at two energy densities,  $0.6$  and  $6.1 \text{ J cm}^{-2}$ , in vacuum. The ions are observed to precede the neutrals in the plume at both low and high fluence, and the growth of a low-energy Y velocity component produces an apparent bimodal appearance to the velocity distribution at  $6.1 \text{ J cm}^{-2}$ . (Reprinted from C. E. Otis and P. M. Goodwin (1993) with permission.)

at both low and high fluence, and the growth of a low-energy Y velocity component produces an apparent bimodal appearance to the velocity distribution at  $6.1 \text{ J cm}^{-2}$ .

Finally, tuning the dye laser wavelength slightly off line-center results in Doppler-shifted absorption ( $\Delta\lambda = \lambda(v_z/c)$ ) by species traveling with a specific velocity,  $v_z$ , along the probe beam axis (Arlinghaus et al., 1989). The small region of laser-induced fluorescence in the laser plume can be moved about by tuning the dye laser to provide a spatial map of the species' angular velocity distribution (Lynds et al., 1989).

### 5.3.5 Photography and Imaging

Photography and other imaging techniques add another dimension to ablation diagnostics by providing two-dimensional snapshots of the three-dimensional plume propagation. This capability becomes essential for a hydrodynamic understanding of the plume propagation and reactive scattering.

High-speed cameras with electronic gates and image converters can be used to image the plume emission, as in *high-speed framing photography*, *streak photography*, and *intensified-CCD array (ICCD) photography*. Alternatively, slow cameras can be utilized with a delayed pulsed laser, which serves as a coherent flashbulb for interference imaging by *Schlieren photography* or scattering imaging by *shadow photography*. Tuning the wavelength of the delayed laser to image the absorption of a particular species is utilized in dye laser resonance absorption photography (DLRAP) and LIF imaging.

And *ultrafast imaging* techniques with  $\sim 2$ -ps temporal resolution are now allowing investigations of molecular energy transfer ablation processes to be investigated (Kim et al., 1989a; Kim et al., 1989b). All of these techniques involve a considerable monetary investment.

While imaging techniques are extremely useful for studies of ablation plumes in vacuum, they are invaluable for studies of the complex hydrodynamic phenomena associated with plume propagation into background gases. They are excellent diagnostics for PLD plumes since PLD is often performed in the presence of an ambient background gas, such as oxygen for the high- $T_c$  superconductors. This utility is illustrated in the next section by a variety of imaging techniques.

## 5.4 BACKGROUND GAS EFFECTS

Ambient gases present during PLD scatter, attenuate, and thermalize the plume, changing important film growth parameters such as the spatial distribution, deposition rate, and kinetic energy distribution of the depositing species. In addition, reactive scattering can result in the formation of molecules or clusters that can aid in the incorporation of the gas into the growing film, such

as the formation of YO from the ablation of Y into  $\text{O}_2$  (Lynds et al., 1989; Girault et al., 1989).

In general, raising the background pressure results in the following effects: (1) an increase in fluorescence from all species due to collisions on the expansion front and subsequent interplume collisions; (2) a sharpening of the plume boundary, indicative of a shock front; (3) a slowing of the plume relative to the propagation in vacuum, resulting in (4) spatial confinement of the plume.

Figure 5.20 shows a direct comparison between laser ablation of YBCO into vacuum and into 100 mTorr oxygen under typical PLD conditions (Geohegan, 1992). These images were recorded with an ICCD camera, which converts a light image into photoelectrons at a photocathode, amplifies these electrons (gain  $\sim 5 \times 10^6$ ) through a microchannel plate (MCP), reconverts the electrons to light on a phosphor screen, and captures these images with a CCD array. A fast voltage pulse temporarily removes a reverse bias on the MCP and serves as the shutter for the camera, giving  $\sim 5$ -ns resolution.

In vacuum, (Figure 5.20a-f) the ICCD photographs record the relatively weak fluorescence due to interbeam collisions and show that the highly forward-directed spatial distribution does not change after Figure 5.20a. In 100-mTorr oxygen, the dense plasma expands in much the same manner during

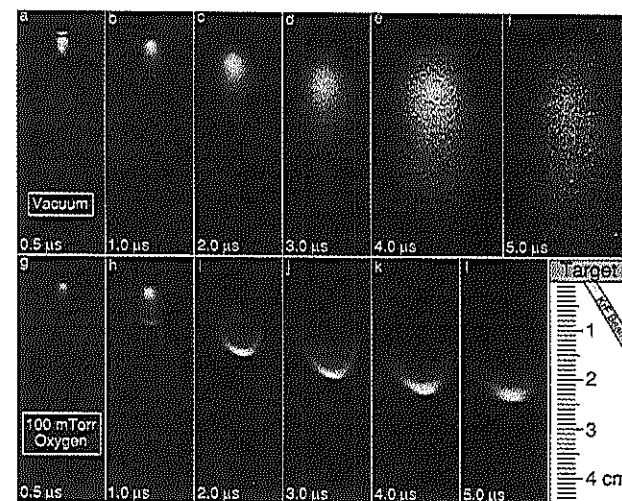


**Figure 5.20.** ICCD photographs of the visible plasma emission (exposure times 20 ns) following  $1.0\text{-J-cm}^{-2}$  KrF/YBCO ablation into [(a)–(f)]  $1 \times 10^{-6}$  torr and [(g)–(l)] 100-m torr oxygen at the indicated delay times from the arrival of the laser pulse. The  $0.2\text{-cm} \times 0.2\text{-cm}$  248-nm laser pulse irradiated the YBCO target at an angle of  $30^\circ$ , as shown. (Reprinted from D. B. Geohegan, *Appl. Phys. Lett.*, **60**, 2732 (1992) with permission.)

the first microsecond, virtually unhindered by the background oxygen. Collisions on the expanding front of the plume lead to increased fluorescence there, however, while the emission from the rest of the plume remains unperturbed.

Figure 5.21 illustrates the three regions of emission at  $\Delta t = 1.0 \mu\text{s}$  for vacuum and  $p_{\text{O}_2} = 100 \text{ mTorr}$  [plots of Figure 5.20(b) and (h)] (Geohegan, 1992). The notable difference is the formation of the contact front on the leading edge of the plume expansion. The dense plume appears to have pushed the background gas ahead in much the same manner as a "snowplow." The slower moving bulk of the plume appears unaffected at this point, as does the nearly stationary region of plasma emission near the hot pellet.

As the plume continues to expand, the pressure in the plume continues to

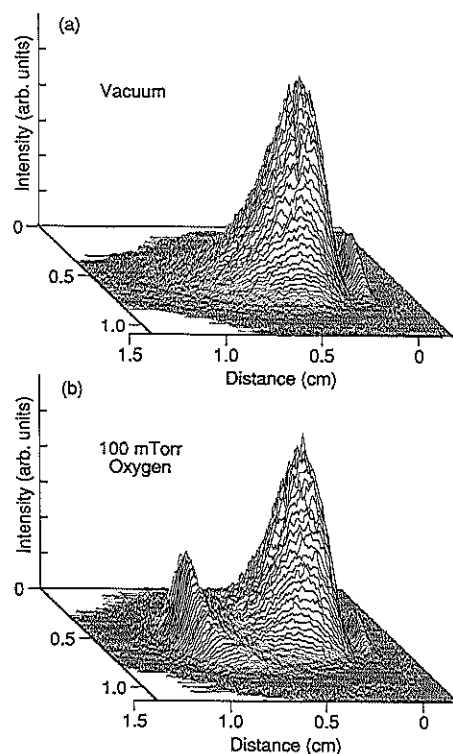


**Figure 5.21.** Visible plasma emission intensity at  $\Delta t = 1.0 \mu\text{s}$  following  $1.0\text{-J-cm}^{-2}$  KrF-laser ablation of YBCO in (a)  $1 \times 10^{-6}$  torr and (b) 100-m torr oxygen. These are intensity plots of the ICCD photographs of Figure 5.20 (b) and (h) illustrating the formation of an expansion front due to background gas collisions. (Reprinted from D. B. Geohegan, *Appl. Phys. Lett.*, 60, 2732 (1992) with permission.)

decrease, the expansion front is slowed more noticeably, and the shielded slower components propagate to coalesce with the slowed material on the contact front. This coalescence and slowing can be seen from  $\Delta t = 1.0\text{--}2.0 \mu\text{s}$  in Figure 5.20 as the emission becomes dominated by that at the expansion front. The plume continues to slow behind this sharp front until nearly stopped ( $v_{1e} \sim 0.06 \text{ cm-}\mu\text{s}^{-1}$  at  $\Delta t = 8.0 \mu\text{s}$  under these conditions).

Fast photography with ICCD sensitivity is extremely useful for studying these hydrodynamic effects. Emission spectroscopy along a particular line-of-sight is less useful without previous knowledge of the hydrodynamics. Absorption spectroscopy is useful for the leading edge of the expansion, but motion of the trailing material is muddled with absorption from the stopped vapor. Ion probes, being flux sensitive, record only the flux of ions that penetrate to their positions and are therefore very useful in background gases.

The combined effects of attenuation and slowing of the plume are evident in the ion-probe data of Figure 5.22 (Geohegan, 1991). Figure 5.22a shows that the integrated ion-probe current drops exponentially with pressure ( $N$ ) and distance ( $x$ ) as might be expected from a simple Beer's law  $I = I_0 e^{-N\sigma x}$  scattering model, yielding a generalized cross section  $\sigma \approx 2 \times 10^{-16} \text{ cm}^2$  for ion-oxygen collisions. Of course, the details of the plume thermalization involve highly velocity-dependent and generally unknown scattering cross sections for the various species, diffusion at the expansion front, and hydrodynamic effects (Waldeer and Urbassek, 1991; Valles-Abarca and Gras-Marti, 1984).

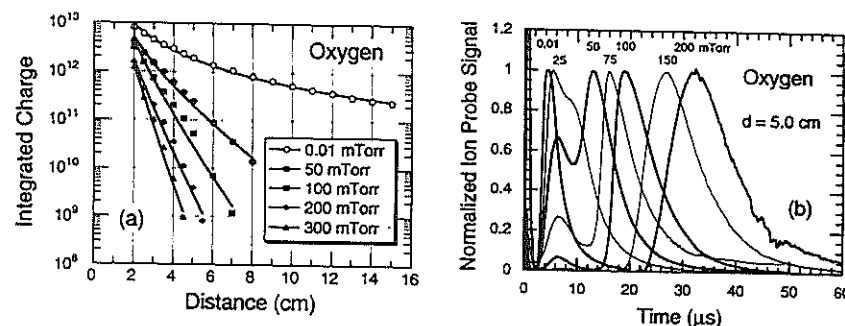


**Figure 5.22.** (a) Integrated positive-ion charge transmitted through oxygen backpressures of 0.01, 50, 100, 200, and 300 m torr and measured by fast ion probe along the normal to a YBCO pellet irradiated with  $3.0\text{-J-cm}^{-2}$  248-nm irradiation. Fits to the data are of the form  $d^{-1.8} e^{-\beta d}$ , where  $\beta$  is the attenuation coefficient and  $d$  is the distance from the pellet. (b) Normalized ion-probe current waveforms measured at  $d = 5.0 \text{ cm}$  along the normal to a YBCO pellet irradiated with  $3.0\text{-J-cm}^{-2}$  248-nm irradiation in 0.01-, 25-, 50-, 75-, 100-, 150-, and 200-m torr oxygen. (Reprinted from D. B. Geohegan p.28 in *Laser Ablation: Mechanisms and Applications*, ed. by J. C. Miller and R. F. Haglund, Springer-Verlag, Heidelberg, 1991.)

Figure 5.22b shows the slowing effects of several pressures of background oxygen on the arrival of the plasma plume at  $d = 5$  cm (Geohegan, 1991). The ion-current waveforms give another perspective of the transition region noted in Figure 5.20(h)–(j) and Figure 5.21. As the pressure is increased, the ion current displays a two-component character: a fast component that is transmitted with little delay, and a component that has undergone pronounced slowing. As the background pressure is increased, more of the plume is delayed to longer times and a single-component pulse shape is acquired past  $\sim 100$  mtorr. This effect is seen even with single-element targets. Modeling of the shape of the ion-probe signal following the transition region shows that it propagates in a generalized  $R = at^n$  shock model (Geohegan, 1992).

Different diagnostics of the background gas interaction therefore indicate that the plume interacts hydrodynamically with the background gas, undergoing a transition to a stable shock front as the plume material scatters off the background gas, becomes delayed, and coalesces with the slower moving material. The ion probe shows nonemitting positive ions, while the fast photography follows the densest collisional (delayed) component. Emission spectroscopy confirms that the different species bunch up behind this slowed shock front.

Since the slowing appears velocity dependent, the velocity  $v(t) \neq R/\Delta t$ , but is best determined by the slope of a measured position–time ( $R$ – $t$ ) plot. Figure 5.23 gives an ( $R$ – $t$ ) plot of the leading edge of the plasma emission (along the normal to the irradiated region) from ICCD images including those of Figure 5.20 (Geohegan, 1992). In vacuum, the leading edge maintains a constant velocity of  $1.0 \text{ cm} \cdot \mu\text{s}^{-1}$ . In 100-mtorr oxygen, however, the plume appears unaffected by the background gas for the first microsecond and then slows

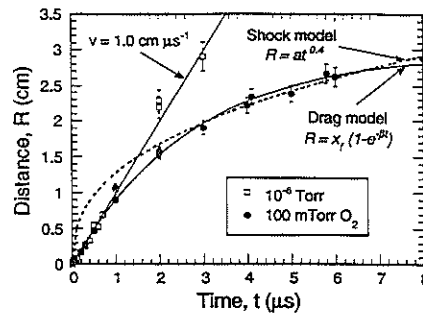


**Figure 5.23.**  $R$ – $t$  plots of the expansion-front boundary of the luminous plume along the normal to the YBCO pellet measured from gated ICCD images including those of Figure 5.21. Two fits to the 100-m torr oxygen expansion data are shown: (dashed line) shock model  $R = at^{0.4}$  with  $a = 1.26 \text{ cm} \cdot \mu\text{s}^{-0.4}$ ; (solid line) drag model  $R = x_f [1 - \exp(-bt)]$ , with  $x_f = 3.0 \text{ cm}$ ,  $b = 0.36 \mu\text{s}^{-1}$ . The error bars account only for uncertainties in estimating the position of the expansion front boundary. (Reprinted from D. B. Geohegan, *Appl. Phys. Lett.*, **60**, 2732 (1992) with permission.)

progressively as shown. Two fits to the 100-mtorr data are given in Figure 5.23: (dashed line) shock model  $R = at^{0.4}$  and (solid line) drag model  $R = x_f [1 - \exp(-bt)]$ . These models are briefly discussed below.

For high background pressures a blast wave model (Zel'dovich and Raizer, 1966) has been used to describe the luminous shock front caused by the expansion of laser ablation plasmas. This model was developed to describe the propagation of a shock wave through a background gas (density  $\rho_0$ ) caused by the sudden release of energy,  $E_0$ , in an explosion. The propagation of a spherical shock front through a background gas follows the distance–time relation

$$R = \xi_0 \left( \frac{E_0}{\rho_0} \right)^{1/5} t^{2/5} \quad (5.8)$$

where  $\xi_0$  is a constant (for a planar shock wave  $R(t) \propto (E_0/\rho_0)^{1/3} t^{2/3}$ ). This model strictly applies when the mass of the ejected products is small compared with the mass of the background gas set in motion by the shock (Zel'dovich and Raizer, 1966), a situation that does not typically apply for PLD plumes here. For PLD, ambient gas pressures must be kept low enough that some of the ablated species reach the substrate, irrespective of the background gas shock wave.

At low pressures, such as those used for PLD, fits of the form  $R = at^{0.4}$  to  $R$ – $t$  plots like Figure 5.23 consistently predict greater propagation distances than actually measured at early times. Fits of the form  $R = at^n$  suggest exponents  $n > 0.4$  (Geohegan, 1991) for limited improvement at early times. Ignoring the temporal region prior to the observed formation of the shock front, the blast wave model describes this phase of the expansion increasingly well at higher background pressures (Dyer et al., 1990a; Dyer et al., 1990b; Gilgenbach and Ventzek, 1991).

A classic drag-force model (solid line in Figure 5.23) shows better agreement at low pressures and early times. The ejected pulse of ablation products is regarded as an ensemble that experiences a viscous force proportional to its velocity through the background gas. The equation of motion is  $a = -\beta v$ , giving

$$v = v_0 \exp(-\beta t) = v_0 - \beta x$$

$$x = x_f [1 - \exp(-\beta t)]$$

where  $\beta$  is the slowing coefficient and  $x_f = v_0/\beta$  is the stopping distance of the plume (Geohegan, 1992).

The drag model predicts that the plume will eventually come to rest, due to resistance from collisions with the background gas, while the shock model (neglecting viscosity) predicts continued propagation  $R \sim t^{0.4}$ . Experimentally, PLD plumes are observed traveling a path that can be described by a



composite of these two models, the overlap occurring during the transition region described earlier when the viscous slowing of the leading edge of the plume coalesces to form a stable shock structure.

High-speed framing photography (with 10-ns resolution) has been applied to study plume propagation into background gases since 1963 when Ready studied the laser ablation of carbon into air with  $\sim 20$ -ns FWHM laser pulses (Ready, 1963). Fast-framing photography has the advantage of capturing several images of the same laser plume in rapid succession. Figure 5.24 shows

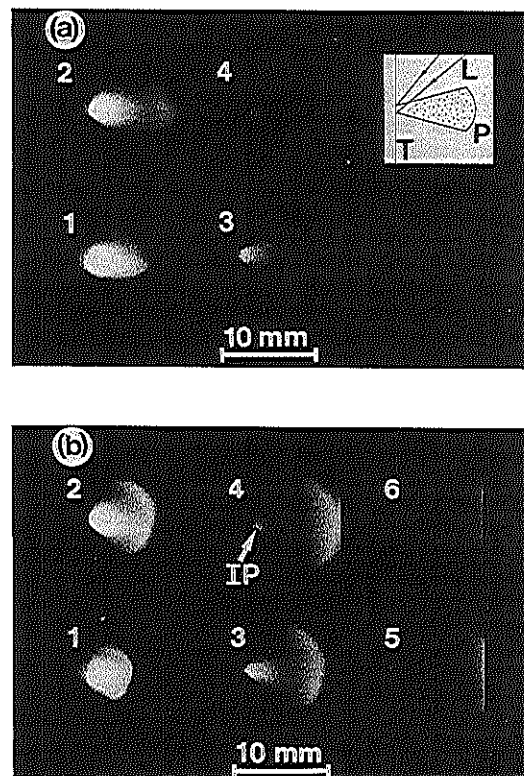


**Figure 5.24.** Fast-framing photography sequences of YBCO laser ablation ( $4.6 \text{ J cm}^{-2}$ ,  $\lambda = 1.054 \text{ }\mu\text{m}$ ,  $\tau_{\text{FWHM}} = 50 \text{ ns}$ ) into (a) 0.04-mbar and (b) 0.25-mbar oxygen where each frame has dimensions shown in the inset. Exposures were 16 ns in duration, and spaced 200 ns apart starting at 175 ns (i.e., 175, 375, 575, . . . ns) after the start of the laser pulse. Two regions of plasma emission are shown, including relatively short-lived emission from the inner region of the plume [IP in (b)]. (Reprinted from K. Scott, J. M. Huntley, W. A. Phillips, John Clarke, and J. E. Field, *Appl. Phys. Lett.*, 57, 922 (1990) with permission.)

recent photographs of the laser ablation ( $4.6 \text{ J cm}^{-2}$ ,  $\lambda = 1.054 \text{ }\mu\text{m}$ ,  $\tau_{\text{FWHM}} = 50 \text{ ns}$ ) of YBCO into (a) 0.04-mbar and (b) 0.25-mbar oxygen, recorded with a fast-framing camera that contained an image converter yielding a light intensity gain of  $\sim 160$  (Scott et al., 1990). The images also show a region of plume emission remaining near the target while the fast ejecta move away at initial velocities approaching  $4 \times 10^6 \text{ cm s}^{-1}$ . At higher pressures other photographs revealed plasma jetting, hydrodynamic instabilities along the hemispherical shock front (not shown) (Scott et al., 1990).

Dyer and Sidhu observed similar regions of plume emission (as those shown earlier in Figures 5.20, 5.21, and 5.24) in their study of XeCl laser ablation of polyimide into air using framing and streak photography (Dyer and Sidhu, 1988). The streak photographs of Figure 5.25 show two regions of plume emission at 0.5 mb (one slow and another fast region appearing later) and a significantly slowed single component at 15 mb. The high-pressure  $R$ - $t$  behavior was described well by blast wave theory (Eq. 5.8). The low-pressure  $R$ - $t$  behavior was not expected to conform to blast wave propagation until the mass of gas (density  $\rho_0$ ) displaced by the shock wave was much greater than the ablated mass  $M_0$ . This was expected to occur at distances  $R \gg (3M_0/2\pi\rho_0)^{1/3}$  [0.73 cm in Figure 5.25(a) and 0.24 cm in Figure 5.25(b)]. (Zel'dovich and Raizer, 1966; Dyer and Sidhu, 1988). The blast wave behavior can be expected to be maintained for distances much less than the distance  $R \sim (E_0/\rho_0)^{1/3}$ , where the pressure in the expanding bubble of ablation products becomes nearly equal to the ambient pressure  $P_0$  [2.4 and 7.4 cm, respectively in Figure 5.25(a) and (b)] (Zel'dovich and Raizer, 1966; Dyer and Sidhu, 1988). Thus, blast wave theory is expected to describe the propagation of PLD laser plumes within limits that depend on the plume and background pressures.

Ground-state neutrals can be imaged in absorption by dye laser resonance absorption photography (DLRAP) (Gilgenbach and Ventzek, 1991). Figure 5.26 shows a series of photographs in which a time-delayed, pulsed dye laser

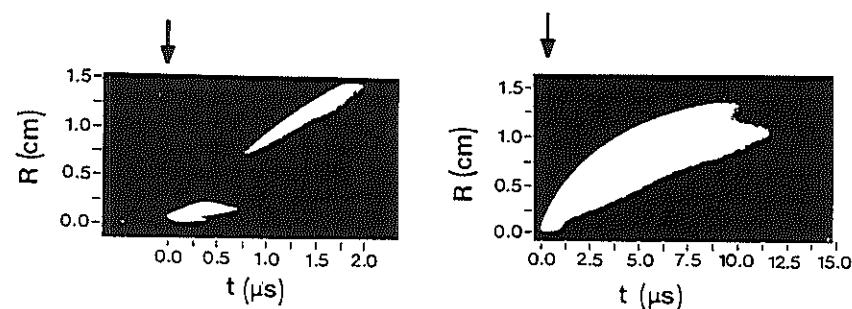


**Figure 5.25.** Streak photographs of plume emission produced by  $1\text{-J cm}^{-2}$ , 308-nm laser ablation of polyimide into air pressures of (a) 0.5 mb and (b) 15 mb. (Reprinted from P. E. Dyer and J. Sidhu, *J. Appl. Phys.* 64, 4657 (1988), with permission.)



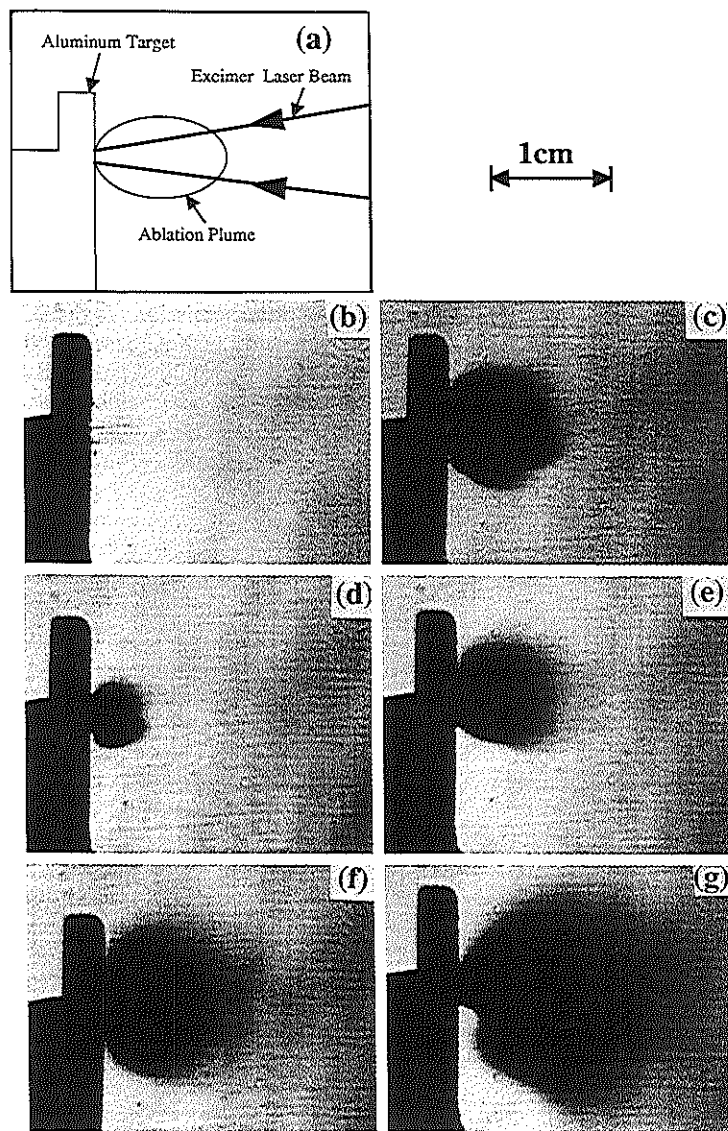


Figure 5.26. Dye laser absorption photographs of ground-state aluminum atoms following 248-nm laser ablation in vacuum. (b) and (c):  $7\text{-J cm}^{-2}$  ablation and time delay of 300 ns with dye laser tuned 0.1 nm off-resonance in (b) and dye laser tuned on-resonance in (c). (d)–(g)  $3.7\text{-J cm}^{-2}$  ablation laser and dye laser delayed by (d) 340 ns, (e) 460 ns, (f) 540 ns, and (g)  $1.04\text{ }\mu\text{s}$ . (Reprinted from R. M. Gilgenbach and P. L. G. Ventzek, *Appl. Phys. Lett.*, **58**, 1597 (1991) with permission.)

was tuned to the aluminum resonance line transition at 394.4 nm, back-illuminating an aluminum target undergoing 248-nm laser ablation at  $3.7\text{--}7\text{ J cm}^{-2}$  in vacuum. This technique should be applicable for observation of different ground-state species in multicomponent PLD plumes.

Ground-state neutrals can also be imaged using LIF. Figure 5.27 shows ICCD images of the cross section of an ablation plume probed by LIF using a planar sheet (200  $\mu\text{m}$  thick) of dye laser light. Ground-state neutral barium atoms from an ablated barium target were stimulated to fluoresce at 472.8 nm by LIF using planar dye laser light tuned to the  $6^1\text{S--}7^1\text{P}$  neutral barium transition (Cappelli et al., 1990).

Shadow photography is also possible due to scattering and absorption of light by the extreme densities present in the early stages of plume expansion. Figure 5.28 shows images of absorption and scattering from fragments following  $1.5\text{--}2\text{-J cm}^{-2}$  KrF-laser ablation of YBCO in background oxygen (Gupta et al., 1991). These images were recorded with a 596-nm dye laser beam ( $\sim 1\text{-ns}$  FWHM) pulse illuminating the surface of the target at glancing incidence and a bandpass filter on an ordinary camera to reject most of the bright plume emission. Fragments were imageable up to times  $\Delta t \leq 500\text{ ns}$ , which was, as the authors point out, probably due to an imaging threshold rather than an absence of fragments. The blast wave propagation through the 760-torr oxygen is clearly seen in Figure 5.28b. This wave is the origin of the audible “crack”

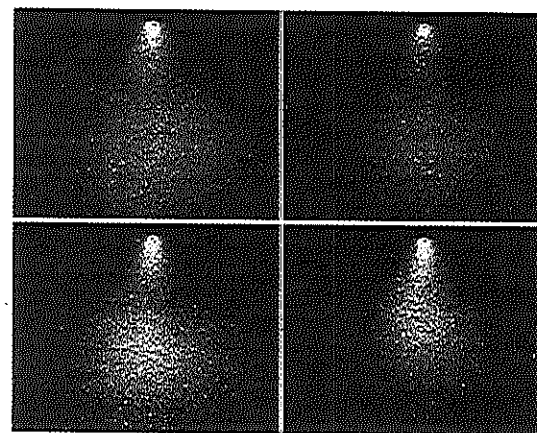
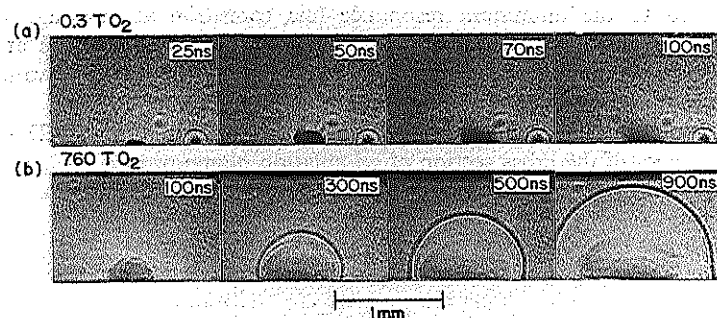


Figure 5.27. ICCD images of laser-induced fluorescence from neutral barium atoms 10  $\mu\text{s}$  after 10-mJ, 532-nm irradiation of solid barium in helium. A planar dye laser beam tuned to the  $6^1\text{S--}7^1\text{P}$  barium transition induced the 472.8-nm fluorescence for the helium backpressures of 34 m torr (top left), 45 m torr (top right), 60 m torr (bottom left), 80 m torr (bottom right). (Reprinted from M. A. Cappelli, P. H. Paul and R. K. Hanson, *Appl. Phys. Lett.*, **56**, 1715 (1990) with permission.)



**Figure 5.28.** Imaging of ablated fragments in the KrF-laser ablation ( $1.5\text{--}2\text{ J cm}^{-2}$ , 25-ns FWHM, 60-ns total pulse width) of YBCO in (a) 0.3 torr and (b) 760 torr oxygen, using a dye laser pulse ( $\sim 1\text{-ns}$  FWHM) to backlight the target at glancing incidence. (Reprinted from A. Gupta, B. Braren, K. G. Casey, B. W. Hussey and Roger Kelly, *Appl. Phys. Lett.*, 59, 1302 (1991) with permission.)

heard in the laboratory during laser ablation at atmospheric pressure. The wave is visible because of the change in refractive index due to the pressure pulse.

*Photoacoustic and photothermal beam deflection* utilizes this change in refractive index by measuring the deflection of a parallel continuous wave (CW)-laser beam passing above the target surface with a position-sensitive detector (Sell et al., 1991). The measurements are most effective in background gases where the blast wave is present, but can detect ablation product velocities and thresholds in vacuum very close to the surface. A technique has also been developed in which etch-pit depths can be measured remotely by a sonarlike technique that measures the difference in transit time of an acoustic wave from the target to the probe beam before and after ablation (Ventzek, et al., 1991).

Similarly, passing a CW laser beam through a transparent solid also results in *photothermal beam deflection* due to the refractive index change caused by transient thermal heating (Spear and Russo, 1991). *Time-dependent transmission*, *time-resolved reflectivity*, and *time-resolved ellipsometry* utilize the changes in refractive indices of a material under laser irradiation to change the reflectivity of a CW probe beam as monitored by an avalanche photodiode to obtain nanosecond resolution data on the melting and recrystallization of a material (Jellison et al., 1986).

The change in index of refraction of the vaporized material can be measured if the plume is positioned in one arm of a *Michelson interferometer*, as was done for  $\text{Al}_2\text{O}_3$  ablation ( $2\text{ J cm}^{-2}$ , 248 nm) (Walkup et al., 1986). The phase change of a HeNe beam is measured and used to determine time dependences and integrated densities of free electrons (negative phase change) or neutral atoms (positive phase change). Very high plasma densities can produce multiple shifts in phase that can be imaged as *interferograms* (Mostovych et al., 1991).

The recoil momentum transferred back to the target by the ablated products can also be measured using *piezoelectric transducers*, onto which targets or films can be attached. Figure 5.29a shows the transient surface pressure measured on a YBCO target undergoing  $2\text{-J cm}^{-2}$  KrF-laser ablation (Dyer, et al., 1992b). The recoil pressure begins within the first few nanoseconds of irradiation and peaks at  $\sim 400\text{ atm}$ ! This *acoustic measurement* is sensitive at low laser energy densities as well, as shown in Figure 5.29b, which shows that low levels of material removal occur below the nominal  $\sim 0.11\text{-J cm}^{-2}$  ablation threshold for YBCO (Dyer et al., 1992b). On the basis of models for (a) the surface recession velocity due to vaporization and (b) the surface temperatures, the measured recoil pressure (see Figure 5.29) was used to estimate the average mass of ablated species at  $\sim 1000\text{--}2000\text{ amu}$  (Dyer et al., 1992b). This would tend to indicate that relatively high average mass fragments are produced in the initial ablation step by an “explosive removal” process, which may then still absorb some of the remainder of the laser pulse to produce the hot plasma and smaller fragments observed by other techniques. *Mechanical impulse gauges* based on sliding transducers and target levitation in vacuum have also been used to provide estimates of surface pressures (Phipps et al., 1988).

Still more sensitive CCD exposures reveal plume emission not observed by eye or ordinary photography at very long times. Figure 5.30 shows the penetration of a YBCO plasma plume through 200-mtorr oxygen toward a cold heater. Observing the penetration of the plume by eye would lead to the

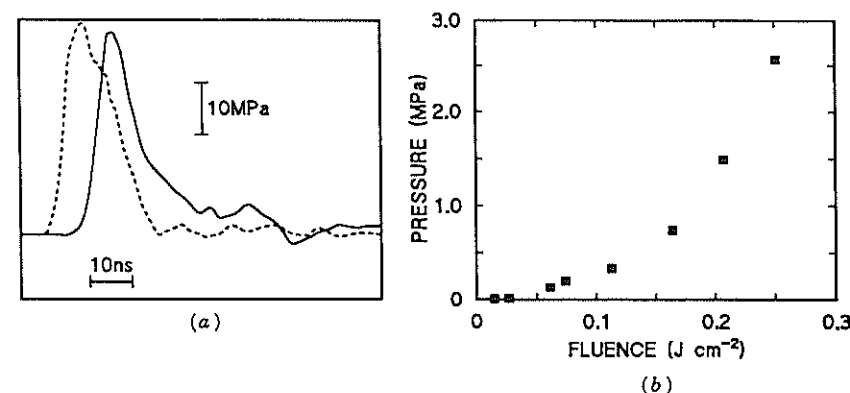


**Figure 5.29.** (a) Transient surface pressure induced by  $2\text{-J cm}^{-2}$  KrF laser ablation of YBCO, measured using a PVDF piezoelectric film (—). The time dependence is time synchronized with that of the KrF-laser pulse (---) in the figure. (b) Peak surface pressure as a function of KrF laser fluence. (Reprinted from P. E. Dyer, S. R. Farrar, A. Issa and P. H. Key, p.101 in *Laser Ablation of Electronic Materials: Basic Mechanisms and Applications*, ed. by E. Fogarassy and S. Lazare, North-Holland (1992) with permission.)

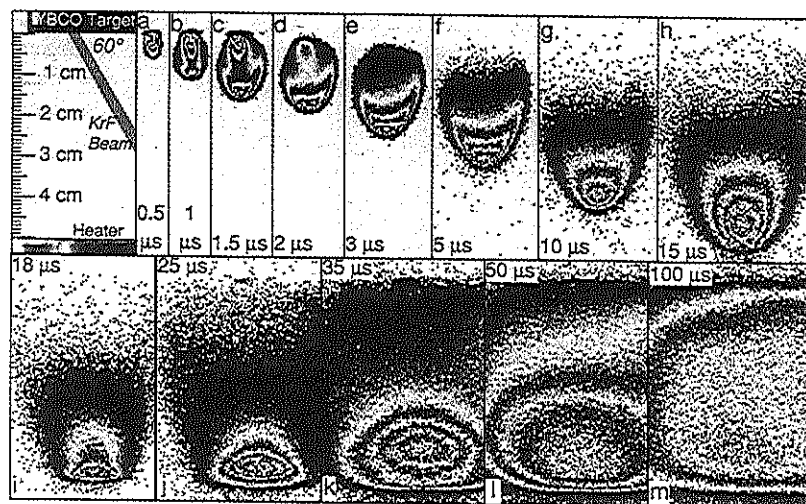


**Figure 5.30.** ICCD photographs of the visible plasma emission following  $2.5\text{-J-cm}^{-2}$  KrF/YBCO ablation into 200-mtorr oxygen at the indicated delay times from the arrival of the laser pulse. Exposure times were increased from 20 ns to  $2\text{ }\mu\text{s}$ . The digitized intensity data have been evenly divided into five contours to reveal the fainter regions of emission. The plume collides with a cold, stainless steel heater in (h)–(m), partially rebounding to fill the space between the target and heater at late times. Weak emission at the target surface is just observable in (j)–(m) and is due to blackbody emission from slow-moving, hot particulates (see Figure 5.33).

judgment that the plume had stopped short of the heater 5 cm away. Weak emission at long times indicates, however, that the slowed plume continues to diffuse toward the heater and partially rebound in a reflected shock. The velocity of the plume boundary just before impact with the heater (from an  $R-t$  plot for the data of Figure 5.30, not shown) is  $0.07\text{ cm }\mu\text{s}^{-1}$ , which yields a kinetic energy (for a 100-amu atom) of  $\sim 0.25\text{ eV}$ . As the reflected vapor encounters the rest of the incoming plume, the collision rate and fluorescence increase to reveal the nearly thermalized layer of material at the surface (Akhsakhalyan et al., 1982b). This layer continues to collectively move away from the heater while diffusing in an apparent afterglow, eventually filling the gap between target and heater as it continues to emit light for over  $100\text{ }\mu\text{s}$ . Even longer exposures and photon counting emission spectroscopy are able to detect extremely weak emission from the plume and particulates at even longer times (see below).

## 5.5 CLUSTERS AND PARTICULATES

The least-explored, but perhaps very important, components of the plume are clusters and particles. It has been speculated that the observed stoichiometry of pulsed laser deposited thin films may be transported by large clusters generated in the ablation process (Dijkkamp et al., 1987). The term “cluster” here refers to groups of bonded atoms from dimers and trimers on up to particles  $\leq 1000\text{ }\text{\AA}$  in diameter. The fraction of the overall mass transported by clusters and particulates during PLD is still unknown. Unfortunately, from a diagnostic viewpoint, the optical absorption and emission properties of clusters are generally unknown and expected to be spectrally very broad. Furthermore, the large mass of all but the smallest clusters exceeds the mass limits of common mass spectrometers. Fortunately, some of the clusters and particles can be detected after deposition by scanning tunneling microscopy (STM), scanning electron microscopy (SEM), and from deposits made by passing the plume through *mechanical velocity filters* (see Chapter 6 on particulates, this book) (Lubben et al., 1985; Dupondant et al., 1989).

Thermodynamically, gas-phase clustering requires collisions and cooling. In fact, pulsed molecular valve cluster sources utilize laser ablation of a material into an inert gas where it is thermalized, followed by supersonic expansion through a nozzle jet to induce condensation. Without the thermalization step prior to supersonic expansion in vacuum, the formation of clusters is not expected during ablation for PLD.

Streak photography and TOFQMS measurements of the KrF-laser ablation of YBCO did indicate, however, that the luminous plume emission at high energy densities was caused by photodecomposition of ejected clusters (Eryu et al., 1989). Streak photographs at three laser energy densities are shown in Figure 5.31. Just above threshold, Figure 5.31a, only a fast ( $v \sim 5 \times 10^6\text{ cm/s}$ ) plume emission was observed. TOFQMS measurements showed only clusters lighter than 860 amu in this region. As the energy is increased, a delayed component emerges, time delayed from the laser pulse and detached from the target. Clusters heavier than 1500 amu and atomic peaks appeared in the mass spectrometer at higher energies. The delayed emission, coupled with the TOFQMS results, indicated that the ejecta were principally clusters that underwent dissociation under laser irradiation and plasma formation (Eryu et al., 1989). Similar measurements using streak photography in a wavelength-space imaging technique also implied cluster emission from silicon (Kasuya and Nishina, 1990).

The laser ablation of YBCO in vacuum was also studied with a *reflecting time-of-flight mass spectrometer* in conjunction with a second, delayed laser beam to investigate the effects of plasma formation on cluster production (Becker and Pallix, 1988). This mass spectrometer could resolve laser-ablated ions of mass up to 400,000 amu, and experiments were conducted both before and after the appearance of strong white fluorescence from the plasma plume.

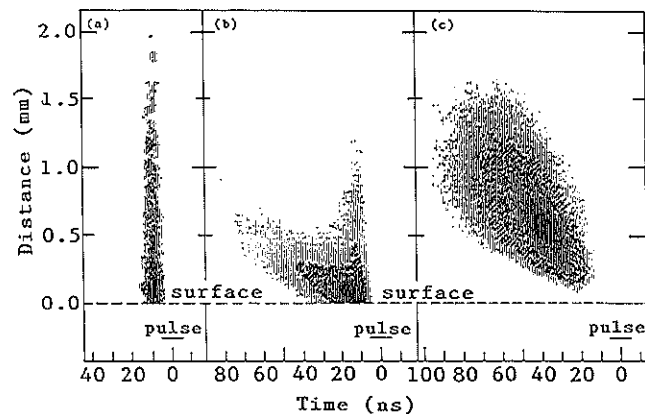


Figure 5.31. Time-resolved streak photographs of the light emission intensity following KrF-laser ablation of YBCO in vacuum with energy densities of (a)  $0.14 \text{ J cm}^{-2}$  (weak white color of emission), (b)  $0.40 \text{ J cm}^{-2}$  (orange color of emission), and (c)  $3.60 \text{ J cm}^{-2}$  (strong white color of emission). Note that the sensitivity of the streak camera was reduced by a factor of 16 for (c) compared to (a) and (b). The time-delayed emission at distances separated from the target may indicate cluster ejection and subsequent photodissociation. (Reprinted from O. Eryu, K. Murakami, K. Masuda, A. Kasuya and Y. Nishina, *Appl. Phys. Lett.*, **54**, 2716 (1989) with permission.)

Figure 5.32 shows the mass distributions measured before (a) and (b) and after (d) strong white emission from the plasma. Even before the white emission, a dense plasma existed (as implied by the inability to fully deflect the ions with a steering field) and clusters of nearly every combination of masses Y, Ba, Cu, and O were observed except  $\text{Y}_1\text{Ba}_2\text{Cu}_3\text{O}_7$ . The major peak spacing in Figure 5.32a and b was 226 amu corresponding to  $\text{Y}_2\text{O}_3$  or YBa. When the strong fluorescence from the plasma became apparent, however, the large cluster peaks all but disappeared and the low-mass cluster peaks gained in intensity.

The sudden loss of high-mass clusters in the ablation plume was attributed to photodissociation within the ablating laser pulse. In order to test this hypothesis, a second, parallel laser was passed 1 mm above the target surface and delayed by  $1 \mu\text{s}$ . The  $50\text{-J cm}^{-2}$ , 193-nm beam effectively photodissociated the large clusters, as shown in Figure 5.32c.

The repetitive pattern of cluster masses seen in Figure 5.32a and b was highly dependent on the presence of a channel in the target, indicating that collisions caused during the expansion of the vapor from the cones or grooves in the surface were responsible for the presence of these clusters, and that gas-phase condensation probably dominated over direct ejection (Becker and Pallix, 1988).

Few in situ studies of the larger particles have been performed. However,

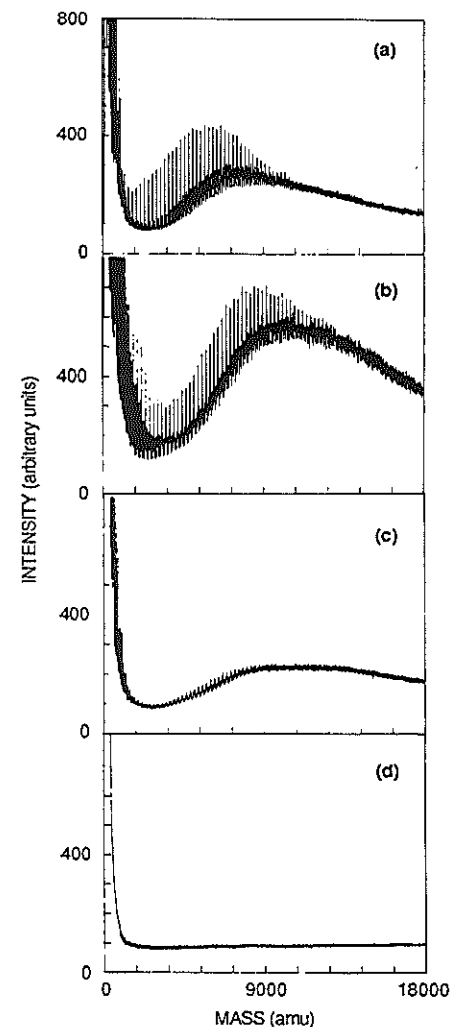
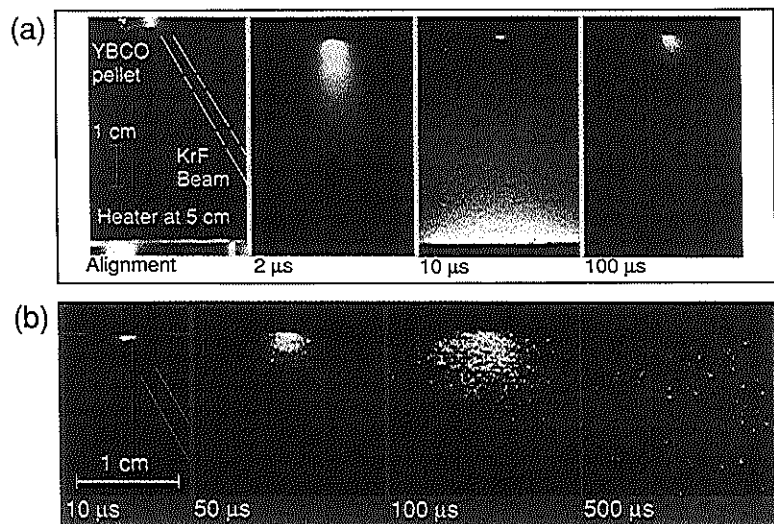


Figure 5.32. Mass distributions for ions in the cluster region produced from 1064-nm plus 532-nm laser ablation of YBCO obtained with a reflecting TOFMS. The laser energy densities are 2.5, 3.4, 3.4, and  $4.3 \text{ J cm}^{-2}$  for (a)–(d), respectively. For (c), an additional laser beam at 193 nm ( $\sim 50 \text{ J cm}^{-2}$ ) was passed parallel to and  $\sim 1 \text{ mm}$  above the sample at a time delay of  $1 \mu\text{s}$  after the ablation laser. For (d), a visible white plume is observed. The base line is offset from zero for visual clarity and in accordance with the arbitrary zero of the analog transient digitization. (Reprinted from C. H. Becker and J. B. Pallix, *J. Appl. Phys.*, **64**, 5152 (1988) with permission.)

improved superconducting film quality has been demonstrated using a delayed, second laser to photodissociate particles in midflight (Chiba et al., 1991; Koren et al., 1990). *Laser plasma X-ray absorption spectroscopy* has recently been applied to characterize ablated Si particles from 100 to 3000  $\mu\text{m}$  from the target surface (Murakami, 1992). Part of a 20-J pulse of 532-nm laser light was used to ablate a c-Si target, and the rest was passed through a delay line and focused onto a Ta target to produce a pulse of X-rays with smooth spectral distribution. The X-rays were focused in a 200- $\mu\text{m}$ -diameter beam parallel to the face of the Si target and delayed up to 60 ns with respect to the ablating laser pulse. Liquid silicon droplets were detected up to 200  $\mu\text{m}$  from the target in vacuum, and just above ablation threshold they constitute the main component of ablated particles.

Recent imaging experiments have detected visible emission from the large particulates at very long times following the laser pulse (Geohegan, 1993; Geohegan, 1992b). Figure 5.33a shows a series of ICCD photographs that trace the appearance of visible emission from laser-ablated particulates after 2.5-



**Figure 5.33.** (a) ICCD photographs tracing the appearance of glowing particulates following the expansion of the plasma plume caused by  $2.5\text{-J cm}^{-2}$  KrF-laser ablation of YBCO in vacuum ( $1 \times 10^{-6}$  torr). Each photograph is a different laser shot, exposures (lens  $f$ -stops/MCP gate widths) are as follows: 2  $\mu\text{s}$  [ $f/32$ , 20 ns]; 10  $\mu\text{s}$  [ $f/11$ , 200 ns]; 100  $\mu\text{s}$  [ $f/4$ , 2.2  $\mu\text{s}$ ]. (b) Close-up ICCD photographs of glowing particulates in the  $d = 0 - 1.5$  cm region under the same conditions with time delays and exposures (lens  $f$ /MCP gate width): 10  $\mu\text{s}$  ( $f/5.6$ , 200 ns), 50  $\mu\text{s}$  ( $f/4.2$   $\mu\text{s}$ ), 500  $\mu\text{s}$  ( $f/4.2$   $\mu\text{s}$ ). (Reprinted from D. B. Geohegan, 1993.)

$\text{J cm}^{-2}$  248-nm irradiation of YBCO in vacuum. The emission is very weak, begins at the hot target surface at early times, and continues long after emission from the plasma has ceased. Figure 5.33b shows a closer view of what are most likely individual photon events from glowing particulates under the same conditions. Nevertheless, the emission is easily observed by optical emission spectroscopy techniques as individual photon spikes on a photomultiplier signal after dispersal by a spectrometer. Gated photon counting of the light revealed blackbody emission from hot (2200–3200 K) particles of YBCO and BN moving at  $0.45\text{--}1.2 \times 10^4 \text{ cm s}^{-1}$ , approximately 100 times slower than the atomic species in the plume. The temperatures of the particles were observed during flight by photon counting at different time delays and curve fitting the blackbody emission data. The cooling was found to be faster than expected by radiative losses alone and the temperatures indicated superheated particulates that are vaporizing in flight.

*Blackbody emission spectra* have also been used to infer the temperatures of carbon clusters undergoing formation following laser ablation of graphite into background gases (Rohlfing, 1988). This diagnostic technique appears to be applicable to a wide variety of materials, detecting hot particulates undergoing either formation or vaporization.

## 5.6 CONCLUSIONS

Improvements in the sensitivity and application of diagnostics continue to reveal new features of the ablation process, plume propagation, and plume-film interaction. This chapter has attempted to present a brief overview of the general characteristics of PLD laser plasmas and the wide variety of diagnostic techniques being applied for their characterization. Each technique provides a different perspective of the plume, given its detection limitations. Only through the overlap of results from several techniques can a comprehensive picture of the plume be revealed.

Clearly, simple diagnostics such as photodiodes, quartz-crystal monitors, ion probes, and small spectrometers can provide a wealth of in situ information that can be interpreted in the context of the comprehensive picture to detail and ensure reproducible film growth conditions. As new materials are attempted by PLD, gas phase diagnostics can quickly reproduce key conditions (ion current, kinetic energy, deposition rate) utilized successfully for similar materials. As PLD progresses into high-vacuum laser-molecular-beam-epitaxy (MBE) chambers for deposition over large areas, more costly on-line diagnostics such as imaging and mass spectrometry will likely be warranted as well.

The information provided by laser-ablation diagnostics may significantly change PLD as opportunities for new deposition techniques are revealed. Utilization of reactive collisions in the gas phase, cluster formation, particle generation, and electromagnetic stimulation and steering of the plume are



possibilities. Diagnostic input is also necessary for comprehensive computer modeling of the PLD process.

## ACKNOWLEDGMENTS

The author gratefully acknowledges the many researchers who contributed to this chapter, either by contributing figures or by sharing insight through many stimulating discussions. This work was supported by the Division of Materials Sciences, U.S. Department of Energy under contract DE-AC05-84OR21400 with Martin Marietta Energy Systems, Inc.

## REFERENCES

- Akhsakhalyan, A. D., Yu. A. Bityurin, S. V. Gaponov, A. A. Gudkov, and V. I. Luchin (1982a), *Sov. Phys. Tech. Phys.* **27**, 969.
- Akhsakhalyan, A. D., Yu. A. Bityurin, S. V. Gaponov, A. A. Gudkov, and V. I. Luchin (1982b), *Sov. Phys. Tech. Phys.* **27**, 973.
- Anderson, J. B. (1974), in *Molecular Beams and Low Density Gas Dynamics*, (P. P. Wegener, ed.), Dekker, New York, p. 1.
- Arlinghaus, H. F., W. F. Calaway, C. E. Young, M. J. Pellin, D. M. Gruen, L. L. Chase (1989), *J. Appl. Phys.* **65**, 281.
- Balazs, L., R. Gijbels, and A. Vertes (1991), *Anal. Chem.* **63**, 315.
- Becker, C. H., and J. B. Pallix (1988), *J. Appl. Phys.* **64**, 5152.
- Bekefi, G. (1976), *Principles of Laser Plasmas*, New York.
- Bhat, P. K., J. J. Dubowski, and D. F. Williams (1986), *Chemtronics* **1**, 83.
- Bykovskii, Yu. A., N. N. Degtyarenko, V. F. Elesin, V. E. Kondrashov, and E. E. Lovetskii (1974), *Sov. Phys. Tech. Phys.* **18**, 1597.
- Cappelli, M. A., P. H. Paul, and R. K. Hanson (1990), *Appl. Phys. Lett.* **56**, 1715.
- Champeaux, C., D. Damiani, C. Girault, P. Marchet, J. Aubreton, J. P. Mercurio, and A. Catherinot (1992), in *Laser Ablation of Electronic Materials: Basic Mechanisms and Applications*, (E. Fogarassy and S. Lazare, eds.), North Holland, Amsterdam, p. 141.
- Chen, F. F. (1965), in *Plasma Diagnostic Techniques*, (Richard H. Huddleston and Stanley L. Leonard, eds.), Academic Press, London, ch. 4.
- Chen, F. F. (1974), *Introduction to Plasma Physics*, Plenum, New York, ch. 1.
- Cheung, J. T., and H. Sankur (1988), *CRC Crit. Rev. Solid State Mat. Sci.* **15**, 63.
- Chiba, H., K. Murakami, O. Eryu, K. Shihoyama, T. Mochizuki, and K. Masuda (1991), *Jpn. J. Appl. Phys.* **30**, L32.
- Chrisey, D. B., J. S. Horwitz, K. S. Grabowski, M. E. Reeves, M. S. Osofsky, and C. R. Gossett (1990), *Mater. Res. Soc. Symp. Proc.* **169**, 435.
- Chuang, T. J. (1985), *J. Vac. Sci. Technol.* **B3**, 1408 (and references cited therein).
- Demtröder, W. (1982), *Laser Spectroscopy—Basic Concepts and Instrumentation*, Springer-Verlag, Berlin-Heidelberg.
- Demtröder, W., and W. Jantz (1970), *Plasma Phys.* **12**, 691.
- Dickinson, J. T., S. C. Langford, and L. C. Jensen (1991), in *Laser Ablation: Mechanisms and Applications* (J. C. Miller and R. F. Haglund, eds.), Springer-Verlag, Heidelberg, p. 301.
- Dijkkamp, D., T. Venkatesan, X. D. Wu, S. A. Shaheen, N. Jisrawi, Y. H. Min-Lee, W. L. McLean, and M. Croft (1987), *Appl. Phys. Lett.* **51**, 619.
- Dreyfus, R. W. (1990), *High Temp. Sci.* **27**, 503.
- Dreyfus, R. W. (1991), *J. Appl. Phys.* **69**, 1721.
- Dreyfus, R. W., R. Kelly, and R. E. Walkup (1986), *Appl. Phys. Lett.* **49**, 1478.
- Dubowski, J. J. (1988), *Chemtronics* **3**, 66.
- Dupendant, H., J. P. Gavigan, D. Givord, A. Lienard, J. P. Rebouillat, and Y. Souche (1989), *Appl. Surf. Sci.* **43**, 369.
- Dyer, P. E., and J. Sidhu (1988), *J. Appl. Phys.* **64**, 4657.
- Dyer, P. E., S. R. Farrar, and P. H. Key (1992a), *Appl. Surf. Sci.* **54**, 255.
- Dyer, P. E., S. R. Farrar, A. Issa, and P. H. Key (1992b), in *Laser Ablation of Electronic Materials: Basic Mechanisms and Applications* (E. Fogarassy and S. Lazare, eds.), North Holland, Amsterdam, p. 101.
- Dyer, P. E., A. Issa, and P. H. Key (1990a), *Appl. Phys. Lett.* **57**, 186.
- Dyer, P. E., A. Issa, and P. H. Key (1990b), *Appl. Surf. Sci.* **46**, 89.
- Ehler, W., (1972), *Phys. Fluids* **16**, 339.
- Eryu, O., K. Murakami, K. Masuda, A. Kasuya, and Y. Nishina (1989), *Appl. Phys. Lett.* **54**, 2716.
- Estler, R. C., and N. S. Nogar (1991), *J. Appl. Phys.* **69**, 1654.
- Foltyn, S. R., R. E. Muenchausen, R. C. Estler, E. Peterson, W. B. Hutchinson, K. C. Ott, N. S. Nogar, K. M. Hubbard, R. C. Dye, and X. D. Wu (1990), *Mater. Res. Soc. Symp. Proc.* **191**, 205.
- Früchtenicht, J. F. (1974), *Rev. Sci. Instrum.* **45**, 51.
- Gekelman, W., V. Vanek, and A. Y. Wong. (1978), *J. Appl. Phys.* **49**, 3049.
- Geohegan, D. B. (1991), in *Laser Ablation: Mechanisms and Applications*, (J. C. Miller and R. F. Haglund, eds.), Springer-Verlag, Heidelberg, p. 28.
- Geohegan, D. B. (1992a), in *Laser Ablation of Electronic Materials: Basic Mechanisms and Applications*, (E. Fogarassy and S. Lazare, eds.), North Holland, p. 73.
- Geohegan, D. B. (1992b), *Appl. Phys. Lett.* **60**, 2732.
- Geohegan, D. B. (1993), *Mater. Res. Soc. Symp. Proc.*, **285** 27.
- Geohegan, D. B. (1992d), *Thin Solid Films* **220**, 138.
- Geohegan, D. B. (1993), *Appl. Phys. Lett.* **62**, 1463.
- Geohegan, D. B., and D. N. Mashburn (1989), *Appl. Phys. Lett.* **55**, 2345.
- Gilgenbach, R. M., and P. L. G. Ventzek (1991), *Appl. Phys. Lett.* **58**, 1597.
- Girault, C., D. Damiani, J. Aubreton, and A. Catherinot (1989), *Appl. Phys. Lett.* **55**, 182.
- Goel, S. K., P. D. Gupta, and D. D. Bhawalkar (1982), *J. Appl. Phys.* **53**, 2971.

- Griem, H. R. (1964), *Plasma Spectroscopy*, McGraw-Hill, New York.
- Griem, H. R. (1974), *Spectral Line Broadening by Plasmas*, Academic Press, New York.
- Gupta, A., B. Braren, K. G. Casey, B. W. Hussey, and R. Kelly (1991), *Appl. Phys. Lett.* **59**, 1302.
- Hughes, T. P. (1975), *Plasmas and Laser Light*, Wiley, New York.
- Irons, F. E., R. W. P. McWhirter, and N. J. Peacock (1972), *J. Phys. B: Atom. Molec. Phys.* **5**, 1975.
- Itoh, N., K. Hattori, Y. Nakai, J. Kanasaki, A. Okano, and R. F. Haglund, Jr. (1991), in *Laser Ablation: Mechanisms and Applications*, (J. C. Miller and R. F. Haglund, eds.), Springer-Verlag, Heidelberg, p. 213.
- Jellison, G. E. Jr., D. H. Lowndes, and R. F. Wood (1986), *SPIE Proc.* **710**, 24.
- Kasuya, A., and Y. Nishina (1990), *Mater. Res. Soc. Symp. Proc.* **191**, 73.
- Kelly, R. (1979), *Surf. Sci.* **90**, 280.
- Kelly, R. (1990), *J. Chem. Phys.* **92**, 5047.
- Kelly, R., and R. W. Dreyfus (1988), *Surf. Sci.* **198**, 263.
- Kim, H., J. C. Postlewaite, T. Zyung, and D. Dlott (1989a), *Appl. Phys. Lett.* **22**, 2274.
- Kim, H., J. C. Postlewaite, T. Zyung, and D. Dlott (1989b), *J. Appl. Phys.* **65**, 4548.
- Knudtson, J. T., W. B. Green, and D. G. Sutton (1987), *J. Appl. Phys.* **61**, 4771.
- Koren, G., R. J. Baseman, A. Gupta, M. I. Lutwyche, and R. B. Laibowitz (1990), *Appl. Phys. Lett.* **56**, 2144.
- Laframboise, J. (1966), in *Rarefied Gas Dynamics* (J. H. DeLeeuw, ed.), Academic Press, New York, vol. II, p. 22.
- Lubben, D., S. A. Barnett, K. Suzuki, S. Gorbalkin, and J. E. Greene (1985), *J. Vac. Sci. Technol.* **B3**, 968.
- Lynds, L., B. R. Weinberger, D. M. Potrepka, G. G. Peterson, and M. P. Lindsay (1989), *Physica C* **159**, 61.
- Mashburn, D. N., and D. B. Geohegan (1989), in *Processing of Films for High  $T_c$  Superconducting Electronics* (T. Venkatesan, ed.), Proc. SPIE, volume 1187, p. 172.
- Mostovych, A. N., K. J. Kearney, J. A. Stamper, and A. J. Schmitt (1991), *Phys. Rev. Lett.* **66**, 612.
- Murakami, K. (1992), in *Laser Ablation of Electronic Materials: Basic Mechanisms and Applications* (E. Fogarassy and S. Lazare, eds.), North Holland, Amsterdam, p. 125.
- Nakayama, T. (1983), *Surf. Sci.* **133**, 101.
- Namiki, A., T. Kawai, and K. Ichige (1986), *Surf. Sci.* **166**, 129.
- Opower, H., and W. Press (1966), *Z. Nat. Forsch.* **21a**, 344.
- Otis, C. E., and R. W. Dreyfus (1991), *Phys. Rev. Lett.* **67**, 2102.
- Otis, C. E., and P. M. Goodwin, (1993), *J. Appl. Phys.* **73**, 1957.
- Phipps, C. R., Jr., T. P. Turner, R. F. Harrison, G. W. York, W. Z. Osborne, G. K. Anderson, X. F. Corlis, L. C. Haynes, H. S. Steele, K. C. Spicochi, and T. R. King (1988), *J. Appl. Phys.* **64**, 1083.
- Radziemski, L. J., and D. A. Cremers (1989), *Laser Induced Plasmas and Applications*, Marcel Dekker, New York.
- Ready, J. F. (1963), *Appl. Phys. Lett.* **3**, 11.
- Ready, J. F. (1971), *Effects of High-Power Laser Radiation*, Academic Press, London.
- Richter, A. (1990), *Thin Solid Films* **188**, 275.
- Rohlfing, E. A. (1988), *J. Chem. Phys.* **89**, 6103.
- Saenger, K. L. (1989), *J. Appl. Phys.* **66**, 4435.
- Scott, K., J. M. Huntley, W. A. Phillips, J. Clarke, and J. E. Field (1990), *Appl. Phys. Lett.* **57**, 922.
- Segall, S. B., and D. W. Koopman (1973), *Phys. Fluids* **16**, 1149.
- Sell, J. A., D. M. Heffelfinger, P. L. G. Ventzek, R. M. Gilgenbach (1991), *J. Appl. Phys.* **69**, 1330.
- Shea, M. J., R. N. Compton, and R. L. Hettich (1990), *Phys. Rev. A* **42**, 3579.
- Singh, R. K., O. W. Holland, and J. Narayan (1990), *J. Appl. Phys.* **68**, 233.
- Spear, J. D., and R. E. Russo (1991), *J. Appl. Phys.* **70**, 580.
- Swift, J. D., and M. J. R. Schwar (1970), *Electrical Probes for Plasma Diagnostics*, Iliffe, London.
- Talbot, L. (1973), in *Dynamics of Ionized Gases* (M. J. Lighthill, I. Imai, and H. Sato, eds.), Wiley, Tokyo, p. 235.
- Valles-Abarca, J. A., and A. Gras-Marti (1984), *J. Appl. Phys.* **55**, 1370.
- van Veen, G. N. A., T. Baller, and A. E. de Vries (1986), *J. Appl. Phys.* **60**, 3746.
- Venkatesan, T., X. D. Wu, A. Inan, Y. Jeon, M. Croft, E. W. Chase, C. C. Chang, J. B. Wachtman, R. W. Odom, F. R. di Brozolo, and C. A. Magee (1988), *Appl. Phys. Lett.* **53**, 1431.
- Ventzek, P. L. G., R. M. Gilgenbach, D. M. Heffelfinger, and J. A. Sell (1991), *J. Appl. Phys.* **70**, 587.
- Vertes, A., P. Juhasz, P. Jani, and A. Czitrovsky (1988), *Int. J. Mass Spectrom. Ion Process.* **83**, 45.
- Waldeer, K. T., and H. M. Urbassek (1991), *Physica A* **176**, 325.
- Walkup, R. E., J. M. Jasinski, and R. W. Dreyfus (1986), *Appl. Phys. Lett.* **48**, 1690.
- Wiedeman, L., and H. Helvajian (1991), *J. Appl. Phys.* **70**, 4513.
- Wiedeman, L., H. S. Kim, and H. Helvajian (1991), *Mater. Res. Soc. Symp. Proc.* **201**, 575.
- Zel'dovich, Ya. B., and Yu. P. Raizer (1966), in *Physics of Shock Waves and High Temperature Hydrodynamic Phenomena*, vol. 1, Academic Press, New York, p. 94.
- Zheng, J. P., Z. Q. Huang, D. T. Shaw, and H. S. Kwok (1989), *Appl. Phys. Lett.* **54**, 280.



## PARTICULATES GENERATED BY PULSED LASER ABLATION

LI-CHYNG CHEN

Corporate Research and Development Center  
General Electric Company  
Schenectady, New York

### 6.1 INTRODUCTION

The generation of particulates by pulsed laser ablation is of great significance in the deposition of thin films. The presence of the particulates in deposited films is considered to be one of the major factors that impeded the more widespread application of the pulsed laser deposition (PLD) method. The goal of this chapter is to provide a concise overview of the characteristic features of the particulates generated by pulse laser ablation, with the main emphasis on the relationship of processing parameters and the characteristic features that have been reported to date. In addition, feasible approaches to eliminate the particulates as well as possible applications that can make use of the particulates are discussed.

The nature of the particulates, including the generation rate, the energy or velocity, the size, the chemistry, and the microstructure, depends upon the process conditions and the type of material. Characteristic features of the particulates are summarized in Section 6.2. In Section 6.3, the effects of the deposition parameters are discussed in more detail, such as the laser wavelength, laser energy, laser spot size, ambient gas pressure, and the target-to-substrate distance. Examples in pure metals, binary metallic alloys, and ceramics are given. Though a complete understanding of the phenomenon is difficult, simple, qualitative explanations are suggested for some of the observed features.

In high-performance optical and electronic applications, stringent constraints exist for surface smoothness; therefore, the tolerance of particulate density and size is generally very low. Certainly, the specific tolerance of particulate density and size depends on the specific use of the materials. By proper choice of process parameters, the particulate size and density can be

minimized. When particulate-free films are required, further reduction of the particulates can be accomplished by various techniques. A number of mechanical approaches, such as velocity filters, off-axis deposition, as well as substrate bias, and the use of a second laser are described in Section 6.4.

By far the most widely researched and developed area in PLD process is related to the deposition of oxide superconductors. Research on other materials grown by PLD, such as those described in Chapters 15–26, has also experienced phenomenal growth. However, the development of applications that deliberately make use of the particulates is still at a very early stage. In Section 6.5, it is demonstrated that, in some applications, the incorporation of the particulates into the films can be advantageous. Other examples, such as ultrafine powders produced by pulsed laser ablation with proper choice of ambient gas species and pressure, are described in Section 6.5, as well.

## 6.2 PARTICULATES CHARACTERIZATION

Briefly, particulates generated by pulsed laser ablation can be classified into three categories. A specific type of particulate is distinguished by whether the original matter, when just ejected from the target, is in the solid, liquid, or vapor state. The origin of the particulate generation is multifaceted. In addition, multiple mechanisms may be operative at the same time. Some existing models regarding the cause and dynamics of the particulate have been reviewed by Cheung and Sankur (1988), and more recently by Saenger (1992). Several mechanisms proposed in the literature are recapped here: (1) protruding surface features or pits, craters, microcracks, that exist in a fresh target or are progressively formed after substantial laser irradiation, being mechanically dislodged from the target due to laser-induced thermal and mechanical shock; (2) rapid expansion of trapped gas bubbles beneath the surface during laser irradiation, causing forcible ejection of surface matter; (3) splashing of the molten layer caused by the presence of a subsurface superheated layer or from the laser-induced recoil pressure due to rapid surface evaporation, most commonly observed when a fast, high-power laser is used; and (4) condensation from vapor species due to supersaturation, most likely observed when high gas pressure is used.

In general, the size of the particulates formed from the vapor state tends to be in the nanometer range, while the other two counterparts are in the micron and submicron range. The shape of the particulates formed from liquid ejecta tends to be spherical, while the particulates formed from solid ejecta tend to be irregular in shape. The shape of the particulates formed from vaporized species may be spherical or polyhedral.

In this section, unless specified otherwise, the "particulates" refer to the ones originated from the liquid droplets that are expelled by laser-induced recoil pressure or subsurface superheated layer. This type of particulate is commonly observed when the laser power density exceeds approximately  $10^7 \text{ W/cm}^2$ . The "threshold" power density for the formation of the liquid droplets depends on

several laser as well as material parameters and is discussed later in this chapter. The particulates originated from condensation of vapor species are discussed in more detail along with the effect of ambient gas pressure in Section 6.3. Fractured solid ejecta related to rough surface features usually occur at a lower power level. The irregularly shaped particulates are more often observed in brittle material systems, but appear to be a less acute problem in metallic systems.

### 6.2.1 Velocity

The velocities of the particulates have been investigated by a number of groups. Measuring techniques involved the use of a high-speed camera (Gagliano and Paek, 1974; Geohegan, 1993), a rotating velocity filter or shutter (Lubben et al., 1985; Dubowski, 1986), a rotating substrate device (Dupendant et al., 1989), or laser beam deflection measurements (Murakami, 1992). For a variety of materials investigated and lasers used, the reported velocities of the particulates all fall within a very narrow range. For example, Gagliano and Paek (1974) reported a velocity of about  $2 \times 10^3 \text{ cm/sec}$  from high-speed photographic analysis of the  $\text{Al}_2\text{O}_3$  particulates generated by a ruby-laser pulse with a power density of the order of  $10^7 \text{ W/cm}^2$ . Lubben et al. (1985) estimated that the majority of Ge particulates, produced by a KrF excimer laser with a typical peak power density of  $5 \times 10^7 \text{ W/cm}^2$ , had velocities between  $2.5 \times 10^3$  and  $1.2 \times 10^4 \text{ cm/s}$ . Geohegan (1992) determined a peak velocity of  $(0.45 - 1.2) \times 10^4 \text{ cm/s}$  from the time-of-flight emission measurements for YBCO ( $\text{YBa}_2\text{Cu}_3\text{O}_{7-x}$ ) and BN systems irradiated by a KrF excimer laser at a fluence of  $1.5 \text{ J/cm}^2$ .

The rotating-disc-substrate technique established by Dupendant et al. (1989) and Gavigan (1991) is described in more detail here. Figure 6.1 shows the schematic diagram of the rotating substrate device, consisting of a rotating disc substrate with a stationary slit along the radius, which allows the ablated matter to pass. The laser is fired in synchronization with the rotation of the substrate, so that at time  $t = 0$  for each laser pulse, the same position of the substrate would face the slit. A typical deposited feature, especially, along the

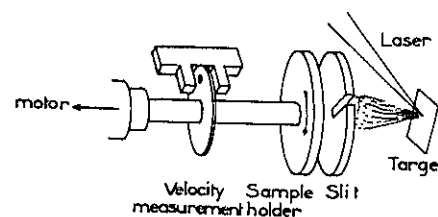


Figure 6.1. Schematic diagram of the rotating substrate device used for obtaining the time-resolved deposits. (From Dupendant et al., 1989, p. 369.)

circumference of the disc substrate, consists of a slit-size film followed by a fan of particulates (Figure 6.2). The slit-size film is condensed from the rapidly moving atoms and ions with velocities on the order of  $10^5$ – $10^6$  cm/s. Toward the center of the substrate, the resolution is reduced since the particulates, atoms, and ions are all deposited in the same area. The velocity of the particulate can be deduced from the angular position where a particulate is deposited. For a number of metallic systems with considerably different atomic masses and densities, the particulate velocity distribution maxima were found to vary only between  $(1 \text{ and } 2) \times 10^4$  cm/s, which is an order of magnitude smaller than the velocity of atomic and ionic species. The particulate velocity distributions for Al and Y are shown in Figures 6.3–6.4. The results for Al indicate that, while the velocity maximum increases slightly with increasing fluence, the ensemble of data does not show any dependence on the three Nd:YAG laser wavelengths (1064, 532, and 335 nm) used in the work by Dupondant et al. (1989). In the case of Y, it appears that the velocity maximum varies with neither the laser fluence nor the laser wavelength. Dupondant et al. (1989) also reported that the particulates generated from ablating YBCO have similar velocities as metals.

Lubben and coworkers (1985) observed that the maximum radius of particulates embedded in deposited Ge films decreases linearly as the delay time of inserting a shutter to block the ejected matter decreases, suggesting that the particulate velocity is perhaps size-dependent through an inverse linear relationship. At present, no simple correlation can be established for the velocity and the laser parameters or the material parameters.

## 6.2.2 Chemistry

While most workers reported that the film produced by PLD has a chemistry quite similar to that of the target, the retention of chemical composition in the

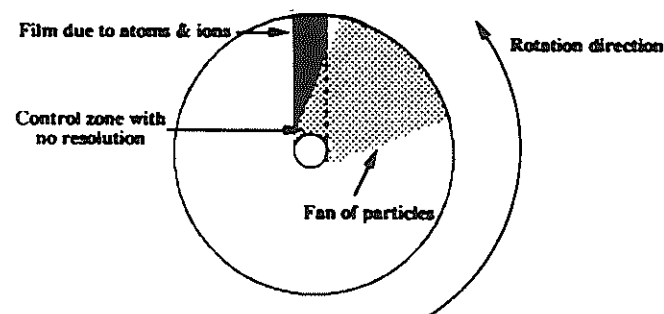


Figure 6.2. Schematic diagram of deposits obtained with the rotating substrate device. (From Dupondant et al., 1989, p. 369.)

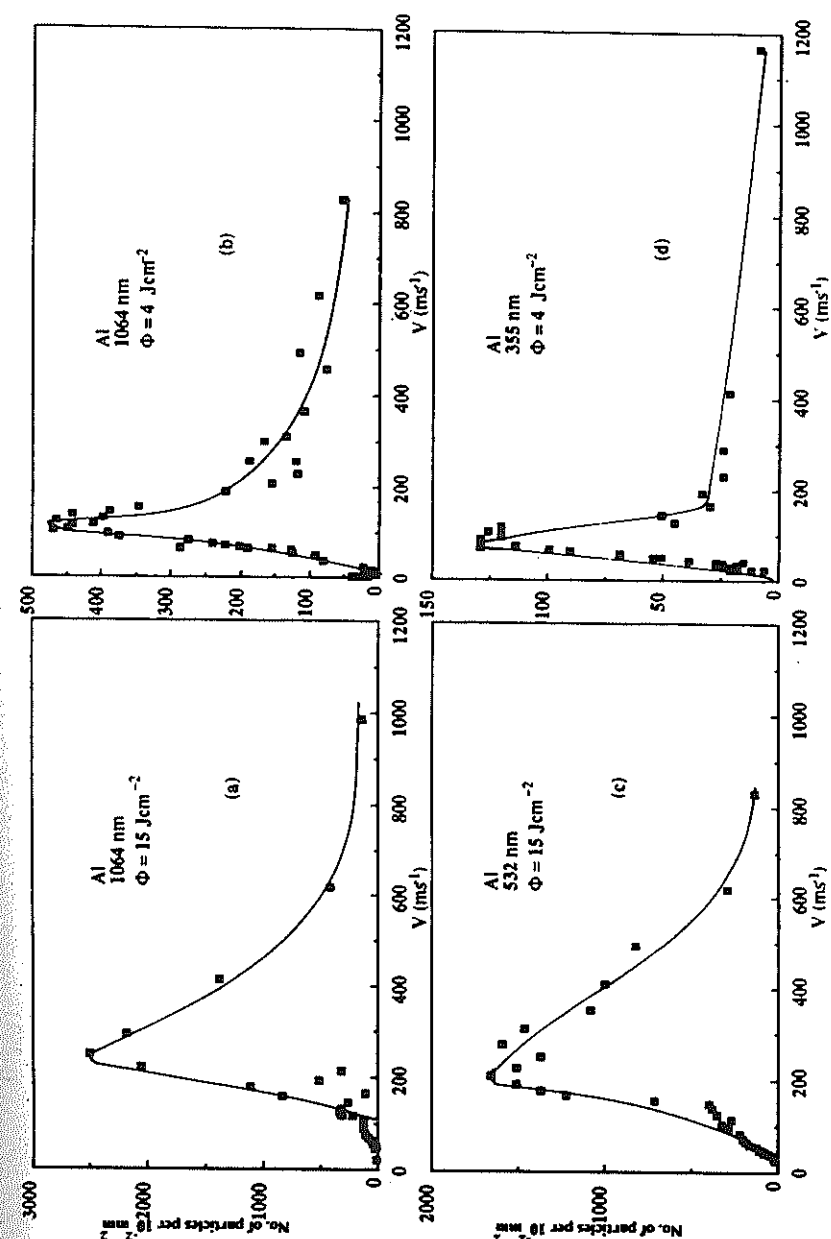


Figure 6.3. Particulate velocity distribution for 4 Al deposits prepared for different conditions of laser wavelength and target irradiance  $\phi$ . (From Dupondant et al., 1989, p. 369.)

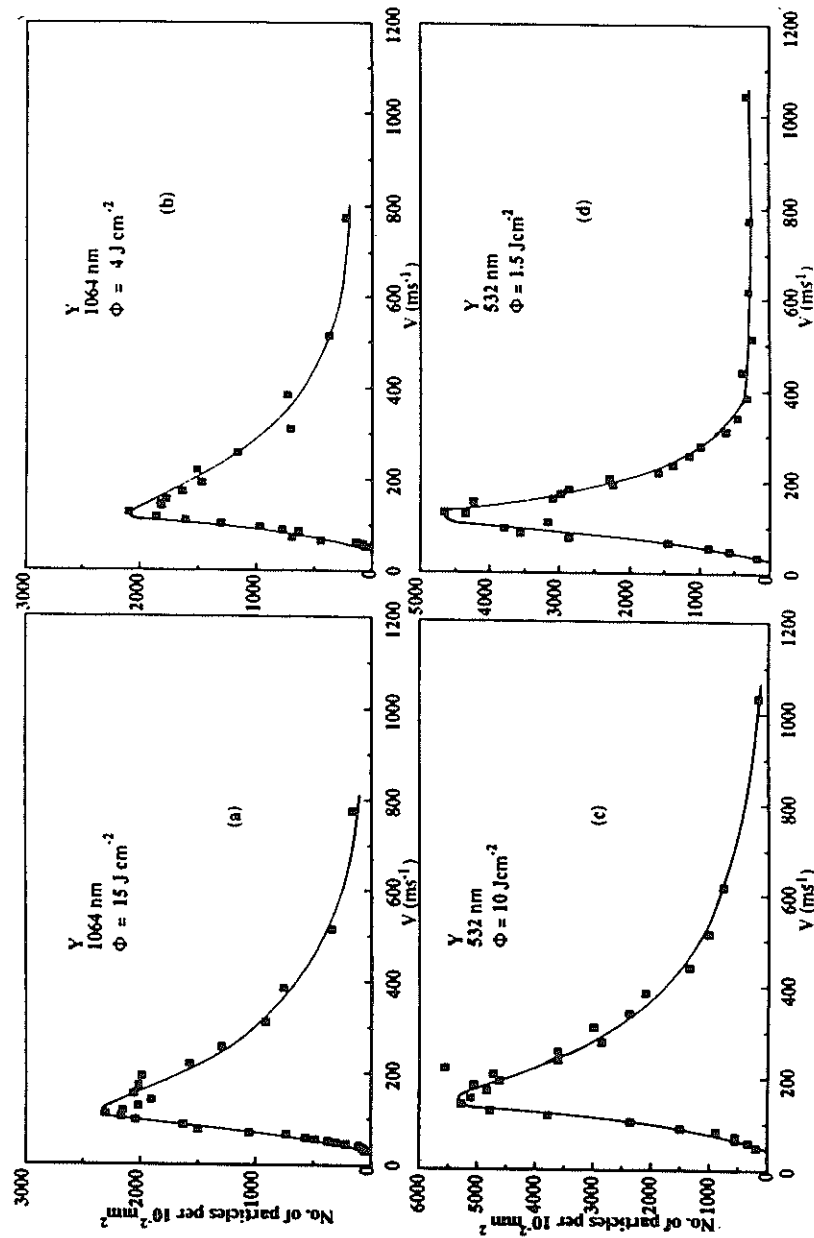


Figure 6.4. Particulate velocity distribution for 4 Y deposits prepared for different conditions of laser wavelength and target irradiance  $\phi$ . (From Dupond et al., 1989, p. 369.)

particulate has been questionable. Chen and Hall (1993) have shown that, in binary metallic systems, the particulates are usually deficient in the element with lower melting temperature, and the difference is a very strong function of the size of the particulate. For example, in both Nb–Al and Nb–Cr systems, the particulates are all enriched in Nb. In contrast, the matrix has a higher concentration of either Al or Cr than the target. The correlation of the particulate size and the overall composition of individual particulates is shown in Figure 6.5. There is a considerable and variable loss of Al or Cr in the particulates. In general, as the size of the particulate decreases, the element with a lower melting temperature, and therefore a higher vapor pressure, becomes more deficient. The depletion of the low melting element in the particulate

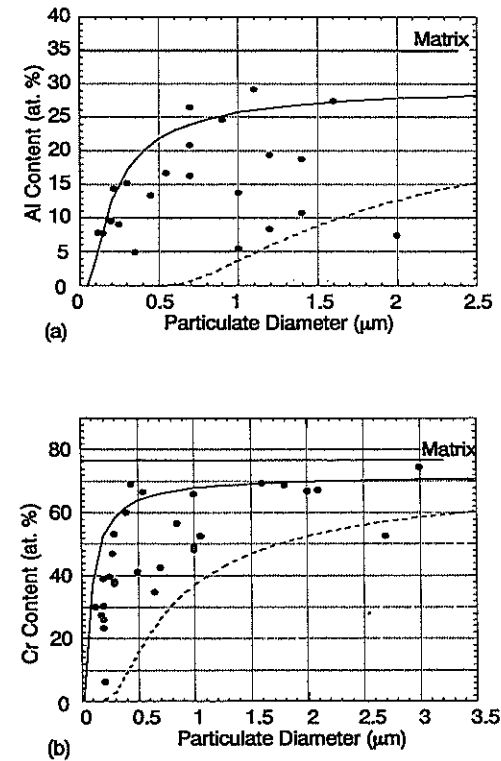


Figure 6.5. Energy dispersive X-ray results showing the (a) Al, and (b) Cr content against particulate diameter for a random selection of PLD-generated Nb–Al and CR–Nb particulates, respectively. The composition of the underlying film is also indicated as the “matrix.” The solid and dashed curves are calculated envelopes representing the upper and lower limits of the depletion according to Eq. 6.1. (From Chen and Hall, 1993.)

appears to be more pronounced in the binary metallic systems having larger melting temperature difference.

A plausible mechanism whereby the lower melting temperature element in the particulate is depleted has been proposed (Chen and Hall, 1993) and is described here. It is hypothesized that the composition of the expelled liquid droplet right above the surface of the target is quite close to that of the target, and the loss of the low melting temperature element occurs mainly during the flight to the substrate. Calculation based on existing literature formulas and thermodynamic functions (Dushman, 1955) shows that both the vapor pressures and the rates of evaporation for Al and Cr are almost identical at temperatures around 1500–2000°C and, at the same time, are several orders of magnitude higher than those of Nb. Consequently, preferential evaporation of the Al or Cr occurs and results in the enrichment of Nb in the particulates. The degree of Al or Cr deficiency would then be determined by how fast the Al or Cr can diffuse to the surface of the droplet and the dwell time during the flight. For a particulate of radius  $r$ , assuming a depletion layer of thickness  $l$ , the normalized resultant content of the depleted element can be estimated as

$$\frac{\text{Resultant \%}}{\text{Initial \%}} = \left(\frac{r-l}{r}\right)^3 \quad (6.1)$$

Calculated normalized compositions of the particulates having 1-, 10-, 100-, and 1000-nm depletion layers are shown in Figure 6.6. These curves might be regarded as indicating the best that one can do for composition control in the particulates generated by a PLD process. Considering the velocity of the particulate to be between  $2 \times 10^3$  to  $2 \times 10^4$  cm/s, the time it takes for a particulate to traverse a 5.5-cm target-to-substrate distance is  $\tau = 275$ –2750 ms. Obviously, the depletion-layer thickness can be estimated as

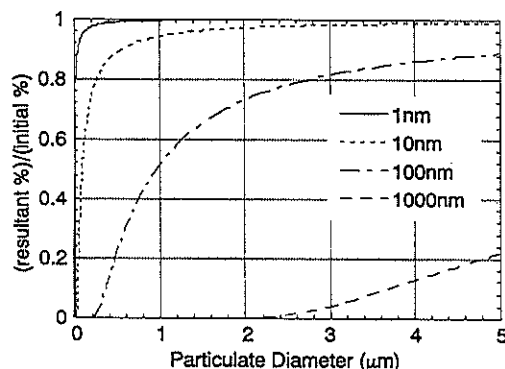


Figure 6.6. Calculated normalized compositions of the particulates having 1-, 10-, 100-, and 1000-nm depletion layer thickness. (From Chen and Hall, 1993.)

$l \approx (D\tau)^{1/2}$ , where  $D$  is the diffusivity of Al or Cr in the binary alloy systems and  $\tau$  is the dwell time. Since the dwell time of particulate varies, the depletion-layer thickness varies accordingly, resulting in a variable loss of Al or Cr in particulate. Using Eq. 6.1 and an initial composition of  $\text{Nb}_7\text{Al}_3$  and  $\text{Cr}_{72}\text{Nb}_{28}$ , the upper and lower limits of depletion-layer thickness can be determined from the best fitting parameters of the composition envelopes within which the data locate (Figure 6.5). The upper (lower) limit of depletion-layer thickness is 250 (25) nm for Nb–Al, and 100 (10) nm for Cr–Nb. The difference in the depletion-layer thickness of the Nb–Al and Cr–Nb particulates is related to the difference in diffusivities of Al in Nb–Al and Cr in Cr–Nb, which is related to the melting temperature differences between the terminal elements of the binary alloys (Chen and Hall, 1993).

In the extreme case when the constituted elements have very similar atomic masses as well as melting and boiling temperatures, the composition of the particulates is expected to be similar to that of the target. For example, Thompson et al. (1990) have found that the composition of the Fe and Cr in PLD-generated particulates is indistinguishable from that in the stainless steel target.

While the chemistry difference between particulates and matrix can be substantial for metallic systems, the chemistry difference is usually small for most ceramics. For instances, energy dispersive X-ray (EDX) analyses for the PLD oxide superconductors indicate that the chemistry of the particulates is the same as the underlying film to within  $\pm 3.5\%$  (Misra and Palmer, 1991). Although the accuracy of the EDX analysis is rather limited ( $\sim 3$ –5%) and the variation of chemistry on a lower scale cannot be ruled out, the fact that there is no significant loss of the constituted element in oxide superconductor particulates is likely due to a lower diffusivity and a lower vapor pressure of the element in the ionic or covalent bound materials.

There has been a considerable interest in developing the laser-ablation technique as a means of introducing solid materials for analytical spectrometry (Mitchell and Sneddon, 1987; Arrowsmith and Hughes, 1988; Hagar, 1989; Thompson et al. 1989 and 1990; Chenery et al., 1992). The application of laser ablation techniques to geological materials was reasonably satisfactory for oxides, while most sulfide minerals gave anomalously low results for sulfur. The investigation by Thompson et al. (1990) on the composition of the spheres and angular fragments ablated from a mineral pyrite  $\text{FeS}_2$  revealed some interesting features of PLD generated particulates. While the spherical particulates formed from liquid droplets have compositions in the range of  $\text{FeS}_{0.5-0.9}$ , indicating a severe loss of sulfur, the irregular fragments have compositions lying between  $\text{FeS}_2$  and  $\text{FeS}$ , presumably due to the loss of sulfur through moderate heating in the solid state, but not through melting. Although a dramatic depletion in the sulfur content of the spherical particulates is noticed, no obvious size dependence of the particulate composition can be derived from their analyses.

### 6.2.3 Microstructure

Since the particulates are solidified from molten droplets expelled from the target, cooling rate is the major parameter that controls the microstructure of the particulates. At the time of writing this chapter, there is still scarcely any available theory pertinent to the cooling process of the laser-ablated liquid droplets. Few in situ diagnostics (Rohlfing, 1988; Murakami, 1992; Geohegan, (1993) have been reported to investigate particulate properties such as temperature, ejection time, and size. Crude estimates of the cooling rate obtained by two different methods are presented here. When the ablation experiment is done in vacuum, cooling is predominantly radiant rather than convective. The cooling rate can be expressed as

$$\dot{T} = \left( \frac{6}{D\rho C_p} \right) \varepsilon \sigma (T^4 - T_0^4) \quad (6.2)$$

where  $D$  is the particulate diameter,  $\rho$  is the material density,  $C_p$  is the heat capacity of the material,  $\varepsilon$  is the radiant emissivity,  $\sigma$  is the Stefan-Boltzmann constant,  $T$  is the temperature of the particulate, and  $T_0$  is the ambient temperature. This formula is adapted from a more general formula applicable to "conventional" powder fabrication process such as atomization (see, for example, German, 1984). Considering a micron-sized Nb molten droplet ablated into an ambient background at room temperature, and assuming the physical properties of the molten state are similar to those of its solid-state counterpart, namely,  $\rho = 8.55 \text{ g/cm}^3$ ,  $C_p = 0.16 \text{ Jg}^{-1} \text{ K}^{-1}$ ,  $\varepsilon = 0.19$ , and typical  $T \approx T_m = 2740 \text{ K}$ , the cooling rate  $\dot{T}$  is of the order of  $1.6 \times 10^6 \text{ K/s}$ . Alternatively, considering the particulates remain spherical with little deformation upon impact with the substrate, the cooling rate can be estimated as  $\dot{T} \approx T_m/2\tau$ , where  $T_m/2$  is half the melting temperature and  $\tau$  is the time of flight from target to substrate. Using  $\tau = 275\text{--}2750 \text{ ms}$ , as estimated in Section 6.2.1, and  $T_m = 2740 \text{ K}$  for Nb,  $\dot{T} \approx (0.5\text{--}5) \times 10^6 \text{ K/s}$ . Measurements done on BN and YBCO particulates (Geohegan, 1993) gave a cooling rate of  $(0.5\text{--}10) \times 10^6 \text{ K/s}$  during the first 1 ms after laser pulse.

At such a high cooling rate, the solidified particulates appear to have a fine-grain microstructure. Chen et al. (1992) observed that, for PLD-produced Nb-Al particulates, while many submicron-size particulates are single crystals, the large particulates are polycrystalline with grain size of the order of  $0.2 \mu\text{m}$ . Closer transmission electron microscopy (TEM) examination indicates that the smaller particulates also contain a higher density of defects than the larger particulates. This observation provides additional evidence that the smaller particulates are, indeed, subject to a higher cooling rate and a larger undercooling. As a consequence of rapid cooling, metastable structure can also be formed. For example, Chen and Hall (1993) reported that, the Cr(Nb) and Nb(Cr) particulates are body-centered cubic (bcc) solid solutions containing a minor element concentration far beyond the solubility limit predicted in the

equilibrium phase diagram. Furthermore, the Cr-Nb particulates of approximate composition  $\text{Cr}_2\text{Nb}$  have a nanocrystalline diamond cubic structure, which is a new metastable phase, instead of a hexagonal Laves structure as predicted in the phase diagram.

### 6.2.4 Spatial Distribution

While film thickness profiles and in situ diagnostic techniques have been used to analyze the distribution of the vapor ejecta quantitatively (see Chapters 5 and 7 in this book), the characterization methods for the spatial distribution of PLD-generated particulates are far from established. Since the number density and the average particulate size could vary across the film (Chen, 1992; Leuchtner et al., 1992), it is quite clear both factors need to be considered in analyses. The assessment of spatial distribution is also affected by whether the number density is normalized to underlying film thickness, which varies strongly with angle. Furthermore, due to centrifugal force, the trajectories of particulates may be altered by target spinning, which is commonly practiced during PLD.

Greer and Van Hook (1990b) and Lowndes et al. (1990) found the particulate number density (per unit area and film thickness) to be higher off the deposition axis, while Cheenne et al. (1990) reported lower particulate densities (per unit area) off the deposition axis. IJsselsteijn et al. (1992) reported that, when normalized to local film thickness, there is virtually no difference in the spatial distribution between the particulates and the film deposited from vapor species. The results from IJsselsteijn et al. (1992) are shown in Figure 6.7. The normalized distributions of the vapor species and particulates overlap each other. These particulate density distributions are not necessarily inconsistent with one another, however, since the particulate density was not normalized in the same way. In addition, the corresponding particulate size as a function of the position in the film was not addressed in these four investigations. Therefore, generalization of the preceding observations can be misleading.

Chen (1992) observed that the spatial distribution is a strong function of laser fluence. For the Nb-Al and Cr-Nb systems, when a laser fluence below  $12 \text{ J/cm}^2$  was used, no significant variation was found for both the average particulate size and the particulate number density (per unit area) over a 2-in substrate, suggesting the spatial distribution of the particulate was less forward scattered than that for the vapor species. As the laser fluence increases, the distribution function becomes quite complex. The average particulate size is larger, while the particulate number density (in terms of per unit area as well as per unit area and film thickness) is lower, nearer the plume center than farther radially out. The particulate mass distribution (particulate number density multiplied by average particulate mass, which is proportional to the cube of average particulate size) appears to scale with film thickness in that the



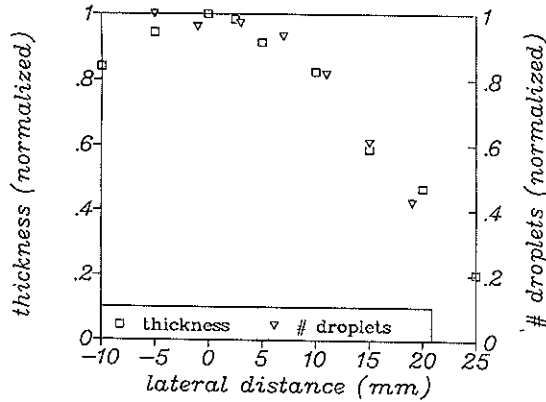


Figure 6.7. Spatial distributions of the atomic material and particulates in a PLD-produced YBCO film. (From IJsselstein et al., 1992, p. 251.)

accumulative mass of particulates is smaller off the deposition axis. In contrast, Leuchtner et al (1992) reported that, for Pt particulates generated in the fluence range between 0.83 and 3.33 J/cm<sup>2</sup>, the distribution functions appear to be more peaked at the lower laser fluences. At the present time, no conclusive trend can be derived from the limited literature information.

### 6.3 EFFECTS OF PROCESSING PARAMETERS

Considerable amount of effort has been devoted to problems related to laser-material interaction and is discussed in Chapter 4 of this book. The governing equations describing the process are quite complex and often involve material and optical parameters that are not available in the literature. Although it is difficult to establish a correlation between deposition parameters and particulate generation with rigor, some consensus and guidelines can be found from the literature and are described here. Practically, it is desirable to find a scaling factor, which relates to the particulate generation with the laser parameters and material properties. Thus, by comparing the change of this scaling factor as a function of processing parameters, one can predict whether the PLD plume is dominated by either molten droplets or vapor species.

The particulates originated from splashing of molten droplets most likely occur when the transfer of laser energy into heat occurs at a faster rate than is needed to evaporate a mass volume of depth equal to half the skin depth (Ready, 1963). Based on Ready's model, Schwarz and Tourtellotte (1969) estimated the maximum laser power density that a solid surface could absorb without causing splashing to be

$$I_{\max} \approx \alpha^{-1} \rho H_v / 2t_r \quad (6.3)$$

where  $\alpha$  is the absorption coefficient ( $\alpha^{-1}$  is the attenuation distance for an electromagnetic wave whose intensity has decreased by a factor of  $1/e$ ),  $\rho$  is the solid mass density,  $H_v$  is the heat of vaporization (per unit mass), and  $t_r$  is the relaxation time of the hot electrons in the surface layer, which is about 1% of the reciprocal frequency of an equivalent Debye oscillator. For a metal surface such as titanium with a typical skin depth of 10 nm,  $I_{\max}$  corresponds to approximately  $5 \times 10^8$  W/cm<sup>2</sup>. This power density is easily attained by pulsed lasers, including the passive Q-switched ruby laser, as well as the Nd:YAG laser, transferred-electron amplifier (TEA) CO<sub>2</sub> laser, and ultraviolet (UV) excimer lasers.

Another approach is to characterize each PLD condition by a nondimensional absorption parameter (Dabby and Paek, 1972; Gagliano and Paek, 1974)

$$B = \frac{K\alpha H_v}{I(1-R)C_p} \quad (6.4)$$

where  $K$  is the thermal conductivity,  $I$  is the laser power density,  $R$  is the reflectivity, and  $C_p$  is the heat capacity. The thermal diffusivity,  $D_{th}$ , is given by  $D_{th} = K/\rho C_p$ , and the thermal diffusion length,  $l_{th}$ , is related to the thermal diffusivity by  $l_{th} = (2D_{th}\tau_p)^{1/2}$ , where  $\tau_p$  is the laser-pulse duration. For convenience, the nondimensional absorption parameter can be rewritten as

$$B = \frac{l_{th}^2 \alpha (\rho H_v)}{2\tau_p I (1-R) \gamma} \quad (6.5)$$

where  $\gamma$  is the ratio of specific heats ( $C_p/C_v$ ). At the end of the laser pulse, the deposited heat (per unit area),  $\tau_p I (1-R)$ , is confined approximately to a heated depth of  $a$ , which can be estimated as  $a \approx l_{th}$ , or  $a \approx \alpha^{-1}$ , in the case of  $l_{th} \gg \alpha^{-1}$ , or  $l_{th} \ll \alpha^{-1}$ , respectively. The corresponding heat (per unit area) required to evaporate a layer of thickness  $a$  is  $l_{th} \rho H_v$  or  $\alpha^{-1} \rho H_v$ , in the case of  $l_{th} \gg \alpha^{-1}$ , or  $l_{th} \ll \alpha^{-1}$ , respectively. Therefore, apart from a multiplication factor ( $l_{th} \alpha / 2\gamma$ , or  $l_{th}^2 \alpha^2 / 2\gamma$ ), the nondimensional absorption parameter  $B$  can be regarded as a ratio of the heat (per unit area) required to evaporate a layer of thickness  $a$  and the deposited heat (per unit area) from laser irradiation. In general, for a higher value of  $B$  ( $\gg 1$ ), the material removal process is predominantly vaporization, whereas for smaller  $B$  ( $\ll 1$ ), particulates are the dominant form of material removal. Although an absolute dividing scaling factor cannot be obtained due to limited literature data and the complex nature of laser-material interaction, a remarkable correlation of the degree of splashing and the  $B$  parameter is observed. The choice of material or laser parameters for a desired deposition structure can be conveniently inferred from comparing the magnitude of the change of  $B$  parameters.

Obviously, the generation of particulates strongly depends on the material type. For instance, Greer and van Hook (1990a) found that, under similar



processing conditions, 8% yttria stabilized-ZrO<sub>2</sub> (YSZ), LaAlO<sub>3</sub>, and Al<sub>2</sub>O<sub>3</sub> films to be relatively particulate-free, whereas films deposited by ablating from YBCO with various target compositions and Nd<sub>0.5</sub>Sm<sub>0.5</sub>GaO<sub>3</sub> contained a particulate density at least a factor of 10 higher and Nd<sub>2-x</sub>Ce<sub>x</sub>CuO<sub>4</sub> film even showed a particulate content about two orders of magnitude higher. The material dependence of the *B* factor is reflected in various physical parameters: *K*,  $\alpha$ , *H<sub>v</sub>*, *R*, and *C<sub>p</sub>*. Once a material is fixed, one should then consider the effects of laser parameters, which are explicitly expressed in the *B* factor as *I*, *R*, and  $\alpha$ .

### 6.3.1 Laser Fluence

For a chosen material and a fixed laser wavelength, the laser fluence on the target has the most significant effect on the particulate size and density. The laser fluence can be varied by varying the laser power or the laser spot size. At constant laser power, the particulate number density is usually higher with tighter focus. In general, there exists a threshold laser fluence, below which the particulates are barely observable. For example, in the case of high *T<sub>c</sub>* YBCO material, the threshold laser fluence for the occurrence of particulates is about 0.9 J/cm<sup>2</sup> when a XeCl (308-nm) excimer laser with 20-ns pulse duration is used (Blank et al., 1992). Above the threshold laser fluence, the particulate number density increases rapidly with increasing fluence. However, the rate of increase reduces at a higher fluence, indicating saturation (Figure 6.8). The saturation of the particulate deposition and film deposition, in general, is largely due to the saturation in the ablation process (Smith et al., 1992). For example, plasma

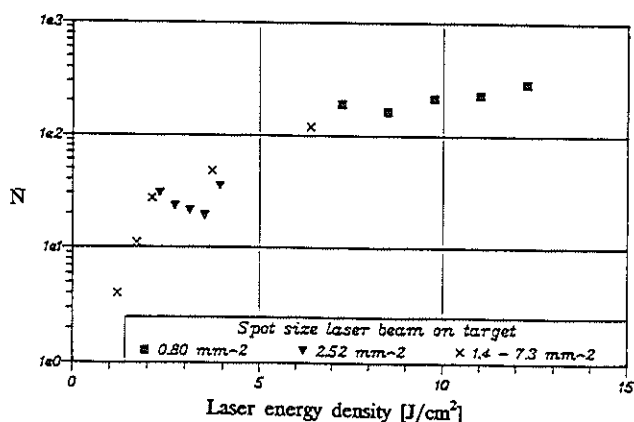


Figure 6.8. The number of particulates corrected for the film thickness vs. the laser energy density in YBCO films produced by XeCl laser ablation. (From Blank et al., 1992, p. 67.)

shielding of the target is one of the mechanisms that reduce the ablation rate (Dyer et al., 1989), and is more often encountered in the laser-ablation deposition using longer wavelength. It should also be noted that, the saturation of the particulate density at higher fluence may be exaggerated somewhat, since the sticking of the particulates to the substrate appears to be poorer at elevated laser fluence (Chen, 1992).

For the Nb-Al and Cr-Nb systems, the average particulate size appears to increase with increasing fluence (Figure 6.9). A similar trend also holds for oxide superconductors (Misra and Palmer, 1991) and Pt (Leuchtner et al., 1992). However, the functional dependence of the average particulate size, and/or the volume fraction of the particulates in the ejected flux, on the laser fluence can be nonmonotonic. Theoretically, Chan and Mazumder (1987) have shown that, in a one-dimensional steady-state model for material removal by vaporization and liquid expulsion due to laser ablation, the liquid-expulsion rate versus absorbed power would go through a maximum as the power increases while the vaporization rate increases with the laser power. At lower power the vaporizing temperature is low. Consequently, the liquid-expulsion rate is low because of low recoil pressure. At high power the vaporizing temperature is high. The thickness of the liquid layer is shallow however, so that the liquid-expulsion rate also becomes small. The power level where the maximum liquid-expulsion rate occurs depends on the material (Chan and Mazumder, 1987).

The preceding discussion on the effects of laser fluence on the particulate size and density applies to the case where the target is considered to be "infinitely" thick to the laser beam. Nishikawa et al. (1991) reported that, when a thin-film target with thickness of 0.05–0.33  $\mu$ m is used, the particulate morphology depends on the combination of target thickness and laser fluence.

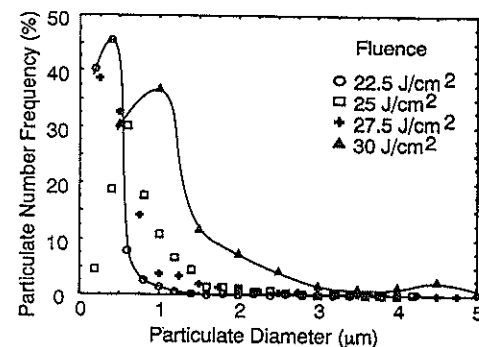


Figure 6.9. Size distributions of Nb-Al particulates produced at various laser fluences. The curves drawn through the data points are for guidance only. (From Chen and Hall, 1993.)

For a target thickness of  $0.33\text{ }\mu\text{m}$ , the average particulate size is smaller when a higher laser fluence is used. This comes as no surprise since, for a film target with finite thickness, the vaporized layer is proportionally increased, leaving behind a shallower molten layer when higher laser fluence is used.

### 6.3.2 Laser Wavelength

The laser wavelength  $\lambda$  comes into play mainly in the effectiveness of the absorption of the laser power into the target. For most metals, the absorption coefficient  $\alpha$  decreases with decreasing  $\lambda$ . Hence, the laser penetration depth in metals is larger in the UV range than in the infrared (IR) range. For other materials, the variation of absorption coefficient with wavelength is more complex since various absorption mechanisms, such as lattice vibration, free carrier absorption, impurity centers, or bandgap transition, can take place. As we discuss in further detail below, for the oxide superconductors, the penetration depth appears to be larger in the near IR than in the UV, somewhat reverse to that of the metals.

It has been demonstrated that the density and size of particulates is much higher for the YBCO films prepared with a Nd:YAG laser at IR wavelengths as compared to ones prepared with an excimer laser at UV wavelengths (Koren et al., 1989; Misra and Palmer, 1991). The particulate problem is most acute in the  $10.6\text{-}\mu\text{m}$   $\text{CO}_2$ -laser-ablation deposition (Dyer et al., 1992). The exact mechanism whereby the particulate density and size is reduced when using UV was once controversial. Koren et al. (1990) hypothesized that the absorption of the UV-laser irradiation by the ejected particulates is responsible for further fragmentation in the hotter plume, which leads to smoother films with fewer and smaller particulates. To check their hypothesis, a deposition experiment was designed in which a Nd:YAG laser was used to irradiate the target and a second excimer UV laser was used to irradiate only the plume. With this two-laser setup, reduction in the number and size of particulates formed in the laser ablation deposition of YBCO films was obtained. The merit of having a second laser to heat the plume formed by the first laser in order to fragment the ejected matter in the plume is clear, since the occurrence of particulates is one of the major impediments in the application of PLD technology. In Section 6.4 we discuss further the use of a second laser along with other techniques that can be employed to eliminate the particulates. One should note, however, that when only one UV laser is used to ablate the target directly, much smoother films are obtained than those shown when a two-laser setup is used (Koren et al., 1990). Thus, the effect of laser wavelength on the nature of particulates due to a fragmentation mechanism appears to be secondary, since in one laser setup, the fraction of plume that will get irradiated by the laser is small. Therefore, the fragmentation mechanism can account for only partial, but not the overall, reduction in particulate size and density.

The primary effect of the laser wavelength on particulate generation is most

likely due to the difference in the absorption coefficient when different laser wavelengths are used. Recent measurements by Kautek et al. (1990) on a  $1\text{-}\mu\text{m}$ -thick YBCO film indicate that, in fact, the absorbance decreases with increasing wavelength and the differences of the absorbance, or of the light penetration depth, are of two orders of magnitude between UV light and near IR. For example, the green light at  $533\text{ nm}$  is almost 10 times less absorbed than at its  $266\text{-nm}$  counterpart. A deeper penetration depth (that is, a larger  $\alpha^{-1}$ ), or equivalently, a smaller  $B$  factor, achieved by the Nd:YAG laser with  $1.06\text{-}\mu\text{m}$  wavelength than the excimer laser in UV is perhaps the most significant factor that determines the particulate size and density. The effects of laser parameters on the nondimensional absorption parameter  $B$  are best demonstrated in the target topography. Scanning electron microscope (SEM) investigation of the laser irradiated surfaces reveals characteristic melting-solidification processes (Kautek et al., 1990). The distinct grain structures, reminiscent of the original ones, provide a coarse measure for the maximum depth of light absorption and heat propagation. After several hundred pulses, troughs, valleys, and cavities develop. As the wavelength increases, the depth and width of the grooves generated on the laser-ablated surface increase (Figure 6.10). The corresponding SEM micrographs of the deposited YBCO at

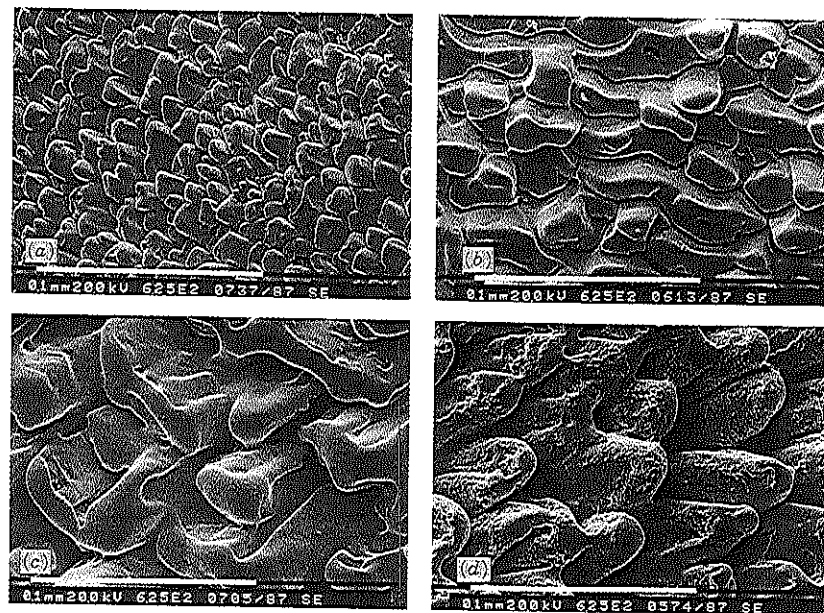


Figure 6.10. SEM micrographs of pellets after irradiation with 500 pulses of  $0.79\text{-GW/cm}^2$  peak power (integral energy,  $395\text{ J/cm}^2$ ): (a)  $266\text{ nm}$ ; (b)  $355\text{ nm}$ ; (c)  $533\text{ nm}$ ; (d)  $1064\text{ nm}$ . Scale marker:  $100\text{ }\mu\text{m}$ . (From Kautek et al., 1990, p. 317.)

various wavelengths are shown in Figure 6.11(Kautek et al., 1990). The correlation of ejected particulate size and the depth or width of grooves on the target surface is remarkable. One should keep in mind that the surface roughness by itself does not a priori lead to the formation of particulates, although a smooth target usually produces fewer particulates. Particulates are generated even when only a few initial pulses of laser are irradiated on the target of which the surface remains quite smooth.

In summary, combining the effects of laser wavelength and laser fluence, more and larger particulates are generated when using laser parameters with smaller  $B$  factors. Massive splashes occur as  $B$  decreases further, which lead to predominantly particulate formation. On the other hand, PLD at an extremely large  $B$  factor is not beneficial either, since it results in incongruent evaporation and very poor, slow deposition. The parameter window for favorable YBCO deposition results, determined by Kautek et al. (1990), is depicted in Figure 6.12.

### 6.3.3 Ambient Gas Pressure

Briefly, the use of an ambient gas during pulsed laser ablation deposition can be characterized as either passive or active. The passive use of an ambient gas

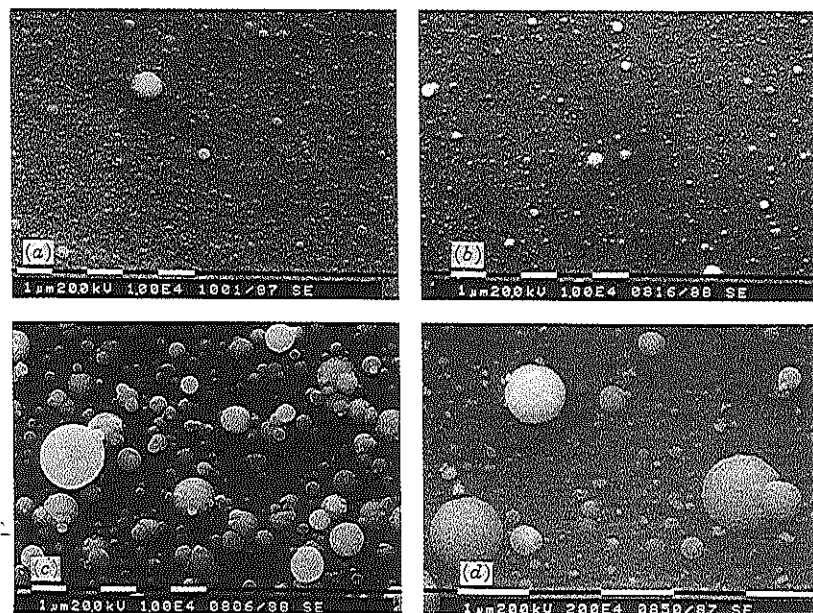


Figure 6.11. SEM micrographs of PLD thin films with a peak power of  $0.79 \text{ GW/cm}^2$ : (a) 266 nm, 9000 pulses; (b) 355 nm, 9000 pulses; (c) 533 nm, 15,000 pulses; (d) 1064 nm, 15,000 pulses. Scale marker:  $1 \mu\text{m}$ . (From Kautek et al., 1990.)

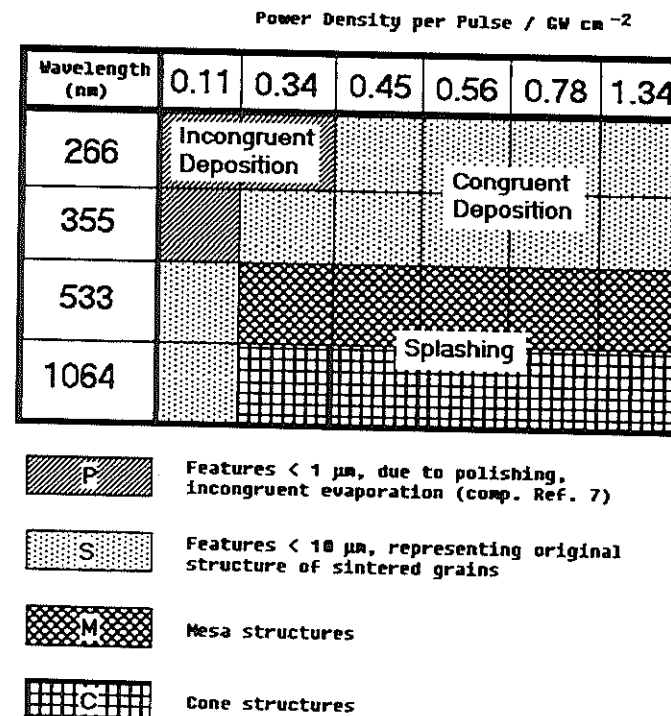


Figure 6.12. Influence of laser wavelength and power density on the target surface structure and the resultant film. (From Kautek et al., 1990, p. 317.)

is mainly to compensate for some loss of a constituent element such as oxygen or nitrogen in ceramics. For example, the deposited oxide ceramics tend to be deficient in oxygen when the ablation experiment is done in vacuum. In situ processing of oxide superconductors typically requires 10–300 mtorr of background oxygen in the chamber during deposition. When the gas is admitted in situ during PLD, however, the typical particulate size does indeed change as the ambient gas pressure varies. In fact, perhaps it has not been realized yet that there could be tremendous potential applications derived from the active use of an ambient gas during PLD, in which either inert or reactive gas can be introduced deliberately to form particulates with a desired size or composition. For example, by incorporating an ambient gas during laser deposition, ultrafine particles can be fabricated with particle diameters ranging from a few nanometers to a few tens of nanometers.

Matsunawa et al. (1986) have investigated the production of ultrafine powders of various metals (Fe, Ni, and Ti) and alloys (Ni–Ti, Fe–Ti, and Cu–Ni) in argon and helium atmospheres. The majority of metal particle

morphologies are spherical or polygonal. Figure 6.13 shows the cumulative particulate size distributions of ultrafine Fe powders made at 200 kPa (2 atm), 13.3 kPa (100 torr), 1.3 kPa (10 torr), and 0.1 kPa (about 1 torr). The decrease in the ambient gas pressure results in a decrease in size and a narrower size distribution.

The compositions of ultrafine alloy powders show some interesting trends. For Ni-Ti and Fe-Ti, the ultrafine particulates have lower Ti than their target alloys. For Cu-Ni, the particulates are deficient in Ni. Considering that the vaporization temperatures (and heats of vaporization) of Ti, Fe, Ni, and Cu elements are 3562 K (421 kJ/mol), 3135 K (349.6 kJ/mol), 3187 K (370.4 kJ/mol), and 2836 K (300.3 kJ/mol), respectively, the elements with lower vaporization temperatures and heats appear to be enriched in the alloy particles. Conversely, in comparison to the situation discussed in section 6.2.2, the PLD-produced Nb-Cr and Nb-Al particulates in vacuum are enriched in Nb, which is the element with a higher vaporization temperature and heat of vaporization. The vaporization temperatures (and heats of vaporization) of Nb, Cr, and Al are 5017 K (682 kJ/mol), 2945 K (344.3 kJ/mol), and 2793 K (293.4 kJ/mol), respectively.

The origins of the formation of the particulates and the mechanisms whereby a specific element is enriched in the particulates are clearly different for PLD processes in vacuum versus those in inert ambient gas. The effect of inert ambient gas pressure on the nature of particulate is most likely related to the increased collisions between the ejected species and the ambient gas as the ambient gas pressure increases. At a pressure of the order of 1 mtorr, the mean free path is approximately 5 cm. The mean free path of ejected species becomes 0.05 cm at a higher pressure of 100 mtorr. When a laser ablation deposition experiment is done in vacuum, there are virtually no collisions between the

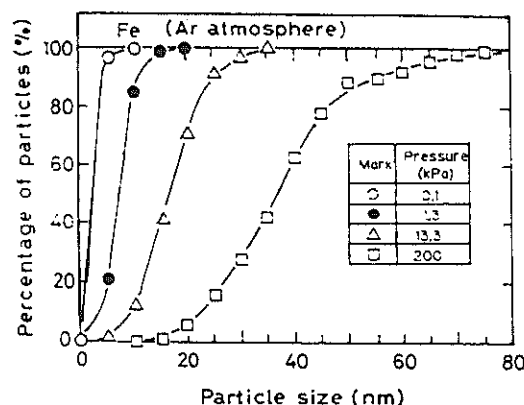


Figure 6.13. Cumulative size distributions of ultrafine Fe particulates made under Ar pressure of 0.1, 1.3, 13.3, and 200 kPa. (From Matsunawa et al., 1986, p. 61.)

ejected species before they reach the substrate. Therefore, particulates are predominantly formed from solidified liquid droplets that are expelled from the target by the recoiled pressure. In the same time, the vapor species are deposited as a uniform background film. When the ambient gas pressure increases, however, the vapor species can undergo enough collisions that nucleation and growth of these vapor species to form particulates can occur before their arrival at the substrate. The fact that the particulate size increases as the ambient gas pressure increases strongly suggests that the ultrafine particulates are formed from the vapor species instead of liquid droplets. Since the growth mechanism is by diffusion, the residence time of the particulate in the vapor controls the size of the particulate. The longer the residence time, as is the case with increased ambient gas pressure, the larger the particulate. Comparison of the size distributions of the ultrafine particulates at various deposition locations reveals that the particulates collected at a larger target-to-substrate distance are larger than those collected near the laser irradiation zone (Matsunawa et al., 1986). This observation is consistent with the growth mechanism described earlier, namely, that the size of the particulate is indeed controlled by the residence time of the particulate when ambient gas is used.

In view of the two different origins for the formation of particulates, the compositional correlation between the particulates and the target materials for PLD processes in vacuum versus the ones in ambient gas can also be understood. When the particulates are formed from the vapor species, assuming the sticking coefficient of each species is the same, the composition of the particulate should be identical to the concentration of the vapor species in the plume. The power density range ( $3 \times 10^4$  to  $6 \times 10^6$  W/cm<sup>2</sup>) that Matsunawa et al. (1986) used for the laser production of ultrafine powders is perhaps not high enough for congruent evaporation. In the incongruent evaporation regime, preferential evaporation of the elements with lower vaporization temperatures and heats occur in the laser-irradiated multicomponent target surface. Consequently, the particulates that are formed from the nucleation and growth of the evaporants are enriched in the elements with lower vaporization temperatures and heats. As expected, the resulting composition of the particulates formed from vapor species is independent of the size of the particulates. In the situation where the particulates are formed from the expelled liquid droplets, as discussed in Section 6.2, the laser power densities are much higher ( $5 \times 10^7$  to  $1 \times 10^9$  W/cm<sup>2</sup>). Therefore, as the regime of congruent ablation is approached, and the loss of the elements with higher vapor pressures among the constituent elements in the expelled liquid droplets occurs during the flight from target to substrate. In this case, the deposited particulates are enriched in the elements with lower vapor pressures (most likely also higher melting temperatures and heats), and the composition of the particulates depends on their size, since a smaller liquid droplet suffers a greater loss than does its larger counterpart.

Addition of a reactive gas such as O<sub>2</sub>, N<sub>2</sub>, or H<sub>2</sub> to the inert gas permits deposition of oxides, nitrides, and hydrides from metallic or elemental dielectric

targets. Typical particulate size produced by reactive PLD is also in the nanometer range. In Section 6.5, there are demonstrated some novel applications that can be derived from reactive PLD, inert gas PLD, in addition to vacuum PLD in which the solidified liquid droplets are deliberately incorporated.

### 6.3.4 Target-to-Substrate Distance

When the film is deposited in vacuum, the effect of target-to-substrate distance is mainly reflected in the angular spread of the ejected flux. The angular distribution of laser-ablated ejecta is described in Chapter 7. In general, the particulate trajectories are more divergent when a defocused laser beam is used, as opposed to emerging as a collimated jet for a tightly focused beam. However, when a PLD experiment is done in a poor vacuum, with an ambient gas, or at a substantially large target-to-substrate distance in which coalescence of particulates can take place, markedly different particulate appearance may occur, depending on the position of the substrate.

The specific effects of target-to-substrate distance and ambient pressure are interrelated. Due to the increased collisions between the laser-produced plume and the background gas, the plume dimension decreases as the background gas pressure increases. Dyer et al. (1990) have shown that  $E/P_0$  is the scaling parameter for plume range, where  $E$  is the laser-pulse energy, and  $P_0$  is the background gas pressure. The length of the plume  $L \propto (E/P_0)^{1/3\gamma}$ , where  $\gamma$  is the ratio of specific heats of the elements in the plume. For an ambient pressure of 35 mtorr and a laser fluence of  $4 \text{ J/cm}^2$ , the plume range  $L$  corresponds to approximately 5.5 cm (Smith et al., 1992). When the target-to-substrate distance is much smaller than  $L$ , there is no marked difference in particulate size and the density. As the target-to-substrate distance increases, the proportion of the smaller particulates decreases, and a few larger particulates appear (Nishikawa et al., 1991), indicating a merge during flight. Once the substrate is located far beyond  $\sim L$ , the adhesion to the substrate of ejected matter, including the particulates and atomic species, is poor.

### 6.3.5 Other Parameters

Both target surface roughness and bulk density can have some effect on the particulate generation rate. Misra and Palmer (1991) reported that a polished target surface produces somewhat fewer particulates, but the effect is not as significant as when laser parameters are changed. Although it is commonly believed that particulates can be minimized by working with targets of high density, IJsselsteijn et al. (1992) reported little observable effect of the target density in the range from 80% to 94% on the particulate generation. The major material parameter that will be affected by the change of bulk density is the thermal conductivity. For dispersed pores in a solid, at low temperatures, the

porosity has a low conductivity as compared with any solid phases present, and a nearly linear decrease in thermal conductivity with increasing porosity is found. At higher temperatures, departure from linearity occurs as radiation across pores contributes to heat transfer, in addition to true conduction. It is likely that the difference of thermal conductivity is small within the narrow range of density that IJsselsteijn et al. (1992) have investigated.

## 6.4 ELIMINATION OF PARTICULATES

In applications for electronic and optical thin-film devices with sophisticated architecture, the incorporation in a film of particulates, having a typical size ranging from a fraction of a micron to a few microns, can severely degrade the performance. For example, in multilayer X-ray mirror applications, the tolerable surface roughness is only of the order of a few nanometers. A microwave strip line incorporating particulates on the track would be rendered useless if the particulates became dislodged. For superconducting material, the presence of particulates could also have an adverse effect or perhaps, could be a blessing in disguise. In a thin film that is to be patterned for a superconducting quantum interference device (SQUID), of which the workings are dependent on the material's coherence length (typically 5–100 nm in the metal-based superconductors and 1–3 nm in the oxide-based superconductors), the presence of such particulates in the path would be problematic. On the other hand, the incorporation of particulates may be beneficial if the particulates are distributed such that they function as pinning centers that help reduce the flux creep. When determining the tolerance of a specific device for particulates, not only the size of the particulates but also their density is of significant concern, particularly as the trend of miniaturizing electronic components continues. Considering an electronic thin-film component with a typical width of  $10 \mu\text{m}$ , a particulate density of less than 1 per  $100 \mu\text{m}^2$  may be desirable.

A simple approach to reduce the number of particulates is to reduce the laser power density to below the threshold level that causes the splashing of the molten layer, as described in Section 6.3. It is also advisable to reduce the laser power density by increasing the spot size rather than by decreasing the laser power. Blank et al. (1992) observed that a simple relation holds for the deposited film thickness,  $d \propto S^2 E$ , where  $S$  is the laser spot size on the target, and  $E$  is the laser energy density. Since the deposited film thickness is directly proportional to the spot size when the laser energy,  $SE$ , is fixed, increasing the spot size is the most efficient way to reduce the particulates as well as to increase the throughput of vapor species. The surface smoothness is dramatically improved by reducing the laser power density; however, at the same time, the advantages of having the high-energy species, which help to produce improved film quality at a lower substrate temperature, is sacrificed. For that reason, several mechanical approaches have been developed to reduce the particulate density and size.



### 6.4.1 Mechanical Approaches

The majority of the mechanical approaches are based on the fact that the particulates travel much slower than the atomic and molecular species. As described in Section 6.2.1, typical particulate velocities are in the range of  $2 \times 10^3$ – $5 \times 10^4$  cm/s, which is at least an order of magnitude smaller than those of the atomic and molecular species. Velocity filters can therefore be used to stop the slowly moving massive particulates, but let the fast atomic and molecular evaporants through (Barr, 1969; Lubben et al., 1985; Dubowski, 1986; Venkatesan et al., 1992).

Figure 6.14 shows a schematic of a rotating vane velocity filter described by Barr (1969), Dubowski (1986), and Venkatesan et al. (1992). The vanelike structure allows only species with velocities exceeding  $nfl$ , where  $n$  is the number of vanes,  $f$  is the number of revolutions per second, and  $l$  is the length of the vane. Particulates having velocities up to the cutoff velocity  $V_c = nfl$  will be completely screened. Particulates with velocities  $v > V_c$  will be transmitted if they arrive within a time  $(l/V_c - l/v)$  of a vane passing the point of entry (Barr, 1969). Hence, the proportion of particulates with velocities  $v$  transmitted by the filter is  $1 - (V_c/v)$ . For a velocity filter containing 18 vanes whose length is 2 cm and having a revolution speed of 3300 rpm, the cutoff velocity is  $\approx 2 \times 10^3$  cm/s. With these operating parameters, the resultant particulate density has shown to be reduced by an order of magnitude (Venkatesan et al., 1992).

Lubben and coworkers (1985) used an electromagnetic shutter, synchronously triggered with the laser pulse through a delay circuit by a time  $\tau$ , to block the ejected matter with velocities less than  $d_{sh}/\tau$ , where  $d_{sh}$  is the distance between the target and the shutter. As shown in Figure 6.15, both the average particulate density and the maximum particulate size are significantly reduced as  $\tau$  decreases. For a typical  $d_{sh} = 3$  cm and a minimum delay time

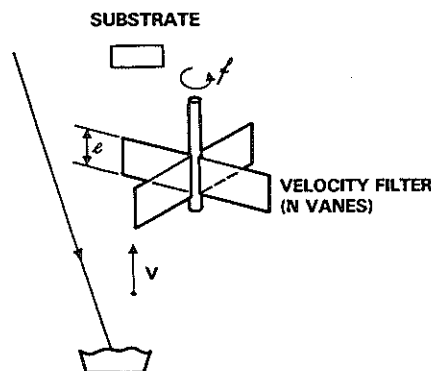


Figure 6.14. Schematic diagram of a velocity filter for eliminating particulates.

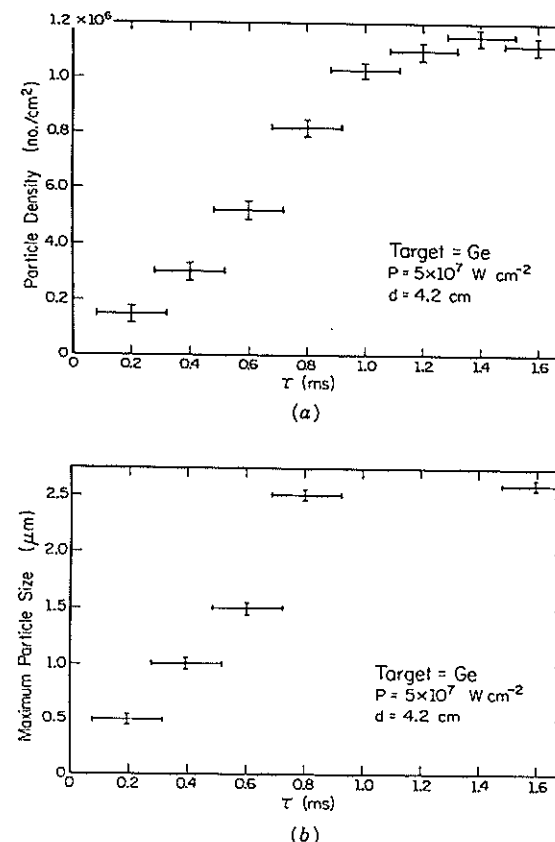


Figure 6.15. The (a) average particulate density and (b) maximum radius of particulates embedded in as-deposited Ge films plotted vs. the delay time  $\tau$ , following the laser pulse, at which the shutter blocked the ejected target material. The laser power density was  $5 \times 10^7$  W/cm $^2$  and the target-to-substrate distance was 4.2 cm. (From Lubben et al., 1985, p. 968.)

$\tau_{\min} = 0.2$  ms that the shutter is inserted, the fastest particulates resolvable and eliminated by Lubben et al. had velocities of  $\approx 1.5 \times 10^4$  cm/s.

Although the use of a vane velocity filter or an electromagnetic shutter results in a dramatic decrease in the particulate density, the throughput for molecular and atomic species is reduced as well. Besides, both methods add significant complexity to the instrumentation. Another mechanical approach is to spin the target at high velocity while focusing the laser beam on the off-center region of the target. Slower particulates are thrown out of their normal trajectories due to centrifugal force. Using a revolution speed of about

6000 rpm, a 50% reduction in particulate density at the substrate was demonstrated (Cheung and Sankur, 1988). Incidentally, spinning the target during laser ablation together with rastering the laser beam with a pair of optical scanners placed outside the process chamber are the two techniques used to avoid drilling a deeply cratered surface, which results in a very narrow angular distribution of ejected flux and effects the film uniformity.

#### 6.4.2 Deposition Geometry

A method based on gas-dynamic separation to eliminate particulate deposition on the substrate was demonstrated by Gaponov et al. (1981, 1982). The essential feature of this method is the creation of an artificial collision region having a high pressure, which can be accomplished by intersecting two beams of sufficient density of pulsed laser-ablated matter from independent sources, or by reflecting one beam from a hot shield at very high temperature. The intersection produces a high-pressure zone that redirects the light species toward the substrate, but has little effect on the trajectories of the heavier particulates. The deposition geometry that Gaponov et al. (1981, 1982), however, used to produce particulate-free film also add noteworthy complexity to the instrumentation.

Recently, Kennedy (1992) presented a new "off-axis" laser-ablation geometry to overcome the particulate problem. The chamber design is shown in Figure 6.16. In this geometry, the substrate is facing 180° to the initial plume direction. By contrast, 0° is the "normal" PLD geometry and 90° is the normal off-axis sputtering geometry. The advantage of indirect or off-axis deposition,

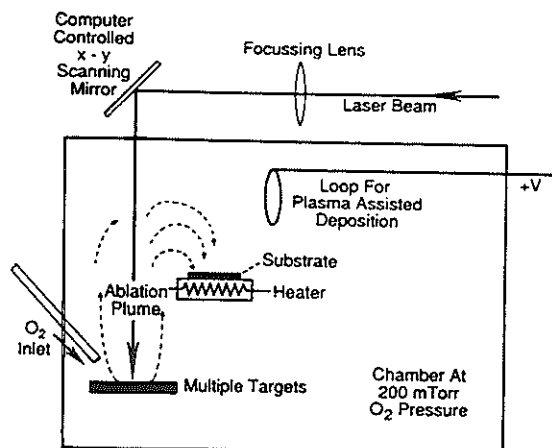


Figure 6.16. A novel "off-axis" PLD geometry used to produce particulate-free films. (From Kennedy, 1992, p. 223.)

as originally applied to sputtering, is due to the fact that while the particulates are constrained to travel along their initial trajectory directions, the light species (presumably ablated ions) undergo significant scattering; consequently their paths are randomized by the plume and ambient gas interactions. The deposition rate is reduced by only a factor of 3 when compared with direct deposition. An additional benefit of this technique includes the coating of irregularly shaped surfaces, since it is not a line-of-sight deposition process. It is also a convenient configuration because both the target and the substrate can be held in position by gravity without the necessity of clamping.

#### 6.4.3 Other Techniques

Lubben et al. (1985) have shown that the application of a negative bias significantly decreases the density of Ge particulates embedded in the resulting film. The particulate density for the -150-V biased sample was about five times less than in the unbiased case. One explanation, provided by Lubben et al. (1985), for the bias effect is that the particulates have a negative charge and are repelled by the biased substrate. The charge is most likely accumulated while the particulate coexists with the laser-induced plasma, charging up to the plasma potential.

By ablating a molten Ge target with a TEA-CO<sub>2</sub> laser, Cheung and Sankur have successfully obtained a particulate-free film (Cheung and Sankur, 1988). The source temperature is maintained above the melting point, yet still low enough so that no appreciable amount of thermal evaporation takes place. Since the target is liquid, the surface morphology is always smooth, and constant pulse-to-pulse ablation can be achieved without rastering the laser beam or rotating the target. However, this technique can only be used with materials that have very low vapor pressure at the melting point.

A reduction in particulate density and size was demonstrated by using a second laser to further heat and fragment the laser-ablated matter in the plume formed by the first laser (Koren et al., 1990). As mentioned in Section 6.3.2, perhaps this novel two-laser setup is not a practical solution to eliminate the particulates, because using only one excimer laser for the ablation deposition process by direct irradiation yields much smoother films than those produced by a two-laser deposition process.

### 6.5 POTENTIAL APPLICATIONS

Contrary to the thesis of the previous section, there are also advantageous aspects of incorporating the particulates generated from PLD. The principal closing comment is that a new and exciting field of research and development has been opened. Potential applications that utilize the novel structures exhibited by the materials synthesized by PLD are yet to be discovered.



Further development of a higher power laser along with progress in process control and scale-up would make this novel technique an indispensable method for fabrication of composites with fine dispersion and nanophases.

### 6.5.1 Composites

As described in Section 6.2.2, the particulates formed from the liquid droplets are deficient in the elements with higher vapor pressures. Because the compositions of the particulates can be very different from that of the codeposited film that is condensed from the vapor species, PLD provides a novel way of producing a particulate composite in one step. Realization of the opportunities to explore systems with unique combinations of physical properties of the particulate and the matrix is still in its infancy, however. Chen et al. (1992) have recently demonstrated one of the possible advantages of incorporating the particulates into the deposited films. The Nb–Al film prepared by laser ablation from a Nb<sub>3</sub>Al target in vacuum consists of a homogeneous matrix with uniformly distributed particulates. While the matrix has a composition of Nb<sub>7</sub>Al<sub>3</sub>, the particulates contain barely detectable amounts of Al. Figure 6.17 is a TEM micrograph that gives the best representation of the overall film. The merit of having a ductile Nb phase embedded in the intermetallic matrix is evident as the cracks generated during the TEM sample thinning process propagate in the brittle matrix and are arrested at the ductile inclusions.

Intermetallic matrix composites have been recognized for several years as a new class of materials that would offer low density and high-temperature strength from the intermetallic matrix, while the intervening ductile reinforcements provide low-temperature fracture toughness. Many techniques have

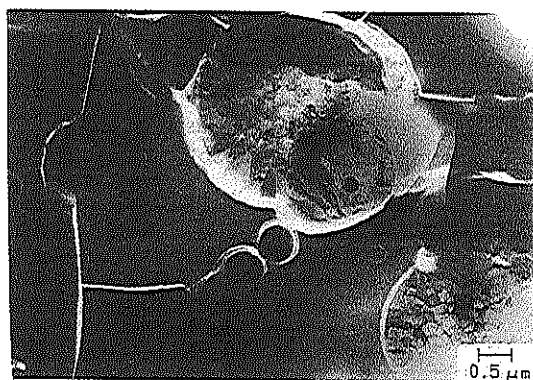


Figure 6.17. TEM micrograph of a Nb–Al film deposited at a fluence of 30 J/cm<sup>2</sup>. Notice that the cracks propagate in the brittle matrix but are arrested at the ductile particulates. (From Chen et al., 1992, p. 377.)

been developed to produce intermetallic matrix composites, of which several representative ones have been reviewed by Stoloff and Alman (1990). PLD provides a unique way to fabricate an in situ intermetallic matrix composite in one step. Above all, the PLD process produces a much finer dispersion than other techniques. The PLD technique also has the flexibility of varying the volume fraction of the reinforcing phase within the matrix phase. Once a volume fraction of particulates in the matrix is chosen, the process parameters can be adjusted, according to the basis provided in Section 6.3, so a proper particulate density, composition, and size distribution can be achieved. Certainly, the main limitation of this technique is the choice of materials.

### 6.5.2 Nanophases

The formation of nanoscale particulates from PLD in ambient gas resembles the gas-condensation process involving a thermal evaporation source (Kimoto et al., 1963; Granqvist and Buhrman, 1979; Tholen, 1979). Although the gas-condensation method for the production of nanoscale particles in a vapor has been studied for decades, only very recently, along with the development of in situ compacting and sintering of these nanoscale particles, has this method become the enabling technique for the synthesis of a new class of materials with engineered properties (Siegel and Hahn, 1987). The incentive of research in nanophases has been the discovery of novel and improved materials properties when their microstructure approaches nanoscale dimension (Gleiter, 1989). Of the possible advantages to the inert gas or reactive gas PLD process, the most important one may be the versatility of synthesizing a broad class of materials. Since no crucible is involved, higher purity end products may also be achieved by the PLD process.

To date, ultrafine powders of metals, alloys, ceramics, and semiconductors have all been reported by either inert gas or reactive gas PLD processes (Oesterreicher et al., 1978; Matsunawa et al., 1986; Fahrenholtz et al., 1991; Johnston et al., 1992; Koyama et al., 1992; and Sharma, 1992). For example, Koyama et al. (1992) have obtained nanocrystallites of CdTe and CdS with an average diameter from 4 nm to 10 nm. CdTe nanocrystallites dispersed in methanol showed a quantum size effect on the measurements of absorption properties. The photoluminescence spectrum of CdS also indicated that PLD-produced materials have improved purity and crystallinity.

## 6.6 SUMMARY

Although particulate generation by pulsed laser ablation is of great concern in the deposition of thin films, especially in high-performance optical and electronic applications, the quality of a variety of films obtainable by this technique has progressed rapidly. The particulate size and density strongly depend on the

deposition parameters, such as the laser wavelength, laser power, laser spot size, and ambient gas pressure. By proper choice of deposition parameters, particulate generation can be minimized. The velocity of PLD-generated particulates is an order of magnitude lower than that of atomic and molecular species. Therefore, further reduction of the particulates can be accomplished by various mechanical screening techniques based on velocity difference. Other techniques, such as the use of an off-axis deposition geometry and substrate bias, have also been used to decrease the density of particulates embedded in the resulting film. On the other hand, by incorporation of the particulates into the films, PLD can produce a particulate composite in one step, since the chemistry of the particulate is often different from that of the underlying film. Novel applications that utilize this composition difference together with the characteristic fine size of particulates are yet to be discovered.

## ACKNOWLEDGMENTS

I would like to thank Dr. K. H. Chen, Dr. E. Hall, Prof. H. Lipsitt, and Dr. A. Taub for many valuable discussions. In particular, I am grateful to Dr. A. Taub for his critical feedback on this manuscript.

## REFERENCES

- Arrowsmith, P., and S. K. Hughes (1988), *Appl. Spectrosc.* **7**, 1232.
- Ashby, C., et al., eds. (1992), *Mater. Res. Soc. Symp. Proc.* **236**, 429.
- Barr, W. P. (1969), *J. Phys. E: J. Sci. Instrum.* **2**(2), 1112.
- Blank, D. H. A., R. P. J. IJsselstein, P. G. Out, H. J. H. Kuiper, J. Floksura, and H. Rogalla (1992), *Mater. Sci. Eng.* **B13**, 67.
- Chan, C. R. and J. Mazumder (1987) *J. Appl. Phys.* **52**, 4579.
- Cheenne, A., J. Perriere, F. Kerherve, G. Hauchecorne, E. Fogarassy, and C. Fuchs (1990), *Mater. Res. Soc. Symp. Proc.* **191**, 229.
- Chen, L. C. (1992), unpublished results.
- Chen, L. C., and E. L. Hall (1993), *Mater. Res. Soc. Symp. Proc.* **285**, p. 519.
- Chen, L. C., E. L. Hall, and K. A. Lou (1992), *Mat. Res. Soc. Symp. Proc.* **273**, 377.
- Chenery, S., A. Hunt, and M. Thompson (1992), *J. Anal. At. Spectrosc.* **7**, 647.
- Cheung, J. T., and H. Sankur (1988), *CRC Crit. Rev. Solid State Mater. Sci.* **15**, 63.
- Dabby, F. W., and U. C. Paek (1972), *IEEE J. Quantum Electron.* **QE-8**, 106.
- Dubowski, J. J. (1986), *Proc. Soc. Photo-Opt. Instrum. Eng.* **668**, 97.
- Dupendant, H., J. P. Gavigan, D. Givord, A. Lienard, J. P. Rebouillat, and Y. Souche (1989), *Appl. Surf. Sci.* **43**, 369.
- Dushman, S. (1955), *Scientific Foundations of Vacuum Technique*, Wiley, New York.
- Dyer, P. E., R. D. Greenough, A. Issa, and P. H. Key (1989), *Appl. Surf. Sci.* **43**, 387.
- Dyer, P. E., A. Issa, and P. H. Key (1990), *Appl. Phys. Lett.* **57**, 186.
- Dyer, P. E., P. H. Key, and P. Monk (1992), *Appl. Surf. Sci.* **54**, 160.
- Fahrenholtz, W. G., S. R. Foltyn, K. C. Ott, and M. Chadwick (1991), *Mater. Res. Soc. Symp. Proc.* **201**, 489.
- Gagliano, F. P., and U. C. Paek (1974), *Appl. Opt.* **13**, 274.
- Gaponov, S. V., A. A. Gudkov, B. M. Luskin, V. I. Luchin, and N. N. Salashchenko (1981), *Sov. Phys. Tech. Phys.* **26**, 598.
- Gaponov, S. V., A. A. Gudkov, and A. A. Fraerman (1982), *Sov. Phys. Tech. Phys.* **27**, 1130.
- Gavigan, J. P. (1991), *NATO ASI B259*, 81.
- Geohegan, D. B. (1993), *Mater. Res. Soc. Symp. Proc.* **285**, 27.
- German, R. M. (1984), *Powder Metallurgy Science*, Metal Powder Industries Federation, Princeton, N.J., p. 86.
- Gleiter, H. (1989), *Prog. Mater. Sci.* **33**, 223.
- Granqvist, C. G., and R. A. Buhrman (1976), *J. Appl. Phys.* **47**, 2200.
- Greer, J. A., and H. J. Van Hook (1990a), *Mater. Res. Soc. Symp. Proc.* **169**, 463.
- Greer, J. A., and H. J. Van Hook (1990b), *Mater. Res. Soc. Symp. Proc.* **191**, 171.
- Hagar, J. W. (1989), *Anal. Chem.* **61**, 1243.
- IJsselstein, R. P. J., D. H. A. Blank, P. G. Out, F. J. G. Roesthuis, J. Flokstra, and H. Rogalla (1992), in *High Tc Superconductor Thin Films*, (L. Corraera, ed.), Elsevier, Amsterdam, p. 251.
- Johnston, G. P., W. Fahrenholtz, D. M. Smith, R. Muenchausen, and S. Foltyn (1992), presented in MRS 92 spring meeting.
- Kautek, W., B. Roas, and L. Schultz (1990), *Thin Solid Films* **191**, 317.
- Kennedy, R. J. (1992), *Thin Solid Films* **214**, 223.
- Kimoto, K., Y. Kamiya, M. Nonoyama, and R. Uyeda (1963), *Jpn. J. Appl. Phys.* **2**, 702.
- Koren, G., R. J. Baseman, A. Gupta, M. I. Lutwyche, and R. B. Laibowitz (1989), *Appl. Phys. Lett.* **55**, 2450.
- Koren, G., R. J. Baseman, A. Gupta, M. I. Lutwyche, and R. B. Laibowitz (1990), *Appl. Phys. Lett.* **56**, 2144.
- Koyama, T., S. Ohtsuka, H. Nagata, and S. Tanaka (1992), *J. Cryst. Growth* **117**, 156.
- Leuchtnner, R. E., D. B. Chrisey, and J. S. Horwitz (1992), *SPIE 1835 Excimer Lasers*, 31.
- Lowndes, D. H., D. P. Norton, J. W. McCamy, R. Feenstra, J. D. Budai, D. K. Christen, and D. B. Poker (1990), *Mater. Res. Soc. Symp. Proc.* **169**, 431.
- Lubben, D., S. A. Barnett, K. Suzuki, S. Gorbalkin, and J. E. Greene (1985), *J. Vac. Sci. Technol.* **B3**, 968.
- Matsunawa, A., S. Katayama, A. Susuki, and T. Ariyasu (1986), *Trans. J. Welding Res. Inc.* **15**, 61.
- Misra, D. S., and S. B. Palmer (1991), *Physica C* **176**, 43.
- Mitchell, J. G., and J. Sneddon (1987), *Appl. Spectrosc.* **41**, 41.
- Murakami, K. (1992), in *Laser Ablation of Electronic Materials: Basic Mechanisms and Applications* (E. Fogarassy and S. Lazare, eds.), North Holland, Amsterdam, p. 125.
- Nachtrieb, N. H. (1972), in *Liquid Metals*, (S. Z. Beer, ed.), Marcel Dekker, New York, p. 507.

- Nishikawa, Y., K. Tanaka, and Y. Yoshida (1991), *Nippon Kinzoku Kaishi* 55, 581.
- Nishikawa, Y., K. Tanaka, and Y. Yoshida (1992), *Jpn. Inst. Metals* 56(4), 430.
- Ready, J. F. (1963), *Appl. Phys. Letters* 3, 11.
- Rohlfing, E. A. (1988), *J. Chem. Phys.* 89, 6103.
- Oesterreicher, H., H. Bittner, and B. Kothari (1978), *J. Solid State Chem.* 26, 97.
- Saenger, K. L. (1992), in *Processing of Advanced Materials*, 2, in press.
- Schwarz, H., and H. A. Tourtellotte (1969), *J. Vac. Sci. Technol.* 6, 3763.
- Sharma, A. (1992), *Phys. Rev. A* 45, 4184.
- Siegel, R. W., and H. Hahn (1987), in *Current Trends in the Physics of Materials*, (M. Yussouff, ed.), World Scientific, Singapore, p. 403.
- Smith, G. A., L. C. Chen, and M. C. Chuang (1992), *Mater. Res. Soc. Symp. Proc.* 235, 843.
- Stoloff, N. S., and D. E. Alman (1990), *Mater. Res. Soc. Symp. Proc.* 194, 31.
- Tholen, A. R. (1979), *Acta Metall.* 27, 1765.
- Thompson, M., S. Chenery, and L. Brett (1989), *J. Anal. At. Spectrosc.* 4, 11.
- Thompson, M., S. Chenery, and L. Brett (1990), *J. Anal. At. Spectrosc.* 5, 49.
- Venkatesan, T., X. D. Wu, R. Muenchausen, and A. Pique (1992), *MRS Bull.* XVII(2), 54 (and the reference therein, in particular, reference number 14).

## CHAPTER 7

# ANGULAR DISTRIBUTION OF ABLATED MATERIAL

KATHERINE L. SAENGER

IBM Research Division  
T. J. Watson Research Center  
Yorktown Heights, New York

## 7.1 INTRODUCTION

Pulsed laser deposition (PLD) is now increasingly being used to prepare a wide variety of materials in thin-film form. In the most basic configuration of PLD, the flux of the material to be deposited is generated by irradiating an appropriate target with a high-intensity beam of pulsed laser light, and a film is grown by collecting this flux on a nearby substrate. The depositing flux is frequently modified and/or supplemented by the presence of a background gas and/or plasma. This chapter deals with the angular distribution of this flux, and the resulting angular profiles of film thickness and composition. These topics are of both fundamental and practical importance, due to their relevance to process dynamics and film uniformity.

Subtopics to be covered in this chapter include methods of measurement, experimental findings, and modeling. Of particular interest are the plume direction and plume angular spread, as well as the dependence of these features on the various laser parameters (wavelength, fluence, and pulse length), system geometry (laser spot dimensions, and target-substrate distance and orientation), target parameters (surface topography and material), and ambient (vacuum or some pressure of background gas). Numerous studies have shown that the angular distribution of the laser-generated flux is often (but not always) much more strongly forward peaked than the flux obtainable from small-area effusive sources operating under collisionless conditions. This forward peaking phenomenon for depositions in vacuum is now generally agreed to arise from collisions of the plume species among themselves. In the presence of a background gas, additional scattering effects must be considered, as well as the possibility of plume confinement. However, even for the basic case of vacuum deposition, many of the factors affecting plume angular distribution are only qualitatively understood.

## 7.2 MEASUREMENT METHODS

Nearly all methods of angular distribution measurement can be classified as either "film-based" or "probe-based." Probe-based methods typically measure the source angular distribution directly, with a scanned, small-area detector (such as an ion probe or mass-sensitive detector). Film-based methods typically measure the deposited film thickness profile; such measurements are extremely simple and among the most widely used.

### 7.2.1 General Considerations

Two angular distributions associated with PLD in vacuum are often referred to interchangeably: the source angular distribution and the film thickness distribution. We denote the source angular distribution as  $f(\theta)$ , where  $\theta$  is the polar angle (of ejection) measured from the target-surface normal,  $\hat{z}$ . Assuming unit sticking probability, the relationship between  $f(\theta)$  and the film thickness distribution depends on the experimental geometry. In the case of a hemispherical substrate having a radius of curvature equal to the target-substrate distance  $h$ , a point source having a  $\cos^p\theta$  source angular distribution would remain unchanged as a  $\cos^p\theta$  thickness profile, since the flux emitted into each solid angle element  $d\Omega$  would be deposited on identically sized substrate area elements  $dA = h^2 d\Omega$ . In a more common configuration (Figure 7.1), the laser-generated flux is collected on a planar substrate positioned parallel to the target. For this case, a point source having an angular distribution of the form  $f(\theta) = \cos^p\theta$  would yield a film thickness profile of the form  $D(\theta) = \cos^{p+3}\theta$ , since the flux emitted into a solid angle element  $d\Omega$  would be deposited on a substrate-area element  $dA = h^2 d\Omega / \cos^3\theta$  (see Section 7.4.1 for details). A source distribution of the form  $f(\theta) = \cos\theta$  would thus be expected to yield a  $D(\theta) = \cos^4\theta$  film thickness profile.

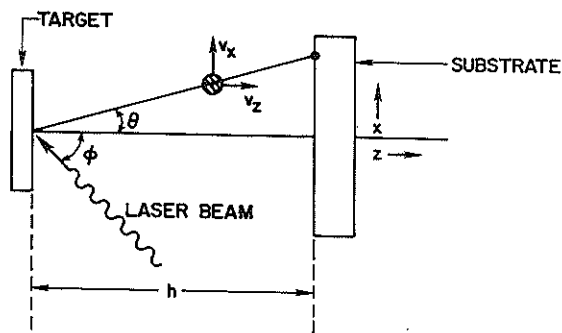


Figure 7.1. Deposition geometry.

Angular distributions may also be described in terms of the "half-angle" of the distribution,  $\theta_{1/2}$ , which is defined as the value of  $\theta$  at which the flux or film thickness is equal to half its maximum. Given a distribution of the form  $\cos^p\theta$ ,  $\theta_{1/2} = \cos^{-1}[(1/2)^{1/p}]$ . The source and film thickness distributions will have different values of  $\theta_{1/2}$  if  $f(\theta)$  and  $D(\theta)$  have different functional forms. For example, if  $f(\theta) = \cos\theta$  and  $D(\theta) = \cos^4\theta$ ,  $\theta_{1/2}$  will be  $60^\circ$  and  $32.8^\circ$  for the source and film thickness distributions, respectively.

### 7.2.2 Film-Based Methods

Film-based methods for determining angular distribution use a substrate as a time-integrated flux detector. The detector is stationary, and the flux into the entire angular range of interest is collected simultaneously. The method is efficient (since no flux is "wasted"), and relatively immune to artifacts from long-term drifts in overall signal magnitude (since the flux at all angles is affected equally).

Film-based methods for determining the flux angular distribution are based on the two major assumptions: (1) that the particle sticking coefficient is unity, and (2) that there is no resputtering of the film by the incident particle flux. The validity of these assumptions has been examined by Akhsakhalyan et al. (1988), who suggest that the flux reflected away from the substrate may scatter with the incoming flux and perturb the angular distribution if either of these assumptions is violated.

Typically, the thickness profile is determined *ex situ*, after deposition, from a measurement of the thickness of the deposited film as a function of radial position ( $r$ ) from the deposition axis. Since the film thickness profile is relatively permanent, measurements can be separated in time from the actual deposition. A number of methods have been used to determine the thickness profile of films deposited by PLD; most require smooth (polished) substrates. The most common method uses a stylus profilometer to determine the film's physical thickness at step edges on the sample (created either by masking the substrate during deposition, or by a selective-area postdeposition etch). Optical methods utilized for film thickness profile determinations include ellipsometry (Hansen and Robitaille, 1987), interferometry (Hansen and Robitaille, 1987; Afonso et al., 1990), and optical density (Afonso et al., 1990). Other methods (usually utilized to obtain relative thicknesses or composition ratios) include Rutherford backscattering spectrometry (RBS) (Perez Casero et al., 1992) and energy dispersive X-ray (EDX) microanalysis (Hau et al., 1992).

Areal densities of macroscopic particulates are typically determined photographically (from optical or scanning electron micrographs) by counting the particles ("boulders") per unit area. As a practical matter, high particulate densities can lead to experimental difficulties in estimating film thickness. Care must be taken to ensure that the measured thickness reflects that of the *film*, and not that of the *boulder*.

### 7.2.3 Probe-Based Methods

A large number of probes have been applied to plume diagnostics; discussed here are some that have been utilized for angle-resolved measurements. Examples in this category include angle-resolved beam current measurements, both time-integrated (Al: Friichtenicht et al., 1976; Y-Ba-Cu-O: Chrisey et al., 1990) and time-resolved (Cu: Kools et al., 1991), and various mass-resolved time-of-flight measurements (CdS: Namiki et al., 1986; polyimide: Ulmer et al., 1990; graphite: Schenck et al., 1989, and Murray et al., 1992).

Several different experimental approaches have been employed to sample the flux emitted into different angles. For example, one can measure the total ion current (from a fixed-position target) as a function of the aperture size of an on-axis detector (Chrisey et al., 1990). Alternatively, the particle flux from a fixed-position target can be measured with multiple detectors located at different positions (Friichtenicht et al., 1976), or a single detector that is scanned over two or more angles (Schenck et al., 1989; Murray et al., 1992). A less satisfactory arrangement utilizes a fixed-position detector whose sampling angle (with respect to the target surface normal) is varied by simultaneously varying both the target tilt and the laser angle of incidence (Namiki et al., 1986). Measurements of the latter type are inherently suspect, since laser-plume interactions may cause the plume energy and composition to vary with the laser angle of incidence on the target (Pappas et al., 1992).

## 7.3 SURVEY OF EXPERIMENTAL FINDINGS

This section covers experimental findings on the plume direction and plume angular spread produced by pulsed laser irradiation of targets, with emphasis on results obtained in vacuum. The first section (7.3.1) deals with the plume orientation. Sections 7.3.2 through 7.3.5 will examine the dependence of the plume angular distribution on target surface topography, target-substrate distance, laser spot dimensions, and laser parameters (wavelength, fluence, and pulse length). Section 7.3.6 examines angular distribution data obtained in the presence of an ambient process gas, and Section 7.3.7 examines experimental results on the angular dependence of film composition uniformity. Measurements relating to the angular distribution of the plume particle speed and mass distributions were briefly discussed in Section 7.2.3.

A number of experimental angular distribution results are summarized in Tables 7.1 and 7.2. Table 7.1 summarizes source angular distribution results (obtained with "film-based" measurement techniques) for a number of materials ablated under "vacuum conditions" (i.e., where scattering effects with a background gas can be neglected). To aid possible correlation of angular distributions with collisional processes in the plume, estimates of target etch depths per pulse are given, where possible. Table 7.2 presents angular distribution data obtained in the presence of a scattering gas. These results are detailed

in Sections 7.3.1 through 7.3.6. Most explanations and/or modeling of these results are deferred to Section 7.4.

### 7.3.1 Plume Orientation

The film-based measurements of Table 7.1 indicate that the axis of the laser-generated plume is always oriented along the target surface normal for normal angles of laser incidence (Davanloo et al., 1992; Fogarassy et al., 1989; Lubben et al., 1985), and frequently oriented along the target normal even for nonnormal angles of laser incidence (Hansen and Robitaille, 1987; Muenchausen et al. 1990; Neifeld et al., 1988; Venkatesan et al., 1988). This can be rationalized from the viewpoint that the laser-heated surface of a perfectly planar, isotropic target retains no "memory" of the direction from which the absorbed photons came. This view is not unreasonable for laser pulses that are over before any plume structure can develop. In practice, however, laser-plume interactions do occur, and real targets are usually not perfectly planar.

Plume tilting, when it occurs, has only been observed for nonnormal angles of laser incidence (i.e., for  $\phi \neq 0^\circ$ ). Film-based measurements (again, see Table 7.1) usually (but not always) indicate a direction of plume tilt toward the direction of the incident laser beam. Plume tilting toward the incident laser beam has been observed for carbon depositions (Davanloo et al., 1992) and for depositions of the high-temperature superconductor Y-Ba-Cu-O (Greer and Van Hook, 1990). Similar Y-Ba-Cu-O tilting has also been reported by Lowndes et al. (1990) and by Foote et al. (1992) for comparable deposition conditions. While one might expect plume-tilting effects to be seen if material removal is from an angled crater, very strong plume tilting ( $\theta_{\max} \sim \phi/2$  toward the incident laser beam) has been observed with high-fluence Nd-YAG laser irradiation of graphite targets even when cratering has been ruled out (Davanloo et al., 1992). The plume tilting ( $\theta_{\max} = 5^\circ$  to  $15^\circ$  toward the incident beam) observed for ArF-excimer-laser-deposited Y-Ba-Cu-O and Bi-Sr-Ca-Cu-O was attributed to vaporization from "pseudocraters" formed in the target surfaces (Fuchs and Fogarassy, 1990). These pseudocraters consist of mechanically deformed liquid depressions oriented parallel to the incident laser beam, and are generated during each laser pulse. One might also expect the presence of columnar structures or other surface asperities to give rise to a skewed plume direction, due to nonuniform laser absorption and shadowing. Such effects (leading to a  $\theta_{\max}$  of  $5^\circ$  for  $\phi = 45^\circ$ ) were observed for KrF-excimer-laser-irradiated Y-Ba-Cu-O targets (Pinto et al., 1992). This effect was documented in more detail for doubled-Nd-YAG laser-irradiated Bi-Sr-Ca-Cu-O targets. In this work the increase in  $\theta_{\max}$  was monitored as a function of time, and shown to change more slowly for denser targets (Perez Casero et al., 1992). However, no evidence was found for an off-normal plume direction for XeCl-excimer-laser-irradiated ( $\phi = 45^\circ$ ) Y-Ba-Cu-O targets, despite the development of columnar structures oriented along the laser beam direction (Foltyn et al., 1991).

TABLE 7.1 Summary of Source Angular Distribution Results from "Film-Based" Measurements of PLD in Vacuum

Material	$\lambda$ , nm	$\tau$	$F$ (J/cm <sup>2</sup> )	$\phi/\theta_{\max}$	$T/p^a$	Spot Dimension	$f(\theta)^b$	Reference/Comment
Au	308	20 ns	14	45°/0°	620 Å	~360 $\mu$ m diam	$\cos^{6.3}\theta$	Gorbunov and Konov, 1989
B	1064	20 ns	30	20°/0°	?	1.4 mm diam	$\cos^{3.7}\theta$	Akhsakhalan et al, 1988
Bi	1064	20 ns	30	20°/0°	?	1.4 mm diam	$\cos^{5.9}\theta$	Akhsakhalan et al, 1988
BiSrCaCuO	193	20 ns	0.6-2	0°/0°	?	?	$\cos\theta + \cos^{2.1}\theta$	Fogarassy et al, 1989
C	308	20 ns	6	45°/0°	530 Å	~360 $\mu$ m diam	$\cos^{5.9}\theta$	Gorbunov and Konov, 1989
	308	20 ns	14	45°/0°	0.2-1 $\mu$ m	~360 $\mu$ m diam	$\cos^{3.9}\theta$	near ( $h = 11.5$ nm)
	308	20 ns	14	45°/0°	0.2-1 $\mu$ m	~360 $\mu$ m diam	$\cos^{7.8}\theta$	far ( $h \geq 25$ nm)
C	1064	20 ns	30	20°/0°	?	1.4 mm diam	$\cos^{2.3}\theta$	Akhsakhalan et al, 1988
C	1064	8 ns	800	0°/0°	?	~100 $\mu$ m diam <sup>c</sup>	$\cos^4\theta$	Davanloo et al, 1992
	1064	8 ns	800	25°/13°	?	~100 $\mu$ m diam <sup>c</sup>	$\cos^4\theta$	
	1064	8 ns	800	50°/25°	?	~100 $\mu$ m diam <sup>c</sup>	$\cos^4\theta$	
Ca <sub>10</sub> (PO <sub>4</sub> ) <sub>6</sub> (OH) <sub>2</sub>	694	25 ns	0.2	0°/0°	13 $\mu$ m	500 $\mu$ m diam	$\cos\theta + \cos^3\theta$	Baeri et al, 1992
Ge	193	12 ns	~11 $\pm$ 5	45°/0°	0.4 $\mu$ m?	0.4 $\times$ 0.9 mm <sup>2</sup> ( $\hat{x} \times \hat{y}$ )?	$\hat{x}: \cos^5\theta + \cos^{2.7}\theta$ $\hat{y}: \cos^{1.1-1.3}\theta$	Afonso et al, 1990 near ( $h = 28$ nm) far ( $h \geq 36$ nm)
Ge	248	15 ns	0.75	0°/0°	50 Å	2 mm diam	$\cos^{4.6}\theta$	Lubben et al, 1985
Ge	1064	20 ns	30	20°/0°	?	1.4 mm diam	$\cos^{5.6}\theta$	Akhsakhalan et al, 1988
Mg	1064	20 ns	30	20°/0°	?	1.4 mm diam	$\cos^{1.7}\theta$	Akhsakhalan et al, 1988
Mn	1064	20 ns	30	20°/0°	?	1.4 mm diam	$\cos^{8.2}\theta$	Akhsakhalan et al, 1988
Ni	1064	20 ns	30	20°/0°	?	1.4 mm diam	$\cos^{7.4}\theta$	Akhsakhalan et al, 1988
Pb	1064	20 ns	30	20°/0°	?	~0.2-2 mm diam	$\cos^{3.6}\theta$ to $\cos^{9.6}\theta$	Akhsakhalan et al, 1988
PbZr <sub>0.48</sub> Ti <sub>0.52</sub> O <sub>3</sub>	308	?	0.2-5	45°/~0°	?	?	$\cos^{-7}\theta + \cos^{4-2.6}\theta$	Hau et al, 1992
Polymer	192	25 ns	?	0°/0°	900 Å	3 mm diam	$\cos^{2.0}\theta$	Lazare and Granier, 1990 (polyphenylquinoxaline)
	248	25 ns	0.063	0°/0°	~200 Å	3 mm diam	$\cos^{2.0}\theta$	
	248	25 ns	0.19-0.45	0°/0°	0.1-0.23 $\mu$ m	3 mm diam	$\cos^7\theta$ to $\cos^{11}\theta$	
	351	25 ns	?	0°/0°	900 Å	3 mm diam	$\cos^{3.2}\theta$	
Re	1064	20 ns	30	20°/0°	?	1.4 mm diam	$\cos^{18-7}\theta$	Akhsakhalan et al, 1988
Sb	1064	20 ns	30	20°/0°	?	1.4 mm diam	$\cos^{4.3}\theta$	Akhsakhalan et al, 1988
Se	266	5 ns	0.05	20°/0°	~300 Å	Ring (6/3 mm od/id)	$\sim \cos^{3.0}\theta$	Hansen and Robitaille, 1987
	532	5 ns	0.1	20°/0°	~400 Å	Ring	$\sim \cos^{3.0}\theta$	
	1064	5 ns	0.15-0.25	20°/0°	1700-1900 Å	Ring	$\sim \cos\theta$	
	1064	200 $\mu$ s	0.25-0.4	20°/0°	230-1100 Å	Ring	$\sim \cos\theta$	
SmBa <sub>2</sub> Cu <sub>3</sub> O <sub>7</sub>	308	20 ns	2-14.5	15°/0°	$\leq 0.1$ $\mu$ m	~3.5-1.3 mm diam <sup>c</sup>	$\cos^7\theta$	Neifeld et al, 1988
	308	20 ns	$> 14.5$	15°/0°	$\geq 0.1$ $\mu$ m	$\leq 1.3$ mm diam <sup>c</sup>	$\cos^{5.7}\theta$	
Sn	1064	20 ns	30	20°/0°	?	1.4 mm diam	$\cos^{5.0}\theta$	Akhsakhalan et al, 1988
Ti	1064	20 ns	30	20°/0°	?	1.4 mm diam	$\cos^{5.7}\theta$	Akhsakhalan et al, 1988
TiN	308	27 ns	5-8	40°/0°	?	0.7 mm diam	$\cos^6\theta$	Kools et al, 1992
W	1064	20 ns	30	20°/0°	?	~0.2-2 mm diam	$\cos^{5.6}\theta$ to $\cos^{2.6}\theta$	Akhsakhalan et al, 1988
Y-Ba-Cu-O	193	20 ns	2	0°/0°	?	?	$\cos\theta + \cos^{2.1}\theta$	Fogarassy et al, 1989
Y-Ba-Cu-O	248	30 ns	1.5	45°/0°	~260 Å	2 $\times$ 3 mm <sup>2</sup>	$\cos\theta + \cos^{2.1}\theta$	Venkatesan et al, 1988
Y-Ba-Cu-O	248	20 ns	1	60°/5°	?	1 $\times$ 3 mm <sup>2</sup>	$\cos^{2.3}\theta$	Greer and Van Hook, 1990
Y-Ba-Cu-O	248	29 ns	1.1	55°/0-5°	?	1.7 $\times$ 5.1 mm <sup>2</sup> ( $\hat{x} \times \hat{y}$ )	$\hat{y}: \cos^{4.0-7.0}\theta$	Footo et al, 1992
Y-Ba-Cu-O	308	20 ns	1-7	45°/0°	~200 Å	0.3 $\times$ 1.5 mm <sup>2</sup> ( $\hat{x} \times \hat{y}$ )	$\hat{x}: \cos^{1.5+0.5}\theta$	Muenchausen et al, 1990
							$\hat{y}: \cos^{3.5+0.5}\theta$	(10 <sup>-5</sup> to 0.1 torr)
Y-Ba-Cu-O	308	20 ns	4-15	45°/0°	?	0.8 $\times$ 1.9 mm <sup>2</sup> ( $\hat{x} \times \hat{y}$ )	$\hat{x}: \cos^6\theta$	Foltyn, 1992
							$\hat{y}: \cos^{1.2}\theta$	
Y-Ba-Cu-O	308	20 ns	4	45°/0°	?	1.2 $\times$ 4.9 mm <sup>2</sup> ( $\hat{x} \times \hat{y}$ )	$\hat{x}: \cos^{1.2}\theta$	
							$\hat{y}: \cos^{3.0}\theta$	
Y-Ba-Cu-O	1064	90 ns	20	40°/0°	0.9 $\mu$ m	~0.35 mm diam	$\cos^3\theta$	Marine et al, 1989
Y-Ba-Cu-O	1064	0.5 ms	1500	45°/0°?	375 $\mu$ m	4.5 mm diam	$\cos\theta$	Balooch et al, 1989

Note: These results as a function of laser wavelength ( $\lambda$ ), pulse duration ( $\tau$ ), laser angle of incidence ( $\phi$ ), and spot dimension. The deposition geometry is shown in Figure 7-1;  $\theta_{\max}$  refers to the angle at which the laser-generated flux is a maximum.

<sup>a</sup> $T/p$ : Thickness of target etched per pulse. If not provided, this is estimated as the film volume deposited per pulse divided by the irradiated spot area. The film volume deposited per pulse is computed by integrating the film thickness distribution over the entire substrate plane and dividing by the number of laser pulses. For a film thickness distribution (on a flat substrate) of the form  $D(\theta) = A \cos^{p+3}\theta$  (corresponding to a source distribution of the form  $f(\theta) \propto \cos^p\theta$ ) the film volume is  $\pi R^2 h^2 (p+1)$ , where  $h$  is the target-substrate distance.

<sup>b</sup>Source Angular Distribution. Note: (1) if only the film thickness distribution is specified, a source angular distribution  $f(\theta) = \cos^p\theta$  is assumed for a film thickness distribution (on a flat substrate) of  $D(\theta) = \cos^{p+3}\theta$ ; (2) if only the "half angle" ( $\theta_{1/2}$ ) of the film thickness distribution is specified, the exponent  $p$  is computed from  $p = [(\log_e 0.5)/(\log_e \cos \theta_{1/2})] - 3$ .

<sup>c</sup>Private communication with the authors.



TABLE 7.2 Summary of Angular Distribution Results for PLD in Gas Ambient

Material	$\lambda$ (nm)	$\tau$ (ns)	$F$ (J/cm <sup>2</sup> )	$\phi/\theta_{\max}$	$h$ (mm)	Gas	$P$ (mT)	Spot Size	$D(\theta)^a$	Type	Reference
C	308	20	14	45°/0°	25	Vac	0	~360 $\mu$ m diam	$\cos^{10.8\theta}$	Film	Gorbanov and Konov 1989
	308	20	14	45°/0°	25	"Air"	75	~360 $\mu$ m diam	$\cos^{5.6\theta}$	Film	
Y-Ba-Cu-O	248	25	3	45°/0°	45	O <sub>2</sub>	200	0.8 $\times$ 3 mm <sup>2</sup> ( $x \times y$ )	$\hat{y}: \cos^{8.8\theta}$	Film	Pinto et al., 1992
	248	25	3	45°/0°	45	O <sub>2</sub>	200	1 $\times$ 3.5 mm <sup>2</sup> ( $x \times y$ )	$\hat{y}: \cos^{9.3\theta}$	Film	
	248	25	3	45°/0°	45	O <sub>2</sub>	200	1.2 $\times$ 3.5 mm <sup>2</sup> ( $x \times y$ )	$\hat{y}: \cos^{10.1\theta}$	Film	
Y-Ba-Cu-O	248	29	1.1	55°/0°	90	Vac	0	1.7 $\times$ 5.1 mm <sup>2</sup> ( $x \times y$ )	$\hat{y}: \cos^{10-70\theta}$	Film	Foote et al., 1992
	248	29	1.1	55°/0°	90	O <sub>2</sub>	20	1.7 $\times$ 5.1 mm <sup>2</sup> ( $x \times y$ )	$\hat{y}: \cos^{8-14\theta}$	Film	
Y-Ba-Cu-O	248	25	2	45 $\pm$ 17°/0°	30	Vac	0	$\lesssim$ 4 mm diam?	$\cos^{4.6\theta}$	Ion probe	Chrissey et al., 1990
	248	25	2	45 $\pm$ 17°/0°	30	O <sub>2</sub>	100	$\lesssim$ 4 mm diam?	$\cos^{33.6\theta}$	Ion probe	
Y-Ba-Cu-O	308	20	1-7	45°/0°	30	O <sub>2</sub>	0-100	0.3 $\times$ 1.5 mm <sup>2</sup> ( $x \times y$ )	$\hat{x}: \cos^{1.5 \pm 0.5\theta}$	Film	Muenchausen et al., 1990
	308	20	4	45°/0°	80	Vac	0	1.2 $\times$ 4.9 mm <sup>2</sup> ( $x \times y$ )	$\hat{x}: \cos^{3.5 \pm 0.5\theta}$	Film	Folyn, 1992
	308	20	4	45°/0°	80	O <sub>2</sub>	100	1.2 $\times$ 9 mm <sup>2</sup> ( $x \times y$ )	$\hat{y}: \cos^{4.5\theta}$		
	308	20	4	45°/0°	80	O <sub>2</sub>	200	1.2 $\times$ 4.9 mm <sup>2</sup> ( $x \times y$ )	$\hat{x}: \cos^{1.7\theta}$	Film	
	308	20	4	45°/0°	80	O <sub>2</sub>	200	1.2 $\times$ 4.9 mm <sup>2</sup> ( $x \times y$ )	$\hat{y}: \cos^{2.2\theta}$	Film	
	308	20	4	45°/0°	80	O <sub>2</sub>	200	1.2 $\times$ 4.9 mm <sup>2</sup> ( $x \times y$ )	$\hat{x}: \cos^{1.7\theta}$	Film	
	308	20	4	45°/0°	80	O <sub>2</sub>	200	1.2 $\times$ 4.9 mm <sup>2</sup> ( $x \times y$ )	$\hat{y}: \cos^{2.2\theta}$	Film	

Note: Comparisons to vacuum are given when available; "type" refers to the type of measurement.

<sup>a</sup>Angular Distribution of film thickness on a substrate oriented parallel to the target (or, in the case of the ion-probe measurements,  $\theta$ -dependence of the ion flux incident on the substrate plane). Note: if original data are not fit to the form  $D(\theta) = \cos^m \theta$ , the exponent  $m$  is computed from  $m = [(\log_{10} D(\theta)) / (\log_{10} \cos \theta)]$ , where  $\theta_{1/2}$  is the angle for which  $D(\theta_{1/2}) / D(0) = 1/2$ .

Examples of plume tilting away from the incident beam have been seen for very high fluence irradiation of Y-Ba-Cu-O targets with  $\phi = 30^\circ$  at both 248 and 1064 nm. With 1064-nm irradiation (with fluences of several hundred J/cm<sup>2</sup> in a  $\sim 0.15$  ms pulse train), plume tilting characterized by  $\theta_{\max} = -8^\circ$  to  $-25^\circ$  was observed, with the greater tilt for the off-stoichiometry (Y-enriched) target (Lynds et al., 1989). With 248-nm irradiation, minimal tilting was seen for a fluence of 0.78 J/cm<sup>2</sup>, but a tilt characterized by  $\theta_{\max} = -12^\circ$  was seen for a fluence of 120 J/cm<sup>2</sup> (Lynds et al., 1990). Plume tilting away from the incident laser beam has also been observed with long-pulse-length laser irradiation (Gapanov and Strikovskii, 1982).

As in the case of film-based measurements, probe-based measurements show no plume tilting for near-normal angles of laser incidence. Examples include measurements on Ge targets (Lubben et al., 1985) and measurements on Al targets (Friichtenicht et al., 1976). At nonnormal angles of laser incidence, strong tilting of the ion flux has been observed. For example, ion fluxes having  $\theta_{\max} \sim 40^\circ$  have been observed for Al targets irradiated at  $\phi = 45^\circ$  with a Q-switched ruby laser at fluences of  $\sim 20$  and 200 J/cm<sup>2</sup> (Friichtenicht et al., 1976).

Optical emission measurements of Y-Ba-Cu-O ablation with a streak camera (Eryu et al., 1989) have also indicated a tilting of the plume toward the laser beam, an observation attributed by the authors to the presence of large mass clusters. One might speculate that electron or atom emission from these clusters induced by absorption of laser photons might be expected to preferentially occur from their illuminated surfaces that face the direction of the incoming laser beam. It should be noted as a general point, however, that both optical and ion-probe measurements share a common drawback, namely that such measurements are not necessarily representative of the total flux, a large part of which may be neutral and/or nonluminous.

Plume tilting might also be expected to arise if the laser beam intensity profile on the target is asymmetric and/or nonuniform. Asymmetric target irradiance is obviously present for asymmetric spot shapes. Less obvious asymmetries in target irradiance may easily arise if the target plane intersects the laser beam over a region in which the laser beam diameter (and thus the degree of focus) is significantly changing. These effects will be most evident for short focal length lenses and highly oblique angles of laser incidence. Spatially nonuniform target irradiance even if symmetric, may also lead to plume tilting. For example, a "hot spot" at the center of the laser beam profile may introduce asymmetries in target irradiance due to the shadowing effects of the denser plasma above the corresponding hot spot on the target.

### 7.3.2 Angular Distribution: Influence on Target Topography

The shape of the angular distribution can be affected by target cratering. For example, thickness profiles of Y-Ba-Cu-O films produced with both rotating



and stationary targets under similar conditions indicated a 2-component distribution for both configurations [a  $\cos \theta$  component plus a more highly forward-directed one (Fogarassy et al., 1989)]. However, the relative intensity of the forward-directed component was markedly lower from the stationary target (in which a crater had been etched).

### 7.3.3 Angular Distribution: Influence of Target-Substrate Distance

Noninteracting particles emitted in vacuum from a small-area source are expected to have an angular distribution that does not change with distance from the source. Simple geometric arguments predict an inverse square relationship between the time-integrated flux per pulse of such a source and the source-substrate distance. With no collisions to disrupt the particle trajectories, the constant number of particles directed into a given angular range must be distributed over an area element whose dimensions increase in proportion  $h^2$ , where  $h$  is the target-substrate distance. This ideal case is well approximated when (1) the irradiated spot on the target is small compared to  $h$ , and (2) nearly all of the collisions among plume particles occur while the plume is small and close to the target. This simple analysis does not apply when the laser-generated flux is significantly perturbed by collisions with a background gas. In this case (treated in more detail in Section 7.3.6), the angular distribution is expected to broaden with increasing distance from the target.

Contrary to expectations, film-based measurements for depositions in vacuum suggest that the source angular distribution may change with distance from the source. As indicated in Table 7.1, these effects have been observed for carbon (Gorbunov and Konov, 1989) and germanium (Afonso et al., 1990). The carbon data suggested a broader angular distribution close to the target ( $f(\theta) = \cos^{3.9}\theta$  for  $h = 11.5$  mm) and an  $h$ -independent one at distances far from the target ( $f(\theta) = \cos^{7.8}\theta$  for  $h \geq 25$  mm). In addition, the thickness deposited per pulse followed an  $h^{-2}$  dependence only in the  $h \geq 25$ -mm regime where  $f(\theta)$  was independent of  $h$ ; at closer distances (e.g., at  $h = 11.5$  mm) the deposited thickness was much less than predicted by an  $h^{-2}$  dependence. These findings were attributed to scattering of the incident flux with particles reflected and/or resputtered from the substrate. These effects were judged to be significant only when the deposited film thickness per pulse exceeded  $\sim 1$  Å. However, this threshold rate was empirically determined only for carbon, and is likely to be lower for materials having higher ablation yields. For instance, distance-dependent results were found for Ge at deposition rates per pulse of only 0.3 Å (Afonso et al., 1990).

The possibility that a still-evolving angular distribution (due to intraplume collisions far from the target) might be responsible for these effects cannot be completely ruled out. However, the significant temperature dependence of  $D(\theta)$  for near-target carbon depositions (Scheibe et al., 1990) strongly supports the

argument that a distance-dependent  $D(\theta)$  is mainly due to substrate-induced perturbations of the intrinsic angular distribution.

### 7.3.4 Angular Distribution: Influence of Laser Spot Dimensions

The effect of the laser spot dimensions on the angular distribution of the vaporized material has been examined in several studies in which the laser spot size or shape was altered, keeping the *fluence* (e.g., J/cm<sup>2</sup>) over the spot area *fixed*. A striking and consistently observed finding (detailed below) is that the film thickness profiles become more peaked as the spot dimensions *increase* (providing the laser spot dimensions are much smaller than the target-substrate distance  $h$ ). This behavior contrasts with that of a small-area effusive source, which retains a  $\cos \theta$  angular distribution independent of source diameter ( $d$ ), providing  $d \ll h$ . It also contrasts with the behavior of a larger area effusive source, whose angular distribution can be reproduced by the superposition of several appropriately positioned small-area sources. With PLD, there is a clear nonequivalence between a single large spot and a small spot scanned over the same area (Muenchausen et al., 1990); the latter providing a much broader angular distribution than the former. Qualitatively, these effects stem from the fact that forward peaking increases with the number of intraplume collisions per particle, which increases roughly as the ratio of the initial plume dimensions (given by the spot size) to the particle's initial mean free path.

The influence of laser spot dimension is typically determined by either systematically varying the diameter of round spots (in which case the angular distribution is usually symmetric) or by using rectangular or oval spots (with measurements in the two directions defined by the spot's long and short axes). Measurements have been made for targets of Pb and W (Akhsakhalyan et al., 1988), Ge (Afonso et al., 1990), and the high-temperature superconductors (Muenchausen et al., 1990; Fuchs and Fogarassy, 1990; Cheenne et al., 1990; Foltyn, 1992). Measurements have been both qualitative and quantitative; quantitative measurements for Ge (Afonso et al., 1990), Pb and W (Akhsakhalyan et al., 1988), and Y-Ba-Cu-O (Muenchausen et al., 1990; Foltyn, 1992) are summarized in Table 7.1. For the case of Pb and W, angular distributions of  $\sim \cos^4 \theta$  were produced for spot diameters of  $\lesssim 200$  μm, but significantly narrower distributions ( $\sim \cos^{10} \theta$  and  $\sim \cos^{26} \theta$  for Pb and W, respectively) were found for larger diameter ( $\simeq 2$  mm) spots.

### 7.3.5 Angular Distribution: Influence of Laser Parameters

Laser fluence ( $F$ ), wavelength ( $\lambda$ ), and pulse length ( $\tau$ ) have all been investigated for their possible influence on the plume angular distribution. Few generalizations are possible; even laser fluence, the best studied of these parameters, has not been examined in detail for more than a few materials. In addition, interpretation is often complicated by the fact that variation of a

single parameter may change several aspects of the ablation process simultaneously. For instance, a change in laser wavelength (keeping all other laser parameters constant) may change both the initial density and energy of the plume, due to wavelength-dependent changes in the target or plume absorptivity. Alternatively, an increase in fluence might inadvertently increase the dimensions of the target area from which material is removed.

The effect of laser pulse length on the plume angular distribution is negligible for the case of Se (Hansen and Robitaille, 1987). For 1064-nm irradiation, approximately  $\cos \theta$  distributions were found for pulse lengths of both 5 ns and 200  $\mu$ s (for fluences of order 0.3 J/cm<sup>2</sup> and spot diameters of order 5 mm). However, laser pulse length does appear to have some effects on Y-Ba-Cu-O films, as measured by variations in the superconducting transition temperature ( $T_c$ ) with  $\theta$  for films produced by 1064-nm Nd-YAG laser irradiation at 4.5 J/cm<sup>2</sup> with pulse lengths of 15 and 150 ns (Vorob'ev et al., 1991). The different rates of fall-off in  $T_c$  with increasing  $\theta$  suggested that the film angular distributions were more compositionally uniform for  $\tau = 150$  ns.

The effect of laser wavelength on the plume angular distribution has also been examined for Se (Hansen and Robitaille, 1987). These data suggest that the angular distributions produced with infrared (IR) wavelengths (e.g., 1064 nm) are significantly broader than those produced with wavelengths in the visible and ultraviolet (UV). The effects are less clear for the other materials listed in Table 7.1, since the available comparisons are not controlled for fluence, spot size, and pulse length. If the effects of laser pulse length are neglected, however, data for Y-Ba-Cu-O (Balooch et al., 1989) suggest that wider distributions might be obtained in the IR for this material as well. Similar broadening with IR wavelengths may also occur for the case of carbon, but the effects tend to be masked by the spot-size differences between the data at 308 nm (Gorbunov and Konov, 1989) and 1064 nm (Akhsakhalan et al., 1988). Comparisons of the angular distributions produced by 351- and 193-nm irradiation of the polymer polyphenylquinoxaline (at fluences giving comparable etch depths per pulse) indicated a broader distribution for the more poorly absorbed 351-nm light (Lazare and Granier, 1990). This is consistent (perhaps accidentally) with the Y-Ba-Cu-O data, since Y-Ba-Cu-O is also more poorly absorbing at longer wavelengths.

The effects of laser fluence on the angular distribution are documented for a wider range of materials. Film-based studies frequently suggest that the degree of forward peaking is relatively insensitive to fluence. As indicated in Table 7.1, this was found for carbon (Gorbunov and Konov, 1989), SmBa<sub>2</sub>Cu<sub>3</sub>O<sub>7</sub> (Neifeld et al., 1988), and Y-Ba-Cu-O (Foltyn, 1992). Qualitative measurements (Cheenne et al., 1990) indicate this to be the case for Bi-Sr-Ca-Cu-O as well; the angular distributions were found to be unaffected by varying the laser fluence from below to way above the plasma threshold for depositions using  $\lambda = 1064$ , 532, and 355 nm (with  $\tau \sim 5$  ns), and 193 nm (with  $\tau \sim 20$  ns). Strongly contrasting behavior is shown in the angular

distributions by the material produced during polymer ablation, which become increasingly peaked as the fluence is increased. Table 7.1 summarizes the results for polyphenylquinoxaline; several other polymers examined in the same study showed similar behavior (Lazare and Granier, 1990). Several measurements on Y-Ba-Cu-O films suggest however, that the source angular distribution may consist of a fluence-dependent mixture of two component angular distributions: a broad, "thermal" one with a  $\cos \theta$  dependence, and a much more highly forward peaked one, whose intensity increases with fluence (Venkatesan et al., 1988; Fuchs and Fogarassy, 1990).

### 7.3.6 Ambient Gas Effects

In vacuum, the plume angular distribution is determined by collisions of the plume particles among themselves. To a good approximation, most of these collisions occur while the plume is small and close to the target. In the presence of an ambient gas, the nascent plume angular distribution is perturbed by additional plume particle collisions with the background gas. These collisions scatter the plume particles from their original trajectories and broaden the angular distribution. This broadening is evident for several of the entries in Table 7.2, which gives the angular distribution data measured in the presence of a background gas (with comparisons to vacuum, when available).

Collision-induced broadening effects might be expected to begin appearing when the mean free path of a particle in the background gas starts to become less than the target-substrate distance,  $h$ . The particle mean free path,  $\Lambda$ , is roughly  $(\sqrt{2} n \sigma)^{-1}$ , where  $n$  is the number density of the gas (proportional to pressure) and  $\sigma$  is the collision cross section. Collisional effects would thus be expected to increase as the pressure-distant product,  $P \times h$  (see, for example, Muenchausen et al., 1991).

Experimental findings frequently suggest that the  $\Lambda \simeq h$  threshold for the appearance of a collisionally broadened angular distribution overestimates the effect of collisions. For example, the angular distributions of carbon deposits collected at  $h = 25$  mm appear to be collisionally broadened only at pressures above  $\sim 22$  mtorr (Gorbunov and Konov, 1989), that is, at  $h/\Lambda \gtrsim 10$ . A similar insensitivity of the angular distributions to pressure was seen for Y-Ba-Cu-O depositions in the pressure range  $10^{-5}$  to  $10^{-1}$  torr (Muenchausen et al., 1990). This suggests that quite a few collisions may be required to significantly change the trajectories of the (typically highly energetic) plume particles. For a given background gas mass and plume particle velocity, one qualitatively expects the dispersive effects of collisions to be relatively more (less) severe for the low (high-) mass plume species. Conversely, a high-mass scattering gas will have a greater effect on the plume particle trajectories than a low-mass scattering gas.

Several groups have investigated the background-gas-induced attenuation, slowing, and reaction of plume species generated during Y-Ba-Cu-O deposi-

tions as a function of background gas pressure (see, for example, Geohegan, 1991). Consistent with the apparently negligible effect on the plume particle trajectories of even several collisions with background gas species, time-resolved ion-probe measurements at a target-substrate distance of 100 mm indicate minimal slowing of the ions at  $O_2$  pressures up to 10 mtorr, despite severe (factor of 5) attenuation (presumably by neutralization). These attenuation effects might possibly account for the marked sharpening in the ion distribution produced from Y-Ba-Cu-O targets observed by Chrisey et al. (1990) as the background gas pressure was increased from vacuum to 100 mtorr  $O_2$  ( $D(\theta) \sim \cos^{>300}\theta$  versus  $\sim \cos^{<46}\theta$  for  $h = 3$  cm).

### 7.3.7 Angular Dependence of Film and Plume Composition

While PLD may provide films with the correct *average* stoichiometry, more detailed measurements frequently show the film stoichiometry to vary with the deposition angle  $\theta$ . This is a potentially serious problem for materials in which film stoichiometry is critical. Fortunately, film stoichiometry is often satisfactorily uniform within some (smaller) range of angles about the deposition axis.

If the basic assumptions of film-based angular distribution measurements are valid (i.e., unit sticking coefficient and no resputtering), an angular variation in film composition implies that different components of the plume have different angular distributions. The different angular distributions of the component plume species may be associated with differences in species charge (e.g., ions or neutrals) as well as mass (e.g., heavy or light). For example, the ions and neutrals in the plume have been observed to have distinctly different angular distributions, usually with the positive-ion distribution being more sharply forward peaked. This was found for plumes produced from targets of polyimide, which had a source distribution of  $\cos\theta$  for the neutrals versus  $\cos^4\theta$  for the ions (Ulmer et al., 1990), and for targets of Y-Ba-Cu-O, which had a source distribution of  $\cos^{>11}\theta$  for the neutrals versus  $\cos^{>40}\theta$  for the ions (Table 7.2, Chrisey et al., 1990). For the case of ablation from targets of Cu and Si, however, the ions are found to be more isotropic than the neutrals, presumably due to spacecharge repulsion effects (Dieleman et al., 1992).

Composition measurements on films produced by PLD (in vacuum) from multicomponent targets indicate a variety of results. Some data suggest a relative enrichment of the lower mass elements near  $\theta = 0^\circ$ . For example, higher on-axis Cu/Ba (light/heavy) ratios were seen in Y-Ba-Cu-O films deposited at moderate laser fluence (Venkatesan et al., 1988; Singh et al., 1990). At higher fluences, this effect is less pronounced and the Cu/Ba ratio is more spatially uniform. A simple mass relationship between the angular distributions of the various components of Y-Ba-Cu-O films appears to be ruled out by the on-axis Y-enrichment found in both vacuum (Venkatesan et al., 1988) and 100-mTorr  $O_2$  (Muenchausen et al., 1990). However, it has been suggested that the atomic masses may not reflect the mass of the "carrier species" (e.g., a

heavier molecule or cluster) in which the atom is transported (Saenger, 1991; Foote et al., 1992).

Higher on-axis (light/heavy) ratios have also been observed in vacuum depositions of Bi-Sr-Ca-Cu-O and  $PbZr_xTi_{1-x}O_3$  (PZT) films. For Bi-Sr-Ca-Cu-O, the Sr/Bi and Ca/Bi ratios were higher on-axis, although the magnitude of this effect was less pronounced with less-dense targets and in the presence of  $\sim 80$  mtorr  $O_2$  (Perez Casero et al., 1992). In the case of PZT, higher (Zr + Ti)/Pb ratios were found on-axis (Roy and Saenger, 1990; Hau et al., 1992). In contrast to the Y-Ba-Cu-O data, however, the composition nonuniformities in the PZT films became more pronounced as the fluence increased from  $0.2 \text{ J/cm}^2$  to  $5 \text{ J/cm}^2$  (Hau et al., 1992). Quite remarkably, for fluences in the range  $1\text{--}5 \text{ J/cm}^2$ , the Pb distribution was found to be bimodal, with a pronounced local minimum at  $\theta = 0$ .

Detailed film composition uniformity data on the Y-Ba-Cu-O system have been reported by Foote et al. (1992). Factors investigated included laser fluence, spot size, oxygen pressure, and target-substrate distance. In vacuum, they found slight on-axis enrichments of copper and barium. In an oxygen gas ambient, however, an on-axis enrichment could be found for yttrium, due to gas scattering effects (which increase with increasing target-substrate distance,  $h$ ). They concluded that the deposition of compositionally uniform films at intermediate values of  $h$  results from the near cancellation of the intrinsic (vacuum) composition nonuniformities by species-dependent gas scattering effects.

At least two groups (Greer and Van Hook, 1990; Lowndes et al., 1990) have investigated the angular distribution of particulates in Y-Ba-Cu-O films (prepared with  $\lambda = 248 \text{ nm}$  and  $F \sim 1 \text{ J/cm}^2$ ), and found the particulate density (per unit area  $\times$  film thickness) to be higher off the deposition axis. In one case, submicron to micron-sized pits were actually found near the deposition axis, suggesting that some particles may have melted or evaporated after impact (Lowndes et al., 1990). Another group measured the angular distributions of particulates in Bi-Sr-Ca-Cu-O films (prepared with  $\lambda = 1.06 \mu\text{m}$  and  $F = 0.34$  and  $1.26 \text{ J/cm}^2$ ) (Cheenne et al., 1990). They found *lower* particulate densities (per unit area) off the deposition axis, with substantially increased on-axis peaking at higher fluences. These particle density distributions are not, however, necessarily inconsistent with those found for Y-Ba-Cu-O with  $\lambda = 248 \text{ nm}$ , since they were not normalized to film thickness, which also varies strongly with angle.

## 7.4 MODELS

A wide variety of approaches have been utilized to model the angular distribution data from pulsed laser ablation sources in vacuum. In this section we describe some numerical approaches and their predictions, but emphasize

simple physical models that can explain specific features of the data. In particular, one would like to understand the reasons for the high degree of forward peaking, the strong dependence of the angular distribution on spot size, and the frequent insensitivity of the angular distribution to fluence. Section 7.4.1 shows how the observed angular distributions are a mathematical consequence of plume velocity distributions characterized by nonzero flow velocities (i.e., "shifted Boltzmann" distributions). The higher the flow velocity, the more peaked the distribution. Section 7.4.2 outlines the results and assumptions of a few numerical approaches that have been used to model plume angular distributions, and focus on some simple expressions that relate the angular distribution to spot size for circular spots. Section 7.4.3 discusses possible mechanisms responsible for the deviations of the observed angular distributions from the predictions of simple models, with special attention directed toward explanations for the fluence-independent distributions and 2-component distributions that are frequently observed. Section 7.4.4 is analogous to Section 7.4.3, but directed toward the mechanisms responsible for compositionally varying distributions. Section 7.4.5 provides some qualitative explanations for the effects of background gas on the angular distributions.

#### 7.4.1 Derivation of the Cosine-Power ( $\cos^p \theta$ ) Distribution

In this section we show that the strongly forward-peaked film thickness profiles frequently described as  $D(\theta) = \cos^{p+3}\theta$  (corresponding to source angular distributions of the form  $f(\theta) = \cos^p \theta$ ) excellently approximate the exact angular distributions calculated for the expected plume velocity distribution (i.e., the "shifted Boltzmann" distribution of Eq. (7.1) with a flow velocity  $u > 0$ ). It should be noted that the development of a flow velocity is due to collisions of the plume particles among themselves; for an effusive source (i.e., under collisionless conditions), the flow velocity is zero and the source angular distribution is ideally  $f(\theta) = \cos \theta$ . The interrelationship between collisions and flow velocity was discussed earlier in Chapter 3 (Kelly and Miotello, this book). Typically, collisional effects start to become important when fractions of a monolayer are removed in some tens of nanoseconds (Kelly, 1990). The derivation that follows is based on a previous treatment by the author (Saenger, 1991).

Assumed for this derivation is a point source of particles with a probability distribution for velocity given by

$$f(v_x, v_y, v_z) dv_x dv_y dv_z = B v_z e^{-(m/2kT)[v_x^2 + v_y^2 + (v_z - u)^2]} dv_x dv_y dv_z \quad (7.1)$$

where  $v_x$ ,  $v_y$ , and  $v_z$  are the particle velocity components in Cartesian coordinates in which  $\hat{z}$  is the target surface normal (assumed to be coincident with the deposition axis),  $B$  is a normalization constant,  $m$  is the particle mass,  $k$  is

the Boltzmann constant,  $u$  is the flow velocity, and  $T$  is the local temperature. The substrate is taken to be a flat surface oriented parallel to the target. In spherical coordinates, Eq. 7.1 for the probability distribution becomes

$$f(v, \Omega) d\Omega dv = B v^3 \cos \theta e^{-(m/2kT)[v^2 \sin^2 \theta + (v \cos \theta - u)^2]} d\Omega dv \quad (7.2)$$

where  $\Omega$  is the solid angle and  $v$  is the particle speed. In the (collision-free) effusive limit,  $u = 0$ , and Eq. 7.2 reduces to the familiar "cos  $\theta$ " distribution expected for an effusive source at temperature  $T$ . The probability for material to leave the source within an angle  $d\Omega = \sin \theta d\theta d\phi$  of  $\Omega$  is given by  $P(\Omega) d\Omega = d\Omega \int_0^\infty f(v, \Omega) dv$ . Assuming unit sticking probability, the deposition profile  $D(\Omega)$  is given by  $P(\Omega) d\Omega / dA$ , where  $dA$  is the area on the substrate subtended by the angle  $d\Omega$ . With  $R = (x^2 + y^2 + z^2)^{1/2}$  and  $dA$  (for a substrate oriented as in Figure 7.1)  $= (R^2 d\Omega / \cos \theta) = (z^2 d\Omega / \cos^3 \theta) = (h^2 d\Omega / \cos^3 \theta)$ , one then has

$$D(\Omega) = P(\Omega) \frac{d\Omega}{dA} = \frac{\cos^3 \theta}{h^2} \int_0^\infty f(v, \Omega) dv \quad (7.3)$$

After some rearrangement, one obtains

$$D(\theta) \equiv D(\Omega) = \frac{B'}{h^2} \cos^4 \theta e^{-(\gamma/2)\tilde{M}^2 \sin^2 \theta} \int_0^\infty s^3 e^{-[S - (\gamma/2)^{1/2} \tilde{M} \cos \theta]^2} ds \quad (7.4)$$

where  $B'$  is a normalization constant,  $h$  is the distance along the  $z$  axis from the target to the substrate, the dimensionless velocity  $s \equiv v/\tilde{v}_1$ , where  $\tilde{v}_1 \equiv (2kT/m)^{1/2}$ , and  $(\gamma/2)\tilde{M}^2$  is equal to  $(u/\tilde{v}_1)^2$ . Since  $D(\Omega)$  is independent of the azimuthal angle  $\phi$ , it will be referred to as  $D(\theta)$  with the understanding that it represents the deposit thickness on the substrate at a single point whose angular coordinates are  $(\theta, \phi)$ .

The parameter  $\tilde{M}$  in Eq. 7.4 should be viewed as a "pseudo-Mach number" (details later; see Eq. 7.15), which is the same as the conventionally defined Mach number for expansions consisting of single-mass particles. The conventional Mach number  $M$  is defined as the ratio of flow velocity,  $u$ , and the local speed of sound,  $a = (\gamma kT/m)^{1/2}$ , that is,

$$M \equiv \frac{u}{a} = \frac{u}{(\gamma kT/m)^{1/2}} \quad (7.5)$$

where  $\gamma \equiv C_p/C_v$  is the ratio of the specific heats at constant pressure and volume, respectively.

The integral in Eq. 7.4 can be evaluated numerically to give the distribution

shown by diamonds in Figure 7.2. This exact solution for  $D(\theta)$  can be extremely well reproduced by

$$D_{\text{sum}}(\theta) \equiv \frac{B'}{h^2} \cos^4 \theta e^{-(\gamma/2)\tilde{M}^2 \sin^2 \theta} \sum_{l=0}^3 a_l \left[ \left( \frac{\gamma}{2} \right)^{1/2} \tilde{M} \cos \theta \right]^l \quad (7.6)$$

where the four coefficients in the sum are  $a_0 = 0.5$ ,  $a_1 = 1.8$ ,  $a_2 = 0.25$ , and  $a_3 = \pi^{1/2}$ .

Another estimate for  $D(\theta)$  can be generated by the approximation, reasonable for high Mach number supersonic expansions, that  $v_z = u$ . This yields

$$D_{\text{ss}}(\theta) \equiv \frac{B'_{\text{ss}}}{h^2} e^{-(\gamma/2)\tilde{M}^2 \tan^2 \theta} \quad (7.7)$$

where  $B'_{\text{ss}}$  is again a normalization constant independent of  $\theta$ . Figure 7.2 indicates that for  $(\gamma/2)^{1/2}\tilde{M} \equiv (u/\tilde{v}_\perp) = 5$ ,  $D_{\text{ss}}(\theta)$  is in reasonable agreement with the exact solution given in Eq. 7.4, at least for small angles, where the bulk of the material is deposited. Additional plots (not shown) confirm that the  $D_{\text{ss}}(\theta)$  approximation for  $D(\theta)$  improves as  $\tilde{M}$  increases.

The exponential factor of Eq. 7.7 can also be obtained by simply considering the probability function for transverse velocity,  $f(v_\perp) \propto e^{-(m/2kT)v_\perp^2}$ . In this

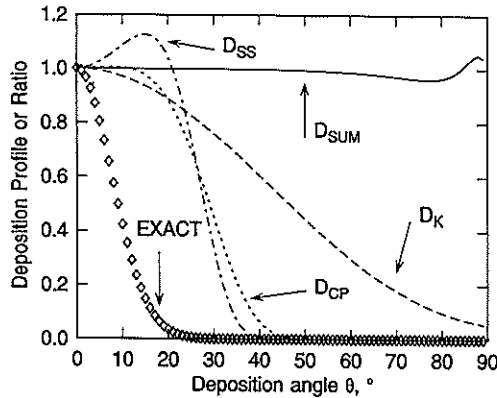


Figure 7.2. Comparison of calculated deposit profiles for  $(\gamma/2)^{1/2}\tilde{M} \equiv (u/\tilde{v}_\perp) = 5$ . Exact numerical solution of Eq. 7.4 shown by diamonds; ratios of various approximations to the exact solution shown by lines: (i) Polynomial approximation  $D_{\text{sum}}(\theta)$  of Eq. 7.6—solid line; (ii) Kelly approximation  $D_K(\theta)$  of Eq. 7.8—dashed line; (iii) Strongly supersonic approximation  $D_{\text{ss}}(\theta)$  of Eq. 7.7—dashdot line; (iv) cosine-power approximation  $D_{\text{CP}}(\theta)$  of Eq. 7.9, with  $p+3=55.9$ —dotted line. All profiles have been normalized to unity at  $\theta = 0$ .

approximation of  $v_z = u$ , all species have a flight time of  $h/u$ , and  $v_\perp$  is given by  $r/(h/u)$ . The transverse velocity distribution then directly mirrors the deposit profile, that is,  $f(v_\perp) \propto e^{-(\gamma/2)\tilde{M}^2 \tan^2 \theta}$ . Higher values of  $\tilde{M} \propto u/\tilde{v}_\perp$  will narrow the deposit, since as  $u$  increases, particles with a given radial velocity  $v_\perp$  will be in flight for less time and traverse a smaller radial distance.

Another approximate solution (Kelly, 1990) for the deposition profile is based on a time-of-flight analysis with the assumption that all particles have a flight time equal to the most probable flight time. This approach (with the assumption of flux-sensitive detection) yields

$$D_K(\theta) \equiv \frac{B'_K}{h^2} \cos^4 \theta \eta^{2.5} e^\eta \quad (7.8a)$$

where  $B'_K$  is a normalization constant,

$$\eta \equiv \frac{\gamma \tilde{M}^2 \cos^2 \theta}{8} \left[ 1 + \left( \frac{20}{\gamma \tilde{M}^2 \cos^2 \theta} \right)^{1/2} \right]^2 \quad (7.8b)$$

and an extra  $\cos^2 \theta$  term has been included to account for the fact that the original expression given by Kelly (1990) assumed the distance from the target to the detector to be independent of  $\theta$ .

The expression for  $D(\theta)$  in Eq. 7.4, as well as the  $D_K(\theta)$  and  $D_{\text{sum}}$  approximations, can be fairly well represented by a cosine-power (CP) expression:

$$D_{\text{CP}}(\theta) \equiv \frac{B'_{\text{CP}}}{h^2} \cos^{p+3} \theta \quad (7.9a)$$

where  $B'_{\text{CP}}$  is a normalization constant, and

$$p = 1 + 2.13 \frac{\gamma^{1/2} \tilde{M}}{\gamma^{1/2} \tilde{M} + 1} + \gamma \tilde{M}^2 \quad (7.9b)$$

Eq. 7.9b is an empirical expression that was found to accurately reproduce the values of  $p$  returned by nonlinear least squares fits of  $\cos^{p+3} \theta$  to  $D(\theta)$  profiles numerically generated for  $\gamma^{1/2}\tilde{M}$  values between 0 and 14. For the case  $\tilde{M} = 1$ , Eq. 7.9b predicts  $p$  to be  $\approx 3.9$  for  $\gamma = 5/3$ , in reasonable agreement with the  $p \approx 4$  prediction of Kelly (1990).

The ratios of these various approximations for  $D(\theta)$  to the exact numerical solution of Eq. 7.4 are compared for  $(\gamma/2)^{1/2}\tilde{M} = 5$  in Figure 7.2. In the limit that  $\tilde{M}$  or  $u = 0$ , all but the  $D_{\text{ss}}(\theta)$  approximation to  $D(\theta)$  reduce to the  $\cos^4 \theta$  distribution expected for a small-area effusive source.

### 7.4.2 Numerical Models: Assumptions, Results, and Predictions

In this section we outline the results and assumptions of a few (mostly numerical) approaches that have been used to model plume angular distributions in vacuum, and focus on some simple expressions that relate the angular distribution to spot size for circular spots.

We begin by describing a very simple but somewhat limited treatment that predicts the half-angle  $\theta_{1/2}$  (of the source angular distribution) to depend only on the value of  $\gamma$  (Gorbunov and Konov, 1989). The basic assumption is that the average velocity of the plume particles in the  $z$ -direction is increased over the average random velocity by an additive quantity equal to the speed of sound,  $a$ , that is,  $\langle v_z^2 \rangle^{1/2} = \langle v_x^2 \rangle^{1/2} + a$ . By conservation of energy, the sum  $(\langle v_x^2 \rangle + \langle v_y^2 \rangle + \langle v_z^2 \rangle)^{1/2}$  must equal  $u_\infty (= a \times [2/(\gamma - 1)]^{1/2})$ , the value of  $v_z$  in the limit of infinite expansion. This leads to

$$\theta_{1/2} = \tan^{-1} \left[ \frac{\sqrt{8 - 2\gamma} - \sqrt{\gamma - 1}}{\sqrt{8 - 2\gamma} + 2\sqrt{\gamma - 1}} \right] \quad (7.10)$$

This expression differs from that in the original paper, since it is based on  $\langle v_x^2 \rangle + \langle v_y^2 \rangle + \langle v_z^2 \rangle = u_\infty^2$  rather than the original  $\langle v_x^2 \rangle + \langle v_z^2 \rangle = u_\infty^2$ . According to Eq. 7.10, the width of the expansion would be expected to range from  $\theta_{1/2} = 19.5^\circ$  ( $p = 11.7$ ) for  $\gamma = 5/3$  to  $\theta_{1/2} = 28.9^\circ$  ( $p = 5.2$ ) for  $\gamma = 1.25$ .

In the approach of Kools et al. (1993) the evolution of the ablated cloud is divided into three consecutive stages: (i) generation of the vaporized material, (ii) one-dimensional expansion along the target normal for a distance  $Z_0$  (roughly comparable to the laser spot dimensions  $X_0$  and  $Y_0$ ), resulting in a velocity distribution having the form of a shifted Boltzmann with axial temperature  $T_z$  and lateral temperatures  $T_x$  and  $T_y$ , and (iii) a three-dimensional spread of noninteracting particles having the velocity distribution reached at  $Z_0$ . For a circular spot and the assumptions  $\gamma = 5/3$  and  $\tilde{M} = 2.33$ , they obtain

$$p = 3.9 \left( 1 + 2 \left( \frac{Z_0}{X_0} \right)^{1.2} \right)^{3/4} \left( \frac{X_0}{Z_0} \right)^{1.2} \quad (7.11)$$

for the exponent  $p$  in the source angular distribution  $f(\theta) = \cos^p \theta$ . This expression is claimed to be generally applicable to any ablation process in which the collision rate is high enough in the region  $z = 0$  to  $z = Z_0$  for hydrodynamics to apply, and for which the plume consists mostly of atoms. The value of  $Z_0$  is assumed to be roughly independent of particle mass, spot size, and laser fluence, and is taken to be around 0.4 mm from fits of data for W (Akhsakhalyan et al., 1988). With a  $Z_0$  value of 0.4 mm, reasonable agreement between the predicted and observed values of  $p$  is found for a number of materials listed in Table 7.1, including graphite and gold (Gor-

bunov and Konov, 1989), Y-Ba-Cu-O (Venkatesan et al., 1988), and TiN (Kools et al., 1992). Much less satisfactory agreement is found for data on W and Pb (Akhsakhalyan et al., 1988); for spot diameters of 0.2 mm and 2 mm, Eq. 7.11 predicts  $p$  values of 6.2 and 33, respectively (for  $Z_0 = 0.4$  mm), significantly above the observed  $p(d = 0.2$  mm) and  $p(d = 2$  mm) values of 3.6 and 9.6 for Pb and 4.6 and 26 for W.

An alternative approach to predicting the dependence of  $p$  on the spot dimensions has been developed by Saenger, 1993. This approach utilizes Eq. 7.9b to get the dependence of  $p$  on the final or terminal Mach number reached in the expansion and the following expression to get the dependence of the terminal Mach number on the spot diameter  $d$ ,

$$\tilde{M} \propto \left( \frac{d}{\Lambda_0} \right)^{(\gamma-1)/\gamma} \quad (7.12)$$

where  $\Lambda_0$  is the mean free path of the plume particles immediately after vaporization. Equation 7.12 is based on the "sudden freeze model" (Anderson, 1974; McClelland et al., 1979; Saenger, 1991), and is expected to be valid for continuous (or very long pulse-length) supersonic expansions. The physical reason why  $\tilde{M}$  is higher for larger  $d$  stems from the fact that changes in  $\tilde{M}$  are due to collisions between plume particles. The number of collisions expected for a particle emitted from the center of a large spot is clearly higher than that expected for the equivalent particle emitted from a center of a small spot. Qualitatively, this is because the spatial zone in which the plume density is high enough for collisions to take place is larger both laterally, and in the  $z$ -direction (since three-dimensional expansion and its associated more rapid density decrease does not begin until larger values of  $z$ ).

For known  $\gamma$ , it is possible to predict  $p$  from Eq. 7.12 for arbitrary  $d$  if  $p(d)$  is known for one value of  $d$ . For example, the data for Pb indicate  $p(d = 0.2$  mm) = 3.6 and  $p(d = 2$  mm) = 9.6; assuming  $\gamma = \frac{5}{3}$ , the predicted value of  $p(d = 2$  mm) would be 11.6. Similarly, the data for W giving  $p(d = 0.2$  mm) = 4.6 implies that  $p(d = 2$  mm) should be about 18 (versus the measured value of 26).

In the approach of Akhsakhalyan et al. (1988) the half-angle of the source angular distribution is numerically calculated to provide  $\theta_{1/2}$  for  $\gamma = 5/3$  and a specific value of  $\tilde{M}$  as a function of a dimensionless parameter which is denoted here as  $\Sigma$ .  $\Sigma$  is given by

$$\Sigma = \frac{2v_0\tau_e}{d} = \frac{2\tilde{M}[\gamma k T_0/m]^{1/2}}{d} \quad (7.13)$$

where  $v_0$  is the initial particle velocity,  $\tau_e$  is the evaporation (or particle release) time,  $d$  is the laser spot diameter, and  $T_0$  is the temperature of the plume at the end of the laser pulse. The results of these calculations are shown in Figure 7.3.



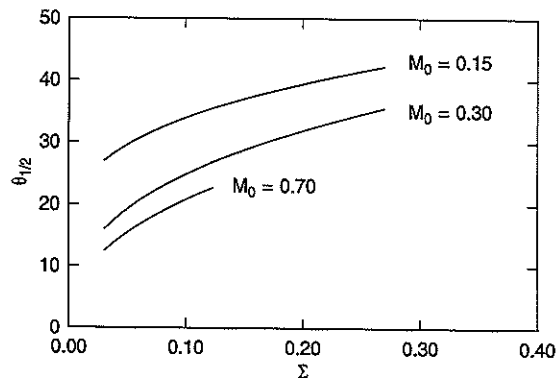


Figure 7.3. Source angular distributions of ablated material calculated as a function of the dimensionless parameter  $\Sigma$ . (Adapted from Akhsakhalyan et al., 1988.)

Additional refinements to the calculations include the consideration of laser-plume interactions.

This model very accurately reproduces the data (Akhsakhalyan et al., 1988) for the angular distribution of W as a function of spot size investigated over the range  $d = 0.2$  mm to 2 mm. Additional plume absorption corrections must be included to fit the analogous data for Pb. These authors use their model to predict the dependence of  $\theta_{1/2}$  on particle mass, laser power density ( $q = 1 - 4 \times 10^9$  W/cm<sup>2</sup>) and laser pulse length ( $\tau = 10$  to 30 ns, where it is assumed that  $\tau_e = \tau$ ) and find good agreement between experiment and theory.

To calculate the angular distributions produced by pulsed laser ablation, Singh and Carignan (1992) solve the three-dimensional expansion equation

$$X(t) \frac{d^2 X(t)}{dt^2} = Y(t) \frac{d^2 Y(t)}{dt^2} = Z(t) \frac{d^2 Z(t)}{dt^2} = \frac{kT_0}{m} \left[ \frac{X_0 Y_0 Z_0}{X(t) Y(t) Z(t)} \right]^{\gamma-1} \quad (7.14)$$

where  $X_0$ ,  $Y_0$ , and  $Z_0$  are the three dimensions of the plasma at the end of the isothermal regime,  $X(t)$ ,  $Y(t)$ , and  $Z(t)$  are the time-dependent dimensions of the plasma in the adiabatic regime, and  $T_0$  is the isothermal plasma temperature, to determine the flux of particles incident on the substrate plane. They found the film angular distribution to depend negligibly on the value of  $T_0$  (over the range 10,000 K to 40,000 K). They also found the angular distributions to broaden as  $\gamma$  is decreased from 5/3 to 1.2; for a laser spot diameter  $d = 2$  mm, this broadening would be equivalent to decreasing the exponent  $p$  in the flux angular distribution  $\cos^p \theta$  from 9.0 to 3.0, in qualitative agreement with the predictions of Eq. 7.10. They also examined the angular distributions resulting from spot diameters between  $<0.1$  mm and  $>10$  mm for a target-substrate distance  $h = 3$  cm. For  $d$  in the range  $<0.1$  mm to 3 mm, the width

of the angular distribution was found to monotonically decrease as the spot size was increased, with  $p \leq 3.2$  for  $d \leq 0.1$  mm and  $p \approx 13.1$  for  $d = 3$  mm. For  $d$  greater than 3 mm, the angular distribution broadened with increasing spot size, due to the breakdown of the small-area approximation (i.e.,  $d$  is no longer  $\ll h$ ).

### 7.4.3 Explanations for 2-Component and Fluence-Independent Angular Distributions

In this section we speculate on some possible reasons for the observations of 2-component angular distributions and fluence-independent angular distributions. Intuitively, one might expect the angular distributions to become more peaked with increasing fluence, based on the idea that a higher fluence should produce a higher density of removed particles and thus a greater number of collisions per particle. Such trends have been observed for polymers (Lazare and Granier, 1990). However, as can be seen from the entries in Table 7.1, they are far from universal, the best documented exception being Y-Ba-Cu-O.

We begin by qualitatively discussing the expected effects on the plume of a change in laser fluence (assuming a fixed spot size and laser pulse duration  $\tau$ ). In nearly all cases, the amount of target material removed increases with fluence. This does *not necessarily* imply an increase in the initial plume density, however, since the larger amount of "evaporated" material may be emitted over a longer time. The time over which material evaporates from the target surface,  $\tau_e$ , can be significantly longer than the laser pulse length  $\tau$ , as implied by ps-scale ablation results for LiNbO<sub>3</sub> (Beuermann et al., 1990), and definitively found for Y-Ba-Cu-O ( $\tau_e \approx$  several hundred ns for  $\tau = 20$  ns; Gupta et al., 1991) and the polymer PMMA ( $\tau_e \approx 6 \mu$ s for  $\tau = 20$  ns; Braren et al., 1991). Changes in laser fluence might also be expected to affect the initial plume temperature, or the value of  $\gamma$ . In the limit of no plume absorption, and a roughly linear dependence of etch depth per pulse on fluence (above some threshold), one expects a plume temperature that is approximately independent of fluence, since the increased laser energy is spread over a proportionately increased quantity of particles. When plume absorption is significant, one usually sees a sublinear dependence of etch depth on fluence. Thus, strongly absorbing (but nonreflecting) plumes would be expected to have temperatures that increase with fluence, because a greater fraction of the laser energy is being diverted to the plume. Higher plume temperatures would be expected to correlate with greater dissociation and higher ionization fractions. Greater dissociation would tend to increase  $\gamma$  (i.e., to a value closer to 5/3), while a greater degree of ionization would be expected to lower  $\gamma$  (to a value closer to 1).

Models of pulsed supersonic expansions (Saenger, 1981; Saenger and Fenn, 1983) suggest that the evaporation time  $\tau_e$  should exceed a time  $\tau_{\min} \approx 10 - 20 \mu$ s to produce an expansion having a Mach number as high as that which

could be produced by a continuous expansion having the same initial density. According to this model, the expansion properties of the plume are relatively independent of  $\tau_e$  once  $\tau_e$  exceeds several  $\tau_{\min}$ . In the regime  $\tau_e \sim \tau_{\min}$ , increases in  $\tau_e$  increase the "average" Mach number of the plume, since a greater proportion of the plume particles have attained the continuous expansion Mach number. These models are not applicable to the regime  $\tau_e \ll \tau_{\min}$ . However, the dependence of  $\theta_{1/2}$  on  $\Sigma$  (Figure 7.3) and the linear dependence of  $\Sigma (=2v_0\tau_e/d)$  on  $\tau_e$  (Eq. 7.13) suggest that the angular distributions should become *less peaked with increasing  $\tau_e$* . This suggests the possibility that the fluence-independent angular distributions may result from the cancellation of density effects (which would tend to narrow the distribution as fluence is increased) and evaporation time effects (which would tend to widen the distribution as fluence is increased). However, it may just be that for easily ionized plasmas such as that formed from Y–Ba–Cu–O, the effect of a density increase with fluence is cancelled out by the effects of a decreasing  $\gamma$ .

Two-component angular distributions consisting of a strongly forward-peaked component superimposed on a much broader distribution have frequently been observed. An early observation of this phenomenon (Venkatesan et al., 1988) was attributed to the coexistence of a rapidly desorbed, highly forward-peaked ablative component and a more slowly desorbed evaporative component. However, it has also been suggested (Kelly, 1990) that particles at the relatively low-density wings of the expansion, as well as particles at the leading and trailing edges of the pulse, will contribute to a broadened distribution, since these particles will have suffered fewer collisions and thus have a more "effusivelike" velocity distribution. Finally, we mention the possible role of ions in the angular distribution. Ions can collisionally interact over larger distances, and can be accelerated by ambipolar diffusion to velocities much higher than those of the surrounding neutrals. Their angular distributions may be quite different from that of the neutrals. One could speculate that the highly forward-peaked component of the distribution is comprised of plume species that were all originally ions, and that the broad component consists of species that remained as neutrals. Such an argument is partially supported by data on the source angular distributions of ablated polyimide fragments, where a  $\cos^4\theta$  distribution was observed for the positive ions, but a  $\cos\theta$  distribution was observed for the neutrals and negative ions (Ulmer et al., 1990), as well as by the fact that the relative intensity of the forward-peaked component increases with fluence (Venkatesan et al., 1988; Fuchs and Fogarassy, 1990).

#### 7.4.4 Models for Composition Nonuniformity

Film composition nonuniformities are present if any of the film's constituent elements do not have the same angular distribution. Film composition nonuniformities can usually be attributed to one of three causes: intrinsic

nonuniformities in the source angular distribution, resputtering effects, and species-dependent background gas scattering effects. Collision of plume species with background gas would be expected to preferentially broaden the angular distributions of the low-mass species, since even small collisionally induced momentum changes would be likely to result in large velocity changes. Similarly, the trajectories of high-mass plume particles are relatively unaffected by background gas collisions, since a larger change in momentum would be required to effect any change in the particle velocity.

Models for intrinsic nonuniformities in the source angular distribution have been developed by the author (Saenger, 1991) and by Singh et al. (1990). Both of these models seek to account for the on-axis enrichment of low-mass plume species. Composition nonuniformities in Y–Ba–Cu–O films were numerically simulated (Singh et al., 1990) quite accurately using a model in which the particle masses were changed in midexpansion from the average mass to their true mass, as the plume evolved from an isothermal plasma regime to an adiabatic expansion regime.

In the model of the author (Saenger, 1991), composition nonuniformities result when different species in the plume have different Mach numbers. However, the relevant Mach number in this case is the "pseudo-Mach number," defined as

$$\tilde{M} \equiv \left(\frac{2}{\gamma}\right)^{1/2} \frac{u}{\tilde{v}_1} = \left(\frac{2}{\gamma}\right)^{1/2} \frac{u}{(2kT/m_j)^{1/2}} \quad (7.15)$$

where  $m_j$  is the mass of plume species  $j$  and  $\tilde{v}_1 = (2kT/m_j)^{1/2}$  is (roughly) the mean random thermal velocity, which characterizes motion in the radial direction. The conventional and pseudo-Mach numbers (Eqs. 7.5 and 7.15) are the same for single-component systems, but diverge due to the different mass dependencies of the sound speed and  $\tilde{v}_1$ . The sound speed is a collective property of the gas mixture and thus equal to  $(\gamma kT/m_{av})^{1/2}$ , where  $m_{av}$  is the mixture's average weighted mass. In contrast, the  $\tilde{v}_1$  are different for species of different mass, that is,  $\tilde{v}_1 \equiv (2kT/m_j)^{1/2}$ . In weak expansions (i.e.,  $0 < \tilde{M} \lesssim 1$ ), the higher collision rate of the light species tends to leave them with higher flow velocities and lower local temperatures relative to their heavier counterparts. This leads to higher  $\tilde{M}$  values and on-axis enrichment for the light species, in agreement with a number of observations on Y–Ba–Cu–O depositions at low to moderate fluence (Venkatesan et al., 1988). In strong expansions (i.e.,  $\tilde{M} > 1$ ), the opposite effect is expected. In this case, all species in the plume will tend to have the same flow velocity  $u$  and local temperature  $T$ . It then follows from Eq. 7.15 that the high-mass species will have higher Mach numbers, and thus an on-axis enrichment. The improved compositional uniformity observed for Y–Ba–Cu–O films with increasing fluence (Venkatesan et al., 1988) is attributed to a transition from the weak expansion regime to a regime intermediate between the weak and strong expansion extremes (where these various effects cancel out).

The observed on-axis enrichment of the low-mass species can also be predicted intuitively. In a nearly effusive source, enhanced forward peaking results from even a few collisions (Kelly, 1990). Since the lighter species have both a higher collision rate and velocities that are more easily changed by collisions, one would expect them to have more collisions with greater effect, and thus to be relatively more forward peaked.

Resputtering and sticking coefficient effects can also introduce composition nonuniformities in films deposited from a compositionally uniform source, but only under a restricted set of circumstances. For example, it is not enough to simply have an angle-dependent sticking coefficient for species  $j$  of  $\alpha_j(\theta) = A_j$  (a  $\theta$ -independent constant)  $\times \alpha(\theta)$ , despite the fact that this would alter both the overall deposit profile  $D(\theta)$  and the film composition. Composition nonuniformities can only occur if the  $\alpha_j(\theta)$  depend *differently* on  $\theta$ , that is, only if the ratio of  $\alpha_j(\theta)$  and  $\alpha_k(\theta)$  is not a constant.

Resputtering effects can introduce composition nonuniformities via two mechanisms, each of which requires different sputter yields  $\beta_i$  for the film's constituent elements. In one mechanism, the sputter yield for species  $j$  is angle-dependent, that is,  $\beta_j = B_j$  (a  $\theta$ -independent constant)  $\times \beta(\theta)$ . In the other mechanism, the sputter yield is independent of angle (i.e.,  $\beta_j = B_j$ ), but the flux of sputterers has a different angular distribution from that of the bulk of the depositing material. This could occur if the resputtering was due to energetic ions having an angular distribution different from that of the neutrals. Resputtering effects of this sort could account for the angular distributions of Pb, Zr, and Ti in pulsed laser deposited  $\text{Pb}(\text{Zr}_{0.48}\text{Ti}_{0.52})\text{O}_3$  films (Hau et al., 1992). At low fluences, the angular distributions are all forward peaked, but at higher fluences the distribution for Pb develops a minimum on the deposition axis. These findings can be simply explained by the high sputter yield of Pb and a highly forward-directed flux of energetic ions whose number and energy increase with fluence.

## 7.5 SUMMARY/CONCLUSIONS

This chapter has covered measurement methods, experimental findings, and models relating to the angular distribution of the material generated during PLD. Under most circumstances, the widely used film thickness-based measurements are simple and accurate. However, these measurements rely on the tacit assumptions that the particle sticking coefficients are unity and that there is no resputtering of the film by the incident particle flux.

A number of experimental findings were reviewed. Plume orientation for nonnormal angles of laser incidence on the target is usually slightly skewed ( $0-5^\circ$ ) toward the incoming laser beam. The angular distribution of the ablated material (in vacuum) is usually strongly forward peaked (i.e., with a flux distribution  $f(\theta) \sim \cos^p \theta$ , where  $p \gg 1$ ). This forward peaking phenomenon

originates from collisions of the plume species among themselves. One of the most important parameters affecting the degree of forward peaking was shown to be the size of the laser spot on the target. Other factors, such as target topography and laser pulse length and wavelength, were found to have a lesser influence. Somewhat surprisingly, laser fluence appears to have relatively little effect on the angular distributions for many target materials (although polymer targets are a notable exception). The angular distribution of the ablated material typically broadens in the presence of a background gas, due to scattering effects.

Several approaches have been utilized to model the angular distribution of the ablated material, none of them entirely satisfactory. However, a simple expression was provided to relate the degree of forward peaking (described by the exponent  $p$ ) to the plume Mach number. There is still a need for simple models that would allow a priori prediction of the Mach number from the deposition process parameters (laser fluence, pulse length, etc.) and the physical properties of the target (thermal conductivity, heat capacity, absorptivity, etc.), although some preliminary work has been done in this area. Likewise, an improved understanding of the origins of plume and film composition nonuniformities (especially those stemming from the presence of charged particles) is also needed. Further advances in these areas will be especially valuable as PLD continues to evolve into a mainstream deposition technique.

## REFERENCES

- Afonso, C. N., R. Serna, F. Catalina, and D. Bermejo (1990), *Appl. Surf. Sci.* **46**, 249–253.
- Akhsakhan, A. D., S. V. Gaponov, V. I. Luchin, and A. P. Chirimanov (1988), *Sov. Phys. Tech. Phys.* **33**, 1885–1892.
- Anderson, J. B., (1974), in *Molecular Beams and Low Density Gas Dynamics* (P. O. Wegener, ed.), Marcel Dekker, New York.
- Baeri, P., L. Torrisi, N. Marino, and G. Foti (1992), *Appl. Surf. Sci.* **54**, 210–214.
- Balooch, M., D. R. Olander, and R. E. Russo (1989), *Appl. Phys. Lett.* **55**, 197–199.
- Beuermann, Th., H. J. Brinkmann, T. Damm, and M. Stuke (1990), *Mater. Res. Soc. Symp. Proc.* **191**, 37–42.
- Braren, B., K. G. Casey, and R. Kelly (1991), *Nucl. Instrum. Methods Phys. Res.* **B58**, 463–472.
- Cheenne, A., J. Perriere, F. Kerherve, G. Hauchecorne, E. Fogarassy, and C. Fuchs (1990), *Mater. Res. Soc. Symp. Proc.* **191**, 229–234.
- Chrisey, D. B., J. S. Horwitz, K. S. Grabowski, M. E. Reeves, M. S. Osofsky, and C. R. Gosset (1990), *Mater. Res. Soc. Symp. Proc.* **169**, 435–438.
- Davanloo, F., E. M. Juengerman, D. R. Jander, T. J. Lee, C. B. Collins, and E. Matthias (1992), *Appl. Phys. A: Solids Surf* **A54**, 369–372.

- Dieleman, J., E. van de Riet, and J. C. S. Kools (1992), *Jpn. J. Appl. Phys.* **131**, 1964–1971.
- Eryu, O., K. Murakami, K. Masuda, A. Kasuya, and Y. Nishina (1989), *Appl. Phys. Lett.* **54**, 2716–2718.
- Fogarassy, E., C. Fuchs, J. P. Stoquert, P. Siffert, J. Perriere, and F. Rochet (1989), *J. Less Common Metals* **151**, 249–256.
- Foltyn, S. R., R. C. Dye, K. C. Ott, E. Peterson, K. M. Hubbard, W. Hutchinson, R. E. Muenchausen, R. C. Estler, and X. D. Wu (1991), *Appl. Phys. Lett.* **59**, 594–596.
- Foltyn, S. R., unpubl.; (1992), see also Dye et al., (1993), *SPIE Conf. Proc.* **1835**, 42–49.
- Foote, M. C., B. B. Jones, B. D. Hunt, J. B. Barner, R. P. Vasquez, and L. J. Bajuk (1992), *Physica C* **201**, 176–182.
- Friichtenicht, J. F., N. G. Utterback, and J. R. Valles (1976), *Rev. Sci. Instrum.* **47**, 1489–1495.
- Fuchs, C., and E. Fogarassy (1990), *Mater. Res. Soc. Symp. Proc.* **169**, 517–521.
- Gaponov S. V., and M. D. Strikovskii (1982), *Sov. Phys. Tech. Phys.* **27**, 1127–1130.
- Geohegan, D. B., (1991), *Mater. Res. Soc. Symp. Proc.* **201**, 557–562.
- Gorbunov A. A., and V. I. Konov (1989), *Sov. Phys. Tech. Phys.* **34**, 77–83; see also Scheibe et al., 1990.
- Greer, J. A., and H. J. Van Hook (1990), *Mater. Res. Soc. Symp. Proc.* **169**, 463–468.
- Gupta, A., B. Braren, K. G. Casey, B. W. Hussey, and R. Kelly (1991), *Appl. Phys. Lett.* **59**, 1302–1304.
- Hansen, S. G., and T. E. Robitaille (1987), *Appl. Phys. Lett.* **50**, 359–361.
- Hau, S. K., K. H. Wong, P. W. Chan, C. L. Choy, and H. K. Wong (1992), *J. Mater. Sci. Lett.* **11**, 1266–1268.
- Kelly, R., (1990), *J. Chem. Phys.* **92**, 5047–5056.
- Kools, J. C. S., S. H. Brongersma, E. van de Riet, and J. Dieleman (1991), *Appl. Phys. B: Photophys. Laser Chem.* **B53**, 125–130.
- Kools, J. C. S., C. J. C. M. Nillesen, S. H. Brongersma, E. van de Riet, and J. Dieleman (1992), *J. Vac. Sci. Technol. A* **10**, 1809–1814.
- Kools, J. C. S., E. van de Riet, and J. Dieleman (1993), *Appl. Surf. Sci.* **69**, 133–139.
- Lazare, S., and V. Granier (1990), *Chem. Phys. Lett.* **168**, 593–597.
- Lowndes, D. H., D. P. Norton, J. W. McCamy, R. Feenstra, J. D. Budai, D. K. Christen, and D. B. Poker (1990), *Mater. Res. Soc. Symp. Proc.* **169**, 431–434.
- Lubben, D., S. A. Barnett, K. Suzuki, S. Gorbalkin, and J. E. Greene (1985), *J. Vac. Sci. Technol. B* **3**, 968–974.
- Lynds, L., B. R. Weinberger, D. M. Potrepka, G. G. Peterson, and M. P. Lindsay (1989), *Physica C* **159**, 61–69.
- Lynds, L., B. R. Weinberger, M. P. Lindsay, and D. M. Potrepka (1990) *Mat. Res. Soc. Symp. Proc.* **169**, 443–446.
- Marine, W., M. Peray, Y. Mathey, and D. Pailharey (1989), *Appl. Surf. Sci.* **43**, 377–381.
- McClelland, G. M., K. L. Saenger, J. J. Valentini, and D. R. Herschbach (1979), *J. Phys. Chem.* **83**, 947–959.
- Muenchausen, R. E., K. M. Hubbard, S. Foltyn, R. C. Estler, N. S. Nogar, and C. Jenkins (1990), *Appl. Phys. Lett.* **56**, 578–580.
- Muenchausen, R. E., S. R. Foltyn, N. S. Nogar, R. C. Estler, E. J. Peterson, and X. D. Wu (1991), *Nucl. Instrum. Meth. A* **303**, 204–207.
- Murray, P. T., D. T. Peeler, and D. V. Dempsey (1992), *Mater. Res. Soc. Symp. Proc.* **236**, 411–416.
- Namiki A., T. Kawai, and K. Ichige (1986), *Surf. Sci.* **166**, 129–140.
- Neifeld, R. A., S. Gunapala, C. Liang, S. A. Shaheen, M. Croft, J. Price, D. Simons, and W. T. Hill (1988), *Appl. Phys. Lett.* **53**, 703–704.
- Pappas, D. L., K. L. Saenger, J. J. Cuomo, and R. W. Dreyfus (1992), *J. Appl. Phys.* **72**, 3966–3970.
- Perez Casero, R., F. Kerherve, J. P. Enard, J. Perriere, and P. Regnier (1992), *Appl. Surf. Sci.* **54**, 147–153.
- Pinto, R., S. P. Pai, C. P. D'Suozza, L. C. Gupta, R. Vijayaraghavan, D. Kumar, and M. Sharon (1992), *Physica C* **196**, 264–270.
- Roy, R., and K. L. Saenger (1990), unpub.
- Saenger, K. L., (1981), *J. Chem. Phys.* **75**, 2467–2469.
- Saenger, K. L., (1993), in preparation.
- Saenger, K. L., and J. B. Fenn (1983), *J. Chem. Phys.* **79**, 6043–6045.
- Saenger, K. L., (1991), *J. Appl. Phys.* **70**, 5629–5635.
- Scheibe, H.-J., A. A. Gorbunov, G. K. Baranova, N. V. Klassen, V. I. Konov, M. P. Kulakov, W. Pompe, A. M. Prokhorov, and H.-J. Weiss (1990), *Thin Solid Films* **189**, 283–291.
- Schenck, P. K., D. W. Bonnell, and J. W. Hastie (1989), *J. Vac. Sci. Technol. A* **7**, 1745–1749.
- Singh, R. K., O. W. Holland, and J. Narayan (1990), *J. Appl. Phys.* **68**, 233–247.
- Singh, R. K., and J. Carignan (1992), *Mater. Res. Soc. Symp. Proc.* **236**, 539–544. (Note that the ordinate axis in Figs. 1b and 3 is mislabelled as the FWHM when it is actually twice the FWHM.)
- Ulmer, G., B. Hasselberger, H. G. Busmann, and E. E. B. Cambell (1990), *Appl. Surf. Sci.* **46**, 277–278.
- Venkatesan, T., X. D. Wu, A. Inam, and J. B. Wachtman (1988), *Appl. Phys. Lett.* **52**, 1193–1195.
- Vorob'ev, O. B., V. I. Kozlov, V. V. Korneev, V. N. Okhrimenko, B. V. Seleznev, and O. Yu. Tkachenko (1991), *Supercond. Phys. Chem. Technol.* **4**, 1935–1937.

## REFERENCES

- Anissimov, S. I., Ya. A. Imas, et al. (1970) "Action of Powerful Laser Radiation on Metals," Nauka, Moscow.
- Gaponov, S., B. Luskin, and N. Salashchenko (1981), *JETP Lett.* 33, 517.
- Glang, R. (1977), "Thin film technology," Soviet Radio, Moscow.
- Kashchiev, D. (1977), *J. Cryst. Growth* 40, 29.
- Kashchiev, D. (1978), *Thin Solid Films* 55, 399.
- Landau, L., and E. Lifshitz (1976), *Statistical Physics*, Nauka, Moscow.
- Metev, S. (1986), in *Laser Processing and Diagnostics (II)* (D. Bäuerle, K. L. Kompa, and L. Laude, eds.), European Materials Research Society Symposium Proceedings, Les Ulis Cedex, France, p. 143.
- Metev, S., and K. Meteva, (1989), *Appl. Surf. Sci.* 43, 402.
- Metev, S., and K. Meteva (1992), in *Photons and Low Energy Particles in Surface Processing*, volume 236, Materials Research Society, Pittsburgh, p. 417.
- Metev, S., and M. Sendova, (1988), in *Trends in Quantum Electronics*, volume 1033, SPIE, Bellingham, p. 260.
- Sankur, H., and J. T. Cheung, (1988), *Appl. Phys.* A47, 271.
- Veiko, V., S. Metev, et al. (1980), *J. Phys. D: Appl. Phys.* 13, 1565.
- Venables, J. A., G. D. T. Spiller, and M. Hanbuecken, (1984), *Rep. Prog. Phys.* 47, 399.

## CHAPTER 10

## NOVEL PULSED LASER DEPOSITION APPROACHES

ARUNAVA GUPTA

IBM Research Division  
 Thomas J. Watson Research Center  
 Yorktown Heights, New York

## 10.1 INTRODUCTION

Over the past few years, the pulsed laser deposition (PLD) technique has emerged as one of the simplest and most versatile methods for the deposition of thin films of a wide variety of materials. The stoichiometric removal of constituent species from the target during ablation, as well as the relatively small number of control parameters, are two major advantages of PLD over some of the other physical vapor-deposition techniques. While the limited number of control parameters certainly reduces the process complexity, it also often restricts the ability to optimize the growth conditions and properties of the films in order to meet the requirements for their practical applications. In this respect, it is advantageous to have additional process parameters, with preferably independent control, which can be varied for affecting film growth properties. In particular, the ability to independently manipulate the growth kinetics during PLD in order to tailor the properties of resulting films is highly desirable.

This chapter focuses on some of the novel approaches that have been pursued to either enhance the process capabilities, or to modify the properties of the films produced by the PLD technique. Considering that the capabilities of the so-called basic PLD technique itself have yet to be fully explored, there is already a large body of literature on an impressive variety of enhancement and modification features to the basic approach. In most of these novel approaches, an additional source is added to the conventional PLD setup, whereby either the plume properties or the species mix incident on the substrate is modified in attempts to influence film growth. It should be mentioned that, with some exceptions, most of these enhancement sources are

not truly unique to PLD, but have also been successfully used in the past in other deposition techniques, like evaporation and sputtering.

The utilization of novel approaches has essentially mirrored the growth of the basic PLD technique itself, with most of the activity in this area being reported after the success of PLD in the growth of high  $T_c$  films. It is therefore not surprising that an overwhelming majority of the novel PLD approaches have so far been devoted primarily to the growth of high  $T_c$  films, particularly  $\text{YBa}_2\text{Cu}_3\text{O}_{7-x}$  (YBCO). There has also been some novel process development work reported on other materials, however, notably ferroelectric oxides and diamondlike carbon films. A number of the novel deposition approaches have been motivated by the need to grow films, like the superconducting oxides, at lower temperatures and pressures. Another major thrust area for these novel approaches has been in influencing and modifying the growth properties of PLD films. These include growth of films with preferred crystalline orientations, stabilization of metastable phases, and improvements in surface morphology.

An overview of some of the novel PLD approaches has recently appeared in the literature as part of a general review on PLD (Saenger, 1993). The present chapter provides an updated and more comprehensive review of the subject. The first three sections provide an overview of some of the novel approaches that have been employed for enhancing the gas-phase and/or surface interactions during PLD growth by supplying additional molecular, atomic, or ionic species. The use of background gases during deposition is reviewed in Section 10.2, with particular emphasis on the use of molecular oxidizer gases other than  $\text{O}_2$ . Section 10.3 contains a description of the work reported in the literature on the use of a concurrent source of neutral atomic species, primarily O atoms, during PLD. Plasma and ion beam-assisted deposition approaches are discussed in Section 10.4. This has been a particularly active field of investigation, with many different experimental configurations and techniques being utilized for ion bombardment during growth. The last two sections contain an overview of the work involving additional laser irradiation during deposition, both for enhancing the growth properties of films, and also for gaining a better understanding of the ablation and growth processes. Experiments employing surface irradiation and heating of the film during growth are discussed in Section 10.5, while Section 10.6 presents a description of the work involving the use of two laser beams for target ablation. Section 10.7 provides some concluding remarks.

## 10.2 DEPOSITION IN THE PRESENCE OF A BACKGROUND GAS

One of the most common modifications to the basic PLD approach involves the addition of a background gas during the deposition process. The addition of a background gas helps not only in slowing down, and thereby moderating

the energy of the ablated species, but also causes a significant reduction in the concentration of ejected ions from the target that are transmitted to the substrate (Geohegan, 1991). Additionally, for the formation of compound thin films like oxides and nitrides, the interaction of the plume with a reactive background gas plays an important role in producing the atomic and molecular precursors required for the growth of the compound phase.

For the growth of oxide films, it is usually necessary to maintain an oxidizing environment during the deposition process in order to help form and stabilize the desired crystal phase at the deposition temperature. Nonetheless, there are some oxides (e.g.,  $\text{CeO}_2$ ) that are extremely stable, even at high temperatures, and can be easily deposited in a vacuum environment from an oxide target (Koinuma et al., 1991). In an early report of reactive PLD, Gaponov et al. (1979) demonstrated the growth of single-crystalline  $\text{ZrO}_2$  on a NaCl substrate by ablation of a Zr target in an oxygen background. More recently, the use of an oxidizing gas has become relatively routine for the in situ growth of high  $T_c$  oxide films. For obvious practical reasons, most of the early work related to the in situ growth of high  $T_c$  oxides was limited to the use of molecular oxygen as the oxidizer gas. While generally successful, the effectiveness of  $\text{O}_2$  as an oxidizing agent is somewhat limited because its low activity requires the use of relatively high pressures and deposition temperatures for the growth of good-quality superconducting oxide films. For example, PLD growth of YBCO films with  $T_c \sim 90\text{ K}$  usually requires the use of 100–200-mtorr background  $\text{O}_2$  and a deposition temperature of 700–750°C. Recently, a number of other oxidants, for example, nitrous oxide ( $\text{N}_2\text{O}$ ), nitrogen dioxide ( $\text{NO}_2$ ), and ozone ( $\text{O}_3$ ) have been shown to be more effective for the growth of superconducting oxide films at lower pressures and at somewhat reduced temperatures.

Depending on the background gas pressure during deposition, both gas-phase (i.e., plume-background gas) and surface reactions will be important for the oxidation process, with the latter contributing almost exclusively at lower pressures. A schematic diagram illustrating some of the possible gas-phase and surface oxidation reactions occurring during deposition of YBCO films is shown in Figure 10.1. For the sake of simplicity, only interactions involving neutral cation and anion species have been included. For background gas pressures typically used for the growth of good-quality films, there will be significant interaction of the ablated cation species with the oxidizer gas leading to the formation of oxides. The oxidizer gas can also undergo photon and electron-impact dissociation during the ablation process, primarily in the vicinity of the target, to produce atomic oxygen. This is in addition to the atomic oxygen directly released from the target along with molecular oxygen and the cation species. Some of the generated atomic oxygen will be lost during transport to the substrate as a result of chemical reactions with the background gas. Similarly, the cation species are also attenuated due to reactions and elastic scattering during passage. The unattenuated atomic and molecular



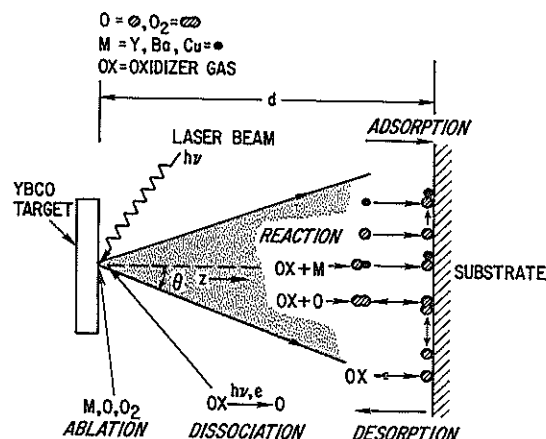


Figure 10.1. Schematic illustration of the various gas-phase and surface processes relevant for oxidation during PLD of YBCO films in an oxidizing background gas. (From Gupta, 1993.)

species that arrive and are adsorbed on the substrate surface undergo a complex series of oxidation, recombination, and desorption steps, which eventually lead to the formation of the YBCO phase.

Other than molecular oxygen, nitrous oxide has perhaps been the most commonly used oxidizer gas during growth of superconducting oxide films. It has been successfully used as a background gas during growth of YBCO (Koren et al., 1989),  $Bi_2Sr_2CaCu_2O_8$  (Kanai et al., 1989), and  $Nd_{1.85}Ce_{0.15}CuO_4$  (Kusmaul et al., 1992; Mao et al., 1992) films. Interestingly, despite its low dissociation energy (1.67 eV),  $N_2O$  is thermally quite stable and relatively unreactive in the gas phase at temperatures below 700°C. It can, however, be efficiently dissociated to produce atomic oxygen by photon and electron-impact dissociation during the ablation process for incorporation into the growing film (Gupta et al., 1992a). Kanai et al. (1989) have observed the crystallization of  $Bi_2Sr_2CaCu_2O_8$  films at a substrate temperature as low as 480°C under  $N_2O$  gas flow. Similarly, the growth temperature for obtaining good-quality YBCO films can be reduced by 50–100°C by using  $N_2O$  instead of  $O_2$  (Koren et al., 1989). High-quality  $Nd_{1.85}Ce_{0.15}CuO_4$  (NCCO) films, exhibiting sharp resistive transitions, have also been produced using  $N_2O$ . It has been speculated that, while  $N_2O$  allows sufficient oxygen to be incorporated into the growing NCCO film due to the formation of atomic oxygen, in between laser pulses the oxygen activity for  $N_2O$  is lower than for  $O_2$ , resulting in a lower overall oxygen concentration in the film (Kusmaul et al., 1992).

Another oxidizer gas that has gained some attention lately, particularly for use at low pressures, is nitrogen dioxide. It has been successfully used for epitaxial growth of a variety of cuprate films, including  $Bi_2Sr_2CuO_6$  (Kanai et

al., 1990),  $Sr(Ba)CuO_2$  (Yoshimoto et al., 1991),  $Ca_{1-x}Sr_xCuO_2$  (Li et al., 1992), and YBCO (Gupta et al., 1992a). The high sticking coefficient and rapid dissociation of  $NO_2$  to produce a large concentration of oxygen adatoms on the surface is most likely responsible for its high effectiveness. Moreover, because of its substantial vertical electron affinity, the gas-phase reaction cross sections for formation of oxides are also much higher for  $NO_2$  (Gupta, 1993). Recent experiments using laser-induced fluorescence have indeed shown that  $NO_2$  and  $N_2O$  are much more effective than  $O_2$  in the gas-phase production of  $CuO$ , with the order of reactivity being  $O_2 < N_2O < NO_2$  (Otis et al., 1993). In addition to the formation of oxides, the gas-phase production of atomic oxygen by photochemical and electron-impact dissociation is also very efficient with  $NO_2$ . The effectiveness of  $NO_2$  for the formation of the  $Bi_2Sr_2CuO_6$  (BSCO) phase under low-pressure conditions has been demonstrated by Kanai et al. (1990), with crystallized films of BSCO being obtained at pressures as low as 0.1 mtorr. Similarly, films of the infinite-layer phase,  $Ca_{1-x}Sr_xCuO_2$ , have been grown in a low-pressure  $NO_2$  ambient both by codeposition and successive stacking of atomic layers (Li et al., 1992).

Ozone is even more effective as an oxidizing agent than nitrogen dioxide. It is readily dissociated both in the gas phase and on the surface to produce atomic oxygen. Moreover, unlike  $N_2O$  and  $NO_2$ , there is no possibility of nitrogen contamination of the film. Because of these advantages, ozone is being increasingly used for the low-pressure growth of superconducting oxide films, particularly in molecular beam epitaxy and coevaporation. However, so far there are only a few reports of its usage during PLD. Tabata et al. (1991a) have reported the use of an 8%  $O_3/O_2$  mixture at 100 mtorr pressure for the growth of  $(La, Sr)_2CuO_4/Sm_2CuO_4$  superlattices. A similar gas mixture has been used by Hontsu et al. (1991) for the deposition of YBCO films on  $LaSrGaO_4$  substrate. The 8%  $O_3/O_2$  gas mixture is relatively safe to handle, since it can be continuously produced in a silent arc discharge ozone generator and fed directly into the chamber. On the other hand, special care has to be taken for distilling and storing ozone for its use in the pure state because of its extreme instability and propensity for explosive decomposition. Horvath et al. (1985) have discussed in detail the precautions to be taken for the stabilization, storage, and safe handling of pure ozone.

In a direct comparison of the effectiveness of different oxidizer gases, Kanai et al. (1990) have studied the crystallization of BSCO films grown in  $O_2$ ,  $N_2O$ , and  $NO_2$  gas ambients. In a more detailed comparison, Gupta et al. (1992a) have studied the efficacy of  $O_2$ ,  $N_2O$ , and  $NO_2$  as oxidizing agents for the in situ growth of YBCO films as a function of deposition temperature and laser wavelength, for a wide range of oxidizer gas pressure (0.1–200 mtorr). For the three gases used, the superconducting transition temperature of the YBCO films has been found to increase with increasing oxidant pressure, with zero-resistance temperature  $\sim 90$  K only obtained in films prepared in a relatively high pressure (150–200 mtorr) of oxidizer gas. At lower pressures, the

transition temperature, while being depressed, has been found to be quite sensitive to the nature of the oxidant, the laser wavelength, and the deposition temperature. The fact that a relatively high background pressure is required for all the oxidizer gases to obtain films with optimal  $T_c$  is consistent with the suggestion that oxidation during growth of YBCO by PLD is kinetically limited by the instantaneous flux of species impinging onto the substrate (Gupta and Hussey, 1991). The films grown in a low-pressure background of oxidizer gas, with depressed  $T_c$ , generally exhibit an expanded  $c$ -lattice parameter, as has also been observed in films deposited by other techniques (Gupta et al. 1992a). It should be pointed out that the high oxygen requirement, which has been observed for the growth of optimal  $T_c$  YBCO films, may not be generally true for all cuprates. It is quite likely that some of the oxides, especially those with simpler structures, can be stabilized as an oxygen-deficient phase without any additional cation defects, which can then be oxygenated in between laser pulses, or during the cooldown cycle.

For the growth of some multicomponent oxides, the presence of an oxidizing background gas may not be sufficient to form the desired phase. This is particularly valid in instances where preferential loss of cation species can occur during deposition, either due to excessive gas-phase scattering during transport to the substrate, or volatilization from the film surface at high temperatures. In such cases, it is usually necessary to use an off-stoichiometric ablation target to compensate for the loss. For example, during deposition of  $\text{LiNbO}_3$  films, the lighter Li atoms are readily scattered in collisions with the background gas, and are also lost from the surface at high growth temperatures due to its high volatility, resulting in growth of multiphased films enriched in Nb. However, by using a Li-enriched target for ablation, and reducing the background oxygen pressure during deposition, Shibata et al. (1992) have been able to grow good-quality epitaxial films of  $\text{LiNbO}_3$  on (001) sapphire substrates. In another novel approach,  $\text{LiNbO}_3$  films have been grown on Si substrates from a stoichiometric target by using an appropriate background gas mixture comprised of oxygen and argon (Ogale et al., 1992). Although the exact role of the argon-oxygen mixture in compensating for the loss of Li during growth is unclear, it has been suggested that the mixed gas ambient offers a way to partially separate the physical and the chemical aspects of the radicals impinging onto the substrate, thereby providing flexibility in controlling the film stoichiometry. Gas mixtures of oxygen and nonreactive buffer gases may also prove to be useful for the growth of other multicomponent oxide films where loss of cation stoichiometry is a problem.

Apart from the use of oxidizer gases, there are only a few reports of the use of other reactive background gases during PLD of compound thin films. Some of the other reactive gases that have been used include:  $\text{H}_2$  for the growth of hydrogenated diamondlike carbon films (Malshe et al., 1990; Bourdon and Prince, 1991; Pappas et al., 1992),  $\text{NH}_3$  for BN films (Murray et al., 1989), and  $\text{N}_2$  for the growth of AlN (Norton et al., 1991) and TiN (Craciun and Craciun, 1992) films.

In the commonly used configuration for the use of a reactive gas, as discussed earlier, the gas is bled into the vacuum chamber continuously at a fixed flow rate, while the chamber is simultaneously pumped to maintain a constant background pressure during deposition. Considering the directed nature of the ablated plume, a collimated beam of the gas can also be efficiently used during deposition for interaction with the plume, or for reaction at the substrate surface (Singh et al., 1989). This approach can help in preserving, or even enhancing, the interaction between the ablated species and the introduced gas to facilitate formation of the desired phase, while maintaining a low-pressure background in the chamber.

A pulsed, high-intensity jet of oxidizing gas has been used for growth of YBCO films in a low-pressure background (Gupta and Hussey, 1991). In this approach, a pulsed source of  $\text{O}_2$  or  $\text{N}_2\text{O}$  is directed at the substrate, with the opening of the pulsed valve and the triggering of the laser synchronized with appropriate delay so that the gas jet and ablated fragments arrive at the substrate at the same time. This supplies the necessary oxygen to form the YBCO phase, while maintaining a low oxygen background. The ability to grow superconducting films at low background pressures has allowed usage of reflection high-energy electron diffraction (RHEED) for in situ monitoring of film growth during PLD (Chern et al., 1992).

In another novel approach for the introduction of gases, a Smalley-type cluster beam source has been used for entraining, within a high-pressure molecular beam expansion, the ablated fragments from a rotating target rod (Ögmen and Duley, 1989; Herron and Garvey, 1991). Besides transport of the ablated species to the target, the rapidly expanding gas stream also functions to cool the ablated fragments and enhance the chemical interaction in the presence of a reactive gas. Using an expanding gas mixture of  $\text{He-H}_2$  during ablation of graphite, Ögmen and Duley (1989) have been able to produce good-quality hydrogenated carbon films. Furthermore, by adjusting the  $\text{H}_2$  concentration in the flowing  $\text{He-H}_2$  mixture, they have demonstrated the possibility of varying the bandgap of the deposited films. In a slightly modified approach, Herron and Garvey (1991) have used pulsed sources of  $\text{H}_2$ ,  $\text{O}_2$ ,  $\text{N}_2$ , and Ar gases for expansion during ablation of copper to deposit thin films of Cu and CuO on various substrates.

### 10.3 DEPOSITION IN THE PRESENCE OF A SEPARATE SOURCE OF NEUTRAL ATOMIC SPECIES

Besides the high flux of neutral and ionic species produced during the ablation process, a continuous flux of separately generated neutral atomic species can also be directed at the substrate for incorporation into the growing film. This includes both stable and unstable atomic species, that may be produced by dissociation, evaporation, or sputtering from a separate source.

Unstable gas-phase species, like atomic O, are extremely reactive and are much more efficiently adsorbed on the surface to produce adatoms than the

molecular oxidizer gases. Atomic oxygen can thus be used for efficient, low-pressure oxidation of films. A steady flow of O atoms can be produced quite readily by dissociation of  $O_2$ , or other molecular sources of oxygen, in a downstream microwave or radio frequency discharge. Although some ionic species are also produced in the discharge, the concentration of ions actually reaching the substrate from the remote source is extremely small as compared to ion beam sources, which are discussed in the next section. Atomic nitrogen can similarly be produced in a  $N_2$  discharge for the growth of nitrides, although the efficiency of producing N atoms in a discharge is significantly lower than that of O atoms.

The use of microwave and radio frequency atomic oxygen sources have been shown to be very effective for the low-pressure PLD growth of YBCO films (Greer and Van Hook, 1990; Frey et al., 1992). Likewise, the oxygenation of as-deposited tetragonal YBCO films to form the orthorhombic phase can also be enhanced in the presence of atomic oxygen at low pressures (Yamamoto et al., 1990). An atomic oxygen source has also been employed in conjunction with a pulsed source of  $O_2$  for the growth of YBCO and  $La_{1.85}Sr_{0.15}CuO_4$  films (Gupta et al., 1992b; Chern et al., 1992). The continuous source of atomic oxygen provides the necessary oxygen activity at low pressures for thermodynamic stability of the phase at the growth temperature, while the additional high instantaneous  $O_2$  flux from the pulsed source supplies the oxygen required to oxidize the ablated cation species during the time of their arrival and condensation on the substrate.

Atomic oxygen can also be supplied by a pulsed source. For example, Koren et al. (1989) have generated O atoms in the vicinity of the substrate by synchronized 193-nm excimer laser photolysis of an  $N_2O$  background gas during PLD of YBCO. The films are deposited using a frequency-tripled Nd:YAG laser at a substrate temperature of 600°C. The  $T_c$  of the films has been observed to vary as a function of delay between the ablation and photolysis pulse, with the best properties obtained when the atomic oxygen is provided during the time of arrival of the ablated fragments at the substrate. On the other hand, an analogous experiment by Schwab et al. (1992), using higher laser fluences ( $1-7.5 \text{ J/cm}^2$ ) for the photolysis of  $N_2O$ , actually shows a deterioration in the superconducting properties of YBCO films, irrespective of time delay. The authors have tentatively ascribed the decrease in  $T_c$  to the reducing behavior of NO, which is formed from the reaction of the O atoms with the background  $N_2O$  gas. In a related experiment, Minamikawa et al. (1990) have used 193-nm radiation for ablation of YBCO in an  $N_2O$  ambient, in which a part of the laser beam is split up and directed at the substrate for surface irradiation (see Section 10.5). They have observed that at a deposition temperature of 580°C, the  $T_c$  of YBCO films grown on (100) MgO substrates initially increases with increasing irradiation fluence up to  $\sim 60 \text{ mJ/cm}^2$ , before decreasing at higher fluences.

Additional source(s) of stable atomic species can also be supplied during

PLD from a continuous source for incorporation into the growing film. This approach has been used by Dikshit et al. (1989) to demonstrate the synthesis of composite materials in thin-film form. They have shown that PLD of  $\alpha\text{-Fe}_2O_3$ , concurrently with thermal evaporation of aluminum, leads to a composite state defined by the presence of clusters of iron-related material in the aluminum matrix.

## 10.4 PLASMA AND ION BEAM-ASSISTED DEPOSITION

The presence of ionic species during deposition, even in low concentrations, can strongly influence the growth and properties of films. A wide range of film properties can be modified in the presence of ions because of enhanced physical and chemical processes occurring on the surface during growth. Some of the beneficial effects of ion-assisted deposition include: improved adhesion and surface morphology, preferred formation of a specific phase or crystal orientation, and lower epitaxial growth temperatures. These effects have been observed and well documented for a wide variety of thin-film materials grown by conventional deposition techniques in the presence of ions [for example, see Kay and Rossmagel (1989)]. In particular, the energy of the ions and the ion-to-atom arrival ratio have an important influence on the microstructure and chemical composition of a growing film. Theoretical simulations, using molecular dynamics and collision cascade approaches, have been successful in explaining some of these effects (Muller, 1989).

Ionic species are ordinarily produced during the ablation process, and depending on the target composition, laser fluence, background gas pressure, and other process parameters, the concentration, and energy of these species can vary over a wide range. In a simple and elegant experiment, Gaponov et al. (1977) have isolated the effect of ions during PLD growth of PbTe films at room temperature on KCl substrates. In this experiment, they have monotonically varied the ion flux arriving at three identical substrates by placing them symmetrically between a pair of biased electrodes during deposition. They have observed that with increasing ion flux arriving at a substrate, the film structure improves from polycrystalline to single crystalline. It is worth pointing out that while low- and medium-energy ion irradiation can often be beneficial for film growth, as demonstrated by the preceding experiment, the presence of high-energy ions can cause significant damage, or even sputtering, during film growth. In this respect, the use of a background gas during PLD provides a simple and effective way for controlling the energy of the ablated ionic (and neutral) species in the plume, as was mentioned previously.

Several experimental techniques have been used in conventional deposition processes to enhance the bombardment of the surface with moderate-energy ionic species during film growth. These techniques can also be easily adapted with minor modifications for PLD. For example, a plasma discharge can be

initiated during PLD to produce additional reactive species. Alternatively, a DC bias voltage can be applied to the substrate to accelerate and attract the positively or negatively charged ionic species in the plasma, and thereby subject the growing film surface to pronounced ion bombardment. Reactive and nonreactive ionic species, with controlled energies, can also be externally generated using ion beam sources. A sampling of some of the ion-assisted processes that have been used during PLD are schematically illustrated in Figure 10.2. The details of the different experimental configurations and techniques, and the properties of some of the films that have been obtained using ion-assisted techniques, are discussed in the following sections.

#### 10.4.1 Plasma-Assisted Deposition

Perhaps the simplest method for enhancing the ablated plasma plume in vacuum, or for creating an additional plasma discharge in the presence of a background gas, involves placing a biased ring-shaped electrode between the target and the substrate (Figure 10.2a). The plasma is normally initiated by the laser pulse, and a continuous discharge can be sustained under appropriate bias voltage and gas pressure conditions.

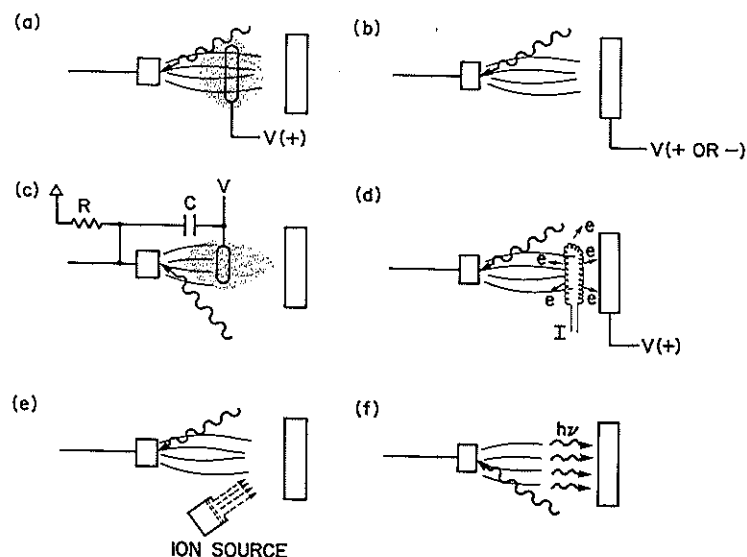


**Figure 10.2.** Schematic illustrations of some of the novel ion- and photon-assisted PLD approaches. (a) PLD with biased electrode placed between target and substrates. (b) PLD with biased substrate. (c) PLD with pulsed capacitive discharge. (d) Filament-assisted PLD. (e) Ion beam-assisted PLD. (f) PLD with simultaneous or time-delayed surface irradiation. (Adapted from Saenger, 1993.)

In an early report on plasma-assisted deposition of high  $T_c$  oxide films, Witanachchi et al. (1988) reported the growth of YBCO with  $T_c$  of  $\sim 85$  K at a substrate temperature as low as  $400^\circ\text{C}$ . They deposited the films in a low-pressure (0.1-mtorr) oxygen discharge, with a ring electrode voltage of  $+300$  V and the target held at ground potential. More recent experiments from the same group, however, show that the reduction in deposition temperature achieved by use of a bias ring is more moderate, being of the order of  $50$ – $70^\circ\text{C}$  (Kwok et al., 1991). This reduction in temperature has been correlated with an increase in the ion (primarily  $\text{O}_2^+$ ) flux arriving at the substrate. A reduction of the YBCO processing temperature has also been reported by Singh et al. (1989) using a biased ring with  $+300$ – $400$  V DC, with background  $\text{O}_2$  pressure in the range of  $180$ – $200$  mtorr. For the higher  $\text{O}_2$  pressure and substrate-ring-target geometry used in this experiment, the bias voltage is not sufficient to introduce a continuous discharge. Excellent quality films, exhibiting high  $T_c$  and sharp resistive transitions, have been obtained at  $650^\circ\text{C}$  with the biased ring. However, the epitaxial quality and superconducting properties of the films are observed to degrade at lower temperatures. Fried et al. (1991) have determined from the optical emission of the ablated plume species from a YBCO target that the intensity of all the emitting species, including the oxides produced by reactions in the gas phase, is enhanced in the presence of an electric field. They suggest that electron collisions with constituents in the plume are responsible for the enhanced emission.

Plasma-assisted deposition has also been recently used for the growth of ferroelectric oxide films. Roy et al. (1992) have shown that the incorporation of a low pressure  $\text{O}_2^+$  DC glow discharge using a ring electrode (up to  $300$  V) between the substrate and the target facilitates the formation of the ferroelectric perovskite phase, over the nonferroelectric pyrochlore phase, during the growth of  $\text{PbZr}_{1-x}\text{Ti}_x\text{O}_3$  (PZT) films. These films have also exhibited increased crystallinity and improved electrical behavior as compared to films deposited without the plasma discharge. The investigators have suggested that the role of the low-pressure discharge may be a combination of (a) enhancing the chemical activity via activated oxygen species, and (b) probable intrinsic bombardment by low energetic species.

In an alternative biased deposition approach, which is also commonly used in conventional plasma processing, a DC voltage is applied to the substrate to enhance ion bombardment of the growing film (Figure 10.2b). The effects of both positive and negative biasing of the substrate for the deposition of YBCO films in a low-pressure oxygen ambient, at different substrate temperatures, have been studied using this technique. It has been observed that at substrate temperatures high enough to yield good films, the bias field has little effect on the YBCO film properties (Chrisey et al., 1990). On the other hand, at reduced deposition temperatures ( $< 700^\circ\text{C}$ ), Izumi et al. (1990) have shown that the addition of a negative or positive bias voltage ( $300$ – $500$  V) to the substrate significantly reduces the degradation of film properties that is normally observed in films prepared at these temperatures using standard PLD in an  $\text{O}_2$

ambient. The dependence of  $T_c$  on deposition temperature, for various bias fields, is shown in Figure 10.3. It is observed that both positive and negative bias voltages improve the  $T_c$  of the films at low temperatures, with positive bias voltages being somewhat more effective. At low temperatures, the deposited films in the presence of a bias field also exhibits an enhancement of the degree of  $c$ -axis preferential orientation. Moreover, it has been noted that positively biased films exhibit greater  $c$ -axis preferential orientation than do negatively biased ones. Time-resolved optical observations in the presence of a bias field have revealed that an additional emission component of short duration, probably from the oxygen plasma, occurs a few microseconds after the arrival of the laser pulse (Izumi et al., 1990). The improvement in crystallinity at low temperatures has been attributed to this emission.

A substrate bias field has also been used during PLD growth of Ge (Lubben et al., 1985) and carbon films (Sato et al., 1988; Wagal et al., 1988) in vacuum. By applying a negative bias to the substrate with respect to the target during deposition of Ge films, Lubben et al. (1985) have observed a decrease in the film growth rate due to increased sputtering of the film by accelerated ions. The negative bias also results in a significant reduction in the particulate density in the films, suggesting that the particles produced during ablation are negatively charged. Reduction in particulate density has also been observed by Sato et al. (1988) when a  $-500$ -V bias field is applied during deposition of carbon on an unheated substrate. Additionally, films deposited at  $50^\circ\text{C}$  exhibit properties

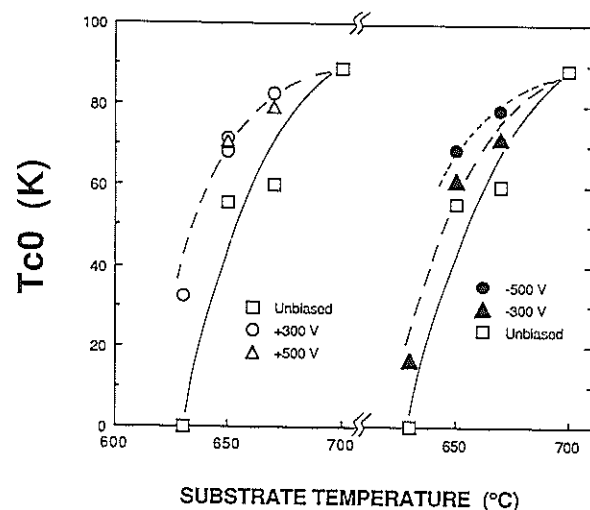


Figure 10.3. Dependence of the zero-resistance temperature of YBCO films as a function of deposition temperature for different positive and negative substrate bias voltage conditions. (From Izumi et al., 1990.)

characteristic of diamondlike carbon (DLC), with improved adhesion, as compared to films deposited at room temperature.

In another ion-assisted approach for improving film properties, the level of plume excitation during PLD is increased by coupling capacitively stored energy to the laser-ablated spot in synchronism with the laser pulse (Figure 10.3c). This plasma hybrid technique has been used for deposition of DLC films from a graphite target in vacuum (Krishnaswamy et al., 1989; Collins et al., 1989; Davanaloo et al., 1990; Pappas et al., 1992). Krishnaswamy et al. (1989) have obtained uniform deposition of DLC films over a significantly large area by using this technique. Furthermore, films deposited on (100) Si substrates using 308-nm radiation show improved optical properties and increased hardness as compared to films deposited by conventional PLD. Using 248-nm radiation, however, Pappas et al. (1992) have reported obtaining good-quality DLC films using the excimer laser alone, with no significant improvement in properties observed with the enhanced-plasma process. They have attributed their results to the intrinsically higher excitation of the plume because of increased absorption at 248 nm. The plasma hybrid technique has also been used by Rengan et al. (1990) to produce a hydrogen discharge during ablation of graphite. The hydrogen plasma has been found to aid in the nucleation and growth of diamond-shaped particles on Si substrates at  $860^\circ\text{C}$ .

In a related plume excitation approach, termed *laser-assisted vacuum arc deposition* (laser arc), the PLD technique has been combined with the efficiency of the vacuum arc (Scheibe et al., 1990; Pompe et al., 1992) to aid film growth at low temperatures. In this arrangement, a ring-shaped or planar anode is arranged parallel to the target. The anode and the target-cathode are connected with a pulsed current so that the laser-induced plasma initiates a vacuum arc discharge as soon as it reaches the anode. The arc-discharge-induced plasma has a significantly higher degree of ionization (up to 90% for metals) than conventional PLD, with moderate ion energies (10–50 eV). This technique has been used to grow films of carbon, titanium, and Ti/TiC multilayers with reduced density of particulates.

An ion-assisted technique, which has been successfully used in the past for enhancing the production of negative ions during plasma-deposition processes, involves injection of electrons into the plasma from an external source, such as a thermoionic filament or a hollow cathode. Leuchtner et al. (1992) have adapted the filament-assisted technique for the PLD growth of PZT films in an oxygen ambient. A low-energy electron-emitting filament is placed between the substrate and the target (Figure 10.2d), which produces oxygen ions (primarily  $\text{O}_2^-$  and  $\text{O}^-$ ) due to electron attachment. These ions are collected at the substrate by application of a small positive bias field. The oxygen anions have been found to substantially improve the quality of PZT films deposited on MgO substrates at  $550^\circ\text{C}$  by enhancing surface reactions.

Figure 10.4a shows the X-ray diffraction patterns of PZT films, prepared using the filament-assisted deposition technique, for three different electron-

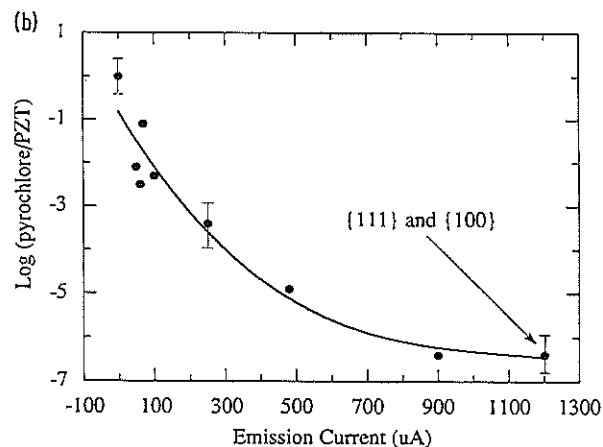
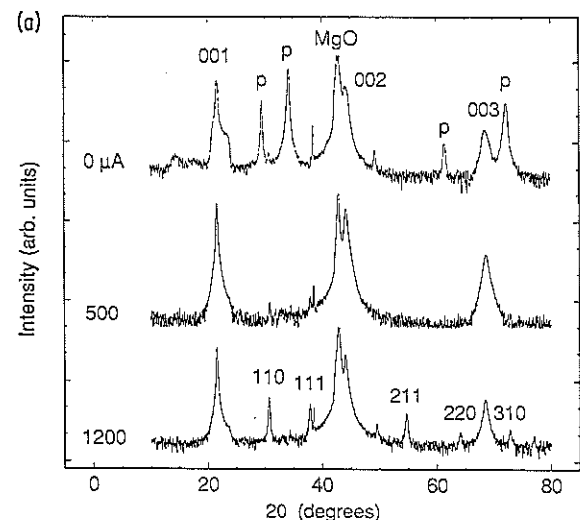


**Figure 10.4.** (a) X-ray diffraction patterns of PZT films, deposited on (100) MgO substrates at a temperature of 550°C, for three different filament emission currents. The pyrochlore peaks are marked with P, while the other indexed peaks correspond to the perovskite phase. (b) Semilog plot of the measured pyrochlore/perovskite ratio as a function of filament emission current. (From Leuchtner et al., 1992.)

emission currents. Without any electron emission (0  $\mu\text{A}$ ), a significant fraction of the film is composed of the nonferroelectric pyrochlore phase (marked p). On the other hand, for an emission current of 500  $\mu\text{A}$ , the X-ray pattern of the films shows an entirely *c*-axis-oriented, ferroelectric perovskite phase. As the emission current is increased to 1200  $\mu\text{A}$ , additional crystalline orientations of the perovskite phase are also observed. When optimized in terms of emission current, the use of the filament causes a decrease by almost six orders of magnitude in the ratio of the pyrochlore phase relative to the perovskite phase, as seen in Figure 10.4b. Aside from the structural modifications, a significant improvement in the surface morphology has also been observed with increase in the electron-emission current from 0  $\mu\text{A}$  to 400  $\mu\text{A}$  (Leuchtner et al., 1992).

#### 10.4.2 Ion Beam-Assisted Deposition

While the various plasma-assisted deposition techniques discussed in the previous section are relatively easy to implement in a conventional PLD apparatus, they do not always provide adequate control on the physical and chemical characteristics of the ions incident on the substrate during film growth. In this regard, an independent source of ions, such as from Kaufmann-type grid sources or from electron cyclotron resonance (ECR) sources, can supply a much more controlled source of ions (Figure 10.2e). These broad-beam sources provide high ion fluxes over relatively large working areas, with independent control of the flux, energy, direction, and charged state of the ions. Ion beam-assisted deposition therefore offers a distinctive advantage for the controlled and reproducible growth of films. Normally, the ion beam sources are operated in a continuous mode with ion energies typically in the range 10 eV to 2000 eV. Moreover, to avoid significant background scattering, the ion beam-assisted deposition has to be carried out in a relatively low-pressure background.

Ion beam-assisted evaporation has been particularly successful for the growth of high-quality dielectric and optical coatings with the desired bulk properties. Gluck et al. (1989) have reported the growth of dense, environmentally stable coatings of  $\text{CaF}_2$  thin films, with bulk refractive indices, grown at low temperatures (20°C) using ion beam-assisted laser deposition. A (CW) continuous wave  $\text{CO}_2$  laser beam is used for the evaporation of  $\text{CaF}_2$ , with concurrent bombardment of the substrate (GaAs and Si wafers) with  $\text{Ar}^+$ ,  $\text{O}_2^+$ , or  $\text{CF}_4^+$  ions from a Kaufmann-type ion gun. Without the ion beam, the films have lower refractive indices when grown at these low temperatures. In addition to increasing the film refractive index, the ion beam-assisted deposition also results in significantly reduced optical scatter because of the much smoother surface morphology.

Another application of ion beam bombardment during film growth is in stabilization of thermodynamically metastable phases, which are normally



difficult, or even impossible, to produce by conventional techniques. As an example, CW CO<sub>2</sub> laser evaporation, assisted by a simultaneous reactive nitrogen ion supply, has been used for the deposition of hard, cubic boron nitride (c-BN) rich films (Mineta et al., 1990). Without the ion beam, the evaporated films are amorphous with a low composition ratio of N:B. The N:B ratio in the film increases with increasing bias voltage and reaches stoichiometric value above 1 kV. The c-BN phase has been clearly identified in films grown at ion acceleration bias voltages above 0.5 kV, and increases substantially at higher acceleration voltages. Recently, a KrF excimer laser, assisted by a simultaneous supply of nitrogen ions from a Kaufmann-type ion source, has also been successfully used for the growth of oriented and adherent c-BN films on (001) oriented silicon wafers at 400°C (Ballal et al., 1992).

Besides the flux and energy density of the bombarding ions, the angle of incidence of the ion beam also has an important influence on film growth. It has generally been observed that off-normal ion bombardment of the substrate during growth can often lead to production of films with preferred orientation, even in cases where the film is poorly lattice-matched to the substrate. This is possibly caused by the preferential sputtering of grains that are not oriented, and are thus not channeled, in the direction of the ion beam. In recent work, which has important implications for large-scale applications of high  $T_c$  oxides, Reade et al. (1992) have deposited oriented yttria-stabilized zirconia (YSZ) buffer layers on polycrystalline nickel-based superalloy substrates using PLD in the presence of an Ar<sup>+</sup> beam at 30–60° incidence to the substrate. The ion beam-assisted growth produces YSZ layers with alignment of the in-plane axes in addition to the (001)-normal texture. Highly *c*-axis-oriented biaxially aligned YBCO thin films have been subsequently deposited on these layers, with  $T_c$  of 92 K and  $J_c$  (77 K,  $B = 0$  T) =  $6 \times 10^5$  A/cm<sup>2</sup> and  $J_c$  (77 K,  $B = 0.4$  T) =  $8 \times 10^4$  A/cm<sup>2</sup>. Similar improvements in the current-carrying capacity of YBCO films have also been previously observed by Iijima et al. (1992) for YBCO films deposited by PLD on biaxially oriented YSZ buffer layers that are deposited by ion-assisted sputtering. These results are very promising, and it is believed that, with further improvements of the YSZ texture, the current-carrying capacity of YBCO films on polycrystalline metallic alloys might approach that on single-crystal substrates (Reade et al., 1992).

A high concentration of atomic and ionic species can also be generated using an ECR plasma source. There have been a number of reports of the use of an ECR oxygen source for the low-temperature growth of YBCO films (Gupta et al., 1989; Deneffe et al., 1990; O'Keeffe et al., 1991). In addition to producing O<sub>2</sub><sup>+</sup> ions, an ECR oxygen plasma also produces copious amounts of atomic O. O'Keeffe et al. (1991) have observed, however, that the oxygen ions produced in the ECR plasma do not play a beneficial role in the oxidation process, and increasing the atomic-oxygen-to-ion ratio in the beam by the application of a magnetic field has actually been found to result in higher  $T_c$  in films deposited at a temperature of 640°C. Enhanced surface interactions due

to atomic O, and the reduction of damage caused by energetic ions and electrons, have been considered as possible explanations for the observed behavior. It is worth pointing out that, even under optimized conditions, YBCO films deposited at low pressures using an oxygen discharge exhibit depressed  $T_c$  as compared to films grown at higher pressures using molecular oxidizer gases.

## 10.5 LASER IRRADIATION AND HEATING OF SUBSTRATE DURING DEPOSITION

Some of the beneficial effects of ion beam-assisted deposition, such as improvements in surface morphology, preferred crystalline orientation, and lower growth temperature, can also be achieved by photon irradiation of the growing film during deposition (Figure 10.2f). Photon irradiation provides a source of energy for the selective excitation and enhancement of film growth. Improvements in film properties due to surface photo-excitation has been previously observed, using ultraviolet (UV) lamps or laser radiation, for films grown by molecular beam epitaxy and chemical vapor deposition (Bicknell et al., 1986; Abber, 1988). From a practical viewpoint, a monochromatic source of photons from a laser beam is ideally suited for surface irradiation during PLD, although other photon sources can also be used effectively with a suitable focusing arrangement.

Film-surface irradiation during growth can be effective in enhancing the surface mobility of adatoms due to photothermal and photochemical effects. This is in contrast to ion bombardment, where the kinetic energy is primarily transferred to the adatoms via momentum-transfer collision effects. Increased adatom surface mobility usually results in improvements in film-surface morphology because of enhanced nucleation and annealing of defects during growth. In the presence of a background gas, laser irradiation can also lead to selective excitation and photodissociation of the gas in the proximity of the substrate, or adsorbed on the surface, to produce precursor atoms for film growth. Energy from a laser beam, especially in the infrared, can also be used as a purely thermal source for continuous or transient heating of the substrate during deposition.

In most of the early experiments involving surface irradiation, a single laser has been used for both ablation and irradiation by splitting into two beams, where most of the laser energy is directed at the target for ablation, whereas a weaker beam ( $\sim 10$ – $100$  mJ/cm<sup>2</sup>) is incident on the substrate. In this experimental configuration, there is essentially no time delay between the arrival of the ablation beam onto the target and the arrival of the excitation beam onto the substrate. Under such conditions, the excitation laser in effect interacts with the material deposited from the previous pulses, since it arrives at the substrate prior to the arrival of the ablated plume species.

Using the split-beam arrangement with a 193-nm excimer laser, Otsubo et al. (1989) have observed some improvements in the superconducting properties of YBCO films grown at a relatively low substrate temperature (600°C) in an  $O_2$  ambient. The irradiation has also been observed to enhance the crystallization and improve the film-surface morphology. These effects have been ascribed to a photothermally induced temperature increase in the growing film-surface layer from irradiation. Substrate irradiation using 193-nm laser radiation has also been shown to be effective for the low-temperature growth of YBCO (Minamikawa et al., 1990) and BSCO (Kanai et al., 1990) films in an  $N_2O$  ambient. In these instances, the reduction of the growth temperature has, however, been primarily attributed to an increase of active O radicals generated by the photodecomposition of  $N_2O$ .

More recent experiments have used a separate laser for surface irradiation, with the expectation that the surface-irradiation effect can be enhanced by using an optimized delay between the ablation and the irradiation pulses. Superconducting films of YBCO have been grown by Estler et al. (1990) on YSZ substrates at 650°C using 308-nm laser ablation. The films have been grown both with and without the presence of a second 308-nm excimer radiation pulse incident on the substrate. In these experiments, time delays between the synchronized excimer lasers is varied from 0  $\mu s$  to 1000  $\mu s$  to explore the effect of laser irradiation (0.01–0.02 J/cm<sup>2</sup>) throughout the mass arrival time range of the ablated plume at the substrate. Surprisingly, little improvement has been observed in the overall quality of the deposited films for any time delay. Estler et al. have suggested that the lack of any major improvements in the irradiated films is due to the temporal width mismatch of the temperature increase of the substrate and growing film to that of the mass arrival on the substrate surface. This conclusion is based on model calculations that show that, while the maximum surface-temperature increase achieved by irradiation is of the order of a few hundred degrees, a significant fraction of the increase occurs for only a very short duration ( $\sim 100$  ns) because of the relatively fast conductive heat loss to the underlying substrate. Thermal calculations by Minamikawa et al. (1991) have also shown qualitatively similar results. This suggests that for photothermal enhancement of film growth, the pulse length and wavelength of the irradiation laser beam have to be carefully optimized.

The influence of laser irradiation as a function of delay, during growth of YBCO films on MgO substrates, has also been recently studied by Morimoto et al. (1992). They have used a shorter wavelength excimer laser (193 nm) and also a somewhat higher fluence (50 mJ/cm<sup>2</sup>) for irradiation than used by Estler et al. In these experiments, delayed laser irradiation of the growing film has actually been found to have a pronounced effect on the crystal orientation of YBCO films grown at temperatures below 600°C. Figure 10.5a shows the X-ray diffraction patterns of various YBCO films prepared as function of delay between the irradiation and ablation laser pulses. The films are grown on (100) oriented MgO substrates at a temperature of 540°C. It is observed that the

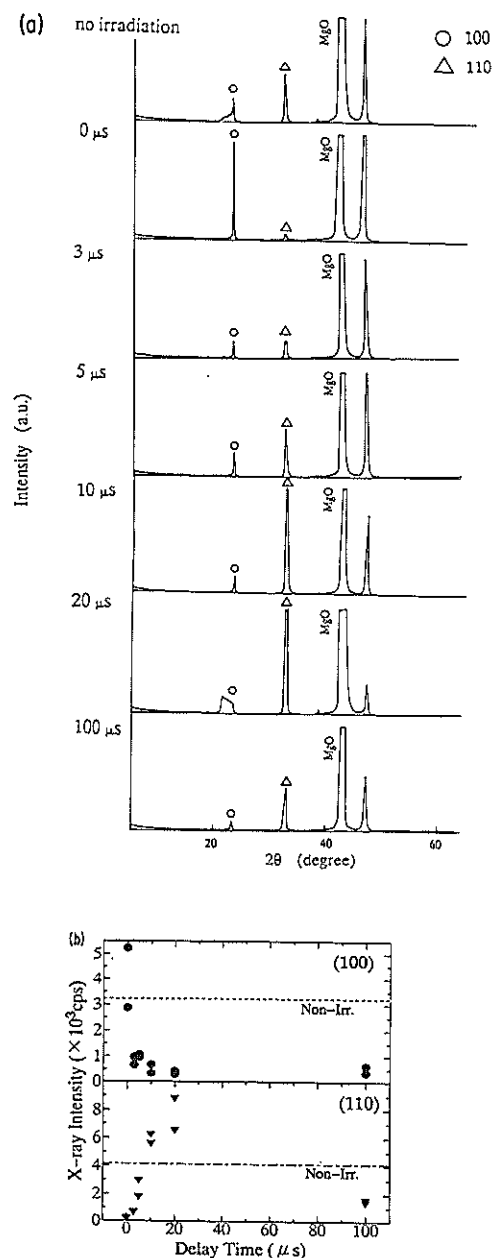


Figure 10.5. (a) X-ray diffraction patterns of YBCO films, deposited at 540°C on (100) MgO substrates, as a function of delay time between the substrate irradiation and ablation pulses. (b) Delay time dependence of the (100) and (110) diffraction peak intensities. (From Morimoto et al., 1992.)

intensity of the (110) YBCO peak increases with increasing delay, and then subsequently decreases for longer delay periods. The effect is seen more clearly in the X-ray intensity plots of the (100) and (110) peaks as a function of delay, shown in Figure 10.5b. It is observed that the optimum delay period for maximum enhancement of the (110) orientation is in the range of 10–20  $\mu$ s. This corresponds quite closely to the time of arrival of the ablated species at the substrate, suggesting that the enhancement in the (110) orientation is possibly due to reexcitation and enhanced mobility of the adsorbed species on the surface. Transient heating of the surface during irradiation may also play a role in influencing growth of grains with preferred orientation.

Surface excitation has also been observed to play an important role during the PLD growth of Pb-based ferroelectric oxides. Just as in the case of high  $T_c$  materials, there is a need for the growth of these films at low growth temperatures to minimize interfacial diffusion, and also to prevent volatilization of the Pb in the film. Additionally, the growth kinetics of the ferroelectric perovskite phase has to be enhanced, while suppressing the formation of the nonferroelectric pyrochlore phase that is normally favored at low growth temperatures. Morimoto et al. (1990) have observed that, at a growth temperature of 700°C, the fraction of the perovskite phase in laser-deposited PZT films can be increased with 193-nm irradiation in  $O_2$  and  $N_2O$  ambients. For the growth of ferroelectric  $PbTiO_3$  thin films, Tabata et al. (1991b) have reported that the epitaxial growth temperature of the films can be reduced from 500°C to as low as 300°C by simultaneous laser excitation of the growing film on a lattice-matched  $SrTiO_3$  substrate. More recently, the same group has reported results using a separate laser beam, with variable delay, for surface irradiation during growth of  $PbTiO_3$  on Pt and oxide superconductor base-electrodes (Tabata et al., 1992). They have found that laser irradiation of the substrate is most effective in improving the crystallinity of the film if it is delayed 1  $\mu$ s after the ablation pulse, which corresponds to the average arrival time of the ablated species at the substrate. The improvement in crystallinity has been observed to be essentially independent of the irradiation laser fluence in the range of 50–100 mJ/cm<sup>2</sup>. At higher fluences, however, the films become rougher because of the damaging influence of the radiation. Surface irradiation has also been recently used for lowering the epitaxial growth temperature of magnetic barium hexaferrite ( $BaFe_{12}O_{19}$ ) thin films. By using a secondary excimer laser with a fluence of  $\sim 60$  mJ/cm<sup>2</sup> for surface excitation, Horwitz et al. (1993) have achieved growth of thin films of the hexaferrite phase, with an extremely smooth surface morphology, on basal plane sapphire substrates at a deposition temperature of 600°C. In the absence of surface irradiation, films deposited at this temperature are mostly amorphous, and require much higher temperatures ( $\sim 900^\circ\text{C}$ ) for epitaxial growth.

Apart from surface excitation, a secondary laser beam can also be used as a purely radiative source of energy for heating of the substrate during PLD. Continuous substrate heating by active transfer using a CW  $CO_2$  laser has

been reported by several groups. This process is intrinsically clean since the problems of outgassing from the vacuum seals and oxidation of the heating elements commonly encountered by using resistive heaters can be avoided. Moreover, the power requirements may be kept small by limiting the mass and area of the heated material. An additional practical feature is the ability to rapidly achieve stable high temperatures in minutes, as well as rapid cooldown after deposition. The  $CO_2$  laser can be used to heat the substrate either by thermal conduction from an irradiated substrate mounting block (Dyer et al., 1990; Wu et al., 1991), or by direct irradiation of the substrate face (Chu et al., 1990; von der Burg et al., 1992a). In the latter case, the differences in the absorption characteristics of the film and substrate require the laser power to be continuously adjusted during film deposition to maintain a constant surface temperature (von der Burg et al., 1992a). Good-quality YBCO films have been deposited using both modes of heating. By using a mask and a focused  $CO_2$  laser beam, von der Burg et al. (1992b) have further demonstrated the capability of in situ patterned deposition of superconducting films by local laser heating of a selected surface area.

Instead of using a CW laser for continuous heating, a pulsed source, which is synchronized with the firing of the ablation pulse, can be used for transient heating of the substrate during deposition. This can substantially reduce the amount of time that the deposited film has to be subjected to the high temperature required for growth. In this heating arrangement, it is necessary for the laser pulse to be sufficiently long to cover the time period of condensation and crystallization of the ablated species on the substrate. Such a scheme has been reported by Volodin et al. (1981) for the growth of InSb films. In this experiment, a Q-switched Nd:YAG laser (pulse duration  $\sim 30$  ns) is used for ablation of InSb, while a synchronized free-oscillation Nd:YAG laser (pulse duration  $\sim 1$  ms) is used to preheat a PbTe-coated KBr substrate to a steady-state temperature before mass arrival at the substrate from the ablation pulse. With appropriate laser heating of the substrate, high-quality single-crystal InSb films have been deposited. Additionally, these films exhibited fewer defects than in the case where the substrate is heated continuously and maintained at 250°C during deposition. This transient heating scheme is particularly attractive for the growth of multilayer thin-film structures, where it is essential to minimize interlayer diffusion.

## 10.6 DUAL-BEAM LASER ABLATION

This final section concerns a discussion of the experiments that have been reported in the literature on the use of two laser beams for the ablation process. As in the case of surface irradiation, discussed in the previous section, either a single laser beam can be split up into two beams for simultaneous ablation, or two different lasers, which are separated by a variable delay, can be used for

the ablation process. While certainly increasing the complexity of the deposition process, there are some important reasons for the use of the dual-beam ablation approach. A key application of the dual-beam ablation has been in providing a solution to the critical problem of particulates in PLD films. The presence of particulates in PLD films is a serious issue, and has been a major obstacle for the large-scale introduction of this technique for film deposition. As a pulsed process, the dual-beam approach is also uniquely suited as a temporal probe of the ablation and growth dynamics during PLD. Significant insights into the ablation and growth dynamics can be obtained by using two time-delayed laser beams for the ablation of the target(s), akin to their use in the previously discussed experiments on surface irradiation.

In an innovative practical application of the dual-beam approach, Gaponov et al. (1982) have demonstrated that the particulate density in PLD films can be significantly reduced by using two intersecting laser-generated plumes from separate ablation targets. In this gas-dynamic separation scheme, the plasma plumes interact with each other and the light species are selectively redirected onto the substrate, which is placed away from the direct path of the ablation plumes. On the other hand, the heavy particles are not deflected from their original direction and therefore do not reach the substrate. Using this technique, smooth YBCO films, which are essentially free of particulates, have been obtained by Pechen et al. (1992) using two synchronized Nd:YAG lasers ( $1.06\text{ }\mu\text{m}$ ) for ablation. The results are quite spectacular, considering that conventional PLD of YBCO using  $1.06\text{-}\mu\text{m}$  radiation usually produces films with a very rough surface morphology due to the presence of a high density of particulates.

In a modified approach for particulate reduction, a second pulsed laser has been employed to vaporize the particulates while they are in flight (Koren et al., 1990). In this approach, the second laser beam is not actually directed at the target, but passes very close and parallel to the interaction zone of the first laser beam with the target. In order to maximize the probability of interception and destruction of the particulate matter in flight, it is very important to carefully adjust the delay timing, pulse length, and positioning of the second laser beam. Improvements in the smoothness and properties of YBCO films, due to second laser irradiation of particulates, have also been reported by Eryu et al. (1991).

In an experiment designed to study the perturbation of the background gas during passage of the fragments produced during ablation, and its effect on the film properties, Gupta et al. (1990) have grown thin films of YBCO in an  $\text{O}_2$  ambient by PLD using two synchronized lasers, separated by a variable delay. The ablated fragments from the first laser results in the formation of a nonsteady shock wave in  $\text{O}_2$ , leaving behind a rarefied ambient. If the second laser is fired before the background  $\text{O}_2$  returns to equilibrium, the resulting films show a decrease in the transition temperature, with expanded  $c$ -lattice parameter, which is analogous to films grown in a low-pressure ambient. The

experiment demonstrates that, for optimal oxidation of the films, it is necessary to maintain a sufficiently high concentration of oxygen during the time period that the fragments travel and deposit on the substrate. Interestingly, the films with the highest depression in  $T_c$  ( $\sim 50\text{ }\mu\text{s}$  delay between pulses) also show a significantly reduced density of particulates (which was not reported in the original publication). This is possibly a result of hydrodynamic effects due to the interaction of the shock fronts from the two successive laser pulses.

In another experiment, designed to probe the effect of the relative arrival time of the plume components on film growth, two synchronized lasers have been used for the synthesis of YBCO films by ablation from two separate precursor oxide targets (Hussey and Gupta, 1992). The precursor targets,  $\text{YBa}_2\text{O}_x$  and  $\text{CuO}$ , are placed in a triangular arrangement with the heated substrate holder, with the targets positioned so that their center normal vectors intersect at the point where the substrate is located. The films are deposited on (100)  $\text{SrTiO}_3$  substrates heated to  $750^\circ\text{C}$ . The ablation fluences of the two lasers are suitably adjusted to provide the required 1:2:3 cation stoichiometry of the deposit. High-quality YBCO films are obtained as a result of chemical mixing of the ablated plume species after adsorption on the substrate. Moreover, the quality of the YBCO films has been found to be independent of the pulse delay settings between the two lasers, suggesting that the time of arrival of the different cationic species on the substrate surface is not crucial in determining the superconducting properties, or the growth quality, of the films. High-quality YBCO films have also been synthesized by ablation from  $\text{Y}_2\text{Cu}_2\text{O}_5$  and  $\text{BaCuO}_2$  precursor targets in a 1:2 ratio. The facile formation of the YBCO phase, irrespective of the nature of the reacting precursors, points to the high thermodynamic stability of the YBCO phase under the conditions used for in situ film growth. These results have important implications for the layer-by-layer growth of artificially structured films, suggesting that in addition to satisfying the charge neutrality criteria (Terashima et al., 1990), the phase stability and propensity for interdiffusion of the individual layer units under the growth conditions have to be carefully considered in order to achieve layer-by-layer growth of heterostructures.

## 10.7 CONCLUDING REMARKS

An attempt has been made in this review to discuss in a systematic manner the large, and seemingly diverse, number of novel PLD approaches that have been utilized in recent years for film growth. These novel approaches have played a significant role in enhancing the process capabilities of the standard PLD process, thus broadening its scope as a thin-film growth technique for a much wider variety of materials with desirable physical properties. Among the various approaches, the use of a directed flux of neutral and charged species or photons, with independent control of their energy and flux, appear to offer

the maximum degree of flexibility and control for influencing film growth. However, these independent sources generally tend to be much more expensive to implement than some of the simpler modifications, which rely primarily on controlling the plasma plume properties. While both continuous and pulsed sources can be used effectively for manipulating the growth kinetics during PLD, a pulsed source has the advantage of providing a much higher instantaneous flux of species or photons, synchronized with the arrival of the high flux of ablated species at the substrate. Synchronization is expected to be important in situations where the film growth properties are influenced by the interactions that occur during the time of condensation and nucleation of the adatoms. There is already some supporting evidence for this from results obtained using pulsed sources of molecular oxidizer gases and laser irradiation of the surface during deposition. In the future, it will be useful to conduct similar experiments using pulsed sources of neutral and charged atomic species during PLD to probe the effects of interaction dynamics on the growth and properties of the resulting films.

## REFERENCES

- Abber, R. L. (1988), in *Handbook of Thin-Film Deposition Processes and Techniques* (K. Schuegraf, ed.), Noyes Pub., Park Ridge, NJ, pp. 270–290.
- Ballal, A. K., L. Salamanca-Riba, G. L. Doll, et al. (1992), *J. Mater. Res.* **7**, 1618–1680.
- Bicknell, R. N., N. C. Giles, and J. F. Schetzina (1986), *Appl. Phys. Lett.* **49**, 1095–1097.
- Bourdon, E. B. D., and R. H. Prince (1991), *Appl. Surf. Sci.* **48/49**, 50–54.
- Chern, M. Y., A. Gupta, and B. W. Hussey (1992), *Appl. Phys. Lett.* **60**, 3045–3047.
- Chrissey, D. B., J. S. Horwitz, K. S. Grabowski, et al. (1990), *Mater. Res. Soc. Symp. Proc.* **169**, 435–438.
- Chu, W. F., M. V. Przychowski, and H. Stafast (1990), *Supercond. Sci. Technol.* **3**, 497–499.
- Collins, C. B., F. Davanloo, E. M. Juengerman, W. R. Osborn, and D. R. Jander (1989), *Appl. Phys. Lett.* **54**, 216–218.
- Craciun, D., and V. Craciun (1992), *Appl. Surf. Sci.* **54**, 75–77.
- Davanloo, F., E. M. Juengerman, D. R. Jander, T. J. Lee, and C. B. Collins (1990), *J. Appl. Phys.* **67**, 2081–2087.
- Deneffe, K., P. Van Mieghem, B. Brijs, et al. (1990), *J. Less-Common Met.* **164 & 165**, 307–314.
- Dikshit, S. J., V. P. Godbole, S. M. Chaudhari, S. M. Kanetkar, and S. B. Ogale (1989), *Appl. Phys. Lett.* **54**, 775–777.
- Dyer, P. E., A. Issa, P. H. Key, and P. Monk (1990), *Supercond. Sci. Technol.* **3**, 472–475.
- Eryu, O., H. Chiba, K. Murakami, K. Masuda (1991), *Rev. Laser Eng.* **19**, 254–60.
- Estler, R. C., N. S. Nogar, R. E. Muenchausen, R. C. Dye, C. Flamme, J. A. Martin, A. Garcia, and S. Foltyn (1990), *Mater. Lett.* **9**, 342–346.
- Frey, T., C. C. Chi, C. C. Tsuei, T. M. Shaw, and G. Trafas (1992), *Mater. Res. Soc. Symp. Proc.* **275**, 61–66.
- Fried, D., G. P. Reck, T. Kushida, and E. W. Rothe (1991), *J. Phys.* **D24**, 1065–1071.
- Gaponov, S. V., B. M. Luskin, B. A. Nesterov, and N. N. Salashchenko (1977), *Sov. Tech. Phys. Lett.* **3**, 234–235.
- Gaponov, S. V., E. B. Klyuenkov, B. A. Nesterov, N. N. Salashchenko, and M. I. Kheifets (1979), *Sov. Tech. Phys. Lett.* **5**, 193–194.
- Gaponov, S. V., A. A. Gudkov, and A. A. Fraerman (1982), *Sov. Phys. Tech. Phys.* **27**, 1130–1133.
- Geohegan, D. B. (1991), *Mater. Res. Soc. Symp. Proc.* **201**, 557–562.
- Gluck, N. S., H. Sankur, and W. J. Gunning (1989), *J. Vac. Sci. Technol.* **A7**, 2983–2987.
- Greer, J. A., and H. J. Van Hook (1990), *Mater. Res. Soc. Symp. Proc.* **169**, 463–468.
- Gupta, A. (1993), *J. Appl. Phys.* **73**, 7877–7886.
- Gupta, A., and B. W. Hussey (1991), *Appl. Phys. Lett.* **58**, 1211–1213.
- Gupta, A., B. W. Hussey, and M. Y. Chern (1992a), *Physica C* **200**, 263–270.
- Gupta, A., M. Y. Chern, and B. W. Hussey (1992b), *Mater. Res. Soc. Symp. Proc.* **275**, 93–100.
- Gupta, A., G. Koren, R. J. Baseman, A. Segmüller, and W. Holber (1989), *Physica C* **162-164**, 127–128.
- Gupta, A., B. W. Hussey, A. Kussmaul, and A. Segmüller (1990), *Appl. Phys. Lett.* **57**, 2365–2367.
- Herron, W. J., and J. F. Garvey (1991), *Mater. Res. Soc. Symp. Proc.* **206**, 391–396.
- Hontsu, S., J. Ishii, T. Kawai, and S. Kawai (1991), *Appl. Phys. Lett.* **59**, 2886–2888.
- Horvath, M., L. Bilitzky, and J. Huttner (1985), *Ozone*, Topics in Inorganic and General Chemistry Series No. 20, Elsevier, New York.
- Horwitz, J. S., D. B. Chrissey, K. S. Grabowski, C. A. Carosella, P. Lubitz and C. Edmondson (1993), *Mater. Res. Soc. Symp. Proc.* **285**, 391–395.
- Hussey, B. W., and A. Gupta (1992), *J. Appl. Phys.* **72**, 287–289.
- Iijima, Y., N. Tanabe, O. Kohno, and Y. Ikeno (1992), *Appl. Phys. Lett.* **60**, 769–771.
- Izumi, H., K. Ohata, T. Hase, et al. (1990), *J. Appl. Phys.* **68**, 6331–6335.
- Kanai, M., T. Kawai, S. Kawai, and H. Tabata (1989), *Appl. Phys. Lett.* **54**, 1802–1804.
- Kanai, M., K. Horiuchi, T. Kawai, and S. Kawai (1990), *Appl. Phys. Lett.* **57**, 2716–2718.
- Kay, E., and S. M. Rossnagel (1989), in *Handbook of Ion Beam Processing Technology* (J. J. Cuomo, S. M. Rossnagel, and H. R. Kaufman, eds.), Noyes Publications, Park Ridge, New Jersey, pp. 170–193.
- Koinuma, H., H. Nagata, T. Tsukahara, S. Gonda, and M. Yoshimoto (1991), *Appl. Phys. Lett.* **58**, 2027–2029.
- Koren, G., A. Gupta, and R. J. Baseman (1989), *Appl. Phys. Lett.* **54**, 1920–1922.
- Koren, G., R. J. Baseman, A. Gupta, M. I. Lutwyche, R. B. Laibowitz (1990), *Appl. Phys. Lett.* **56**, 2144–2146.
- Krishnaswamy, J., A. Reangan, J. Narayan, K. Vedam, and C. J. McHargue (1989), *Appl. Phys. Lett.* **54**, 2455–2457.
- Kussmaul, A., J. S. Moodera, P. M. Tedrow, and A. Gupta (1992), *Appl. Phys. Lett.* **61**, 2715–2717.
- Kwok, H. S., H. S. Kim, S. Witanachchi, et al. (1991), *Appl. Phys. Lett.* **59**, 3643–3645.

- Leuchtner, R. E., K. S. Grabowski, D. B. Chrisey, and J. S. Horwitz (1992), *Appl. Phys. Lett.* **60**, 1193–1195.
- Li, X. M., Kanai, T., Kawai, and S. Kawai (1992), *Jpn. J. Appl. Phys.* **31**(2), L217–L220.
- Lubben, D., S. A. Barnett, K. Suzuki, S. Gorbatskin, and J. E. Greene (1985), *J. Vac. Sci. Technol.* **B3**, 968–974.
- Malshe, A. P., S. M. Kanetkar, S. B. Ogale, and S. T. Kshirsagar (1990), *J. Appl. Phys.* **68**, 5648–5652.
- Mao, S. N., X. X. Xi, S. Bhattacharya, et al. (1992), *Appl. Phys. Lett.* **61**, 2356–2358.
- Minamikawa, T., Y. Yonezawa, S. Otsubo, et al. (1990), in *Advances in Superconductivity II* (T. Ishiguro and K. Kajimura, eds.), Springer-Verlag, Tokyo, pp. 857–860.
- Minamikawa, T., Y. Yonezawa, K. Segawa, et al. (1991), *Physica C* **185–189**, 1969–1970.
- Mineta, S., M. Kohata, N. Yasunaga, and Y. Kikuta (1990), *Thin Solid Films* **189**, 125–138.
- Morimoto, A., S. Otsubo, T. Shimizu, T. Minamikawa, and Y. Yonezawa (1990), *Mater. Res. Soc. Symp. Proc.* **191**, 31–36.
- Morimoto, A., S. Mizukami, T. Shimizu, et al. (1992), *Mater. Res. Soc. Symp. Proc.* **275**, 371–376.
- Muller, K.-H. (1989), in *Handbook of Ion Beam Processing Technology* (J. J. Cuomo, S. M. Rossnagel, and H. R. Kaufman, eds.), Noyes Publications, Park Ridge, New Jersey, pp. 241–278.
- Murray, P. T., M. S. Donley, and N. T. McDevitt (1989), *Mater. Res. Soc. Symp. Proc.* **140**, 195–200.
- Norton, M. G., P. G. Kotula, and C. B. Carter (1991), *J. Appl. Phys.* **70**, 2871–2873.
- Ogale, S. B., R. Nawathay-Dikshit, S. J. Dikshit, and S. M. Kanetkar (1992), *J. Appl. Phys.* **71**, 5718–5720.
- Ögmen, M., and W. W. Duley (1989), *J. Phys. Chem. Solids* **50**, 1221–1225.
- O'Keeffe, P., S. Komuro, S. Den, T. Morikawa, Y. Aoyagi (1991), *Jpn. J. Appl. Phys.* **30**, L834–L837.
- Otis, C. E., A. Gupta, and B. Braren (1993), *Appl. Phys. Lett.* **62**, 102–104.
- Otsubo, S., T. Minamikawa, Y. Yonezawa, et al. (1989), *Jpn. J. Appl. Phys.* **28**, 2211–2218.
- Pappas, D. L., K. L. Saenger, J. Bruley, et al. (1992), *J. Appl. Phys.* **71**, 5675–5684.
- Pechen, E. V., S. I. Krasnosvobodtsev, G. Kessler, et al. (1992), *Phys. Stat. Sol. (A)* **131**, 179–189.
- Pompe, W., H.-J. Scheibe, P. Seimroth, et al. (1992), *Thin Solid Films* **208**, 11–14.
- Reade, R. P., P. Berdahl, R. E. Russo, S. M. Garrison (1992), *Appl. Phys. Lett.* **61**, 2231–2233.
- Rengan, A., N. Biunno, and J. Narayan (1990), *Mater. Res. Soc. Symp. Proc.* **162**, 185–188.
- Roy, D., S. B. Krupanidhi, and J. P. Dougherty (1992), *J. Vac. Sci. Technol.* **A10**, 1827–1831.
- Saenger, K. L. (1993), *Process. Adv. Mater.* **3**, 1–24.
- Sato, T., S. Furono, S. Iguchi, and M. Hanabusa (1988), *Appl. Phys.* **A45**, 355–360.
- Scheibe, H.-J., W. Pompe, P. Seimroth, et al. (1990), *Thin Solid Films* **193/194**, 788–798.
- Schwab, P., A. Kochemasov, R. Kullmer, and D. Bäuerle (1992), *Appl. Phys.* **A54**, 166–169.
- Shibata, Y., K. Kaya, K. Akashi, et al. (1992), *Appl. Phys. Lett.* **61**, 1000–1002.
- Singh, R. K., J. Narayan, A. K. Singh, and J. Krishnaswamy (1989), *Appl. Phys. Lett.* **54**, 2271–2273.
- Tabata, H., T. Kawai, and S. Kawai (1991), *Appl. Phys. Lett.* **58**, 1443–1445.
- Tabata, H., T. Kawai, S. Kawai, et al. (1991), *Appl. Phys. Lett.* **59**, 2354–2356.
- Tabata, H., O. Murata, T. Kawai, S. Kawai, and M. Okuyama (1992), *Jpn. J. Appl. Phys.* **31**, 2968–2970.
- Terashima, T., Y. Bando, K. Iijima, et al. (1990), *Phys. Rev. Lett.* **65**, 2684–2687.
- Volodin, B. A., S. V. Gaponov, E. B. Klyuenkov, B. A. Besterov, and N. N. Salashchenko (1981), *Sov. Phys. Semicond.* **15**, 688–689.
- von der Burg, E., M. Diegel, H. Stafast, and W. Grill (1992) *Appl. Phys.* **A54**, 373–379.
- von der Burg, E., W. Grill, M. Diegel, and H. Stafast (1992), *Mater. Sci. Eng.* **B13**, 25–28.
- Wagal, S. S., E. M. Juengerman and C. B. Collins (1988), *Appl. Phys. Lett.* **53**, 187–188.
- Witanachchi, S., H. S. Kwok, X. W. Wang, and D. T. Shaw (1988), *Appl. Phys. Lett.* **53**, 234–236.
- Wu, K. H., C. L. Lee, J. Y. Juang, T. M. Uen, and Y. S. Gou (1991), *Appl. Phys. Lett.* **58**, 1089–1091.
- Yamamoto, K., B. M. Lairson, C. B. Eom, et al. (1990), *Appl. Phys. Lett.* **57**, 1936–1938.
- Yoshimoto, M., H. Nagata, J. Gong, H. Ohkubo, and H. Koinuma, *Physica C* **185–189**, 2085–2086.



## COMMERCIAL SCALE-UP OF PULSED LASER DEPOSITION

JAMES A. GREER

Research Division  
Raytheon Company  
Lexington, Massachusetts

### 11.1 INTRODUCTION

"Can you scale your pulsed laser deposition process to coat large substrates compatible with our new device design?" or "The process line handles only 100 mm diameter substrates. Will you be able to deposit the material over these substrates with the uniformity the application requires?" These and similar questions have been or soon will be, asked by managers of materials scientists working in the field of pulsed laser deposition (PLD). Unfortunately, the answer to questions such as these is usually "No way! Not with our present system." The real question is not *whether* PLD can be scaled-up to sizes compatible with industrial applications, but rather "*What large-area application will be the first to drive PLD to become a real production process?*"

One misguided criticism of the PLD process has been the poor uniformity of a variety of film properties that have typically been obtained over relatively small substrate sizes. Obviously, the need to deposit uniform films over large substrates will be required for most commercial applications for a variety of reasons. Large substrates, with diameters of 50 mm or larger, will allow the user to design more sophisticated electronic devices such as superconducting delay lines with long delay times, or fabricate multiple devices on a single substrate. Large substrate sizes will also allow more efficient use of the other related process equipment needed to fabricate devices from deposited films. As we shall see in this chapter, the criticism just discussed is unfounded, as the PLD process is readily scalable to substrates of at least 125 mm in diameter and larger.

This chapter focuses on three of the techniques that have been used to laser-deposit films over large areas. Uniformity of film thickness, composition, and film-specific properties, as well as engineering issues, such as high deposition rates, large-area multilayer deposition, and substrate heating are addressed. Also, PLD of films on nonplanar surfaces are discussed.

## 11.2 LARGE-AREA PLD APPROACHES

To date, three basic approaches to scaling-up PLD have been reported in the literature. Historically, the first published report describing a technique to obtain large-area films utilized a rotating substrate and large-diameter counter-rotating target in conjunction with a rastered laser beam and large target-to-substrate distance (Greer, 1989). The technique has successfully been used to deposit  $\text{Y}_1\text{Ba}_2\text{Cu}_3\text{O}_{7-x}$  (YBCO) over 75-mm-diameter substrates with excellent uniformity in both physical and electrical properties (Greer, 1992, 1993). Figure 11.1 shows a schematic of a more recent version of a large-area raster system modified to deposit films over 125-mm-diameter substrates. In this case a focused laser beam is reflected off of a programmable mirror held in a kinematic mount that allows the beam to be rastered over the entire diameter of the 75-mm-diameter ablation target. The rotating substrate is located 12.7 cm above the ablation target. By adjusting the raster velocity as a function of position, the center of the ablation plume can be made to impinge for longer times near the outer edge of the rotating substrate in order to yield more uniform film properties. Offsetting the ablation target with respect to the substrate as shown in Figure 11.1 offers two advantages over the coaxial arrangement used in earlier raster systems. First, a target with only about half the substrate diameter is needed to uniformly coat a given substrate size, thereby reducing target cost. Second, in the present configuration the rastered laser beam crosses over the center of the ablation target. Thus, as the target rotates, the laser beam will impinge at each target location from the opposite

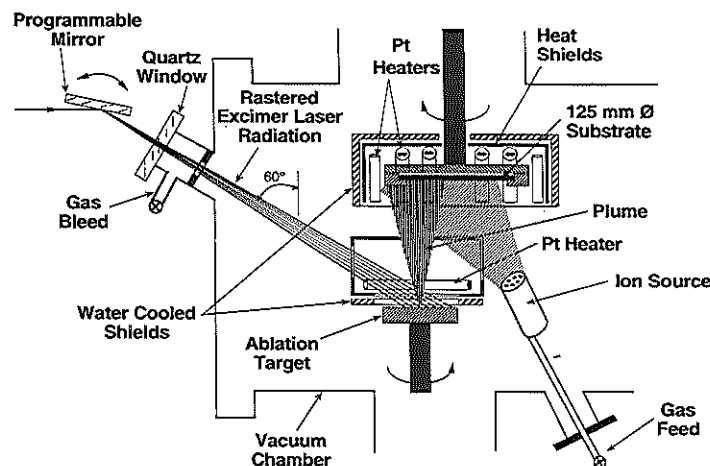


Figure 11.1. Schematic of a large-area PLD system based on the raster approach designed to deposit films on 125-mm-diameter substrates.

direction at a different time, reducing the growth of cones on the target surface (Foltyn et al., 1991b). This in turn may help decrease the number of particulates that are ejected from the target surface. Since the system uses a relatively long focal length lens ( $R = 0.5$  m) and large lens-to-target distance, the change in laser fluence at the target surface will be only  $\pm 5\%$  as the laser beam is rastered across the target. This variation in fluence is on the order of the pulse-to-pulse variation in output energy for most excimer lasers. The system seen in Figure 11.1 also incorporates a resistance-based radiation-type substrate heater discussed later, Kaufman-ion source, and water-cooled shields.

Alternative large-area PLD systems based on a fixed-position laser beam to deposit thin films have been reported on in the literature as well. In both cases the laser beam was focused or imaged down close to the outer edge of a 2.54-cm-diameter rotating ablation target. The simplest static beam approach is called *off-axis* PLD and was first used to deposit films onto 25-mm-diameter substrates (Erlington and Ianno, 1990). In the off-axis approach the center of the rotating substrate is offset a fixed amount,  $d$ , from the center of the ablation plume, as seen schematically in Figure 11.2. The offset distance will depend on the target-substrate spacing as well as the substrate diameter. If desired, a mask can be placed in front of the central portion of the substrate during the deposition run in order to improve the film's thickness uniformity. The off-axis process has been utilized to deposit YBCO films over 50-mm-diameter substrates (Foltyn et al., 1991a), and more recently to deposit  $\text{Bi}_4\text{Ti}_3\text{O}_{12}$  thin films over 100-mm-diameter silicon substrates (Buhay et al., 1992). The off-axis approach allows the substrate to be heated during deposition.

The second large-area PLD technique based on a static-position laser-beam approach utilizes both substrate rotation and computer-controlled substrate translation and has been used to deposit the thallium-based superconducting oxides over 50-mm-diameter substrates (Eddy, 1991; Smith, 1991, 1992).

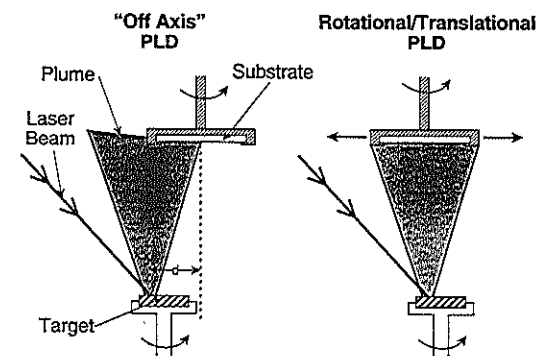


Figure 11.2. Schematic of the large-area fixed-beam off-axis, and rotational/translational PLD approaches.

Rotational/translational (R/T) PLD is also shown schematically in Figure 11.2. In this case the rotating substrate is translated back and forth in one direction with respect to the laser plume using a computer-controlled vacuum feed-through. Again, allowing the center of the ablation plume to impinge close to the outer edge of the rotating substrate for a longer period of time, the properties of the deposited film can be made quite uniform. This process has been further refined to deposit the thallium-based superconducting compound over three 50-mm-diameter substrates simultaneously. This work represents the first real small-scale production system for the PLD process. Due to the large substrate displacement during the deposition process, substrate heating is not practical with the R/T large-area approach.

### 11.3 COMPARISON OF LARGE-AREA PLD APPROACHES

Figure 11.3 shows the normalized film-thickness profiles for the rastered, rotational/translational, and off-axis large-area PLD techniques, respectively. The off-axis data labeled curve *a* in Figure 11.3 was obtained from a  $\text{Bi}_4\text{Ti}_3\text{O}_{12}$  film deposited onto a 100-mm-diameter silicon substrate for random-access memory applications. This work utilized a 7-cm target-substrate distance and an offset distance  $d = 3.2$  cm. Using a fluence of  $2 \text{ J/cm}^2$  (248 nm, 25-ns pulse length) at 10 Hz, with an  $\text{O}_2$  pressure of 200 mtorr, an average growth rate over the central 20-cm<sup>2</sup> (50-mm-diameter) portion of  $0.5 \mu\text{m/hr}$  was obtained. A *maximum* total variation in film thickness of only 3% (defined as the difference

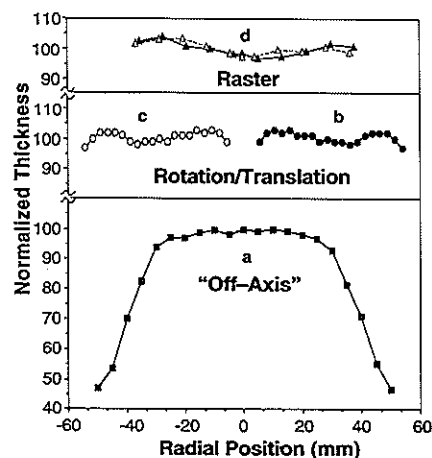


Figure 11.3. Normalized film-thickness profiles obtained from the three large-area PLD techniques.

between the maximum and minimum thickness values divided by the nominal film thickness) was obtained over the central 50 mm of this substrate. The film thickness starts to decrease significantly at radii greater than 25 mm, however, and drops below 50% at the substrate edge. The normalized film thickness obtained using the R/T large-area PLD approach to deposit the precursor (2122)  $\text{TiCaBaCuO}$  compound is seen in Figure 11.3, curve *b*. This data represent the film-thickness profile measured across one complete 50-mm-diameter substrate that was fixed in a large rotating substrate holder supporting three such substrates during the deposition. As noted, the *maximum* total variation in film thickness over this substrate is 6%. The orientation of the substrate was such that the thickness distribution obtained depicts the radial profile of the parent substrate holder. Thus, in principle, these data represent a thickness profile that could be obtained across a single 125-mm-diameter substrate, as depicted by curves *b* and *c* taken together, as seen in Figure 11.3. The deposition conditions for this film were a fluence of  $4 \text{ J/cm}^2$  at 248 nm with a 50-Hz repetition rate, a background oxygen pressure of 20 mtorr, and a target-to-substrate distance of 5 cm, which yields an average deposition rate of  $1.8 \mu\text{m/hr}$  over an area of  $127 \text{ cm}^2$ . Figure 11.3, curve *d* shows the normalized film thickness uniformity of an oxide compound obtained across a 75-mm-diameter substrate using the rastered laser beam approach and a 25-mm off-set target similar to that seen in Figure 11.1. The film thickness was measured in two mutually perpendicular directions across the substrate as indicated by the two curves seen in the figure. The *maximum* total variation in film thickness was found to be 6.5% in this case. Typical deposition conditions for the raster approach include a fluence of  $1 \text{ J/cm}^2$  (248 nm–15 ns), 30 Hz, 50-mtorr background, pressure, which yields an average growth rate of  $1 \mu\text{m/hour}$  for YBCO over a 75-mm-diameter substrate. The normalized profiles curve *b(c)*, and *d* seen in Figure 11.3 clearly demonstrate that excellent film thickness uniformity can be obtained with PLD over substrate diameters of 50 mm and larger.

Uniformity of the deposited film composition is also of importance for most applications, and both the R/T and rastered large-area PLD approaches have demonstrated excellent uniformity over substrates of at least 50 mm in diameter. The R/T approach has demonstrated a compositional variation between 1.0 and 2.8 atomic percent for the Ti, Ba, Ca, and Cu precursor material deposited over a 50-mm-diameter substrate as determined by energy-dispersive X-ray analysis (EDXA). Again these data were obtained from a 50-mm-diameter substrate held in a three-wafer holder, and thus is indicative of that which could be obtained from a 125-mm-diameter substrate. The rastered approach has yielded maximum compositional variations of 1.0 to 2.4 atomic percent (EDXA) for the Y, Ba, and Cu cations deposited from a YBCO target onto a 75-mm-diameter substrate. The variations in atomic composition described for both techniques represent the difference between the maximum and minimum values taken across the given substrate diameters. The quoted

variation in film stoichiometry of  $\pm 5\%$  as determined by Rutherford backscattering for an off-axis-deposited YBCO film is somewhat ambiguous and data for the  $\text{Bi}_4\text{Ti}_3\text{O}_{12}$  film have not yet been reported. It is expected that excellent compositional uniformity can be obtained with the off-axis approach over 100-mm-diameter substrates. However, as the off-axis approach is scaled to larger substrate sizes, the compositional uniformity may start to degrade. This is due to the fact that the film that condensed on the central region of the substrate will consist completely of material ejected at large plume angles, that is, the nonstoichiometric portion of the ablation plume. Coupled with the thickness profile seen in Figure 11.3, it is unlikely that the off-axis is capable of being developed into a large area deposition process compatible with most commercial applications.

All three large-area PLD techniques have demonstrated superconducting films with excellent uniformity in electrical properties. Figure 11.4a and b displays the critical temperature,  $T_c$ , and critical current,  $J_c$ , profiles measured in two mutually perpendicular directions from YBCO films deposited onto the "front side" and "back side" of a 75-mm-diameter (100)  $\text{LaAlO}_3$  substrate, respectively. Here the critical temperature varies by no more than  $\pm 0.3$  K over the entire substrate. Also, the *maximum* total variation in  $J_c$  measured at 77 K and zero field as determined with a noncontact mutual inductance technique (Claassen et al., 1991) for these two YBCO films varied by about  $\pm 10\%$  for both films on either side of the substrate. The nominal normal state DC resistance obtained from the back-side film as measured with a four-point probe at 26 locations on the substrate was  $300 \mu\Omega\text{-cm}$  with *maximum* total variation of only  $35 \mu\Omega\text{-cm}$ , after taking into account the variation in film

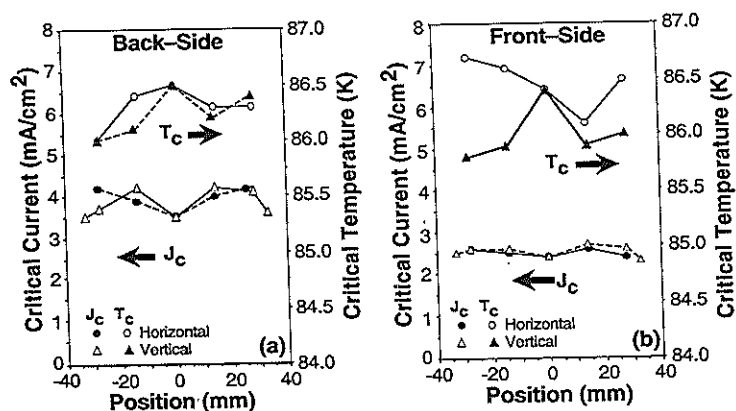


Figure 11.4. Critical-temperature and critical-current profiles measured in mutually perpendicular directions of two YBCO films deposited onto both the front and back sides of a 75-mm-diameter  $\text{LaAlO}_3$  substrate using the large-area raster approach.

thickness. The off-axis approach has demonstrated  $T_c$  of  $89 \pm 0.5$  K measured at two points (center and edge) from both front- and back-side YBCO films deposited over 50-mm-diameter substrates. The R/T approach has reported  $T_c = 101 \pm 0.1$  K for the thallium compound measured at four locations on a 50-mm-diameter substrate after a postdeposition, high-temperature anneal. The nominal microwave surface resistance,  $R_s$ , scaled to 10 GHz, obtained from four photolithographically patterned stripline resonators cut from a 50-mm-diameter  $\text{LaAlO}_3$  substrate was found to be  $650 \pm 50 \mu\Omega$  when measured at 77 K with an incident RF power of  $-3$  dBm. It should be pointed out that the uniformity in electrical properties of these complex superconducting oxides are a strong function of number parameters such as deposition conditions, growth or postdeposition anneal temperature, film composition, crystalline quality, and substrate anomalies. The fact that these compounds can be laser-deposited in thin-film form with excellent uniformity for a variety of superconducting properties provides strong support that other less chemically complex materials can be deposited by the PLD process while maintaining similar uniformity of properties such as dielectric constant, magnetic susceptibility, and micro-hardness.

## 11.4 LARGE-AREA PLD REQUIREMENTS

In order for PLD to become a serious thin-film physical vapor-deposition tool several areas will need to be addressed depending on the type of process, throughput, and substrate size required. Deposition rate, target size and resurfacing, substrate heating (if required), multilayer capability, window purging, particulates, are all areas that need to be considered. Also, for very high throughput, load-locking of both the substrate and target may need to be considered. It should be stressed that as the substrate size increases, the total amount of material that needs to be deposited also increases. Thus, over 125 times more material needs to be deposited on a 125-mm-diameter substrate ( $\sim 125 \text{ cm}^2$ ) than on a substrate 1 cm on a side. This fact has a significant impact on the laser requirements, target size, as well as deposition chamber design.

### 11.4.1 Target Utilization and Resurfacing

One obvious difference between a static and raster laser beam approach is the size and utilization of the ablation target. Both fixed-beam approaches typically focus the laser down to a spot close to the outer edge of a 25-mm-diameter target. As the deposition proceeds, the laser etches a trench in the target surface that can significantly change both the fluence and ejection angle of the ablation plume (Greer, 1993). Such changes in angle can have a serious impact on both growth rate and uniformity of film thickness. Thus,

small targets are typically resurfaced after each run with emery paper in order to obtain more reproducible results. However, target resurfacing wastes about 75% of target material. As substrate sizes increase, the effect of trenching will become a more serious problem for a desired film thickness. One solution is to use larger diameter targets to increase the overall trench length. However, this will waste even more target material when resurfacing. Another approach is to incorporate the ability to slightly reposition either the target or laser beam during the deposition process, but resurfacing will still be necessary.

Rastering the laser beam over a large diameter target makes much more efficient use of target material. In this case, the laser beam ablates over 90% of the target surface, etching it at a much more uniform rate. Thus, the plume ejection angle and fluence are both constant with time and target resurfacing is not required.

#### 11.4.2 Window Purging

As mentioned earlier, large-area films require significant amounts of material to be deposited and thus a large number of laser pulses are required. This has implications for the vacuum window used to transmit the incident radiation. If proper care is not taken the window will become coated during deposition, and this coating can absorb some of the incident radiation, thus reducing the fluence on target. Bleeding in a reactive or inert gas close to the vacuum surface of the window, and including a baffle in the window port to increase the local gas pressure, can help minimize the rate of window coating, as seen in Figure 11.1. Window deposits can be removed when necessary by optical polishing. Also, if quartz is used as the window material, care should be taken to periodically check for indications of color center formation in the quartz material. Formation of color centers will significantly reduce the target fluence and reduce growth rate.

#### 11.4.3 Large-Area Substrate Heating

Certain applications of PLD require substrate heating to temperatures in excess of 900°C, and heating large substrates requires special consideration since at these temperatures radiation becomes dominant. Either quartz lamps or resistive-type heating elements can be used. Since all large-area PLD approaches rely on substrate rotation, direct bonding of the substrate to a heated block is not practical. Also, certain substrates, such as sapphire, magnesium oxide, and lanthanum aluminate do not absorb well in the infrared (IR) portion of the spectrum, making substrate heating by unidirectional radiation difficult. One approach to heating unbonded substrates is the vacuum oven shown in Figure 11.1, and is based on blackbody radiation (Greer, 1992). In this case, the substrate is supported only at the edges. Bonding or clamping the substrate to the holder is not recommended as it is

difficult to obtain uniform pressure and thermal contact over large areas. Two sets of resistive heating elements are placed above and circumferentially around the substrate. Quartz lamps could also be used to heat the substrate holder from above. A third set of elements can be placed directly above the ablation target to heat the substrate from the front surface. Several sets of foil heat shields help confine the radiation and minimize heat loss. With this arrangement the substrate is exposed to radiation from all sides and must heat up to an equilibrium temperature. Photographs of both the upper and lower sections of a vacuum oven are shown in Figure 11.5. The upper elements are shown without the substrate in place exposing the two sets of upper heating elements. The circumferential elements are seen as well. Note the slot cut through the heat shields and water-cooling plate in the lower section, which allows the incident laser beam to hit the large-diameter target and also provides room for the expansion of the ablation plume. Thermocouples can be clamped or welded to the heating-element support structure or placed directly in front of the substrate. Either thermocouple can be used as an input to a programmable temperature controller that drives the input power to the heating elements. An alternative approach to measuring substrate temperature uses a HeNe laser beam reflected off the substrate surface, and may be adaptable to rotating substrates. Input power requirements to heat a 75-mm-diameter  $\text{LaAlO}_3$  substrates to temperatures of 750°C are in excess of 1.2 kW with a radiation-type heater and power levels will increase significantly for both higher temperatures and/or substrates with larger diameters. For substrates heated by radiation to temperatures of about 650°C, Kanthal wire can be used as the resistive heating elements in reactive gases such as oxygen. For higher substrate temperatures platinum or a platinum/rhodium alloy should be used. The more elements incorporated into the heater design, the lower the temperature and longer the life of each element. To minimize outgassing, water-cooled shields are recommended for reduced heating of chamber walls or other internal parts. A water-cooled target shield is also essential when high substrate temperatures are required, as a laser pulse impinging on a hot target can locally melt the target surface. A simple shield placed directly above the target is useful even for low-temperature deposition since it reduces contamination from extraneous particles and redeposited material backscattered from the ablation plane.

#### 11.4.4 Laser Requirements, Deposition Rate, and Rate Monitoring

Large-scale applications of the PLD process will require growth rates over large-area substrates that are competitive with other physical deposition processes. This has implications for the characteristics of the laser that is best suited for a commercial PLD process. Using high repetition rates it has been demonstrated that PLD can grow high-quality YBCO films at average growth rates of 50  $\mu\text{m}/\text{h}$  over small substrates (Wu et al., 1990a, 1990b). Average growth rates between 0.5  $\mu\text{m}/\text{h}$  and 5  $\mu\text{m}/\text{h}$  over areas between 20  $\text{cm}^2$  and

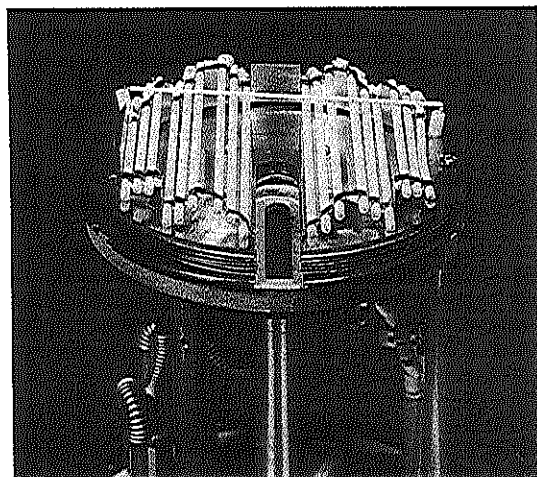
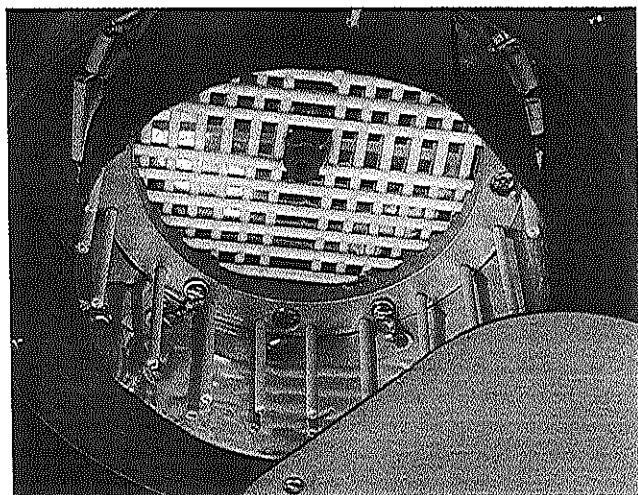


Figure 11.5. Photographs of two sections of a vacuum-oven-type substrate heater. Upper photograph shows both the upper and circumferential heating elements. The lower photograph shows the heating elements that sit directly above the ablation target.

125 cm<sup>2</sup> will be sufficient for most applications. If the application requires substrate heating (such as growth of YBCO or related buffer layers) the heat-up and cooldown times will likely dominate over the actual film-deposition time. In this case, a load-locked PLD system might prove useful if high throughput is desired. Substrate transfer in a load-locked system with a radiation-type vacuum oven of the type described previously will require some significant design work. In order to achieve good uniformity over large-areas the target-substrate distance must be large, which in turn will put an upper limit on the pressure with which one can grow films and still obtain reasonable deposition rates.

Excimer lasers have been commercially available for about 15 years and are still emerging as industrial tools that are continuously undergoing product improvement. In order to determine the best choice of laser for a particular application the substrate size or area to be coated and desired deposition rate must be known. A variety of commercial excimer lasers are currently available in the 50 to 100-W power range. It is wise to overspecify the power requirements for the laser and drive the system at about 60% to 70% of its rated energy and repetition rate if it is to be used in a serious industrial environment. This will improve the longevity of the laser components. Lasers that provide about 500 mJ per pulse (248 nm) and repetition rates of at least 100 Hz are recommended for large-area applications. For industrial-use systems with automatic output, power control to keep the fluence constant and a gas purifier to increase the gas lifetime are both useful.

Another area that needs to be addressed for industrial applications is that of monitoring the film thickness and/or growth rate. Quartz crystal microbalances can be used for both fixed and rastered beam approaches. Due to the forward-scattered nature of the ablation plume, however, only a small fraction of the ablated material will condense on the crystal for most microbalance placements. Also, the accuracy of the deposition monitor will depend on the dynamic geometrical relation of the plume with respect to the quartz microbalance. If small-diameter targets are used with fixed-position laser beams, the apparent variation in deposition rate (and film thickness) as measured by the crystal, caused by changes in the plume angle due to target trenching, may not accurately represent the true change in film-deposition rate. When laser beam rastering is employed the dynamic motion of the ablation plume is cyclic as the beam is scrolled back and forth across the target, but the overall effect on film thickness is taken into account in the average "tooling-factor" of the microbalance electronics. When heated substrates are used, the crystal head needs to be shielded from the thermal radiation to work properly, and above temperatures of about 600°C passively shielded microbalances will become unstable.

A possible alternative to quartz crystal microbalances are optical multichannel analyzers (OMA). An OMA would prove useful for characterizing the natural optical emission of the ablation plume, and could be useful in



optimizing laser fluence and gas pressure. Using the spectrograph of the OMA to look at the emission intensity of one specific wavelength of the plume, the detector output would provide a signal proportional to the deposition rate. Other techniques for monitoring film thickness, such as a modifications to the emission impact spectroscopy (EIS) technique (Gogol et al., 1987) or ellipsometry adapted to rotating substrates, may possibly be used as well.

#### 11.4.5 Vacuum Requirements

The vacuum requirements for large-area PLD systems are similar to other physical vapor deposition techniques. Small chamber volume for quick pump down times and a large hinged door that can provide easy access to internal chamber parts are both extremely useful. A properly sized turbopump, gas-flow controller, and a pressure-controlled gate valve are probably the best choices for most PLD applications. During deposition the local pressure should be sampled close to the ablation region using a tube connected to a capacitance monometer. Windows that transmit the laser beam should be easily changeable.

#### 11.4.6 Large-Area Particulate Reduction Schemes

One serious problem still facing PLD is the particulates that are ejected from the target surface during the ablation process. The normalized particle density (NPD), defined as the number of particles larger than a critical size found in a given film area divided by the film thickness, can vary by several orders of magnitude, depending on the target material and ablation parameters (Greer, 1989). Several approaches have been taken to reduce the NPD of PLD films. First, shorter wavelengths, low fluences in the range of 1 to 2 J/cm<sup>2</sup>, and dense targets with small grain structure have all been found to be beneficial. However, lower fluences will reduce the deposition rate. More sophisticated approaches to reduce the NPD have been tried with some success. One approach utilizes a velocity filter (Venkatesan et al., 1992) that consists of a set of rapidly rotating (~3000 rpm) vanes. This system transmits the atomic and molecular flux, but sweeps a large fraction of the slower moving particulates out of the plume. Such systems may work well for the fixed-position R/T and off-axis larger area PLD approaches, which do not use enclosed ovens for substrate heating. Special vacuum feedthroughs are required for rapidly rotating filters, and when operated in the millitorr range, the vanes will heat up due to friction with the ambient gas. Due to the large target size and laser beam motion, a velocity filter would not be practical for the raster technique. A similar approach utilizes a flat rotating shutter with an appropriately shaped slot and chops the slower moving components of the ablation plume (Kools, 1992). Using a rotation frequency of only 100 Hz, choppers have reduced the NPD by a factor of 30. With a much lower profile and rotation rate than that

of the velocity filter, the particulate chopper arrangement could be used with a rastered laser beam. A third approach to particulate reduction utilizes a secondary laser pulse that intersects the ablation plume 1 to 3 cm above the target surface (Koren et al., 1990). The secondary pulse with a wavelength of 248 nm and a fluence of about 2.5 J/cm<sup>2</sup>, was delayed 1  $\mu$ s from the primary plume-producing pulse. The in-flight particulates are irradiated by the secondary pulse, heated by electronic absorption, and tend to vaporize. This technique has not been optimized in terms of relative time delay between laser pulses, or the secondary beam's location with respect to target surface, fluence wavelength, and pulse length.

#### 11.4.7 Large-Area Multilayer Films

PLD has been successfully utilized to fabricate a variety of electronic devices based on multilayer films. Also, films with graded interfaces (gradually varying the composition from one material to another) have several applications in the optical industry. Currently, several target holders are commercially available for the deposition of multilayers. In fact, these target holders may be useful for target changes in the fixed-beam R/T approach to supply a fresh target surface when trenching becomes a problem. However, these systems utilize 25-mm-diameter targets and cannot be used in large-area systems based on laser beam rastering. Figure 11.6 is a schematic of a large-area multitarget holder currently under development to be used with the raster approach. It consists of a platen that can hold several rectangular targets 75 mm long. The target holder is

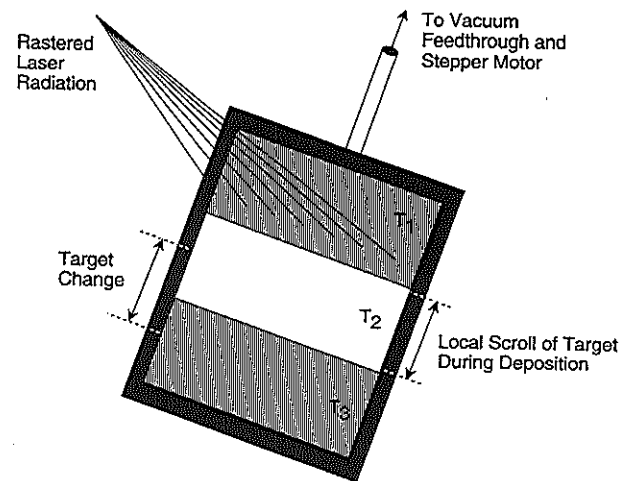


Figure 11.6. Schematic of a multiple-target holder that can be used with the large-area raster PLD approach.

coupled to a computer-controlled stepper motor providing linear motion through a vacuum flange and bellows arrangement. Once properly positioned a target can be programmed to scroll back and forth perpendicular to the direction of motion of the laser beam. Thus, a significant fraction of the target material can be used and target trenching will not occur. Offsetting the target holder with respect to the center of the substrate, as shown in Figure 11.1, will again allow smaller targets to be used. Target changes can be triggered after a given number of pulses or a set thickness value is reached. In this case the target surface is always irradiated from the same direction, which will induce cone growth on the target surface, thus reducing the deposition rate. After each deposition the targets could be rotated 180° to counteract this effect, if desired.

#### 11.4.8 Other Aspects of Large-Area PLD

A variety of issues relevant to scaling up the PLD process to large areas has just been discussed. However, there are still several issues that need to be addressed and phenomena that should be understood before PLD becomes as routine as evaporation and sputtering. For instance, the target-substrate distance will certainly need to be larger than that currently used in "standard" small-area experimental arrangements. Increasing this distance to 10 cm or more will have an impact on the deposition rate, as well as the optimum gas pressure used to grow a given material with a desired set of properties. The size, shape, and uniformity of the laser spot on target is another area where considerable work is needed. As discussed earlier, the geometry of the spot has a direct influence on the plume shape, which in turn influences the film's thickness uniformity. Target fabrication techniques that minimize particulate ejection is an area where significant improvements can be realized. An understanding of growth kinetics at the extremely high *instantaneous* mass fluxes obtained with PLD would be beneficial in understanding the quality of laser-deposited films and possibly provide insight into ways film properties may be manipulated.

### 11.5 PLD ON NONPLANAR SURFACES

Many applications will require films of various compositions to be deposited onto nonplanar substrates. Such applications could include wear coatings on ball bearings and/or bearing races, biological coatings on a variety of surgical implants, or optical coatings on domes and lenses, to name a few. Again the question must be asked "Can PLD be used to deposit nonplanar films?" The answer to this question really depends on the particular geometry of the item to be coated. Given the unique forward-directed nature of the ablation plume, PLD in fact may offer some advantages over other deposition techniques when coating certain nonplanar geometries.

One example of thin films laser-deposited onto nonplanar geometries is that

of a high-temperature superconducting cavity resonator. This application required YBCO to be deposited on the internal surface of a cylindrical cavity (Greer and Van Hook, 1990), and Figure 11.7 displays a schematic of the PLD technique used. The rotating cylindrical cavity, whose internal diameter was larger than the cavity length, was held in a small vacuum oven surrounded by heating elements and could be heated to temperatures in excess of 750°C. The cavity axis made an angle of 45° with respect to the ablation plume. The focused laser beam was rastered back and forth over a relatively narrow track on a large-diameter rotating target during deposition. A photograph of a sapphire cylinder whose internal diameter was coated with 0.5  $\mu\text{m}$  of YBCO is seen in Figure 11.8. As noted, the coating appears quite uniform over the entire internal cavity surface. Films deposited onto cylindrical YSZ substrates displayed superconducting behavior when tested as cavity resonators at temperatures of 89 K. Loaded  $Q$ 's of 10,000 at 19 GHz were measured at temperatures of 50 K for such resonators tested with copper end plates.

Another approach to coating the internal diameter (ID) of cylinders whose ID is less than the overall cylinder length is also shown in Figure 11.9. In this case the cone shaped ablation target sits inside the cylinder as shown. A focused laser beam is reflected off a programmable mirror into the cylinder ID,

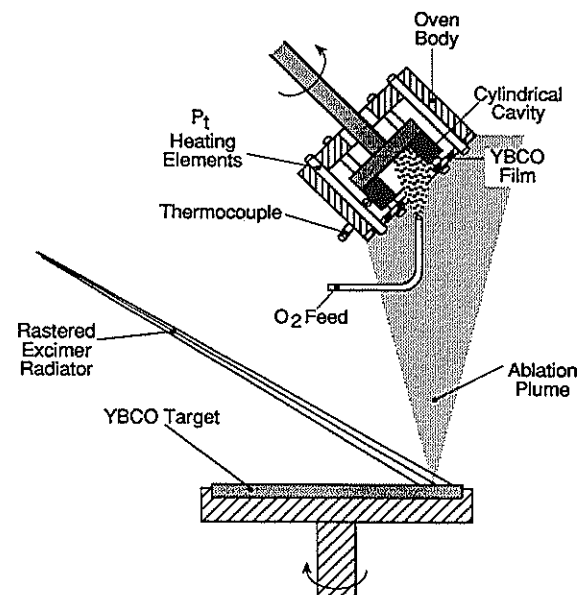
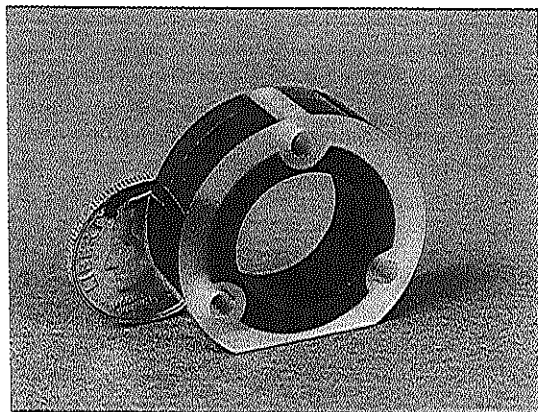
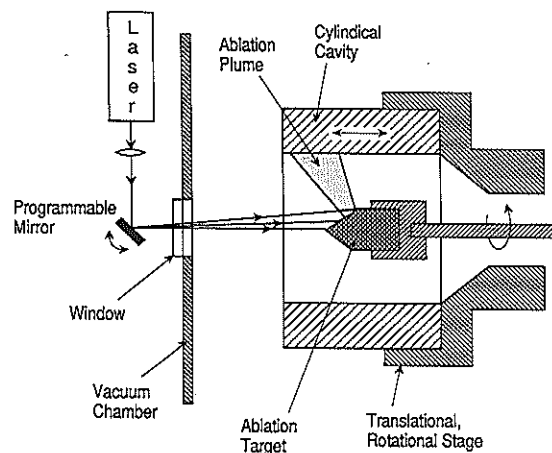


Figure 11.7. Schematic of the deposition technique used to pulse-laser-deposit YBCO films into the internal surface of a cylindrical cavity. (From Greer and Van Hook, 1990a.)



**Figure 11.8.** Photograph of a YBCO film laser deposited onto the internal surface of a sapphire cylinder. (From Greer and Van Hook, 1990.)



**Figure 11.9.** Alternative approach to the laser-depositing films on the internal surfaces of cored cylinders.

and ablates the target. Using both cylinder rotation and translation the ID can be uniformly coated. Depositing films on the outer surfaces of cylinders or other similar objects is quite straightforward.

## 11.6 FUTURE TRENDS IN LARGE-AREA PLD

Figure 11.10 shows a schematic of a potential large-area PLD design for coating single 200-mm-diameter substrates with the rastered laser beam technique. Alternatively, multiple smaller substrates could be coated simultaneously. In this system two ablation targets, each about 50 mm in diameter, are used. One target is offset slightly from the substrate's axis, and the second target is positioned to the outer edge of the substrate as shown. The laser

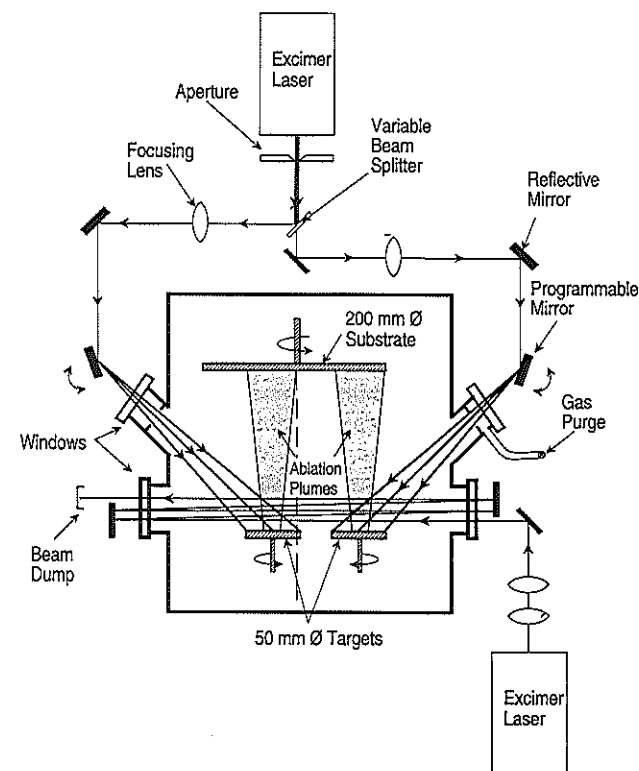


**Figure 11.10.** Schematic of a futuristic large-area PLD system.

output is apertured, broken into two beam lines with a variable energy beam splitter, each of which is focused, reflected off programmable mirrors, pass into the vacuum chamber through purged windows, and impinge upon the two rotating targets. In order to obtain a uniform film thickness with dual laser beams, either the total energy impinging on the two targets could be adjusted with the beam splitter, or the beam line for the "inside" target could include a shutter. Alternatively, two lasers operating at different repetition rates or energies could be used. The system shown also includes a particulate reduction scheme that uses the secondary laser approach. The laser output passes through a lens assembly that produces a parallel beam with the proper fluence. With the aid of external mirrors and the appropriate time delay the secondary beam can be made to pass through both laser plumes several times. In such a system each of the optical components should be AR coated to minimize loss of beam energy. Not shown in this figure are various target shields, substrate heaters, reactive ion, or gas sources [electron cyclotron resonance (ECR), ion neutral atom, etc.] if the application requires them. Also, a window port directed at the substrate would be useful for laser-assisted PLD (Horwitz et al., 1992).

As a variation on this deposition scheme, two targets with different chemistries could be used to codeposit novel film compositions. Each target would be offset an equal distance from the substrate center. Again using dual laser beams with the appropriate fluences the desired film composition could be obtained. Deposition monitors for each target material with feedback to the beam splitter or drive lasers should provide excellent control of film stoichiometry.

Few if any applications of PLD are ready to go to production. At present most PLD systems are comparatively small scale and research-based, focusing on somewhat different requirements. Several commercial research-type deposition systems are currently available from vendors in both the United States and Europe. These systems range in capability from 25 mm to 75 mm-diameter substrates using both fixed-beam or scanning techniques. Systems are available with a variety of capabilities ranging from computerized multitargets, ultrahigh vacuum (UHV) with load-lock, surface analysis, substrate heating, and various atom/ion sources, at prices ranging from \$50,000 to over \$400,000. As mentioned, these systems are all designed for research applications, and little if any data on their performance characteristics are currently available.

As the quality of various laser-deposited materials improves and useful devices are fabricated from laser-deposited films, demand for production laser-deposition systems will increase. Given the wide variety of materials deposited by the PLD process in the past few years, it is likely that several commercial applications (which cannot be adequately addressed by other physical vapor-deposition techniques) will emerge in the near future.

## REFERENCES

- Buhay, H., S. Sinharoy, B. R. Lampe, et al. (1992), *4th International Symposium on Integrated Ferroelectrics*, Monterey, March.
- Claasen, J. H., M. E. Reeves, and R. J. Soulen, Jr. (1991), *Rev. Sci. Instrum.* **62**, 996.
- Eddy, M., (1991), *Fall Meeting of the Materials Research Society*, Boston.
- Erlington, K. B., and N. J. Ianno (1990), *Mater. Res. Soc. Proc.* **191**, 115-120.
- Foltyn, S. R., R. E. Muenchausen, R. C. Dye, et al. (1991a), *Appl. Phys. Lett.* **59** (11), 1374-1376.
- Foltyn, S. R., R. C. Dye, K. C. Ott, et al. (1991b), *Appl. Phys. Lett.* **59** (5), 594-596.
- Gogol, C. A., R. A. Deutschmann, and J. C. Bean (1987), *J. Vac. Sci. Technol. A*(5), 2077-2080.
- Greer, J. A., (1989), in *Superconductivity and Applications* (H. S. Kwok, Y. Kao, and D. Shaw, eds.), Plenum, New York, pp. 117-126.
- Greer, J. A., (1992), *J. Vac. Sci. Technol. A***10**(4), 1821-1826.
- Greer, J. A., (1993), *Proc. SPIE* **1835**, 21-30.
- Greer, J. A., and H. J. Van Hook, (1990), in *Proc. SPIE*, **1377**, 79-90.
- Horwitz, J. S., D. B. Chrisey, K. S. Grabiwski, et al. (1992), *Fall Meeting of the Materials Research Society*, Boston, **285** 391-395.
- Kools J., (1992). "Laser Ablation and Deposition of Metals," Ph.D. thesis, Eindhoven University of Technology.
- Koren, G., R. J. Baseman, A. Gupta, et al. (1990), *Appl. Phys. Lett.* **56**(21), 2144-2146.
- Smith, E. J., (1991), *International Conference on Metallurgical Coatings and Thin Films*, San Diego.
- Smith, E. J., (1992), Presented at *The Fall Meetings of the Materials Research Society*, Boston, Mass.
- Venkatesan, T., X. D. Wu, R. Muenchausen, et al. (1992), *MRS Bull.* **26**(2), 54-58.
- Wu, X. D., R. E. Muenchausen, S. Foltyn, et al. (1990a) **56** 1481-1484.
- Wu, X. D., R. E. Muenchausen, S. Foltyn, et al. (1990b) **57**, 523-526.

## **PULSED LASER DEPOSITION: FUTURE TRENDS**

T. VENKATESAN

Center for Superconductivity Research  
University of Maryland  
College Park, Maryland

### **12.1 INTRODUCTION**

Pulsed laser deposition (PLD) is clearly emerging as one of the premier thin-film deposition technologies. For the case of multielemental compounds such as high-temperature superconductors, ferroelectrics, electrooptic materials, this technique has been extremely successful in a relatively short span of time. What are the limitations of this technique and how will they be overcome? What are the new materials systems to which this technique will be applicable in the future? What are the novel configurations in which this technique will be utilized in the future? In this chapter answers to questions, such as these and future directions in PLD process are speculated upon.

### **12.2 INTRINSIC ADVANTAGES OF PLD**

As the earlier chapters in this book have concluded a number of advantages over conventional deposition processes make PLD unique. Primarily the advantages of the technique stem from the fact that the dislodgements of atoms from a source is accomplished by depositing the energy at the target surface via an ultraviolet (UV) laser pulse. Unlike ions or electrons, laser beams are much easier to transport and manipulate, and since laser interaction with gas-phase species is relatively weak (unless one tailors the gaseous species to act otherwise), the dynamic range of deposition pressures is the largest compared to virtually any deposition process. Furthermore, at wavelengths of 250 nm and below virtually all materials absorb the laser beam either via linear or nonlinear processes whereby coupling of the energy is possible to most surfaces, making the process very ubiquitous. The ability of the technique to reproduce the target composition with relative ease under the appropriate

conditions is one of the key features. Thus production of a variety of multilayers involves the positioning of different targets under the laser beam and this is relatively straightforward to accomplish. The beam-target interaction is relatively independent of other system parameters such as background gas pressure or electrode assemblies, making this one of the most versatile systems to modify to incorporate enhancing features. The spatial confinement of the laser-target interaction and the subsequent confined evaporant make this an inherently clean process unlike say sputtering where the plasma of the sputter process tends to come in contact with various surfaces inside the chamber, thereby contributing to the contaminants in the film. The background gas pressures, laser energy densities, and so on, are well decoupled, giving the process a significant degree of parameter freedom. Virtually any material can be laser evaporated leading to the possibility of multilayers of a variety of materials independent of their electrical properties with superconductors at one extreme to insulators at the other extreme. The process is so different in many ways from conventional deposition processes that it will be many years before all the unique features of PLD are fully realized and utilized. Already to date the research with PLD indicates a breathtaking scenario for this technology.

### 12.3 MATERIALS TREND

In the field of superconductors PLD is being used for the fabrication of commercial quality films of Tl based superconductors (2212 TBCCO) at STI Inc. (Chang et al., 1989) and  $\text{YBa}_2\text{Cu}_3\text{O}_{7-x}$  (YBCO) at Neocera Inc. (Wu et al., 1991a, Venkatesan et al., 1992). Companies such as Conductus have used PLD to fabricate sophisticated multilayered devices and circuits based on the high temperature oxide superconductors (HTS) materials (Char et al., 1991a, b). A number of groups have used PLD for the fabrication of ferroelectric films and multilayer structures consisting of bottom crystalline electrode, epitaxial ferroelectric and the top metallization. Such devices are exhibiting state-of-the-art device properties (Ramesh et al., 1990, 1991; Ogale et al., 1990, Horwitz et al., 1993, Myers et al., 1990) as nonvolatile memories with improved cycling and fatigue properties. A number of dielectric layers have been deposited by PLD such as  $\text{Sr}_2\text{AlTaO}_6$  for microwave devices (Findikoglu et al., 1992),  $\text{CeO}_2$  as buffer layers for YBCO growth (Wu et al., 1991a),  $\text{SrTiO}_3$  layers for flux transformer coils (Miklich et al., 1990) and also for field effect devices (Walkenhorst et al., 1992) and more recently films of  $\text{SrRuO}_x$  with and without Ca doping (Eom et al., 1992). Using PLD high-quality films of  $\text{LiNbO}_3$  have been deposited on sapphire substrates with a doubling of the surface acoustic wave (SAW) velocities thus enabling a doubling of the operating frequency for devices of comparable geometric features on single crystal  $\text{LiNbO}_3$  substrates (Shibata et al., 1992). The use of laser deposited

YBCO electrodes for a  $\text{LiNbO}_3$ -based optical modulator, despite the deteriorated optical performance, exhibited superior modulation speeds suggesting another frontier for research (Imada et al., 1992). The use of PLD deposited potassium tantalate niobate (KTN) films with large electrooptic coefficients in electrically switched planar, optical modulator has been demonstrated (Yilmaz et al., 1991). Recent work with PLD on optical materials exhibiting high optical nonlinearities suggest yet another exciting avenue for the use of PLD systems.

A truly surprising activity with PLD has been in the area of semiconductor films, particularly II-VI-based materials that show high quality photoluminescence (Gaponov, 1979, 1980; Cheung and Magee, 1983, Baleva et al., 1986, Cheung and Sankur, 1988, Kwok et al., 1988a, b), showing that PLD may very well trespass into the domain much dominated today by molecular beam epitaxy (MBE) and metal organic chemical vapor deposition (MOCVD) based technologies, thereby offering a much cheaper and flexible alternative. Some of the early successful work on preparation measurements of II-VI multilayer structures were indeed demonstrated with PLD (Cheung et al., 1986) in which fractional quantized Hall effect was demonstrated for the first time in a II-VI system (Ong et al., 1987). Particularly for the integration of semiconductors with emerging technologies based on metal oxides and other multicomponent materials PLD may be the best alternative.

An exciting frontier area of thin-film-based research is that of solid-state batteries, where films of complex multicomponent ionic conductors are needed. Here is another area where PLD could potentially make an impact. Recently discovered buckyballs or fullerene form of carbon coatings can be readily prepared by PLD (Curl and Smalley, 1991). As a matter of fact, the Buckyballs were first fabricated in a pulsed laser process! Organic films such as conducting polymers, diamondlike carbon coatings and so on may also benefit from PLD (Wagal et al., 1988; Krishnaswamy et al., 1989, Collins et al., 1989, Davanloo et al., 1988). The versatility in terms of the possible materials systems seems to keep expanding with time. Bioceramics such as hydroxylapatite have been successfully deposited by PLD (Cotell et al., 1992) and there may be specific advantages such as depth dependent composition control that may be unique to PLD as opposed to competing techniques such as plasma spray which may make this a more competitive process. In addition to bio-ceramics, tribological coatings in general may be interesting avenues for PLD. A variety of hard materials such as cubic BN (Doll et al., 1991), SiC (Tench et al., 1990), TiN (Auchiello et al., 1989) and AlN (Norton et al., 1991) have been deposited by PLD. Deposition of amorphous fluoropolymer thin films by PLD suggests yet another materials direction for the application of PLD (Blanchet, 1993; Ogale, 1990). The in situ patterning capabilities of the laser makes the deposition of polymers an attractive process enhancement for in situ lithography. Thus the domain of PLD has virtually expanded to be all inclusive in terms of the kind of materials that can be deposited in the form of thin films making this one of the most versatile and innovative thin-film deposition processes to come along.



## 12.4 IMPACT OF PLD ON THIN-FILM DEPOSITION FACILITIES

In comparison to most simple deposition systems, such as the parallel magnetron or cylindrical magnetron sputtering systems the laser deposition system will be more expensive for a single deposition system owing to the cost of a laser. However, in most PLD laboratories today one sees a single laser, time shared by a number of deposition systems (as many as five per laser), laboratory space being the main constraint. Thus the cost of the laser averaged over a number of deposition systems makes the PLD process very price competitive over conventional schemes<sup>1</sup> (Greene, 1993). Thus the concept of an integrated PLD thin-film facility with the capability of a single laser firing into four or five chambers (not necessarily simultaneously), each processing different materials is a reality. In fact, by the use of beam delivery tubes backfilled with inert gases the UV laser beams can be transported over significant distances, as a result of which many surface diagnostic tools could be brought to bear on solving problems relating to thin-film growth by the simple incorporation of an ablation target and substrate holder in systems more hospitable for the diagnostic tools such as scanning tunneling microscope (STM) or atomic force microscope (AFM). Currently PLD systems are also being co-installed in MBE systems alongside conventional Knudsen cells for the evaporation of a variety of species or with off-axis magnetron sputter systems.

## 12.5 SCALE-UP TO LARGE AREAS

One of the major concerns regarding PLD in the early stages has been the ability of scaling up the process to cover large areas. Recent work on large-area deposition (Greer and van Hook, 1990; Muenchausen et al. 1991) has shown the capability of this technique to cover areas as large as two to three inches without significant deterioration of the film property and homogeneity. The PLD process is a forward directed process in the sense that the ejected material has a narrow angular distribution much like in most spray techniques (Venkatesan et al., 1988). The coverage of large areas requires the scanning of both the ejected material and the sample. In the Greer experiment the sample was rotated and the evaporated plume was scanned by moving the laser spot on the target to different positions. The disadvantage of scanning the laser beam is that some of the off-axis evaporant [whose composition is not

<sup>1</sup>The average cost of a PLD system differs from that of a sputter in terms of the cost of a sputter target, target electrode assembly and a power supply versus the cost of a laser target holder, target and a laser. The capital cost of a typical laser for R&D purposes averages about \$70,000.00. When the cost of the laser is averaged over say four different systems then the additional cost is under \$18,000 per deposition system which makes this extremely attractive compared to a sputter system where the cost per system does not come down with increase in the number of systems.

stoichiometric (Venkatesan et al., 1988)] will strike the sample, and though the intensity is small in these angular regions, for very high-quality material a scanning aperture that restricts the evaporant angle may have to be introduced.

One of the key technologies that will be developed in this regard is the substrate heater. Currently popular flat plate type heaters will have to give way to blackbody-type heaters where the sample will not have to be glued down to the holder. This advantage of the black-body heater becomes valuable for depositing films on fragile ultrathin substrates such as 25  $\mu\text{m}$  thick sapphire or 125- $\mu\text{m}$ -thick  $\text{LaAlO}_3$ , often on both sides of the wafer for a variety of device applications. The measurement of the sample temperature by simple pyrometric technique is also further simplified. One of the current problems of the blackbody heaters is the contamination introduced in the film by material that bounces off of the walls of the heater. While the film quality tends to be high in the beginning of the deposition, with passage of time, the quality deteriorates due to increased contamination of the heater walls. A solution to this problem may be the introduction of a removable sleeve of quartz or some other material that will be at a temperature closer to that of the sample. The flow of oxygen or other gases into the system may be utilized to keep the surfaces of the sleeve clean so that the sleeve temperature can afford to be comparable to that of the substrate. Once again the forward-directed plume of the PLD process is ideal for the blackbody heater, which requires a high aspect ratio cylindrical heater to maintain a homogeneous thermal profile over the substrate. The blackbody heater with a reverse entry rotating sample holder will enable rapid turnaround times for film deposition in conjunction with a load-lock system. YBCO films have been made using a black-body heater on a two-sided deposition on a 2-in-diameter wafer of  $\text{LaAlO}_3$ . The homogeneity of the transitions over both surfaces and over the entire wafer illustrates the power of this deposition technique though the problem of redeposition from the walls of the chambers causes significantly nonreproducibility in the deposition process.

## 12.6 ELIMINATION OF PARTICLES

One of the problems unique to PLD has been the deposition of micron-sized particulate matter on the films during the deposition process. The origin of these particles is an area of active research. Target inhomogeneities, laser energy density fluctuations, target texturing and so on have been identified as being responsible for part of the problem. There have been two approaches to solving the problem, one in which the production of particles is minimized, whereas in the other the ejected particles are prevented from landing on the substrate.

Minimization of target inhomogeneity, surface texture, and fluctuations in laser energy density and maximizing target density are the approaches for reducing the particle production (Foltyn et al., 1991; Davis et al., 1991). The fabrication of high-quality targets for laser deposition is indeed getting better

with time, and currently most groups avoid the surface texturing by the use of a scanned beam centered about the target center of rotation or by the use of dual beams. Currently, the excimer lasers are made with energy feedback that significantly minimizes the energy swings in the laser output and further improvements in the discharge column design (with a cheaper alternative to X-ray preionization, for example) will result in improved laser energy outputs both in terms of beam profile uniformity and constancy of the output energy.

In the alternative approach the use of an asynchronous velocity filter as demonstrated by Venkatesan et al. (1992) and Barr (1969) or the use of a synchronous-velocity filter scheme as demonstrated by Kools et al. (1992) are likely to be revisited. Both these principles use the fact that the massive particles are ejected with velocities orders of magnitude smaller than those of the atomic and molecular species. The asynchronous chopper spins with a rotation speed independent of the laser firing, whereas the synchronous chopper spins with a definite phase relationship to the laser triggering. The rotation speeds of the asynchronous chopper will have to be in the range of 20–30 krpm in order to discriminate between the atomic and diatomic species versus the larger and slower particulates. The synchronous chopper, however, can be rotated at speeds that are an order of magnitude less, thus compensating for the increased complexity of the design. While both techniques have been shown to be successful, in both cases the problem of resputtering from the surface of the velocity filter will be an issue that must be contended with.

A more recent development of which we are likely to hear more about is the off-axis PLD by the Siemens group (Holzapfel et al., 1992) where the substrate is positioned parallel to the laser-produced plume in analogy to the off-axis magnetron sputtering. In this process the number density of micron-sized particles is practically zero, with only a factor of 3 reduction in the deposition rate of the film on the substrate. Presumably, the lighter atomic and molecular species are scattered in the lateral directions much more effectively by the chamber gas, whereas the heavier particulate species undergo extremely small angular deviations in their trajectories during the collision processes, which owing to their slower velocities, are larger in number. Surprisingly, the outgrowth density associated with nonstoichiometric phases such as CuO also seem to diminish, the reason for which is not understood. The longitudinal distribution of the atomic and molecular deposits as a function of the chamber gas pressure and the substrate-plume distance needs to be studied and the effect of shock waves reflecting from a stationary gas column, and so on, needs to be understood in order to properly exploit the advantage of this technique. Clearly, this technique holds the promise of rapid deposition over large areas, on both sides and simultaneously over more than a single wafer. However, a number of problems will have to be resolved before this can become a reproducible, high throughput process.

The particulate problem if it persists will seriously limit PLD to the R&D community since many commercial-device applications require the density of micron-sized particles to be less than one per  $\text{cm}^2$ . One of the current serious

possible applications of the HTS films is in their use in multichip modules as low-resistance interconnects. The particle problem will then have to be completely eliminated in order to have zero defect density.

Recently, use of the pulsed laser beam to clean the substrate surface prior to the film deposition has yielded very high-quality films and as such is a very natural advantage of PLD whereby target holders will evolve with a mirror with the appropriate tilt held in the place of one of the targets for the purpose of wafer cleaning.

## 12.7 DEPOSITION RATE AND LAYER-BY-LAYER CONTROL

It has been clearly demonstrated that extremely high deposition rates are possible utilizing PLD. Rates as large as microns-per  $\text{cm}^2\text{-sec}$  are possible with this technique (Wu et al., 1990a,b). However, one of the problems of this technique that will manifest itself in the growth of very high-quality films is the instantaneous deposition rate that is millions of times higher than any conventional deposition process. Thus serious research is needed to investigate the PLD process that will lower the instantaneous deposition rate. This may be readily achieved by lowering the beam energy but keeping the same energy density, and increasing the repetition rate correspondingly to keep the same overall deposition rate. The problem here is that the PLD process is a highly nonlinear process with the collision kinetics of the evaporant playing a significant role in the distribution of the evaporated species. How the deposition will be affected by varying the energy per pulse is an issue that needs to be researched carefully. However, even with current deposition rates reflection high energy electron diffraction (RHEED) oscillations have been demonstrated in a number of thin-film growth process, which have consisted of layer-by-layer deposition (Kanai et al., 1991) as well as stoichiometric deposition (Chern et al., 1992). As a matter of fact, PLD is the only technique known today that can produce a fraction of monolayer of materials on a surface in a short time scale of say a microsecond. In this sense, for study of the dynamics of atoms on surfaces PLD may be an excellent enabling apparatus in combination with a fast surface analysis tool.

The quality of the surface coverage of films deposited by PLD at rates of 0.1–1.0 Å/sec are surprisingly good as a result of which excellent superlattices have been prepared by this technique by a number of groups (Li et al., 1990; Lowndes et al., 1990) with very sharp interfaces (Pennycook et al., 1991) and high critical current densities in 8 T fields even in unit cells thick films of superconductors (Kwon et al., 1993). One of the advantages of PLD is the ease of preparing multilayers of fairly complex materials by simply having a motorized target holder positioning the desired target in the laser beam for the appropriate duration. One can in fact use segmented targets instead of a target carousel so that the laser irradiation can be controlled by appropriate triggering as was used in the preparation of superlattices (Li et al., 1990). Also

electrooptic films of potassium tantalate niobate have been prepared where a segment of potassium nitrate was included along with a potassium niobate titanate target to compensate for the potassium loss at the substrate (Yilmaz et al., 1991).

## 12.8 IN SITU DEPOSITION, PROCESSING, AND ANALYSIS FACILITY

Pulsed excimer lasers have been the tools with which a variety of novel materials processing schemes have been developed. Laser-assisted gas-phase deposition of metal (Boyd et al., 1990) or insulator lines (Boyd et al., 1990), laser-assisted etching both chemically and thermally (Boyd et al., 1990), laser-induced doping of specific impurities (Boyd et al., 1990) and so on have all been demonstrated. Recently, there has been a trend toward the development of submicron projection lithographic tools based on excimer lasers making excimer lasers an invaluable accessory to in-situ processing of surfaces (Boyd et al., 1990). Thus integration of a PLD system with a variety of these tools for in-chamber processing of devices, particularly those that are sensitive to environmental degradation, is a likely future trend. An example of such a device may be a superconductor-insulator-superconductor (SIS) junction made from a high  $T_c$  superconductor where the extremely short coherence length has made it very difficult to fabricate such a device.

An important issue to be discussed at this stage is that of in situ analysis of the beam-target, plume-background gas and plume substrate interactions. Spectroscopic techniques may be the most effective way to monitor both the plume-gas and plume-substrate interactions since a significant amount of characteristic optical radiations are produced at the various stages (Geyer et al., 1989; Girault et al., 1989, 1990; Wu et al., 1989). Techniques such as in situ time of flight apparatus have been used for mass analysis (Lynds et al., 1988, 1989) and more recently in situ time evolved pictures of the laser produced plume have also been used for understanding the process (Dye et al., 1993; Gupta et al., 1991a, b). Some of these analysis tools may be incorporated with actual working systems. The plume-substrate interaction is currently best studied by RHEED (Kanai et al., 1991; Chern et al., 1992) though simple reflectivity studies of surfaces at Brewster's incidence angle may yield results more simply and economically. Simple optical reflection techniques have been used in CVD growth studies where step-like features have been observed in the reflected signal corresponding to growth of full unit cells of YBCO (Oda et al., 1993). Such work remains to be demonstrated with PLD.

## 12.9 ENHANCEMENTS AND ACCESSORIES

Since the process of material ejection at the target surface for PLD is not that sensitive to the background gas pressure or other system parameters, it is

relatively easy to incorporate other accessories such as an electron or ion gun or even a sputter system in a PLD system. Ions can be used in a deposition chamber for cleaning of the substrate surface, for etching patterns in surface layers (say with a focused ion beam), for promoting adhesion of the growing layer, enhancing crystallization by increasing the surface temperature locally, or helping create in-plane crystalline orientation. Recent work (Iijima et al., 1992) has clearly shown the power of ion-assisted evaporation in helping to create in-plane orientation on polycrystalline substrates, namely yttria-stabilized-zirconia (YSZ) on polycrystalline YSZ followed by YBCO deposition. Clearly, for crystalline thin film growth on a variety of substrates, this technique is indeed the way to the highest quality films on nonorienting substrates. Integrated ion-assisted PLD systems are going to become fairly common in thin-film growth environments. Such schemes as the combination of an ion milling station with a PLD system may enable the in situ growth of a variety of interesting structures, which subsequent to a laser patterning process, can be ion beam planarized with further PLD-assisted growth of overlayers. For high-temperature superconductors this is very essential since on nonplanarized features or on polycrystalline surfaces the superconducting film will tend to exhibit weak links (Harshavardhan et al., 1991).

Novel innovations in PLD systems are likely to occur, particularly with the advent of newer UV beam transport technologies. Some of the interesting configurations that are possible with PLD are simple techniques for coating the inner walls of chambers by having a moving stage with a target and a beam delivery port scanned inside a closed volume. Yet another novel PLD configuration is one where the target and samples are located inside a furnace, whereby the system is inside the heater as opposed to the conventional approach of putting the heater inside the deposition system.

## 12.10 REDUCTION IN FILM CRYSTALLIZATION TEMPERATURES

The holy grail of HTS film growth has been to come up with viable techniques that can lead to a significant reduction in the film-deposition temperature without any deterioration of the film properties. A number of schemes involving plasma assisted deposition (Witanachi et al., 1988; Singh et al., 1989), substrate biasing and so forth have been reported with mixed success. One of the assets of the PLD process is the energetic species produced in the evaporation process where particles with superthermal energies are produced (Geohegan and Mashburn, 1989; Dye et al., 1993; Zheng et al., 1989). However, at the pressures at which high-temperature superconducting films are made, these energetic particles lose a substantial amount of their energies in collisional processes, whereby they arrive at the substrate with close to thermal energies (Geohegan and Mashburn, 1989). The high oxygen ambient pressure is needed for both the gas-phase plume reaction and for maintaining the oxygen stoichiometry of the film. Ozone-assisted deposition and the use of

pulsed oxygen sources have been efforts in the right direction with encouraging results (Gupta et al., 1991b; Chern et al., 1992). However, this direction needs to be pursued further. For low-pressure deposition of epitaxial films, PLD has a distinct advantage in lowering the deposition temperature. So experiments at low pressures with accelerating voltages to produce a situation analogous to ion-assisted deposition needs to be done to fully exploit and optimize this technique.

## 12.11 CONCLUSION

The viability of PLD as a deposition technique of the future is clearly demonstrated by the rapidity with which this technique is being adopted by the thin-film community. As further advantages of this technique are discovered and its problems resolved, its popularity will only increase. When eventually and inevitably the semiconductor community (particularly for materials such as the II-VIs where conventional deposition techniques have not been so easy) begins to recognize PLD as a viable, economical choice over existing techniques (at least in the R&D community), then PLD would indeed have arrived!

## REFERENCES

- Auciello, O., T. Barnes, S. Chevacharoenkul, A. F. Schreiner, and G. E. McGuire (1989), *Thin Films* **181**, 65.
- Baleva, M. I., M. H. Maksimov, S. M. Metev, and M. S. Sendova (1986), *J. Mater. Sci. Lett.* **5**, 533.
- Barr, W. P. (1969), *J. Phys.* **E2**, 2.
- Blanchet, G. B. (1993), *Appl. Phys. Lett.* **62**, 479.
- Boyd, I. W., E. Fogarassy, and M. Stuke, editors (1990), in *Surface Processing and Laser Assisted Chemistry*, Proceedings, 1990 E-MRS Spring Conference, Strasbourg, France, North Holland, Amsterdam, and New York.
- Chang, L. D., M. J. Moscovitz, R. B. Hammond, M. M. Eddy, W. L. Olson, D. D. Casavant, E. J. Smith, M. Robinson, L. Drabeck, and G. Gruner (1989), *Appl. Phys. Lett.* **55**, 188.
- Char, K., M. S. Colclough, S. M. Garrison, N. Newman, and G. Zaharchuk (1991a), *Appl. Phys. Lett.* **59**, 733.
- Char, K., M. S. Colclough, L. P. Lee and G. Zaharchuk (1991b), *Appl. Phys. Lett.* **59**, 2177.
- Chern, M. Y., A. Gupta, and B. W. Hussey (1992), *Appl. Phys. Lett.* **60**, 3045.
- Cheung, J. T., and T. Magee (1983), *J. Vac. Sci. and Technol.* **A1**, 1604.
- Cheung, J. T., N. Niizawa, J. Moyle, N. P. Ong, B. M. Paine, and T. Vreeland Jr. (1986), *J. Vac. Sci. Technol.* **A4**, 2086.
- Cheung, J. T. and H. Sankur (1988), *CRC Crit. Rev. Solid State Mater. Sci.* **15**, 63.
- Collins, C. B., F. Davanloo, E. M. Jeungerman, W. R. Osborn, and D. R. Jander (1989), *Appl. Phys. Lett.* **54**, 216.
- Cotell, C. M., D. B. Chrisey, K. Grabowski, J. A. Sprague, and C. R. Gossett (1992), *J. Appl. Biomater.* **3**, 87.
- Curl, R. F., and R. E. Smalley (1991) *Sci. Am.* (October), 54.
- Davanloo, F., E. M. Jeungerman, D. R. Jander, T. J. Lee, and C. B. Collins (1988), *J. Appl. Phys.* **54**, 216.
- Davis, M. F., J. Wosik, K. Forster, S. C. Deshmukh, H. R. Rampersad, S. Shah, P. Siemsen, J. C. Wolfe, and D. J. Economu (1991), *J. Appl. Phys.* **69**, 7182.
- Doll, G. L., J. A. Sell, C. A. Taylor II, and R. Clarke (1991), *Phys. Rev.* **B43**, 6816.
- Dye, R. C., R. Brainard, S. R. Foltyn, R. E. Muenchausen, X. D. Wu, and N. S. Nogar (1993), *Mater. Res. Soc. Proc.* **285**, 15.
- Eom, C. B., R. J. Cava, R. M. Fleming, J. M. Phillips, R. B. van Dover, J. H. Marshall, J. W. P. Hsu, J. J. Krajewski, and W. F. Peck, Jr. (1992), *Science*, **258**, 2165.
- Findikoglu, A. F., S. Bhattacharya, C. Doughty, M. S. Pambianchi, Q. Li, X. X. Xi, S. M. Anlage, R. E. Fahey, A. J. Strauss, Julia M. Phillips, and T. Venkatesan (1992), *Appl. Phys. Lett.* **61**, 1718.
- Foltyn, S. R., R. C. Dye, K. C. Ott, K. M. Hubbard, W. Hutchinson, R. E. Muenchausen, R. C. Estler, and X. D. Wu (1991), *Appl. Phys. Lett.* **59**, 594.
- Gapanov, S. V., B. M. Luskin, and N. N. Salaschenko (1979), *Sov. Tech. Phys. Lett.* **5**, 210.
- Gapanov, S. V., B. M. Luskin, and N. N. Salaschenko (1980), *Sov. Phys. Semicond.* **14**, 873.
- Geohegan, D. B., and D. N. Mashburn (1989), *Appl. Phys. Lett.* **55**, 2766.
- Geyer, T. J., and W. A. Weimer (1989), *Appl. Phys. Lett.* **54**, 469.
- Girault, C., D. Damiani, J. Aubreton, and A. Catherinot (1989), *Appl. Phys. Lett.* **54**, 2035.
- Girault, C., D. Damiani, C. Champeaux, P. Marchet, J. P. Mercurio, J. Aubreton, and A. Catherinot (1990), *Appl. Phys. Lett.* **56**, 1472.
- Greene, S., Neocera Inc. (1993), priv. comm.
- Greer, J. A., and J. B. Van Hook (1990), *SPIE Proc.* **1377**, 79.
- Gupta, A., B. Braren, K. G. Kasey, B. W. Hussey, and R. Kelly (1991a), *Appl. Phys. Lett.* **59**, 1302.
- Gupta, A., and B. W. Hussey (1991b), *Appl. Phys. Lett.* **58**, 1211.
- Harshavardhan, K. S., R. Ramesh, T. S. Ravi, S. Sampere, A. Inam, C. C. Chang, G. Hull, M. Rajeswari, T. Sands, T. Venkatesan, and M. Reeves (1991), *Appl. Phys. Lett.* **59**, 1638.
- Holzappel, B., B. Roas, L. Schultz, P. Bauer, and G. Saemann-Ischenko (1992), *Appl. Phys. Lett.* **61**, 3178.
- Horwitz, J. S., D. B. Chrisey, K. S. Grabowski, C. A. Carosella, P. Lubitz, and C. Edmondson, (1993), *Mater. Res. Soc. Proc.* **285**, 391.
- Iijima, Y., N. Tanabe, O. Kohno, and Y. Ikeno (1992), *Appl. Phys. Lett.* **60**, 769.

- Imada, K., K. Yoshiara, F. Uchikawa, H. Watarai, T. Mizuochi, and T. Kitayama (1992), Proceedings, International Superconductivity Symposium, Nov. 16-19, Kobe, Japan.
- Kanai, M., T. Kawai, and S. Kawai, (1991), *Appl. Phys. Lett.* **58**, 771.
- Kools, J. C. S., C. J. C. M. Nillesen, S. H. Brongersma, E. van de Reit, and J. Dieleman (1992), *J. Vac. Sci. and Technol.* **A10**, 1809.
- Krishnaswamy, J., A. Rengan, J. Narayan, K. Vedam, and C. J. McHargue (1989), *Appl. Phys. Lett.* **54**, 2455.
- Kwok, H. S., J. P. Sheng, S. Witanachi, P. Mattocks, L. Shi, Q. Y. Ying, X. W. Wang, and D. T. Shaw (1988a), *Appl. Phys. Lett.* **52**, 1095.
- Kwok, H. S., J. P. Sheng, S. Witanachi, L. Shi, and D. T. Shaw (1988b), *Appl. Phys. Lett.* **52**, 1815.
- Kwon, C., Di Li, X. X. Xi, S. Bhattacharya, C. Doughty, T. Venkatesan, H. Zhang, J. W. Lynn, J. L. Peng, Z. Y. Li, N. D. Spencer, and K. Feldman (1993), *Appl. Phys. Lett.* **62**, 1289.
- Li, Q., X. X. Xi, X. D. Wu, A. Inam, S. Vadlamannati, W. L. McLean, T. Venkatesan, R. Ramesh, D. M. Hwang, J. A. Martinez, and L. Nazar (1990), *Phys. Rev. Lett.* **64**, 3086.
- Lowndes, D. H., D. P. Norton, and J. D. Budai (1990), *Phys. Rev. Lett.* **65**, 1160.
- Lynds, L., B. R. Weinberger, G. G. Peterson, and H. A. Krasinski (1988), *Appl. Phys. Lett.* **52**, 320.
- Lynds, L., B. R. Weinberger, and D. M. Potrepka, Photochemistry in Thin Films (1989), *SPIE* **1056**, 249.
- Miklich, A. H., J. J. Kingston, P. Lerch, F. C. Wellstood, and John Clarke (1990), *Appl. Phys. Lett.* **56**, 2240.
- Muenchausen, R. E., R. C. Dye, X. D. Wu, L. Luo, and D. W. Cooke (1991), *Appl. Phys. Lett.* **59**, 1374.
- Myers, E. R., and A. I. Kingon (1990), *Mater. Res. Soc. Proc.* **200**.
- Norton, M. G., P. G. Kotula, and C. B. Carter (1991), *J. Appl. Phys.* **70**, 2871.
- Oda, S., K. Sakai, and H. Zama (1993), Proceedings, Sixth Topical Meeting on Crystal Growth Mechanisms, Awara, Japan, Jan. 20-22.
- Ogale, S. B., S. M. Kanetkar, S. M. Chaudhari, V. P. Godbole, R. D. Vispute, S. K. Date, and A. R. Moghe (1990), *Ferroelectrics* **102**, 85.
- Ogale, S. B., Chapter No. x, Same book.
- Ong, N. P., J. K. Moyle, J. Bajaj, and J. T. Cheung (1987), *J. Vac. Sci. and Technol.* **A5**, 3079.
- Pennycook, J., M. F. Chisholm, D. E. Jesson, D. P. Norton, D. H. Lowndes, R. Feenstra, H. R. Kerchner, and J. O. Thomson (1991), *Phys. Rev. Lett.* **67**, 765.
- Ramesh, R., K. Luther, B. Wilkens, D. L. Hart, E. Wang, J. M. Tarascon, A. Inam, X. D. Wu, and T. Venkatesan (1990), *Appl. Phys. Lett.* **57**, 1505.
- Ramesh, R., A. Inam, B. Wilkens, W. K. Chan, D. L. Hart, K. Luther, and J. M. Tarascon (1991), *Science* **252**, 944.
- Shibata, Y., K. Kaya, K. Akashi, M. Kanai, T. Kawai, and S. Kawai (1992), *Appl. Phys. Lett.* **61**, 1000.
- Singh, R. K., J. Narayan, A. K. Singh, and J. Krishnaswamy (1989), *Appl. Phys. Lett.* **54**, 2271.
- Tench, R. J., M. Balooch, A. L. Connor, L. Bernardez, B. Olson, M. J. Allen, and W. J. Siekhaus (1990), *Mater. Res. Soc. Proc.* **191**, 61.
- Venkatesan, T., X. D. Wu, A. Inam, and J. B. Wachtman (1988), *Appl. Phys. Lett.* **52**, 1193.
- Venkatesan, T., X. D. Wu, R. Muenchausen, and A. Pique (1992), *MRS Bull.* **XVII**, 54.
- Wagal, S. S., E. M. Jeungerman, and C. B. Collins (1988), *Appl. Phys. Lett.* **53**, 187.
- Walkenhorst, A., C. Doughty, X. X. Xi, S. N. Mao, Q. Li, and T. Venkatesan (1992), *Appl. Phys. Lett.* **60**, 1744.
- Witanachi, S., H. S. Kwok, X. W. Wang, and D. T. Shaw (1988), *Appl. Phys. Lett.* **53**, 234.
- Wu, X. D., B. Dutta, M. S. Hegde, A. Inam, T. Venkatesan, E. W. Chase, C. C. Chang, and R. Howard, (1989), *Appl. Phys. Lett.* **54**, 179.
- Wu, X. D., R. E. Muenchausen, S. Foltyn, R. C. Estler, C. Flamme, N. Nogar, A. R. Garcia, J. Martin, and J. Tesmer (1990a) *Appl. Phys. Lett.* **56**, 1481.
- Wu, X. D., R. E. Muenchausen, S. Foltyn, R. C. Estler, R. C. Dye, A. R. Garcia, N. Nogar, P. England, R. Ramesh, D. M. Hwang, T. S. Ravi, C. C. Chang, T. Venkatesan, X. X. Xi, Q. Li, and A. Inam (1990b), *Appl. Phys. Lett.* **57**, 523.
- Wu, X. D., R. E. Muenchausen, N. S. Nogar, A. Pique, R. Edwards, B. Wilkens, T. S. Ravi, D. M. Hwang, and C. Y. Chen (1991a), *Appl. Phys. Lett.* **58**, 304.
- Wu, X. D., R. C. Dye, R. E. Muenchausen, S. R. Foltyn, M. Maley, A. D. Rollet, A. R. Garcia, and N. S. Nogar (1991b), *Appl. Phys. Lett.* **58**, 2165.
- Yilmaz, S., T. Venkatesan, and R. Gerhard-Multhaupt (1991), *Appl. Phys. Lett.* **58**, 2479.
- Zheng, J. P., Q. Y. Ying, S. Whitanachi, Z. Q. Huang, D. T. Shaw, and H. S. Kwok (1989), *Appl. Phys. Lett.* **54**, 954.